uc3m | Universidad Carlos III de Madrid

TESIS DOCTORAL:

Analysis of the expansion of a plasma thruster plume into vacuum

Autor:
Filippo Cichocki

Director:
Eduardo Ahedo Galilea

Co-director y tutor:
Mario Merino Martínez

DEPARTAMENTO DE BIOINGENIERÍA E INGENIERÍA AEROESPACIAL

Leganés, Madrid, 26 de septiembre de 2017

TESIS DOCTORAL

Analysis of the expansion of a plasma thruster plume into vacuum

Autor: Filippo Cichocki

Director: Eduardo Ahedo Galilea

Co-director y tutor: Mario Merino Martínez

Firma del Tribunal Calificador:

		Firma
Presidente:	_____	_____
Vocal:	_____	_____
Secretario:	_____	_____
Calificación:	_____	

Leganés, 26 de septiembre de 2017

Aknowledgments

Il primo ringraziamento è diretto ai miei genitori Fabrizio e Nelvia. Aver cominciato questa avventura in Spagna, 4 anni fa e dopo altrettanti di lavoro in Deimos-Space, sempre a Madrid, può essere stato difficile per voi che, probabilmente, avreste preferito che tornassi in Italia. Pertanto, vi ringrazio con tutto il cuore per avermi sempre incoraggiato, nonostante tutto, a fare questo passo ! Inoltre voglio ringraziare mio fratello Mattia e mia cognata Cecilia per il bellissimo regalo di avermi fatto zio di una bellissima bambina. Nonostante non abbia potuto trascorrere lunghi periodi con Maya, vivendo a Madrid, ogni volta che sono tornato a visitarvi, è sempre stato con tanta allegria e voglia di vedere come era cresciuta nel frattempo :). A voi e a papà e mamma, dedico pertanto questo lavoro. Vi voglio bene!

Pasando al español, quiero agradecer a mi tutor Mario y mi director Eduardo por la extensa e intensa labor de revisión de este trabajo de investigación, gracias a la cual su calidad ha mejorado enormemente. Un agradecimiento especial quiero dirigirlo a *"De-Bug finder"* Adrián, gran amigo y compañero de trabajo, gracias al cual he podido encontrar y solucionar una parte importante de los bugs del código híbrido aquí presentado. Además, quiero dar las gracias a Álvaro, por haber sido un inmejorable compañero de meriendas y trabajo durante estos últimos meses de doctorado, y haber aguantado con gran resistencia los altos picos de estrés que han caracterizado mis últimos meses de tesis. Mil gracias !!

Finalmente, una mención particular la merece mi grupo de amigos y amigas de vóley-playa. Gracias a este deporte y a vuestra compañía en los entrenamientos y en los torneos por España, he conseguido desconectar y pasarlo súper bien, cada vez que era necesario. Gracias a mi compi de equipo Raúl, con el cual comparto fecha de nacimiento, pasión por el vóley-playa, carrera aeroespacial, con la excepción de esa sana locura que me ha llevado a empezar un doctorado en propulsión espacial con plasmas :)

Gracias a todos vosotros, grazie mille a tutti !

Abstract

The analysis of the interaction between a plasma plume and a satellite is gradually becoming a very demanded task in the space industry, given the increasing use of electric propulsion. In fact, the plasma plumes generated by the electric thrusters can damage sensitive spacecraft components, such as the solar arrays or onboard optical sensors. Moreover, plasma plumes can be used to one's benefit in the context of the ion beam shepherd technique for space debris removal, in which a shepherd spacecraft relocates a debris object to a different orbit, by directing towards it a plasma plume, at an operational distance of several meters.

This thesis focuses on the numerical study of the expansion of a plasma thruster plume into vacuum and its interaction with the satellite and any downstream object. Two simulation codes have been developed.

The first code, named EASYPLUME, is based on an axisymmetric two-fluid plasma plume model and allows to quickly estimate the plasma plume properties farther downstream. With this code the physics of the plume expansion has been investigated, understanding its dependence on the most important plume parameters, such as the divergence angle, the ion Mach number, and the electron cooling rate. Moreover, the code has been used in the context of the ion beam shepherd technique to estimate the force transmission to a space debris object, and optimize the overall electric propulsion subsystem of the shepherd spacecraft.

The second code, named EP2PLUS, is a three-dimensional hybrid particle-in-cell/fluid code that simulates the complex interaction between a plasma plume, the spacecraft and other objects. The most relevant modeling novelties regard the electron model, which enables the computation of the electric currents in the plume, and the treatment of quasineutral and non-neutral plasma regions. This code has been applied to study both the satellite-plume interaction and a reference ion beam shepherd scenario. In the latter, several operational problems have been evaluated: the ion backscattering towards the shepherd satellite, the sputtering of the debris object (due to the impingement of hypersonic ions), the backsputtering contamination of the spacecraft, and the electric charging of both the satellite and the target debris.

Finally, the report of an experimental campaign, carried out during my PhD visit at the "Laboratoire de Physique des Plasmas" (Paris) and aiming at characterizing the plasma plume of the PEGASES plasma thruster, completes this work.

Resumen

El estudio de la interacción entre el satélite y un chorro de plasma producido por un propulsor eléctrico se está convirtiendo en un análisis muy demandado en la industria espacial, debido al uso cada vez más extenso de la propulsión eléctrica. Dicho chorro puede dañar seriamente componentes sensibles del satélite, como los paneles solares o los sensores ópticos. Por otra parte, puede utilizarse activamente en el contexto de la técnica de eliminación de desechos espaciales conocida como "ion beam shepherd". Esta técnica se basa en trasladar dichos objetos a una órbita diferente, por medio de la presión producida por el impacto de los iones de un chorro de plasma dirigido hacia ellos, desde una distancia de varios metros.

Esta tesis se centra en el estudio numérico de la expansión de un chorro de plasma generado por un propulsor eléctrico en el vacío, y de su interacción con otros objetos. Con este propósito, se han desarrollado dos códigos de simulación.

El primero, llamado EASYPLUME, se basa sobre un modelo axial simétrico con dos fluidos (iones y electrones) y permite estimar rápidamente las propiedades del chorro de plasma a grandes distancias aguas abajo. Con este código, se ha estudiado la física de la expansión del plasma en detalle, comprendiendo la influencia de parámetros como el ángulo de divergencia, el número de Mach y la tasa de enfriamiento electrónico. Además, el código ha sido utilizado en el contexto del "ion beam shepherd" para estimar la fuerza transmitida al objeto y optimizar el sistema de propulsión eléctrica del satélite.

El segundo, llamado EP2PLUS, es un código tridimensional híbrido PIC-fluido que simula la interacción compleja entre un chorro de plasma, el satélite y otros objetos. Entre las novedades más relevantes destacan el nuevo modelo electrónico, que permite estudiar las corrientes eléctricas en el plasma, y el tratamiento de regiones quasi-neutras y no neutras. Este código se ha empleado en el estudio de la interacción chorro-satélite y en el análisis de la interacción chorro-satélite-objeto en el contexto del "ion beam shepherd" para una misión de referencia. En este último estudio, diferentes problemas operacionales han sido evaluados numéricamente: el retorno de los iones lentos hacia el satélite, la emisión de partículas erosionadas desde la superficie del desecho espacial (debido al impacto de los iones hipersónicos), la contaminación por difusión de dichas partículas hacia el satélite, y la acumulación de carga eléctrica de éste y del objeto espacial.

Finalmente, el informe de una campaña de caracterización experimental del chorro del motor de plasma PEGASES completa este trabajo. Dicha campaña se realizó durante mi estancia de visita al "Laboratoire de Physique des Plasmas" en París.

List of publications

The following is a list of journal publications, produced in the frame of this thesis:

- M. Merino, F. Cichocki, and E. Ahedo. Collisionless plasma thruster plume expansion model. *Plasma Sources Sciences and Technology*, 24(3):035006, 2015.
- A. Alpatov, F. Cichocki, A. Fokov, S. Khoroshylov, M. Merino, and A. Zakrzhevskii. Determination of the force transmitted by an ion thruster plasma plume to an orbital object. *Acta Astronautica*, 119:241-251, 2016.
- F. Cichocki, M. Merino, E. Ahedo, M. Smirnova, A. Mingo, and M. Dobkevicius. Electric propulsion subsystem optimization for "Ion Beam Shepherd" missions. *Journal of Propulsion and Power*, 33(2):370-378, 2017.
- F. Cichocki, A. Domínguez, M. Merino, and E. Ahedo. Hybrid 3D model for the interaction of plasma thruster plumes with nearby objects. *Plasma Sources Sciences and Technology*, 26(12):125008, 2017.
- F. Cichocki, M. Merino, and E. Ahedo. Spacecraft-plasma-debris interaction in an ion beam shepherd mission. Submitted to *Acta Astronautica*, 2017.

Moreover, the following contributions in conference proceedings have been made:

- M. Ruiz, I. Urdampilleta, C. Bombardelli, E. Ahedo, M. Merino, and F. Cichocki. The FP7 LEOSWEEP project: improving Low Earth Orbit security with enhanced electric propulsion. In *Space Propulsion Conference*, Cologne, Germany, May 19-22, 2014.
- M. Merino, F. Cichocki, and E. Ahedo. Plasma thruster beam expansion and impingement in space debris. In 13$^{\text{th}}$ *Spacecraft Charging Technology Conference*, Pasadena, California, USA, June 23-27, 2014.
- F. Cichocki, M. Merino, and E. Ahedo. Modeling and simulation of EP plasma plume expansion into vacuum. In 50$^{\text{th}}$ *AIAA/ASME/SAE/ASEE Joint Propulsion Conference*, Cleveland, Ohio, USA, July 28–30, 2014.
- F. Cichocki, M. Merino, E. Ahedo, Y. Hu, and J. Wang. Fluid vs PIC modeling of a plasma plume expansion. In 34$^{\text{th}}$ *International Electric Propulsion Conference* and 6$^{\text{th}}$ *Nano-satellite Symposium*, Yogo-Kobe, Japan, July 6-10, 2015.

- F. Cichocki, M. Merino, E. Ahedo, D. Feili, and M. Ruiz. Electric propulsion subsystem optimization for "Ion Beam Shepherd" missions. In 34$^{\text{th}}$ *International Electric Propulsion Conference* and 6$^{\text{th}}$ *Nano-satellite Symposium*, Yogo-Kobe, Japan, July 6-10, 2015.
- F. Cichocki, A. Domínguez, D. Pérez-Grande, M. Merino, E. Ahedo, and P. Fajardo. Hybrid particle codes for electric propulsion. Poster session at 14$^{\text{th}}$ *Spacecraft Charging Technology Conference*, ESTEC, Noordwijk, The Netherlands, April 4–8, 2016.
- F. Cichocki, A. Domínguez, M. Merino, and E. Ahedo. A 3D hybrid code to study electric thruster plumes. In *Space Propulsion Conference*, Rome, Italy, May 2–6, 2016.
- F. Cichocki, D. Rafalskyi, A. Aanesland, and M. Merino. The plume neutralization process of the PEGASES thruster. In *Space Propulsion Conference*, Rome, Italy, May 2–6, 2016.

Glossary

List of symbols

The following symbols are used throughout this work. When multiple subscripts, superscripts or accents are used and are not explained here, refer to the "subscripts", "superscripts" and "accents" sections for their meaning.

$\mathbf{1}$	Unit vector
α	95% ion current divergence angle of the plume. In the current work, it is defined as the exact slope with respect to the plume axis of the streamtube that contains 95% of the total ion current
β_{tot}	Parameter giving the ratio between the available energy in the plume (pressure and directed motion) and in the external magnetic field
$\beta_1, \beta_2, \beta_s$	Empirical coefficients used to model the dependency of the thruster divergence angle on the beam voltage (β_1), the RF input power on the thruster radius (β_2), and the backscattered particle kinetic energy on the impact angle (β_s)
γ	Electron polytropic cooling coefficient or rate
δ	Divergence angle tangent profile along the normalized radius (with the radius of the 95% ion current streamline), at the initial plane of the far-region
$\delta\phi$	Electric potential correction, required to yield sonic conditions, in the hybrid code context
δn	Plasma density correction, applied by the Bohm's condition forcing algorithm, in the hybrid code context
$\Delta\phi$	Electric potential change or drop (depending on the context)
Δk	Number of time steps, in the hybrid code context
Δl	Linear size of the mesh cell, in the hybrid code context
Δm	Variation of mass or generated mass

Δt	Time interval
ΔV	PIC cell physical volume, or associated volume to a mesh node, in the hybrid code context. Equivalent shepherding phase delta-V (ΔV_{eq}), in the IBS mission study context
$\boldsymbol{\epsilon}$	Error vector along the three physical coordinates, in the computational coordinates estimation algorithm of the hybrid code
ϵ_0	Dielectric constant of a vacuum
ϵ	Relative (ϵ_{rel}) or absolute (ϵ_{abs}) error of a generic algorithm
ϵ_l	Residual error in the momentum balance equation, in the SSM
ε	Expansion parameter used in the AEM, equal to $1/M_0^2$
$\varepsilon_n, \varepsilon_f, \varepsilon_{max}$	Non-neutrality ratio at the mesh nodes (ε_n), cell-faces centers (ε_f), and its maximum value (ε_{max}) below which the node or face is considered quasineutral, in the hybrid code context
(ζ, η)	Non-dimensional coordinates in the axisymmetric fluid model, normalized with the radius R_0 of the 95% ion current streamline, at the initial plane. ζ is along the plume axis, while η labels the streamlines (curved streamlines in the SSM, straight zeroth order streamlines in the AEM) and represents their normalized radius at the initial plane.
η_B	Momentum transfer efficiency of the ion beam shepherd
η_{div}	Plume divergence efficiency
η_m	Propellant utilization efficiency of the electric thruster
η_{PPU}	Power conversion efficiency of the power processing unit
η_T	Total thrust efficiency of an electric thruster
θ	Azimuthal angle (in axisymmetric model) or angle between the plume axis, the plume vertex and the scanning probe (in the divergence efficiency measurement)
Λ	Constant appearing in the electron-ion collision frequency formula
λ_c	Collision mean free path
λ_d	Debye length
μ_0	Magnetic permeability in a vacuum
$\Pi(i, j, k, p)$	Macro-particles track (4-D matrix) containing, for each population, the IDs of the macro-particles located inside each PIC cell. The indices (i, j, k) specify the cell, while p is used for the macro-particles IDs

ν	Non-dimensional density profile along the normalized radius (with the radius of the 95% ion current streamline), at the initial plane of the far-region
ν_{ij}, ν_e	Momentum transfer frequency from the i^{th} to the j^{th} population (ν_{ij}), and total momentum transfer collision frequency for electrons (ν_e)
$\boldsymbol{\xi} = (\xi, \eta, \zeta)$	Computational coordinates vector, in the hybrid code context
ρ_c	Electric charge density
ρ_F	Probability distribution function of the state of an ensemble of elementary particles
ρ_{pwr}	Specific mass of the power generation system, per unit power
Σ	Plasma plume volume
σ	Collision cross section
σ_e	Electron conductivity
σ_s	Surface charge density
$\boldsymbol{\tau}$	Torque vector
υ	Non-dimensional axial velocity profile along the normalized radius (with the radius of the 95% ion current streamline), at the initial plane of the far-region
ϕ	Electric potential
$\boldsymbol{\omega}_B$	Angular velocity vector associated to the Larmor motion of a charged particle (around the magnetic field)
Ω	Velocity space
$\mathcal{P}$	Pressure tensor of a given particle population
$\mathcal{J}$, $\mathcal{J}_i$	Jacobian matrices of the transformation from the computational to the physical coordinates (and viceversa)

A	Generic particle species
A_W	Accomodation coefficient for the material walls
$\boldsymbol{B}$	Magnetic induction field vector
c	Speed of light
c_s	Sonic velocity (or Bohm's velocity)

C	Electric capacity of an object or a generic constant (specified within the text)
d	Operational distance, in the IBS mission study context
d_0	Extension of the near region of a plasma plume
$\boldsymbol{E}$	Electric field vector
E	Kinetic energy of an elementary particle at wall impact (E_{imp}), re-injection (E_{reinj}), or emission from a sputtered surface (E_{emi})
$\boldsymbol{e}$	Total energy flux vector
e	Electric charge of an electron, or total energy flux vector magnitude (depending on the context)
$\boldsymbol{F}$	Force vector (thrust if referred to a thruster)
F	Total distribution function of a given particle population
f	Probability distribution function in the velocity space of a given particle population
f_l	Fraction of the IBS orbit characterized by light conditions
$\boldsymbol{G}$	Momentum gain vector of a given particle population, due to collisions
$\boldsymbol{g}$	Particle flux vector of a given particle population
g_0	Standard gravity acceleration
H_e	Bernoulli's function for the electron fluid, in the hybrid code context
h	Self-similarity or dilation function, used by the Self-Similar methods
h_e	Barotropic function for the electron fluid, in the hybrid code context
I	Electric current
I_B	Total ion current in the beam
I_{sp}	Specific impulse of the electric thruster
(i, j, k)	Indices of either the mesh nodes or the cell-faces, in the hybrid code context
$\boldsymbol{j}$	Current density of a given particle population or total electric current density (when no subscript is used)
Kn	Knudsen number, which is the ratio between the mean free path (for collisions) and the characteristic length of the domain
M	Ion Mach number
m	Elementary particle mass of a given particle population or mass of a specific satellite component (depending on the subscript)
$\dot{m}$	Mass flow rate of the thruster (total mass flow if without subscript)

N	Number of macro-particles (in total, or per cell, depending on the context)
N_{ep}	Number of elementary particles
(N_ξ, N_η, N_ζ)	Number of nodes along the three coordinate directions of the PIC structured mesh
n	Number density of a given particle population. If no subscript is used, it refers to the quasineutral plasma density
$\dot{n}$	Number density rate, appearing in the continuity equation, of a given particle population
L	Number of particle populations. It includes electrons in fully-kinetic or full-PIC codes. It refers to the number of heavy species populations in hybrid codes
P	Power (in the IBS study context) or variable considered for the Bohm's condition criterion evaluation (in the hybrid code context, $P \geq 0$)
$\boldsymbol{p}$	Linear momentum vector
p	Scalar pressure of a given particle population
p_c, p_{bks}	Collision probability (p_c) or backscattering probability (p_{bks}) from a sputtered material surface, in the context of the hybrid code
Q	Volumetric power source for a given particle population
$\boldsymbol{q}$	Thermal flux vector of a given particle population
q	Elementary particle charge of a given particle population
$\boldsymbol{r}$	Position vector
R	95% ion current streamline radius (e.g. R_0 or $R(z)$), or radius of a specific thruster component (e.g. R_{thr} is the thruster exhaust area radius)
R_i	Ionization rate for a given ionization reaction
R_{lm}	Resistance between the l^{th} and m^{th} conductive object, in the equivalent circuit context of the hybrid code
t	Time
T	Temperature (in energy units) of a given population
U	Random number, uniformly distributed between 0 and 1
$\boldsymbol{u}$	Fluid velocity vector of a given particle population
V_{lm}	Applied voltage between the l^{th} and m^{th} conductive object, in the equivalent circuit context of the hybrid code

$\boldsymbol{v}$	Velocity vector of a particle or macro-particle
W	Macro-particle weight (number of elementary particles represented by a single macro-particle), in the hybrid code context
(x, y, z)	Physical domain coordinates, in the hybrid code context
Y	Particle yield of a sputtered material surface (number of sputtered atoms per incident atom/ion)
Z	Charge number of a given particle population ($+1$ for singly charged ions, -1 for electrons, 0 for neutrals, etc...)
(z, r)	Axial and radial coordinates, used in the axisymmetric fluid model

Subscripts

The following list describes the meaning of the subscripts used throughout this work.

$_{\theta}$	along the azimuthal direction (used in the context of axisymmetric models)
$_{\perp}$	perpendicular to the considered surface or cell-face (used in the 3D hybrid code context) and directed towards the plasma
$_{\parallel}$	parallel to the considered surface or cell-face (used in the 3D hybrid code context). In a 3D environment, there are two parallel unit vectors, at each cell-face
$_{\infty}$	referring to infinity
$_{0}$	referring to either a reference node (in the hybrid code context) or to the initial plane of the plume far region, on the axis (in the axisymmetric fluid model context)
$_{acc}$	referring to the acceleration grid of an ion thruster
$_{avg}$	referring to an averaging effect (e.g. Δk_{avg} is the number of averaging PIC time steps)
$_{B}$	referring to the beam
$_{bks}$	referring to backscattered particles
$_{CEX}$	referring to charge-exchange particles (ions and neutrals)
$_{c}$	referring to the conical mesh origin (with coordinates (x_c, y_c, z_c)), cell face center (with computational coordinates (ξ_c, η_c, ζ_c)), plume centerline (density $\tilde{n}_c$) or collisions (probability p_c), depending on the context.
$_{chamber}$	referring to the ionization chamber of an ion thruster
$_{cross}$	referring to a crossing condition (e.g. Δt_{cross} is the elapsed time between the PIC time step start and the time at which a macro-particle crosses a given surface)
$_{DOF}$	referring to the degrees of freedom
$_{d}$	referring to a driving term ($\boldsymbol{j}_d$ is the driving current density in the electron momentum equation)
$_{e}$	referring to electrons
$_{emi}$	referring to an emitted flux of particles, from the wall to the plasma
$_{ep}$	referring to elementary particles
$_{eq}$	referring to an equivalent quantity

F	referring to a final distance (e.g. the distance of the target debris center, in the context of the ion beam shepherd scenario)
f	referring to a cell-face, in the hybrid code context, or to the floating plasma potential, in the experimental characterization of the PEGASES plume
$feed$	referring to the feedthrough of the vacuum chamber
gen	referring to generated macro-particles. For example W_{gen} is the generation weight, at a given cell, for new macro-particles in injection and collision algorithms
hit	referring to macro-particles hitting a given surface, from within the plasma
IBS	referring to the ion beam shepherd spacecraft
ICT	referring to the impulse compensation thruster
ITT	referring to the impulse transfer thruster
i	referring to ions or to ionization (depending on context)
imp	referring to particles property at wall-impact
inj	referring to injection
j	referring to the j^{th} particle
l,m	indices for a generic simulated object
min,max	referring to a minimum or maximum value
n	referring to neutrals, non-neutrality or to a mesh node (depending on the context)
$neut$	referring to the neutralization process in the very near plume
osc	referring to the oscilloscope
out	referring to an output measurement
p	referring to the plasma
$pair$	referring to a pair of macro-particles in the DSMC algorithm
$prop$	referring to the propellant
pwr	referring to the power subsystem
RF	referring to the radio-frequency generator
r	along the radial direction
rel	referring to a relative variable (e.g. relative velocity v_{rel} or relative error ϵ_{rel})

$_{reinj}$	referring to re-injection (due to neutrals reflection or ions wall recombination)
$_{ring}$	referring to the ring-shaped plasma potential sensor
$_{(sw)}$	referring to a surface-weighted version of the variable
$_{S}$	referring to the sheath edge (in quasineutral regions) or to the simulation boundary (in non-neutral regions)
$_{s}$	referring to the generic s^{th} population
$_{screen}$	referring to the screen grid of an ion thruster
$_{sput}$	referring to sputtered particles
$_{TG}$	referring to the target debris object
$_{tg}$	referring to a generic target (e.g. the target material for sputtering, or the targeted number of macro-particles per cell, in the population control algorithm)
$_{th}$	referring to the thermal component (e.g. $\boldsymbol{v}_{th}$ is the thermal component of a particle velocity vector)
$_{thr}$	referring to the thruster
$_{W}$	referring to the material wall
$_{z}$	along the axial direction

Superscripts

The following list describes the meaning of the superscripts used throughout this work.

$^{(exp)}$	referring to a direct experimental measurement
$^{(hit)}$	referring to macro-particles that have crossed a non-transparent cell-face, in the hybrid code context
$^{(k)}$	referring to time step or iteration k
^{O}	referring to an auxiliary variable in the physical to computational coordinates transformation, for a conical mesh, in the hybrid code context
$^{(rem)}$	referring to the macro-particles that need to be removed from the simulation, in the hybrid code context
$^{(sw)}$	referring to a surface-weighted version of the variable
*	referring to the quasineutral solution, in the hybrid code context
*	referring to an optimization property

Accents

The following list describes the meaning of the accents used throughout this work.

- $\tilde{X}$ generic normalized property X. The normalization magnitude is specified within the text
- $\bar{X}$ generic time-averaged property X. Used in the context of the hybrid PIC-fluid code
- $\dot{X}$ generic time derivative of the property X
- X' generic derivative of the property X with respect to the independent variable
- $\hat{X}$ value that maximizes some other property (e.g. $\hat{v}_\perp$ is the normal velocity that maximizes the injection probability, in the hybrid code context)

Acronyms

The following is a description of the acronyms considered in this work.

ADR	Active debris removal
AEM	Asymptotic expansion method
AMU	Atomic mass unit
BCF	Bohm's condition forcing
CEX	Charge-exchange collision
CIC	Cloud-in-cell method for macro-particle weighting
CNES	Centre national d'études spatiales
DCFT	Diverging cusped field Hall thruster
DSMC	Direct Simulation Montecarlo Collisions
ECR	Electron cyclotron resonance
ELP	External Langmuir probe
EPS	Electric propulsion subsystem
EP2PLUS	Extensible parallel plasma plume simulator
ESA	European space agency
FEEP	Field emission electric propulsion
GIT	Gridded ion thruster
GNC	Guidance, navigation and control
HEMP(T)	Highly efficient multistage plasma (thruster)
HET	Hall effect thruster
IBS	Ion beam shepherd
ICT	Impulse compensation thruster
IEDF	Ion energy distribution function
ILP	Internal Langmuir probe
ITT	Impulse transfer thruster
LEO	Low Earth orbit
LEOSWEEP	Low Earth orbit security with enhanced electric propulsion
LPP	Laboratoire de physique des plasmas

MCC	Monte Carlo Collisions
MEX	Momentum exchange collision
MoC	Method of characteristics
MPD(T)	Magneto-plasma dynamic (thruster)
MRFEA	Magnetic retarding field energy analyzer
NASA	National aeronautics and space administration
PEGASES	Plasma propulsion using electronegative gases
PIC	Particle-in-cell
PMD	Post mission disposal
PPT	Pulsed plasma thruster
PPU	Power processing unit
RF	Radio-frequency
RIT	Radio-frequency ion thruster
S/C	Spacecraft
SM-MURF	Spacecraft multi-scale/multi-physics universal research framework
SPIS	Spacecraft-plasma interaction software
SSM	Self-similar method
SUGAR	Scalable unstructured gas dynamics with adaptive mesh refinement
TG	Target debris
USC	University of Southern California
VASIMR	Variable specific impulse magnetoplasma rocket

Contents

List of Figures

List of Tables

Chapter 1

State-of-the-art and research objectives

1.1 Electric propulsion

Electric propulsion [1, 2] has gradually become a mature and widely used technology in modern spacecrafts, given the advantages it offers in terms of propellant consumption with respect to the conventional chemical propulsion. The term "electric" comes from the fact that electric thrusters use the electric energy from a primary power source (like the solar array) to produce an ionized propellant and accelerate it into vacuum. In this way, the propellant exhaust velocity is not limited by the chemical reaction energy, as for the conventional chemical thrusters, although the limited available electric power permits achieving much lower thrust levels.

In terms of the principle behind the thrust generation, electric thrusters can be classified into three categories:

- *Electro-thermal thrusters*: the available electric energy is used to heat up the propellant, which is then accelerated through a conventional nozzle (conversion of thermal energy into directed kinetic energy). This is the case of arcjets and resistojets [2, 3, 4, 5, 6].

- *Electro-static thrusters*: the thrust is generated by the interaction of a positive space-charge region (populated of ions) with the electrodes of an extraction system. This is the case of the gridded ion thruster (GIT) [1, 7, 8, 9, 10, 11], and of the FEEP thrusters [12, 13], in which the thrust density assumes the form $-\rho_c \boldsymbol{E}$, where ρ_c is the charge density, and $\boldsymbol{E}$ is the local electric field.

- *Electro-magnetic thrusters*: the thrust is generated by the interaction of an internal plasma current $\boldsymbol{j}$ with the magnetic field $\boldsymbol{B}$ created by an external magnetic circuit. The thrust density assumes the form $-\boldsymbol{j} \times \boldsymbol{B}$. This is the case of many existing thrusters, such as the annular Hall effect thruster (HET) [1, 14, 15, 16], the HEMP thruster [17], the Helicon thrusters [18, 19, 20, 21, 22],

the electron-cyclotron resonance (ECR) thruster [23, 24], the magnetoplasma-dynamic thruster (MPDT) [25, 26], the pulsed plasma thruster (PPT) [27, 28], or the variable specific impulse magnetoplasma rocket (VASIMR) [29, 30]. The above thrusters differ in terms of the ionization process (based on either an electric discharge or a plasma-wave interaction) and of the physical principle behind the generation of the ambipolar electric field (responsible for the acceleration of the ions). In the case of the HET, this is the electrons reduced axial mobility (due to their closed azimuthal drift), while for the Helicon, the ECR, the MPD thrusters and the VASIMR, the source is a magnetic nozzle [22, 31, 32, 33].

This work focuses on the plumes generated by these electric thrusters, whose composition and properties depend on the thruster type. Although the models developed here are equally applicable to any thruster type, we are primarily interested in the electro-static and electro-magnetic thrusters, since they emit a proper plasma plume, that is a plume constituted by a significant fraction of ion mass flow. For these thrusters, a propellant utilization efficiency is commonly used to measure the ionization efficiency:

$$\eta_m = \frac{\dot{m}_i}{\dot{m}_i + \dot{m}_n} = \frac{\dot{m}_i}{\dot{m}}, \tag{1.1}$$

where $\dot{m}$ is the total mass flow rate, and $\dot{m}_i$, $\dot{m}_n$ respectively the ion and neutral mass flow rates. If F is the total thrust generated by the thruster, then a specific impulse can be defined as:

$$I_{sp} = \frac{F}{g_0 \dot{m}} \approx \frac{\eta_m \bar{u}_{zi}}{g_0}, \tag{1.2}$$

with $\bar{u}_{zi}$ representing the average axial velocity of the exhaust ions, and g_0 the standard gravity acceleration. In the second equality, the contribution of emitted neutrals has been neglected, since they are much slower than the emitted ions.

Electric thrusters can then be divided into cathodeless thrusters and thrusters that need at least one cathode for either sustaining the electric discharge or neutralizing the emitted plume:

- Cathodeless thrusters: this is the case of Helicon, ECR, and VASIMR thrusters, which require neither an internal cathode to ionize the propellant, nor an external one to neutralize the already quasineutral plume.

- Thrusters with cathode: this is the case of HEMP, MPD, Hall Effect, FEEP and gridded ion thrusters. The MPDT requires an internal cathode to generate the electric discharge, the HET features an external cathode to both sustain the discharge and neutralize the emitted ions plume, while the GIT works with either one cathode as neutralizer (Radio-frequency ion thrusters) or two cathodes (electron-bombardment). Finally, the FEEP always requires an external cathode neutralizer, since it only emits ions.

Finally, depending on the type of emitted plasma plume, thrusters can be classified into quasineutral and non-neutral:

- Quasineutral plume thrusters: this is the case of Hall Effect, Helicon, HEMP, ECR, pulsed plasma and MPD thrusters, and of the VASIMR, which emit a quasineutral plasma plume (both ions and electrons with the same current density).
- Space-charge thrusters: this is the case of both the GIT and the FEEP thrusters, which accelerate ions through an electrodes system. Therefore, in the very-near plume region, the plume is non-neutral with an excess of positive ion charge. In the GIT, the electrons of the plasma discharge are collected by the screen grid and must be emitted by the neutralizer into space to avoid charge build-up. The electric power required to move electrons from the screen grid to the emitting neutralizer is commonly known as beam power.

The classification of the presented thrusters according to the above described criteria is finally summarized in Tab. 1.1.

Table 1.1: Existing thrusters classification.

Thruster type	**Thrust principle**	**Cathodeless design**	**Emitted plume type**
GIT	electro-static	no	space-charge
FEEP	electro-static	no	space-charge
HET	electro-magnetic	no	quasineutral
HEMPT	electro-magnetic	no	quasineutral
Helicon	electro-magnetic	yes	quasineutral
ECR	electro-magnetic	yes	quasineutral
PPT	electro-magnetic	no	quasineutral
MPDT	electro-magnetic	no	quasineutral
VASIMR	electro-magnetic	yes	quasineutral

Among all mentioned thrusters, GITs and HETs deserve a particular attention, since they have undergone several decades of development, testing and flight, and represent, nowadays, the most reliable and tested technology. Nevertheless, research is still focusing on improving their performance with innovative designs. For what concerns the HET, new magnetic circuit topologies and thruster geometries are being considered to enhance their lifetime, by applying the so-called magnetic shielding (magnetic fields parallel to the thruster walls to reduce the ion flux). As to the ion thrusters, on the other hand, new cathodeless designs (not requiring an external neutralizer) are being investigated, like the PEGASES thruster concept [34, 35, 36, 37, 38], which accelerates alternatively positive and negative ions, or the NEPTUNE concept [39], in which ions and electrons are alternatively extracted.

1.2 Plasma plume effects on the S/C

The plasma plumes produced by the electro-static and electro-magnetic thrusters, being made of ions and electrons, are strongly affected by the local electric and magnetic fields, so that understanding how they interact with the satellite itself is becoming a very demanded task. In fact, as shown in Fig. 1.1, a plasma plume can induce electric charging, produce mechanical erosion/contamination and exert forces/torques on any object it interacts with [40, 41].

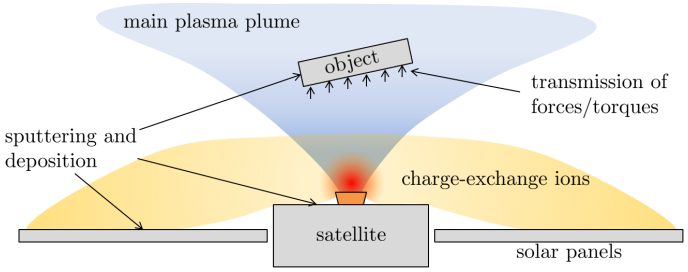

Figure 1.1: Schematic representation of the plasma plume interaction with the emitting S/C and an immersed object.

In the context of spacecraft design, it is therefore crucial to minimize this interaction with different key components, such as the solar array and the onboard sensors, whose performance would be greatly degraded. Apart from avoiding the direct impingement of the hypersonic thruster plume ions, satellite integrators are mostly concerned about the effect of backscattered ions. As shown in Sec. 1.3, these ions are generated by charge-exchange collisions close to the thruster exit, and are easily deflected towards the satellite by the local electric fields. Upon impact with spacecraft surfaces, these ions can produce sputtering, while the sputtered material can deposit on other surfaces, contaminating them. Both the direct sputtering damage and the contamination due to deposition provoke a degradation in the performance of the affected components.

The importance of studying plasma plumes, however, cannot be restricted entirely to modern spacecraft design. In fact, they can also be used to one's benefit, like in the context of the ion beam shepherd (IBS) [42, 43, 44, 45]. This is an active debris removal (ADR) technique, in which an impulse transfer thruster (ITT) directs its main plume at a target debris and, through the consequent ion push, it progressively relocates the object to a different, less crowded orbit. At the same time, an impulse compensation thruster (ICT) pushes the shepherd spacecraft in the opposite direction, in order to maintain formation flying. A schematic of the IBS concept is shown in Fig. 1.2.

Finally, the study of similar plasma jets is also relevant in other research fields, such as plasma material processing [46], in which they are used to obtain special properties, and in astrophysics [47, 48], where a large variety of plasma jets are naturally found. This work shall focus, however, on plasma thruster plumes.

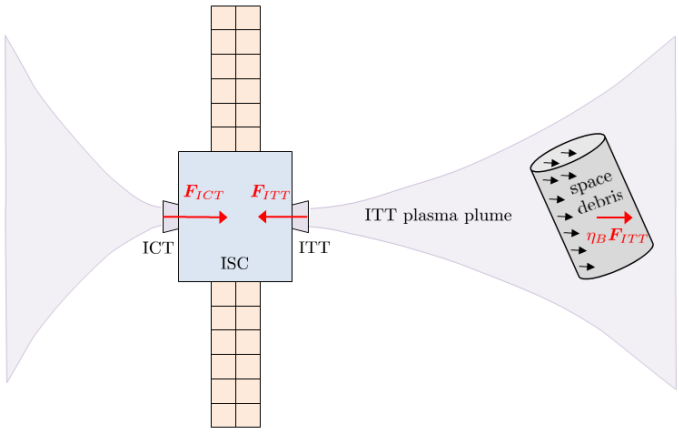

Figure 1.2: Schematic representation of the ion beam shepherd concept.

1.3 The main characteristics of a plasma plume

The plasma plumes produced by electro-static and electro-magnetic thrusters are typically very rarefied and weakly collisional, with peak densities in the order of $10^{16} - 10^{18}$ m^{-3} [1, 2, 49, 50], and a Knudsen number Kn $\gg 1$. This indicates that they don't behave like a classical fluid, in which inter-particle collisions play a major role. In addition, these plumes are characterized by very different dynamics for ions and electrons, with the latter being 4 or 5 orders of magnitude lighter, and responding much more quickly to external perturbations. As a consequence, the self-consistent electric fields depend mostly on the electrons dynamics, and are strongly affected by the presence of any externally applied magnetic field, so that a classification into magnetized and unmagnetized plasma plumes is necessary. Magnetized plumes present anysotropic properties, since electrons are forced to follow Larmor orbits around the local magnetic field direction and can traverse the field lines only through rare collisional events. This hinders the plume expansion in the normal direction (where the electron mobility is lowest) and facilitates it along the parallel direction. When $\boldsymbol{B}$ is along the plume axis, it can then channel the expansion, reducing the plume divergence, whereas, when it is at an angle, it can significantly distort the plume cross section, as claimed by recent research [51, 52, 53] and shown in Fig. 1.3.

Be the plasma plume magnetized or not, two different regions can always be identified, as shown in Fig. 1.4: a *near-region* and a *far-region*. In the near-region, which extends up to a few thruster radii from the thruster exit surface, the plasma is markedly non-homogeneous: a GIT plume consists of numerous "beamlets" that gradually merge into a single beam, while a HET plume features an initially annular profile, given the thruster channel geometry. In this region, several three-dimensional effects play an important role.

First of all, at the thruster exit, the emitted neutral density can reach values up to 100 times the emitted ion density, so that the effect of ion-neutral collisions is non-negligible. These collisions may feature either an elastic momentum exchange

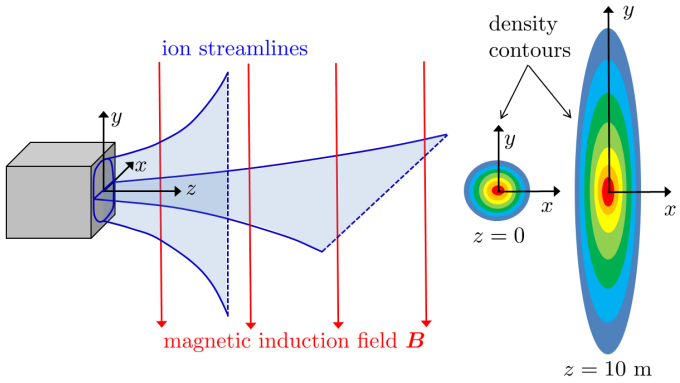

Figure 1.3: Sketch of the plasma plume distorsion effect due to an external magnetic field, perpendicular to the plume axis.

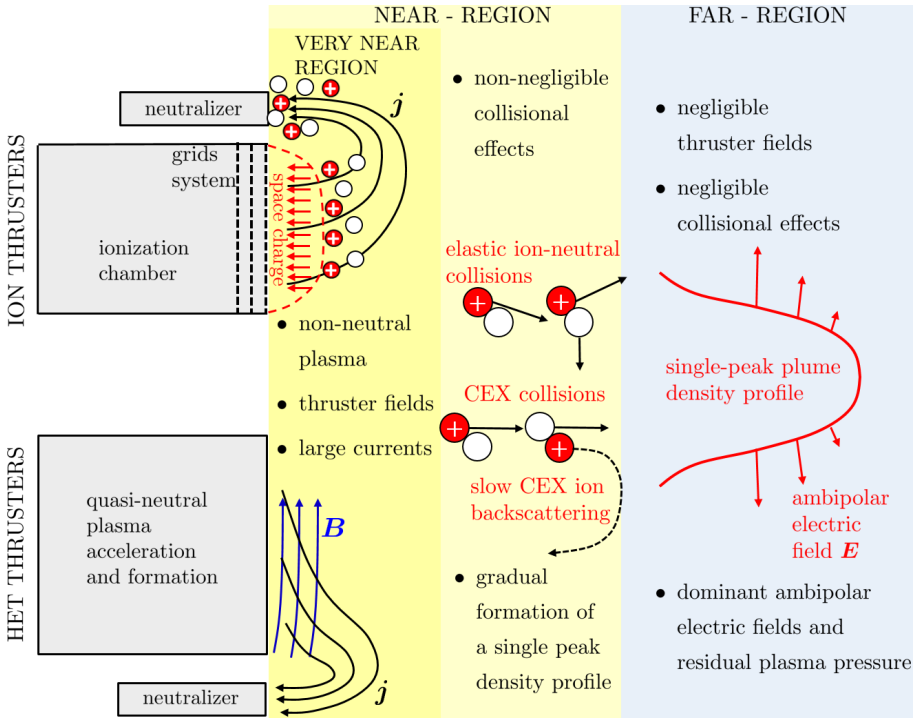

Figure 1.4: Characteristics and most important phenomena occurring in the near and far regions of a plasma plume.

(MEX) or a charge-exchange (CEX) [54, 55], the latter being the most important one. When a fast hypersonic ion transfers its charge to a slow neutral, a slow ion is created, which easily follows the local electric fields and is backscattered towards the S/C, with all the consequences already described in Sec. 1.2. Secondly, the near region is characterized by intense local electric and magnetic fields, created by either the satellite or the thruster (e.g. the potential well at the last grid of a GIT, or the magnetic field generated by the magnetic circuit of a HET). Thirdly, the emitted plume of the neutralizer (consisting of both ions and neutrals) mixes with the main thruster plume, resulting in asymmetric distributions of the plasma

plume properties.

The combined effect of the above phenomena is to produce a smooth, single-peaked plasma profile, after a few thruster radii: when this occurs, the *far-region* begins, where the effects of neutralizer, thruster and collisions become negligible with respect to the plume kinetic energy, the residual thermal pressure, and the self-consistent ambipolar electric field. The subsequent plasma expansion is then current-free, quasineutral, and near-collisionless, and the plume is constituted by highly hypersonic ions with velocity u_i in the order of tens of km/s, and electrons with a mild temperature T_e of 1–5 eV [56, 57, 58], which are nearly confined by the ambipolar electric field. The expansion in this far-region, then depends on the following initial conditions, which refer to an initial plane at the end of the near region (e.g. $50 - 100$ cm downstream from the thruster exit):

- the initial divergence angle α_0,
- the electron cooling rate inside the plume,
- the initial ion Mach number M_0,
- the plume initial shape.

The existing definitions for the divergence angle are shown in Fig. 1.5.

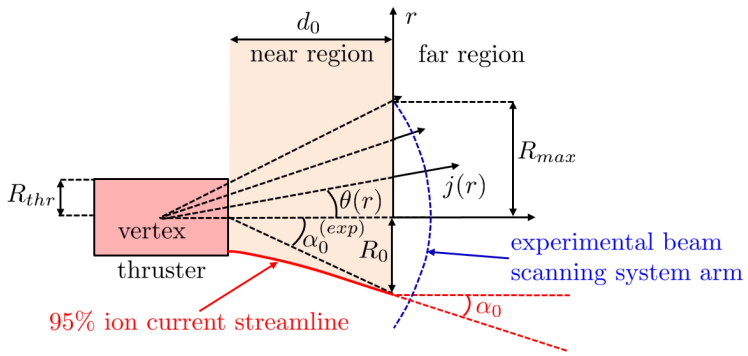

Figure 1.5: Divergence angle geometry. α_0 represents the slope with respect to the thruster axis of the 95% ion current streamline, while $\alpha_0^{(exp)}$ is the angle typically measured in experiments (from the value of its radius R_0). The virtual plume vertex used for the computation of the divergence efficiency and the measured current density profile $\boldsymbol{j}(r)$ (by the beam scanning system) are also shown.

First of all, the radius R_0 of the streamtube that contains 95% of the total emitted ion current is identified. Then, the divergence angle is either defined as the angle α_0 of this streamline with respect to the thruster symmetry axis, or as the angle $\alpha_0^{(exp)}$ at the radius of this ion streamline, as seen from the thruster center. Clearly the two definitions tend to coincide as the ratio between the thruster radius R_{thr} and the near region extension d_0 goes to zero. The $\alpha_0^{(exp)}$ definition, in fact, assumes a point source at the center of the thruster exit area, and does not require the knowledge of the streamlines direction, but only the current density measurements obtained

with a beam scanning system. Therefore, experiments typically determine the angle $\alpha_0^{(exp)}$. Other authors, however, consider a different experimental definition based on the divergence efficiency [1, 59]. As shown in Fig. 1.5, they assume a conical velocity field, with the ion streamlines originating at a common vertex (typically inside the thruster), and they compute this efficiency as:

$$\eta_{div} =< \cos\theta >= \frac{\int_0^{R_{max}} \cos(\theta)\,(2\pi r j(r)\cos(\theta))\,dr}{I_B}, \tag{1.3}$$

where R_{max} is the maximum beam scanning system radius, $j(r)$ is the current density (measured with an array of Faraday cups oriented towards the beam vertex) at an angle $\theta(r)$, as seen from the plume vertex, and I_B is the total emitted ion current. This divergence efficiency thus represents an average divergence angle cosine loss, weighted with the axial current density (and taking into account a cylindrical geometry). A corresponding average divergence angle can be obtained as the $\arccos(\eta_{div})$, and is generally smaller than the α_0 or $\alpha_0^{(exp)}$ angles defined above, which refer to an outer streamline (the 95% ion current streamline). In the present work, we shall assume the α_0 definition, when talking about the plume divergence angle, as it is not based on simplifying assumptions and is valid for any type of velocity profile (not only for a conical one).

The second parameter that influences the far region expansion is the electron cooling in the plume. In this work, although it is not justified for a collisionless plasma plume, this is modeled with a polytropic state law, a common assumption made in both experiments and numerical simulations [16, 49, 50, 60, 61, 62], which is found to predict well the general features of the plume expansion:

$$T_e = T_{e0}\left(\frac{n_e}{n_{e0}}\right)^{\gamma-1}, \tag{1.4}$$

where γ is the polytropic cooling coefficient, and n_{e0}, T_{e0} represent the known electron density and temperature at some reference point. In general, the faster the electrons cool down, and hence the larger the γ, the lower is their effect on the plume divergence growth, because their pressure decays more rapidly. In addition γ also appears in the expression of another important parameter of the far-region expansion, the ion Mach number M_0, which, for a plume made of singly charged ions, is defined as:

$$M_0 = \sqrt{\frac{m_i u_{i0}^2}{\gamma T_{e0}}}, \tag{1.5}$$

where m_i is the ion mass, u_{i0} their initial velocity at the axis, and T_{e0} their initial temperature (in energy units). A quick inspection of Eq. (1.5) shows that the square of the ion Mach number represents the ratio between the directed kinetic energy of the plume ions and the thermal energy of the electrons. As it will be shown in Chapter 2, the divergence angle of the ion streamlines continues to increase as they expand downstream, and this increase is higher the lower the ion Mach number.

Regarding the plume initial shape at the start of the far-region, this depends dimly on the type of thruster considered, since the thruster geometry effects are smeared out in the near region. Finally, Tab. 1.2 summarizes, for the existing electric thrusters, the most important plume properties, like the specific impulse, the divergence angle and the ion Mach number. In the case of the VASIMR, the very high specific impulse (or exhaust velocity) does not correspond to a high ion Mach number, because the collected data refer to a very light propellant, the deuterium. Moreover, the initial divergence angle appears to be well characterized only for the ion and Hall effect thrusters, and it is roughly 10–25 deg for former, and 35–50 deg for latter.

Table 1.2: Typical specific impulse, divergence angle and ion Mach number for different types of electric thrusters (xenon propellant, unless noted).

Thruster type	**Specific impulse [s]**	**Divergence angle [deg.]**	**Ion Mach number**
GIT	$1000 - 10000$	$10 - 25$	$7 - 67$
HEMPT	$1600 - 2600$	45	$11 - 17$
HET	$800 - 3000$	$35 - 50$	$5 - 20$
Helicon	$250 - 500$	> 15	$2 - 3$
ECR	$250 - 600$	$35 - 50$	$2 - 4$
PPT [1]	$1500 - 17000$	n/a	$5 - 62$
MPDT	$250 - 3000$	n/a	$3 - 20$
VASIMR [2]	$5000 - 12000$	n/a	$4 - 10$

1.4 Limitations of the experimental approach

Plasma plumes can be studied both numerically, and experimentally, either in vacuum chambers or onboard real satellites. Of course, experiments are quite limited by the avaiable budget and by the technological limits posed by existing vacuum chambers. For these reasons, they typically focus only on the plume near-region, where the plasma properties are routinely measured at distances of about 1 m from the exit of the thruster [11, 16, 56, 57, 63, 64, 65]. Such measurements, apart from determining the thruster performance figures, also permit identifying important plume properties, such as the 95% ion current divergence angle (refer to Fig. 1.5), or the electron polytropic cooling coefficient γ relating the plasma density with the electron temperature.

The far-region (and the peripheral plasma), on the contrary, present serious challenges for vacuum chamber testing, as large vacuum tanks and high vacuum levels are required to limit the influence of the tank walls and the background plasma density on the measurements of a low-density plume [1]. These difficulties have been confirmed in the test campaign of a recent project, named *LEOSWEEP* [66]

[1] with argon propellant
[2] with deuterium propellant

(2013-2016), which aimed at characterizing the plasma plume in the far region, up to a distance of $7 - 10$ m from the thruster exit, and also studying the effects of the geomagnetic field. Although some matching of the experimental measurements with fluid model predictions could be found, results were characterized by a large uncertainty in several plasma properties (especially in the electron temperature), and, most importantly, by the absence of a proper plume neutralization (the neutralizer was kept off for technical issues). This inconvenient invalidated any conclusion regarding the effect of the geomagnetic field on the plume expansion, since it was not acting over a quasineutral plasma plume.

In order to overcome vacuum chamber limitations, experiments should be carried out directly in orbit, however, up to date, there are only a few cases in which a proper plume characterization has been performed out in space. One of such experiment, presented in Ref. [53], focuses on the distortion effects created by the Earth magnetic field, as predicted by Korsun in 1997 [51]. Another experiment has been carried out onboard the SMART-1 spacecraft [67, 68], focusing on the charge-exchange plasma contamination of sensitive surfaces.

1.5 State of the art of numerical simulations

Due to the obvious limitations of experiments, numerical simulations of plasma plumes have been gaining a larger importance in the last two decades. In this field, it is the simulation of the peripheral plasma and of the near region plume, which becomes the most demanding, due to the abundance of competing physical effects requiring complex numerical codes. In contrast, the far-region of a plume is amenable to simpler models such as collisionless fluid models, which confer a clearer understanding of the main physics of the problem and can be used to propagate experimental data downstream, extrapolate vacuum chamber measurements to space conditions, and identify facility effects on far-region measurements.

In the following, the available approaches for the simulation of a plasma plume and its interaction with a satellite are described:

- Fully-kinetic models
- Full-PIC models
- Multi-fluid models
- Hybrid PIC-fluid models

1.5.1. Fully-kinetic models

When describing an ensemble of particles, the highest level of information is provided by the exact one-particle distribution function [69]:

$$F_{ex}\left(\boldsymbol{r}, \boldsymbol{v}, t\right) = \sum_{j=1}^{N_{ep}} \delta\left(\boldsymbol{r} - \boldsymbol{r}_j(t)\right) \delta\left(\boldsymbol{v} - \boldsymbol{v}_j(t)\right), \tag{1.6}$$

which tells us both the position $\boldsymbol{r}$ and the velocity $\boldsymbol{v}$ of each individual particle of the ensemble. By integrating F_{ex} over the position and velocity space, the total number N_{ep} of elementary particles is obtained. Since such an expression based on Dirac deltas is very noisy, F_{ex} is normally substituted with a smoothed distribution function, representing its ensemble average over the $6N_{ep}$-dimensional space formed by the positions and velocities of the N_{ep} particles.

If $\rho_F(\boldsymbol{r}_1, \cdots, \boldsymbol{r}_{N_{ep}}, \boldsymbol{v}_1, \cdots, \boldsymbol{v}_{N_{ep}}) d\boldsymbol{r}_1 \cdots d\boldsymbol{r}_{N_{ep}} d\boldsymbol{v}_1 \cdots d\boldsymbol{v}_{N_{ep}}$ is the probability of finding the system of N_{ep} particles in the phase space volume $d\boldsymbol{r}_1 \cdots d\boldsymbol{r}_{N_{ep}} d\boldsymbol{v}_1 \cdots d\boldsymbol{v}_{N_{ep}}$ at position $\left(\boldsymbol{r}_1, \cdots, \boldsymbol{r}_{N_{ep}}, \boldsymbol{v}_1, \cdots, \boldsymbol{v}_{N_{ep}}\right)$, then this smoothed particle distribution function can be defined as:

$$\begin{aligned} F(\boldsymbol{r}, \boldsymbol{v}, t) &= \int \rho_F F_{ex} d\boldsymbol{r}_1 \cdots d\boldsymbol{r}_{N_{ep}} d\boldsymbol{v}_1 \cdots d\boldsymbol{v}_{N_{ep}} \\ &= N_{ep} \int \rho_F(\boldsymbol{r}, \boldsymbol{r}_2 \cdots \boldsymbol{r}_{N_{ep}}, \boldsymbol{v}, \boldsymbol{v}_2 \cdots \boldsymbol{v}_{N_{ep}}) d\boldsymbol{r}_2 \cdots d\boldsymbol{r}_{N_{ep}} d\boldsymbol{v}_2 \cdots d\boldsymbol{v}_{N_{ep}}. \end{aligned} \tag{1.7}$$

Then $F(\boldsymbol{r}, \boldsymbol{v}, t)\, d\boldsymbol{r} d\boldsymbol{v}$ represents the average number of particles in the 6-dimensional phase space volume $d\boldsymbol{r} d\boldsymbol{v}$ at position $(\boldsymbol{r}, \boldsymbol{v})$. From Liouville's theorem, and with the use of the BBGKY hierarchy, it is finally possible to obtain Boltzmann's equation [69, 70, 71], which provides an evolution law for this smoothed particle distribution function:

$$\frac{\partial F_s}{\partial t} + \frac{\boldsymbol{p}_s}{m_s} \cdot \nabla F_s + q_s(\boldsymbol{E} + \boldsymbol{v} \times \boldsymbol{B}) \cdot \frac{\partial F_s}{\partial \boldsymbol{p}_s} = \left(\frac{\partial F_s}{\partial t}\right)_c, \tag{1.8}$$

where the subscript 's' refers to a specific particle population (i.e. an ensemble of particles sharing at least the same particle mass m_s and charge q_s), $\boldsymbol{p}_s$ is the linear momentum vector of an elementary particle of the s^{th} population, and $q_s(\boldsymbol{E}+\boldsymbol{v}\times\boldsymbol{B})$ is the total electro-magnetic force acting on it. The right hand side models the effect of collisions for the s^{th} population. Boltzmann's equation is then coupled with Maxwell's equations, in order to determine a self-consistent solution that takes into account the electro-magnetic field produced by the plasma itself:

$$\nabla \cdot \boldsymbol{B} = 0, \tag{1.9}$$

$$\nabla \cdot \boldsymbol{E} = \frac{\rho_c}{\epsilon_0}, \tag{1.10}$$

$$\nabla \times \boldsymbol{E} = -\frac{\partial \boldsymbol{B}}{\partial t}, \tag{1.11}$$

$$\nabla \times \boldsymbol{B} = \mu_0 \boldsymbol{j} + \frac{1}{c^2} \frac{\partial \boldsymbol{E}}{\partial t}, \tag{1.12}$$

where ϵ_0 is the dielectric constant of a vacuum, μ_0 is the vacuum magnetic permeability, c is the speed of light, ρ_c is the plasma charge density, and $\boldsymbol{j}$ is the plasma current density. Maxwell's equations are then coupled with Boltzmann's equation through ρ_c and $\boldsymbol{j}$. If L is the total number of particle populations, these plasma

properties can be computed as:

$$\rho_c = \sum_{s=1}^{L} eZ_s n_s, \tag{1.13}$$

$$\boldsymbol{j} = \sum_{s=1}^{L} \boldsymbol{j}_s = \sum_{s=1}^{L} eZ_s \boldsymbol{g}_s, \tag{1.14}$$

where eZ_s is the electric charge of an elementary particle, n_s the number density and $\boldsymbol{g}_s$ the average particle flux vector of the s^{th} population. Both the number density and the particle flux vector are particular moments of the distribution function F_s over the velocity space. In particular, n_s is the zeroth moment:

$$n_s(\boldsymbol{r}, t) = \int_{\Omega} F_s(\boldsymbol{r}, \boldsymbol{v}, t) d\boldsymbol{v}, \tag{1.15}$$

while $\boldsymbol{g}_s$ is the order-1 moment:

$$\boldsymbol{g}_s(\boldsymbol{r}, t) = \int_{\Omega} \boldsymbol{v} F_s(\boldsymbol{r}, \boldsymbol{v}, t) d\boldsymbol{v}. \tag{1.16}$$

The probability distribution function is then defined as $f_s = F_s/n_s$. At a given position $\boldsymbol{r}$ and time t, the product $f_s(\boldsymbol{r}, \boldsymbol{v}, t)d\boldsymbol{v}$ represents the probability of finding a particle within the velocity interval $d\boldsymbol{v}$, centered at $\boldsymbol{v}$. Obviously, integration over the velocity space of the probability distribution function gives 1 (100% probability of finding the particle with any velocity):

$$\int_{\Omega} f_s(\boldsymbol{r}, \boldsymbol{v}, t) d\boldsymbol{v} = 1. \tag{1.17}$$

Fully-kinetic models then try to solve directly the system formed by Boltzmann's and Maxwell's equations, Eqs. (1.8) to (1.12). Typically, a simplified version of Maxwell's equations is considered, for example one neglecting the wave terms (displacement current), or simply an electrostatic closure, featuring Poisson's equation alone. The high dimensional phase space (6-dimensional for a 3D problem), and the difficulty of modeling the collisional term of Eq. (1.8) make however the fully-kinetic approach only feasible for low dimensional studies, as done in recent studies aimed at solving Vlasov's equation (e.g. Eq. (1.8) with a zero collisional term) for a 1D magnetic nozzle [33, 72].

1.5.2. Full-PIC models

Full particle-in-cell (PIC) models [69, 73, 74, 75, 76, 77, 78, 79] follow an alternative Lagrangian-Eulerian approach, in which the particle populations are modeled as macro-particles and moved self-consistently with the electric and magnetic fields, that are known at dedicated mesh nodes. As shown in Ref. [69], instead of solving

for the Boltzmann's equation, the particle-in cell method discretizes the particle distribution functions with a finite number of macro-particles as:

$$F_s(\boldsymbol{r}, \boldsymbol{v}, t) = \sum_{j=1}^{N_s} W_j \delta\left(\boldsymbol{r} - \boldsymbol{r}_j(t)\right) \delta\left(\boldsymbol{v} - \boldsymbol{v}_j(t)\right), \tag{1.18}$$

where N_s represents the total number of macro-particles considered (for the s^{th} population), W_j is the number of elementary particles represented by the j^{th} macro-particle, referred to as macro-particle weight, and $\boldsymbol{r}_j(t)$, $\boldsymbol{v}_j(t)$ are respectively its position and velocity vector. Full-PIC models then reproduce the total distribution function F_s with a limited number of degrees of freedom, by collapsing a large number of elementary particles into a single macro-particle. This permits saving a large computational time, at the cost a much larger statistical fluctuation of the fluid properties, which is not observed in nature, given the extremely high number of elementary particles.

The trajectory of the j^{th} macro-particle is simply obtained by solving Newton's equation (in which the macro-particle weight appears on both sides and, hence, cancels out):

$$m_j \frac{d\boldsymbol{v}_j}{dt} = eZ_j \left[\boldsymbol{E}(\boldsymbol{r}_j) + \boldsymbol{v}_j \times \boldsymbol{B}(\boldsymbol{r}_j)\right], \tag{1.19}$$

while the ensemble average properties n_s and $\boldsymbol{j}_s$ for each population, necessary to update self-consistently the electro-magnetic field, are obtained by weighting the macro-particles to the nodes of a dedicated mesh (hence the name *particle-in-cell*). The overall scheme is shown, for the sake of clarity, in Fig. 1.6.

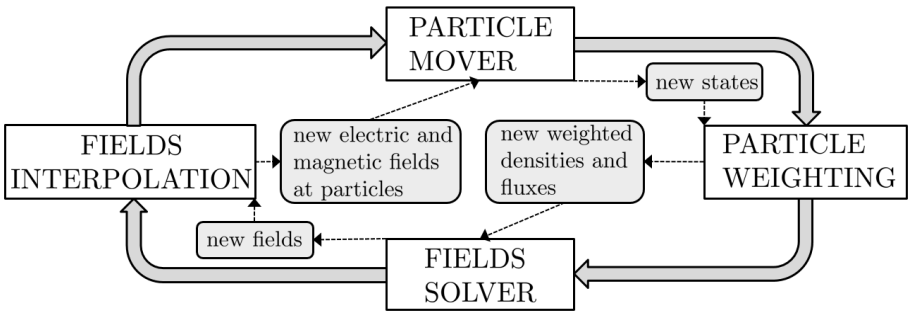

Figure 1.6: Logical loop of a typical PIC code.

The choice of solving for the new fields at the mesh nodes, and then interpolating them to the macro-particle position, permits decreasing the cost of the electromagnetic forces computation from $O(N^2)$ to $O(N)$, since it requires a particle weighting step (with a computational cost proportional to the number of macro-particles N) and a fields solver step (with a computational cost proportional to the number of nodes N_{nodes}, generally lower than N). On the contrary, should the electromagnetic interaction with any of the macro-particles of the domain be considered, the evaluation of the force on each macro-particle would require already $O(N)$ operations, and the total cost would scale as $O(N^2)$. This is the case of particle-particle codes

like those used for molecular dynamics simulations [80], in which the interactions with all surrounding particles (up to a maximum interaction distance) is taken into account. In PIC codes, on the other hand, the electro-magnetic interaction between particles is indirect and simulated through a mesh weighting step, so that, instead of being point masses, macro-particles actually behave like Green's functions (space distributions of mass and velocity), with a shape determined by the weighting algorithm. This is a similar approach to the one done in fully-kinetic codes when substituting the exact one-particle distribution function with an ensemble average one. Moreover, the weighting scheme for assigning macro-particles to the nodes and the interpolation scheme for computing the electro-magnetic field at the macro-particle position must be the same, in order to avoid undesired and unphysical effects, such as the *self-force*, as shown in Ref. [74], consisting in a macro-particle generating an electro-magnetic force on itself. Another cause of the self-force might be the use of a highly deformed mesh [74], so that care is needed when using non-Cartesian meshes, be them structured or not.

Another important advantage of PIC models with respect to fully-kinetic codes is in the simpler approach used for dealing with collisions. As discussed above, macro-particles interact with each-other only through time-averaged, long-range fields known at the mesh nodes. However, an individual macro-particle might be subject to instantaneous fields very different from these time-averaged long-range ones, especially if it happens to approach closely another macro-particle (e.g. due to the Coulomb's interaction in the case of charged particles). Therefore, the total force acting on a macro-particle presents 2 contributions: a long-range and a short-range one. As shown in Ref. [73], PIC models simulate the short-range forces with dedicated collisional algorithms (Direct Simulation Monte Carlo, [73, 81, 82] DSMC, or Monte Carlo collisions, MCC [82, 83]), in which macro-particles in each cell can collide with the others, in a fashion as similar as possible to the elementary particles collisions. In such a way, if the number of simulated macro-particles is high enough, the resulting distribution function resembles the solution of either particle-particle codes or of kinetic codes that solve directly the Boltzmann's equation with the collisional term (approaches that are, most of the times, impractical).

The collision event in PIC codes thus represents the integrated effect (over the interaction time) of the short-range forces. Since the real interaction time is extremely short with respect to the integration PIC time step, collisions are often assumed to be instantaneous and their outcome modeled statistically, every time step (e.g. with the use of collision cross sections or rates, and with an instantaneous update of the colliding macro-particles properties).

1.5.3. Multi-fluid models

Multi-fluid models [49, 50, 60, 61, 84, 85] solve a simplified set of equations, that originate from Eq. (1.8) by taking different moments of the distribution function in the velocity space, and expressing them in terms of ensemble average properties, such as the particle density, velocity, pressure, temperature, etc. By taking the

zeroth moment, the first moment (with $\boldsymbol{v}$), and the second moment (with $mv^2/2$) of Boltzmann's equation, the following three conservation equations are obtained:

$$m_s \frac{\partial n_s}{\partial t} + \nabla \cdot (m_s n_s \boldsymbol{u}_s) = m_s \dot{n}_s, \tag{1.20}$$

$$\frac{\partial}{\partial t}(m_s n_s \boldsymbol{u}_s) + \nabla \cdot (m_s n_s \boldsymbol{u}_s \boldsymbol{u}_s) = -\nabla \cdot \mathcal{P}_s + Z_s e n_s (\boldsymbol{E} + \boldsymbol{u}_s \times \boldsymbol{B}) + \boldsymbol{G}_s, \tag{1.21}$$

$$\begin{aligned} \frac{\partial}{\partial t}\left(\frac{3}{2} n_s T_s + \frac{1}{2} m_s n_s u_s^2\right) + \nabla \cdot \left[\left(\frac{3}{2} n_s T_s + \frac{1}{2} m_s n_s u_s^2\right) \boldsymbol{u}_s + \boldsymbol{q}_s\right] \\ = -\nabla \cdot (\mathcal{P}_s \boldsymbol{u}_s) + Z_s e n_s \boldsymbol{u}_s \cdot \boldsymbol{E} + Q_s. \end{aligned} \tag{1.22}$$

Let us now analyze each one of them. Eq. (1.20) is known as mass continuity equation, and features the number density n_s, defined in Eq. (1.15), and the average velocity $\boldsymbol{u}_s$, which can be obtained from Eq. (1.16), dividing by n_s:

$$\boldsymbol{u}_s = \frac{\boldsymbol{g}_s}{n_s} = \int_\Omega \boldsymbol{v} f_s(\boldsymbol{r}, \boldsymbol{v}, t) d\boldsymbol{v}, \tag{1.23}$$

and the term $\dot{n}_s$, which represents the volumetric source of particles (new particles per unit volume and time, generated or destroyed by collisional events).

Eq. (1.21) is known as momentum balance equation, and features the additional unknowns of collisional momentum gain $\boldsymbol{G}_s$, which models the effects of the collisions with the other populations, and the pressure tensor $\mathcal{P}_s$, defined as:

$$\mathcal{P}_s = \int_\Omega m_s \boldsymbol{v}_{th} \boldsymbol{v}_{th} F_s(\boldsymbol{r}, \boldsymbol{v}, t) d\boldsymbol{v}, \tag{1.24}$$

where the thermal velocity $\boldsymbol{v}_{th} = \boldsymbol{v} - \boldsymbol{u}_s$ is the particle velocity with respect to the average fluid motion. A scalar pressure can then be defined from the trace of this pressure tensor as:

$$p_s = \frac{1}{3} \mathrm{tr}\,(\mathcal{P}_s) = \int_\Omega \frac{1}{3} m_s v_{th}^2 F_s(\boldsymbol{r}, \boldsymbol{v}, t) d\boldsymbol{v}. \tag{1.25}$$

Eq. (1.22) is finally the energy balance equation and features the new unknowns of the isotropic temperature T_s, the thermal flux vector $\boldsymbol{q}_s$ and the energy source Q_s, which represents the volumetric energy creation rate (due to generation or loss of particles with a finite energy). The isotropic temperature T_s and the thermal flux vector $\boldsymbol{q}_s$ are, once again, particular moments of the distribution function:

$$T_s = \frac{p_s}{n_s} = \int_\Omega \frac{1}{3} m_s v_{th}^2 f_s(\boldsymbol{r}, \boldsymbol{v}, t) d\boldsymbol{v}, \tag{1.26}$$

$$\boldsymbol{q}_s(\boldsymbol{r}, t) = \int_\Omega \frac{1}{2} m_s v_{th}^2 \boldsymbol{v}_{th} F_s(\boldsymbol{r}, \boldsymbol{v}, t) d\boldsymbol{v}. \tag{1.27}$$

In order to obtain simplified expressions for the unknowns $\boldsymbol{G}_s$ and $\boldsymbol{q}_s$ in terms of other ensemble averages (density, velocity and temperature), a commonly made assumption in fluid models is to consider an isotropic Maxwellian distribution function,

an hypothesis which is justified only in a highly collisional regime, when equilibrium has been reached (H-theorem, [73]). This means that the particle distribution function, for each population, takes the form:

$$F_s(\boldsymbol{r},\boldsymbol{v},t) = n_s(\boldsymbol{r},t)\left(\frac{m_s}{2\pi T_s(\boldsymbol{r},t)}\right)^{3/2}\exp\left(-\frac{m_s\left|\boldsymbol{v}-\boldsymbol{u}_s(\boldsymbol{r},t)\right|^2}{2T_s(\boldsymbol{r},t)}\right). \tag{1.28}$$

With F_s given by Eq. (1.28), simplified expressions for both the heat flux vector and the momentum gain can be made, as shown below:

$$\boldsymbol{q}_s = -k_s\nabla T_s, \tag{1.29}$$

$$\boldsymbol{G}_s = \sum_{j\neq s}\nu_{sj}m_s n_s(\boldsymbol{u}_j-\boldsymbol{u}_s), \tag{1.30}$$

with Eq. (1.29) commonly known as Fourier law, and ν_{sj} representing a momentum transfer collision frequency from the population s to the population j.

Multi-fluid models finally solve the system of Eqs. (1.20) to (1.22), coupled with Maxwell's equations, by assuming different types of fluid closures:

- Closure at the level of the pressure tensor: in this case the energy equation is discarded and an expression for the pressure tensor is assumed. An example is an isotropic closure based on a polytropic state equation, Eq. (1.4). In this case, the divergence of the pressure tensor simply becomes $\nabla\cdot\mathcal{P}_s = \nabla p_s = \nabla\left(n_s^\gamma T_{s0}/n_{s0}^{\gamma-1}\right)$, where n_{s0}, T_{s0} are the known number density and temperature of the s^{th} population, at some reference location.

- Closure at the level of the heat flux vector: in this case the energy equation is retained (important for simulations of plasma discharges), and the fluid closure consists in assuming a simplified expression for the heat flux vector, typically a Fourier law.

In all cases, the simplifying expressions for $\boldsymbol{G}_s$, $\boldsymbol{q}_s$ and $\mathcal{P}_s$ are only justified for collisional plume regimes. When dealing with low collisonal plasma plumes, the solution of the fluid equations can be tricky, and hardly justified, although some comparison studies with full-PIC simulations, like the one in Ref. [62], have shown that a simple fluid model can reproduce the most important plume expansion physics in the far-region (the ambipolar electric field plays the role of the pressure gradient in a collisional plume).

1.5.4. Hybrid models

An intermediate approach between full-PIC and multi-fluid models, is represented by hybrid PIC models [86, 87, 88, 89, 90, 91, 92, 93, 94, 95, 96, 97, 98], in which the electrons are treated as a fluid and the heavy species are simulated as macro-particles of a PIC sub-model. This choice allows to:

- Reduce significantly the computational cost with respect to full-PIC or fully kinetic codes, because the PIC time step is now dictated by the fastest ion species, which is typically $2-3$ orders of magnitude slower than the electrons.
- Maintain a generic distribution function for all heavy species particles, without relying on unjustified closures, at least for ions and neutrals (as done by multi-fluid models).

Nevertheless, since hybrid models treat electrons as a fluid, strong assumptions must still be made, especially for what concerns the electron thermodynamics, which is typically assumed to follow a kinetic fitting (like a polytropic law approach). Therefore, some fundamental physics studies, such as the electron collisionless cooling, cannot be done using hybrid modeling, but must still rely on more complex kinetic models (fully-kinetic or full-PIC).

While full-PIC and fully kinetic codes are inherently non-neutral codes, in which Poisson's equation, Eq. (1.11), is always solved for, hybrid codes can be classified into quasineutral and non-neutral. The former assume equal and opposite charge densities for ions and electrons, obtaining the electric potential from the electron conservation equations:

$$n_e = \sum_{s=1}^{L} Z_s n_s \quad \rightarrow \quad \phi \text{ from conservation equations.} \tag{1.31}$$

In the above equation L represents the number of heavy particles populations and does not include the electrons, which are now treated as a fluid. As discussed in Sec. 1.3, however, this quasineutrality assumption is only justified in the central, denser regions of the plume, and typically fails when the Debye length becomes comparable to the PIC cell size, like in the peripheral plume regions. This is taken into account by the latter non-neutral codes, which solve the coupled Poisson's and electron conservation equations. In the context of hybrid codes this means to solve a non-linear Poisson's equation, in which the unknown electron density is an explicit function of the unknown electric potential.

While always considering the continuity equation, like multi-fluid models, hybrid codes are finally classified in terms of the fluid closure and the physical effects considered in the conservation equations:

- Momentum equation closure: these approaches can include different physical effects: (I) electron pressure and electric field (II) electron pressure, electric field and collisions (III) electron pressure, electric field, collisions and magnetic field. The first of these approaches reduces to a simple Boltzmann or polytropic relation for the electric potential, as shown in Refs.[49] and [50]. The other approaches, on the other hand, permit determining the electron streamlines and therefore the total electric current density in the plasma.
- Energy equation closure: again different terms of the momentum and energy equations can be considered, with a Fourier closure for the heat flux vector.

1.5.5. Existing plasma plume codes and their capabilities

Table 1.3 provides a summary of the most important tools dedicated to plasma plumes simulation, ordered chronologically.

Table 1.3: Existing plasma plume codes and their capabilities.

Code name or author	**Refs.**	**Publ. date**	**Model type**	**Struct. mesh**	**Non neutral**	**Electron fluid closure**
Parks	[60]	1979	2D fluid	yes	no	Boltzmann
Korsun	[84, 52]	1997	2D fluid	yes	no	Boltzmann
Oh	[99]	1999	3D hybrid	yes	no	Boltzmann
Ashkenazy	[61]	2001	2D fluid	yes	no	Boltzmann
SPIS	[96, 97, 98]	2001	3D hybrid	no	yes	Boltzmann
CNES	[100]	2002	2D hybrid	yes	yes	Boltzmann
AQUILA	[93, 101]	2003	3D hybrid	no	no	polytropic
DRACO	[102]	2004	3D full-pic	yes	yes	n/a
Taccogna	[91]	2011	3D hybrid	yes	no	polytropic
USC	[77, 78]	2014	3D full-pic	yes	yes	n/a
SUGAR	[87, 88]	2014	3D hybrid	no	no	Boltzmann
EASYPLUME	[49, 50]	2015	2D fluid	yes	no	polytropic
Greifswald university	[103] [86]	2014 2015	3D full-pic 2D hybrid	yes yes	yes yes	n/a polytropic
Hall2De	[85]	2015	2D fluid	yes	no	heat flux
New Mexico State university	[90]	2015	3D hybrid	yes	no	heat flux
SM/MURF	[89]	2016	3D hybrid	yes [3]	yes	polytropic

Simplified plume models for the study of the far-region were introduced very early at the end of the 70s by Parks [60], later followed by Korsun [84, 52] and Ashkenazy [61]. These models were two-fluid (ions and electrons) collisionless models, and part of this thesis has been dedicated to unify these approaches under a single Self-Similar Method (SSM) framework, as desribed in Chapter 2. A plasma plume code named EASYPLUME (2015) has been developed following these activities.

For what concerns more complex codes for the study of the near region and its interaction with the satellite, the first published ones date back to the end of the 90s. One of these codes is Oh's code [99], which consisted in a 3D hybrid PIC-fluid code, which considered polytropic electrons and included a non-linear Poisson's solver for the non-neutral regions. The code mesh was Cartesian, with the possibility of embedding more refined meshes inside the initial coarse one (thus testing the improvements of finer meshes quite easily).

Almost at the same time, the "Spacecraft Plasma Interaction Software" (SPIS) [96, 97, 98] was being developed at ONERA, with the goal of providing a reference tool for studying the S/C interaction problem, at least at European level. As such,

[3] it can use also an unstructured mesh.

SPIS includes the possibility of solving for non-neutral regions and features a non-structured mesh to increase the tool flexibility to model complex S/C geometries. Moreover, it presents a complex equivalent circuit for the interaction between the plasma and the satellite surfaces. Nevertheless, the code is still not applicable to direct ion impingement studies (from the main ion plume) on a secondary object, as shown by a bachelor degree study of the plasma bridge of an ion beam shepherd mission [104].

Another code, originally designed to study HET plumes, is one from CNES [100], which is axisymmetric and permits studying non-neutral regions. Shortly afterwards, the AQUILA [93, 101] code became a direct competitor of SPIS, featuring an unstructured mesh, with polytropic electrons. In 2004, DRACO [102] became the first full-PIC 3D code, dedicated to study the plasma plume interaction with the S/C, although no full-PIC simulations can be found in the literature. In 2011, Taccogna [91] completed the coding of yet another 3D hybrid PIC-fluid code, based on polytropic electrons and quasineutrality, and applied it, for the first time, to the study of a HET cluster plume, which is strongly asymmetric (thus requiring a 3D code).

In recent years, since 2014, plasma plume codes have been receiving an ever growing interest, as SUGAR (2014) [87, 88], the codes (both 2D hybrid and 3D full-PIC) from the university of Greifswald [86], Hall2De [85], the code from the New Mexico State university [90], and SM/SMURF [89] (a replacement of the already existing AQUILA code) clearly suggest. Hall2De, originally created to simulate Hall effect thrusters and their near region, is completely based on fluid equations (one population for electrons, one for the neutrals and several for the ions, to model deviations of the total ion distribution function from a Maxwellian). Moreover, it is quasineutral and solves for the energy balance equation, with a Fourier law closure. The same characteristics are shared by the electron fluid model of the hybrid code from the New Mexico State university.

Hybrid codes clearly represent the most popular approach. Full-PIC simulations of plasma plume expansions, on the other hand, have been carried out only by a few authors, such as Wang in Refs. [77] and [78]. In these studies, however, the 3D domain considered is periodic along the y direction, so that the simulated plume is actually bidimensional (a plasma plume slab, as it will be shown in Sec. 2.6). Full-PIC codes have been applied more frequently to the simulation of axisymmetric Hall Effect thruster discharges, like shown in Refs. [105, 106, 107], or to other plasma thrusters, as shown in Ref. [103]. In the HET studies, retaining the full physics (with a full-PIC) was essential to study problems like the anomalous transport of the electrons in the axial direction.

1.5.6. Choice of the optimal modeling approach

The optimal modeling approach clearly depends on the type of problem to be solved. In the case of the plasma plume interaction with either the spacecraft or with downstream objects, as shown in Fig. 1.1, the problem is clearly three-

dimensional, and features a large number of physical phenomena, plasma density variations of several orders of magnitude, and simulation domains of a few meters in all directions. This makes the computational cost of both fully-kinetic and full-PIC models extremely high, given the very small simulation time steps required by the former, and the high dimensional solution space of the latter. As a matter of fact, both 3D full-PIC and fully-kinetic codes are extremely rare in the plasma plumes study context, as it can be observed from Tab. 1.3. Moreover, given the low collisionality of plasma plumes, multi-fluid models are limited by (I) the complexity of introducing a large number of fluids per species (to better represent deviations of the distribution function from a pure Maxwellian), and, (II) the need of assuming kinetically-unjustified closures for the corresponding fluid equations.

Hybrid codes, on the other hand, by treating only ions and neutrals as particles, permit overcoming the full-PIC and fully kinetic codes drawbacks, while solving directly for the heavy particles distribution functions. Although the treatment of electrons still features strong assumptions, which limit the applicability of these codes (e.g. collisionless cooling or anomalous transport, the latter expected to be negligible in most plasma plumes, cannot be tackled), hybrid codes represent the best compromise for modeling a plasma plume expansion and its interaction with the satellite and other objects.

For what concerns the analysis of the far-region plume expansion alone, however, simpler approaches are more convenient, as shown by the existing literature on two-fluid models. The fluid solution, being much quicker, enables parametric studies of plasma plumes expansions, which can be of fundamental importance in order to understand the fundamental physics governing the far-region.

Therefore, in this work, the following choices have been made, for what concerns the modeling approach:

- A multi-fluid model for the study of the plasma plume far-region.
- A hybrid code for the study of the plasma plume interaction with the satellite.

1.6 Objectives and description of this work

This thesis has the objectives of (I) developing and validating numerical codes for the simulation of the plasma plume expansion and interaction with any object, and (II) applying such codes to study both the plasma plume expansion physics and other specific plasma plume applications.

Given the observations of Sec. 1.5.6, two codes have been developed: (I) a fluid code to study the plasma plume expansion in the far-region, and (II) a hybrid PIC-fluid code for the analysis of the plume interaction with the satellite and any downstream object. Since most of the work has been carried out in the framework of LEOSWEEP [66], a European Commission funded project aiming at assessing the feasibility of the IBS technique for space debris removal, the developed codes have been primarily applied to this mission scenario.

Regarding the fluid code, which is dealt with in Chapter 2, the work has focused on (I) synthesizing the existing fluid plume solutions into a common framework, the Self-Similar method (SSM), (II) developing a more flexible method, named Asymptotic Expansion method (AEM), and (III) analyzing parametrically the physics of the plume far region.

For what concerns the hybrid code, described in Chapter 3, being aware of the large number of existing codes (see Tab. 1.3), after a first phase of literature review and identification of poorly-explored areas, the work has focused on introducing (I) a new electron fluid model, and (II) a new approach for dealing with quasineutral and non-neutral plasma regions. More specifically, the major goal of the electron model, presented in Sec. 3.3.1, was to enable the computation of the electron streamlines of an unmagnetized plasma plume. Regarding the latter topic, an automatic criterion for splitting the simulation domain into quasineutral and non-neutral regions has been introduced, as described in Sec. 3.3.3. Moreover, a large importance has been given to validating this hybrid code algorithms, with a full set of validation tests, which are described in the Appendix C.

In what regards the applications, the developed hybrid code has first been applied to the simulation of the interaction between a plasma plume, emitted by a plasma thruster, and the satellite. This study is introduced in Chapter 4.

Then, the developed codes have been applied to relevant studies in the context of the ion beam shepherd technique, which, being a relatively new concept, still features many unexplored areas. These studies are presented in Chapter 5 and consist of (I) an optimization study of the electric propulsion subsystem of a representative IBS mission, with the use of the fluid code, and (II) a study of the complex satellite-plasma plume-debris interaction, with the use of the hybrid code.

A full report of an experimental campaign aiming at characterizing the PEGASES thruster plasma plume, and carried out during my research visit at the "Laboratoire de Physique des Plasmas" between November 2015 and February 2016, is finally provided in Chapter 6 and completes this work.

Chapter 2

Fluid model for the far-region of a plasma plume

This chapter introduces the fluid model for the far-region of a plasma plume. Two different solution methods are presented: the Self-Similar method (SSM) and the Asymptotic Expansion method (AEM), which are validated by benchmarking their results with the exact solution obtained with the Method of Characteristics (MOC). The far-region plume physics is then analyzed in detail in terms of the free parameters: the ion Mach number, the divergence angle, and the polytropic cooling coefficient. Finally the solution obtained with this fluid model is compared with that of a full-PIC code for a two dimensional plasma plume slab geometry. In this way, the validity of a fluid model approach with a polytropic closure, for a collisionless plume expansion, is demonstrated [1]

[1]The contents of this chapter are based on a journal publication [50], and on two conference papers [49, 62]

2.1 Model derivation

The far-region of a plasma plume is near-collisionless, unmagnetized, with the dominant effects being the ion inertia, the electron pressure, and the ambipolar electric field that relates the two charged species (here singly charged ions and electrons). As already discussed in Sec. 1.3, the plasma profile has already become smooth, meaning that in the bulk of the far-region expansion the gradient length is in the order of the thruster radii (typically $\sim$ 10 cm) or more, much greater than the Debye length ($\sim$ 1 mm or less), which means that the expansion can be considered quasineutral in most of the plume. We consider below the expansion of an axisymmetric, non-rotating plume from an initial reference plane $z = 0$, already in the far-region, where ions are assumed to be hypersonic ($M_0 \gg 1$). This reference plane can be chosen at $0.5 - 1$ m distance from the thruster exit, where the ion current and the plasma density are typically measured in laboratory experiments.

Under these considerations, the steady-state, far-region plume expansion is macroscopically described by the following two-fluid equations for singly-charged ions and non-rotating electrons:

$$n_i = n_e \equiv n, \tag{2.1}$$

$$\nabla \cdot (n\boldsymbol{u}_i) = 0, \tag{2.2}$$

$$\nabla \cdot (n\boldsymbol{u}_e) = 0, \tag{2.3}$$

$$nm_i \left(\boldsymbol{u}_i \cdot \nabla\right) \boldsymbol{u}_i = -en\nabla\phi, \tag{2.4}$$

$$0 = -\nabla \cdot \mathcal{P}_e + en\nabla\phi, \tag{2.5}$$

$$u_{\theta i} = u_{\theta e} = 0, \tag{2.6}$$

where ϕ is the ambipolar electric potential, $\mathcal{P}_e$ is the electron pressure tensor, and the rest of symbols are conventional. In these equations, the ion thermal pressure and the electron inertia have been neglected assuming the typical scaling of a propulsive plasma plume in the whole region of interest,

$$m_e u_e^2, T_i \ll T_e \ll m_i u_i^2.$$

A state equation from the kinetic theory is needed to close the fluid model and provide the components of $\mathcal{P}_e$. Solving the plasma plume at a kinetic level is a challenging task beyond the scope of this simplified fluid model. Hence, in the following, $\mathcal{P}_e$ is approximated as a diagonal (isotropic) tensor, so that $\nabla \cdot \mathcal{P}_e = \nabla p_e$, where $p_e = nT_e$ is the scalar electron pressure. Furthermore, a polytropic law is assumed, given by Eq. (1.4), as a simplified electron cooling model. The polytropic coefficient $\gamma = d\ln p_e / d\ln n_e$, which sets the effective cooling rate, can be tuned to fit either experimental measurements or kinetic model studies, with $\gamma = 1$ corresponding to the isothermal limit, and $\gamma = 5/3$ to an adiabatic plasma.

In first approximation, the high conductivity of collisionless electrons, near-totally confined by the electric potential, suggests a near-isothermal behavior or a mild cooling in a large region of the plasma plume. This approximation is supported

by various experimental observations of the far plume, with values in the range $\gamma = 1$–1.3 showing good overall agreement [11, 16, 56, 57, 58, 63, 108].

Using this form for the electron pressure in Eq. (2.5) gives the following dependency for the plasma potential ϕ:

$$\frac{e\phi}{T_{e0}} = \begin{cases} \ln(n/n_0) & \text{for } \gamma = 1, \\ [(n/n_0)^{\gamma-1} - 1]\,\gamma/(\gamma-1) & \text{for } \gamma > 1, \end{cases} \tag{2.7}$$

with subindex 0 denoting values at the origin, and $\phi_0 \equiv 0$. Likewise, the plasma momentum equation, Eq. (2.4) plus Eq. (2.5), becomes

$$m_i\,(\boldsymbol{u}_i \cdot \nabla)\,\boldsymbol{u}_i = -\gamma T_e \nabla \ln n. \tag{2.8}$$

Before proceeding, three comments are due. First, observe that Eqs. (2.2) and (2.8) are coupled and give n and $\boldsymbol{u}_i$. Once n is known, Eq. (2.7) yields ϕ, while $\boldsymbol{u}_e$ cannot be directly obtained, since we have neglected all terms containing it in the electron momentum equation, Eq. (2.5). Note nevertheless that, since the plume needs to be globally current free, the small electron drift (compared to the thermal motion of the nearly-confined electron cloud) satisfies $\boldsymbol{u}_e \simeq \boldsymbol{u}_i$ as a first approximation. We shall see in Chapter 3, that, for an unmagnetized plume, this is a quite good assumption in the far region, and only fails very close to electron emitters (e.g. a neutralizer) and the thruster exit surface. For magnetized plumes, like those emitted by thrusters with a magnetic nozzle [31, 109], such as the helicon plasma thruster [110, 111], both the local electric currents and the applied magnetic field are dominant features of the expansion [32], and the assumption $\boldsymbol{u}_e \simeq \boldsymbol{u}_i$ generally fails. Second, note that the system formed by Eqs. (2.2) and (2.8) is analogous to the fluid equations of a neutral, non-viscid gas expanding into vacuum. The role of the pressure gradient of the neutral gas case is here taken by the ambipolar electric field, which transmits this force from the electrons to the ions. Thus, the solution methods to be presented are equally applicable to the case of a hypersonic neutral gas expanding into vacuum, when the same conditions are satisfied. Third, observe that a plasma plume model with non-negligible ion temperature that obeys the same thermodynamic assumptions as electrons and shares the same parameter γ can be immediately reduced to the model presented above, by redefining the effective temperature and potential as $T_i + T_e \to T_e$ and $e\nabla\phi + \gamma T_i \nabla \ln(n/n_0) \to e\nabla\phi$.

It is convenient to normalize the problem with the values at $z = r = 0$ and with a characteristic length such as the initial radius R_0 of the plasma tube $R = R(z)$ carrying 95% of the ion current, i.e.,

$$\begin{array}{llll} \tilde{z} = z/R_0; & \tilde{r} = r/R_0; & \tilde{R} = R/R_0 & \tilde{n} = n/n_0; \\ \tilde{u}_{zi} = u_{zi}/u_{i0}; & \tilde{u}_{ri} = u_{ri}/u_{i0}; & \tilde{T}_e = T_e/T_{e0}; & \tilde{\phi} = e\phi/T_{e0}. \end{array}$$

In these non-dimensional tilded variables, Eq. (2.2) and (2.8) can be written in cylin-

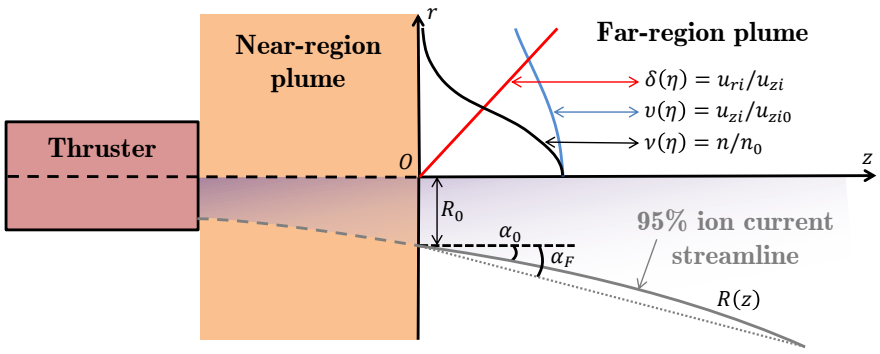

Figure 2.1: Sketch of a plasma plume near and far regions, and the plasma streamtube $R(z)$ containing 95% of the ion current. The reference plane that serves as the initial condition to the far-region, typical shapes for the initial profiles of velocity slope, axial velocity, and density (δ, υ, ν), the initial divergence angle, α_0, and the equivalent final divergence angle, α_F, are schematically shown.

drical coordinates as

$$\tilde{u}_{zi}\frac{\partial \ln \tilde{n}}{\partial \tilde{z}} + \tilde{u}_{ri}\frac{\partial \ln \tilde{n}}{\partial \tilde{r}} + \frac{\partial \tilde{u}_{zi}}{\partial \tilde{z}} + \frac{1}{\tilde{r}}\frac{\partial\left(\tilde{r}\tilde{u}_{ri}\right)}{\partial \tilde{r}} = 0, \tag{2.9}$$

$$\tilde{u}_{zi}\frac{\partial \tilde{u}_{zi}}{\partial \tilde{z}} + \tilde{u}_{ri}\frac{\partial \tilde{u}_{zi}}{\partial \tilde{r}} = -\frac{\tilde{n}^{\gamma-1}}{M_0^2}\frac{\partial \ln \tilde{n}}{\partial \tilde{z}}, \tag{2.10}$$

$$\tilde{u}_{zi}\frac{\partial \tilde{u}_{ri}}{\partial \tilde{z}} + \tilde{u}_{ri}\frac{\partial \tilde{u}_{ri}}{\partial \tilde{r}} = -\frac{\tilde{n}^{\gamma-1}}{M_0^2}\frac{\partial \ln \tilde{n}}{\partial \tilde{r}}, \tag{2.11}$$

where the dependency on the main non-dimensional parameter, the initial ion kinetic energy to electron thermal energy ratio, i.e. the square of the initial ion Mach number,

$$M_0^2 = m_i u_{i0}^2/(\gamma T_{e0}),$$

becomes explicit, with $c_{s0} = \sqrt{\gamma T_{e0}/m_i}$ the ion sonic velocity. Note that $M_0 \simeq 10$–$40 \gg 1$ in the highly-hypersonic plume of a plasma thruster, as shown in Tab. 1.2.

The resulting hyperbolic ion problem, given by Eqs. (2.9)– (2.11), is then closed with the initial profile for both the plasma density n and the ion velocity $\boldsymbol{u}_i$ at the $\tilde{z} = 0$ plane. Introducing a nomenclature that will become useful later, we will refer to these initial conditions as:

$$\tilde{n}(0,\tilde{r}) = \nu(\eta); \quad \tilde{u}_{zi}(0,\tilde{r}) = \upsilon(\eta); \quad \tilde{u}_{ri}(0,\tilde{r})/\tilde{u}_{zi}(0,\tilde{r}) = \delta(\eta), \tag{2.12}$$

where the coordinate η represents the normalized radius $\tilde{r}$ at the *initial* plane. The typical shape of these profiles has been plotted in Fig. 2.1. Also, as done in Sec. 1.3, we will call α_0 the initial divergence angle of the 95% ion current streamtube, i.e., $\tan(\alpha_0) = \delta(\eta = 1)$.

The model can be integrated with different approaches. In particular, the method of characteristics (MoC) can be used to integrate numerically Eqs. (2.9)–(2.11). In

the present work, due to its great accuracy [112], the MoC is used mainly to provide a benchmark solution against which we can compare the semi-analytical integration methods derived in the next sections.

The MoC technique is briefly described as follows: in the meridional plane, ion equations present three families of characteristic lines: two Mach lines, and the ion streamlines. The slopes of these lines are determined by the local plasma properties. After discretizing the initial plasma front in a number of nodes, the characteristic lines are propagated forward and intersected to calculate a new plasma front using a predictor-corrector integration scheme, following an approach similar to that in the DIMAGNO code for the plasma expansion in a magnetic nozzle, as described in Ref. [109]. Further details on the MoC can be found in Ref. [112]. The MoC integrates supersonic plumes with any given initial profile. However, it requires the full numerical solution of the model, and therefore lacks the analytical insight offered by the other two solution methods presented in the next sections. Furthermore, the MoC becomes inadequate in the limit $M_0 \to \infty$, as the three characteristic line families collapse into one (the ion streamlines). This limitation does not affect the semi-analytic methods, which actually require $M_0 \gg 1$, and therefore complement the MoC in the hypersonic limit.

2.2 The AEM solution method

2.2.1. Cold plasma limit

A first approach to reduce the fluid model of Sec. 2.1 to a tractable analytical expression is to neglect the pressure term completely, which is equivalent to taking $M_0 \to \infty$ (fully hypersonic jet). In this cold plasma limit, the plasma momentum equations Eqs. (2.10) and (2.11) (with the right hand side equal to zero) decouple completely from the continuity equation Eq. (2.9) as the three characteristic line families collapse into one (the ion streamlines). Observe also that no electric potential builds up in this case.

The solution for the velocity and density in this cold plasma limit, which we will call $\tilde{\boldsymbol{u}}_i^{(0)}$ and $\tilde{n}^{(0)}$ respectively, depends only trivially on the initial plasma profile functions, ν, υ and δ. It is immediate to see that $\tilde{\boldsymbol{u}}_i^{(0)}$ is simply conserved along the streamlines, which are straight characteristic lines projected from the initial plane ($\tilde{z} = 0$), with radius:

$$\tilde{r} = \eta + \delta(\eta)\tilde{z}, \tag{2.13}$$

where η, their radial position at the initial plane, can be used to label them. Thus, propagating the streamlines to determine the $\eta = \eta(\tilde{z}, \tilde{r})$ map (implicitly given by the equation above) yields $\tilde{u}_{zi}^{(0)}(\tilde{z}, \tilde{r})$ and $\tilde{u}_{ri}^{(0)}(\tilde{z}, \tilde{r})$ from the initial plasma profile.

This map can be understood as the transformation of the reference system $(\tilde{z}, \tilde{r})$ into the new reference system (ζ, η), where simply $\zeta = \tilde{z}$. Differentiation in Eq. (2.13)

provides the Jacobian matrix J,

$$J(\zeta,\eta) = \begin{bmatrix} \partial\tilde{z}/\partial\zeta & \partial\tilde{r}/\partial\zeta \\ \partial\tilde{z}/\partial\eta & \partial\tilde{r}/\partial\eta \end{bmatrix} = \begin{bmatrix} 1 & \delta \\ 0 & 1+\zeta\delta' \end{bmatrix}. \tag{2.14}$$

In the new coordinates and using these relations, Eq. (2.9) allows the straightforward integration of the plasma density:

$$\tilde{n}^{(0)}(\zeta,\eta) = \frac{\nu}{(1+\zeta\delta/\eta)(1+\zeta\delta')}, \tag{2.15}$$

which reflects the decrease in density as the radius of the streamlines increases $(1+\zeta\delta/\eta)$ and as they diverge relative to each other $(1+\zeta\delta')$.

This cold beam solution, while extremely simple, provides a fast first estimate of the plasma plume in the far region as a cone (i.e., without any divergence angle growth). Clearly, the *local* error committed in the momentum equations is of the order $1/M^2$, while the global error (the accumulated integration error, i.e. the difference at each point between the exact solution and the approximation) grows with the distance from the initial plane.

Note that this method requires $\delta, \delta' \geq 0$ to ensure a clean solution exists everywhere. Were such condition not met, streamlines would eventually cross, with density gradients going to infinity locally, a symptom that pressure effects cannot be neglected around that point.

2.2.2. First order corrections

The method presented above can be regarded as the zeroth-order solution of the hypersonic plume when the variables are expanded in the small parameter $\varepsilon = 1/M_0^2 \equiv \gamma T_{e0}/(m_i u_{i0}^2)$, the initial thermal-to-kinetic energy ratio in the beam, i.e.:

$$\begin{aligned} \tilde{u}_{zi} &= \tilde{u}_{zi}^{(0)} + \varepsilon\tilde{u}_{zi}^{(1)} + \varepsilon^2\tilde{u}_{zi}^{(2)} + \dots, \\ \tilde{u}_{ri} &= \tilde{u}_{ri}^{(0)} + \varepsilon\tilde{u}_{ri}^{(1)} + \varepsilon^2\tilde{u}_{ri}^{(2)} + \dots, \\ \ln\tilde{n} &= \ln\tilde{n}^{(0)} + \varepsilon\ln\tilde{n}^{(1)} + \varepsilon^2\ln\tilde{n}^{(2)} + \dots, \end{aligned} \tag{2.16}$$

where all terms of order one or larger are zero at the initial plane, but grow gradually downstream. The quality of the cold beam solution can be improved substantially by including one or more of these corrections, which allow reducing the local error to $O\left(M_0^{-4}\right)$ (for the first order), $O\left(M_0^{-6}\right)$ (second order), etc...

Luckily, momentum and continuity equations remain decoupled at all orders and can be readily integrated *along the zeroth-order streamlines*, requiring only to calculate the gradients of already-known magnitudes.

Introducing these expansions into the problem, the first-order correction for the velocity is given by the two plasma momentum equations at order ε, which are solved

simultaneously by numerical integration in a single variable (ζ):

$$\upsilon\frac{\partial\tilde{u}_{zi}^{(1)}}{\partial\zeta}+\frac{\upsilon'}{1+\zeta\delta'}\left(\tilde{u}_{ri}^{(1)}-\tilde{u}_{zi}^{(1)}\delta\right)=-\left(\tilde{n}^{(0)}\right)^{\gamma-1}\frac{\partial\ln\tilde{n}^{(0)}}{\partial\tilde{z}}, \tag{2.17}$$

$$\upsilon\frac{\partial\tilde{u}_{ri}^{(1)}}{\partial\zeta}+\frac{(\upsilon\delta)'}{1+\zeta\delta'}\left(\tilde{u}_{ri}^{(1)}-\tilde{u}_{zi}^{(1)}\delta\right)=-\left(\tilde{n}^{(0)}\right)^{\gamma-1}\frac{\partial\ln\tilde{n}^{(0)}}{\partial\tilde{r}}, \tag{2.18}$$

where υ,δ are those defined at the initial plane (see Eq. (2.12)), and the right-hand-sides of the equations are fully known, with the derivative terms expressed in terms of $\tilde{z}$ and $\tilde{r}$ for compactness.

Once $\tilde{\boldsymbol{u}}_i^{(1)}$ is known, the first-order correction to density is then similarly given by Eq. (2.9):

$$\upsilon\frac{\partial\ln\tilde{n}^{(1)}}{\partial\zeta}=-\tilde{u}_{zi}^{(1)}\frac{\partial\ln\tilde{n}^{(0)}}{\partial\tilde{z}}-\tilde{u}_{ri}^{(1)}\frac{\partial\ln\tilde{n}^{(0)}}{\partial\tilde{r}}-\frac{\partial\tilde{u}_{zi}^{(1)}}{\partial\tilde{z}}-\frac{1}{\tilde{r}}\frac{\partial\left(\tilde{r}\tilde{u}_{ri}^{(1)}\right)}{\partial\tilde{r}}. \tag{2.19}$$

It is emphasized that in the expressions above, integrating along ζ means integrating along the *known*, straight, zeroth-order streamlines ($\eta=$ const).

The same procedure can be applied to easily obtain higher-order corrections, and the general expressions are given in the Appendix A. Note that the non-linearity introduced by the ion inertia term and the $\tilde{n}^{\gamma-1}$ term in non-isothermal plumes means that all previous-orders contribute to higher-order velocity corrections.

Figure 2.2 shows the second-order solution of the AEM for a representative initial profile with $\alpha_0=15$ deg, $M_0=20$ and two values of γ. A comparison of this solution to the MoC solution shows that a small error develops and grows downstream. Additional simulations show that, in all cases, the committed error is larger, the lower M_0 and γ are, as expected, due to the larger contribution of pressure effects in a wider region of the plume.

2.2.3. Region of convergence

For the AEM solution to be valid, the series expansion of Eq. (2.16) must converge in the region of interest.

Without making any strict statement on the convergence of the series (which depends on the behavior of the i^{th}-perturbations as $i\to\infty$), a practical means to explore the convergence of the method is to equate (in absolute value) the first-order corrections to the zeroth-order solution. The region bounded by this condition is a useful concept to study the behavior of the first terms in the truncated series, and roughly indicates where the error become of order 1. In fact, this analysis helps determine where to stop the integration and "reinitialize" the method before the error becomes too large, taking as a new reference plane a section where the plasma properties have already been calculated. This procedure is further illustrated in Sec. 2.2.4, and permits increasing arbitrarily the method accuracy and validity region.

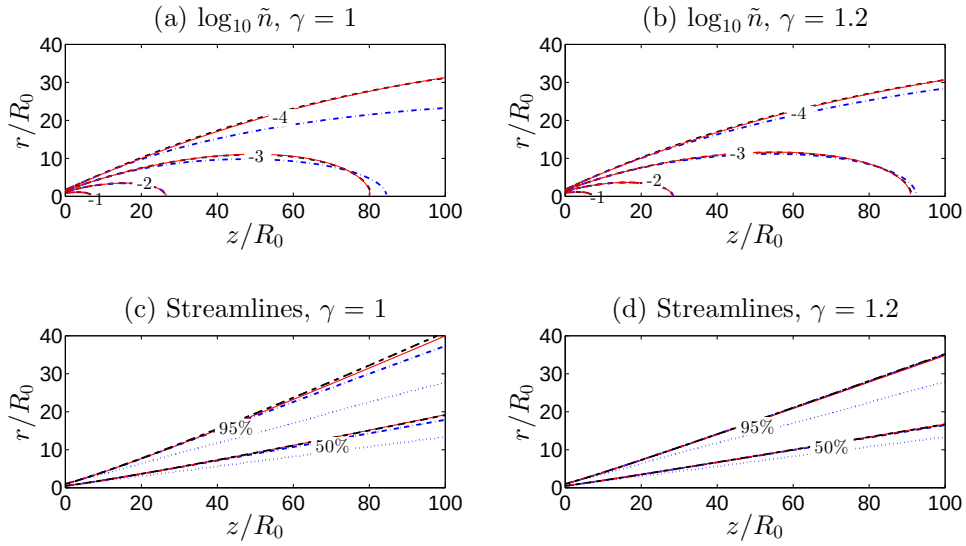

Figure 2.2: Plasma density contour levels (plots (a) and (b)) and plasma streamtubes containing 50% and 95% of the ion current (plots (c), (d)) for two plasma plumes with $M_0 = 20$. The 2nd order AEM is shown in blue dash-dot lines; SSM is shown in red solid lines; MoC solution is given in black dashed lines. The dotted blue lines in (c) and (d) correspond to the cold plasma (conic) approximation, i.e., the 0th order AEM. The initial profiles used in this example are the same as in Fig. 4(a) of Ref. [49] but with $\alpha_0 = 15$ deg.

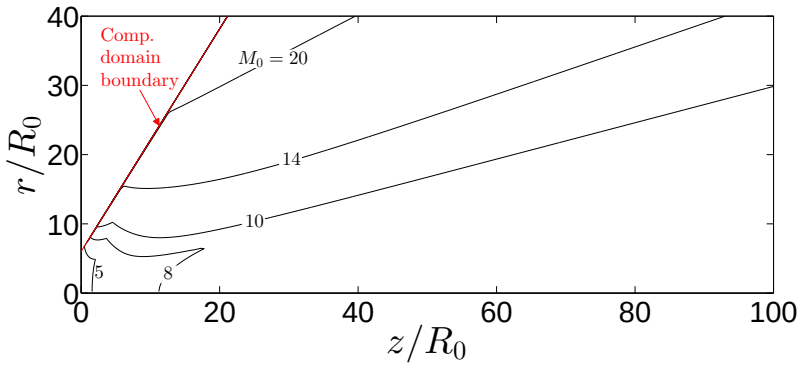

Figure 2.3: Approximate region of convergence of the AEM for $\gamma = 1$, calculated with the condition that the 1st order correction of any one variable be equal or smaller than the 0th order solution. The initial profile is the same as in Fig. 2.2.

While the detailed behavior of this region depends on the initial plasma profile, the general behavior can be summarized as follows: the most critical correction is typically the density one, since it grows faster than the velocity correction. As expected, the convergence region extends axially and radially further downstream the higher M_0 (as the plasma approaches the hypersonic limit) and γ (faster cooling). Thus, the region plotted in Fig. 2.3 is shown for $\gamma = 1$, the most restrictive case in terms of convergence. Also, it is found that the three first-order perturbations are generally larger the smaller the initial divergence angle, as the divergence growth (and therefore the need for a correction) is larger in that case. In the example of Fig. 2.3, $M_0 > 10$ already extends this region far beyond $\tilde{z} = 100$.

2.2.4. Down-marching scheme

In order to extend the convergence region of the AEM, a down-marching scheme can be applied, in which the cold-beam streamlines are updated at regular intervals of $\tilde{z}$, with the velocity corrections predicted by the method. The corrections to the fluid variables are then evaluated in sub-domains of $\tilde{z}$, with the $(j+1)^{\text{th}}$ sub-domain considering the perturbed ion streamlines at the end of the j^{th} sub-domain, as its new zeroth order streamlines. This process is illustrated in Fig. 2.4.

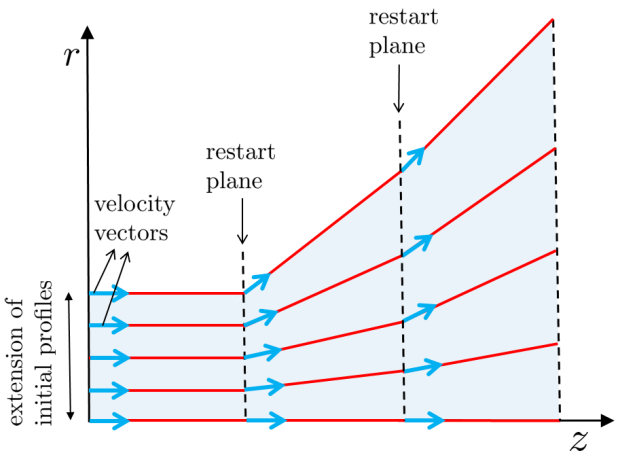

Figure 2.4: The down marching scheme for the AEM. Zeroth order streamlines and initial plume profiles are updated at regular intervals in the $\tilde{z}$ direction, with the corrections predicted by the method. The shaded area represents the effective simulation domain.

With the above described technique, the axial validity of the AEM method can be extended to infinity regardless of the M_0, γ and α_0 values, by choosing an appropriate restarting interval $\Delta\tilde{z}$. This means that the plume does not need to be very supersonic any longer to be able to meaningfully extend the AEM simulation far downstream. Nevertheless, the method might turn out to be very inefficient for $M_0 \sim 1$, for which the restarting interval $\Delta\tilde{z}$ would need to be impractically small. Since the accuracy of the AEM can be arbitrarily increased by decreasing Δz, the solutions of Figs. 2.2 and 2.3 refer to the AEM without this down-marching scheme.

Nevertheless, this scheme has been applied in Sec. 2.6 to obtain an accurate fluid solution for an arbitrary initial plume profile.

2.3 The SSM solution method

Existing measurements and simulations of the far region of GIT and HET beams show the development of a typically smooth, bell-shaped radial plasma profile, which remains essentially invariable along the axial direction, except of course for its radial broadening. This observation suggests modeling the plume expansion as a self-similar phenomenon [60, 61, 84]. While the self-similarity assumption is only an approximation, it turns out to be an accurate one for hypersonic plasma plumes.

We first assume that all the streamlines (given again by $\eta = \text{const}$, with η the initial radius of the streamline) expand self-similarly, so that their radius is expressed through

$$\tilde{r}\,(\zeta, \eta) = \eta h(\zeta), \tag{2.20}$$

where $h(\zeta)$ (with $h(0) = 1$) is a self-similarity or dilation function to be determined, and $(\zeta = z, \eta)$ can be used again as alternative coordinates to describe the plume. Now, however, the lines $\eta = \text{const}$ are no longer straight as in the AEM. Observe that, once h is determined, we can calculate the ion streamlines directly from it.

We further assume that the initial plasma profiles $\nu(\eta)$ and $\upsilon(\eta)$ are simply propagated in ζ with two scaling functions,

$$\tilde{n} = \nu(\eta)\tilde{n}_c(\zeta), \tag{2.21}$$

$$\tilde{u}_{zi} = \upsilon(\eta)\tilde{u}_c(\zeta), \tag{2.22}$$

with $\tilde{n}_c(0) = \tilde{u}_c(0) = 1$. Note that the functions $\tilde{n}_c$ and $\tilde{u}_c$ contain the evolution of density and velocity along $\eta = 0$ (the 'centerline', hence the subindex 'c'). Derivation with respect to time in Eq. (2.20) leads to the following basic relation between the velocity components:

$$\tilde{u}_{ri} = \tilde{u}_{zi}\eta h', \tag{2.23}$$

and its particularization at $\zeta = 0$ reveals a first constraint on the initial plasma profile necessary to find self similar solutions, namely, that δ has to be linear in η (i.e., an initially conical velocity profile),

$$\delta' = \text{const}. \tag{2.24}$$

Using Eqs. (2.21) and (2.22) in the continuity equation, Eq. (2.9), leads to:

$$h^2\tilde{n}_c\tilde{u}_c = 1 \tag{2.25}$$

while the radial momentum equation, Eq. (2.11), can be separated in ζ and η as:

$$\upsilon^2 = -\frac{\nu^{\gamma-2}\nu'}{\eta C}, \tag{2.26}$$

$$M_0^2 \frac{h\tilde{u}_c\,(\tilde{u}_c h')'}{\tilde{n}_c^{\gamma-1}} = C, \tag{2.27}$$

where C is a separation constant.

Eq. (2.26) establishes a ligature between υ and ν, the second constraint on the initial plasma profile for the SSM to be applicable, from which it is apparent that ν must satisfy $\nu' \leq 0$ for all η. Taking $\eta \to 0$ in this equation also states that $C = -\nu''(0) \neq 0$ for consistency.

So far, we have the two equations, Eqs. (2.25) and (2.27), to determine the three unknowns h, $\tilde{n}_c$ and $\tilde{u}_c$. The third and last equation should come from the axial momentum equation, Eq. (2.10). Unfortunately, trying to apply the same approach to it leaves us with an expression that cannot be separated in ζ, η as before:

$$\left(\tilde{u}_c^2\right)' - \tilde{n}_c^{\gamma-2}\tilde{n}_c' \frac{2C\eta^2}{M_0^2}\left(\frac{\nu}{\nu'\eta} - \frac{h'}{h}\frac{\tilde{n}_c}{\tilde{n}_c'}\right) = 0. \tag{2.28}$$

Moreover, Eq. (2.28) renders the system incompatible, since the second term cannot be made independent of η. This proves that no self-similar solutions of this type strictly exist, and provides a means to measure the differential error committed by the SSM at any point, as the residual ϵ_l of Eq. (2.28).

Therefore, in order to proceed with the derivation of the approximate SSM, we need to replace Eq. (2.28) with an appropriate condition. Incidentally, observe that the AEM becomes self-similar in zeroth order when $\delta' = \text{const}$, i.e., for an exact, purely conical expansion.

2.3.1. SSM methods with constant axial velocity profiles

A convenient replacement for Eq. (2.28) in the case of a hypersonic plasma plume is the approximation:

$$\tilde{u}_c = \text{const} \equiv 1, \tag{2.29}$$

which is justified by the fact that relative variations in axial velocity are $O(1/M_0^2)$ and therefore vanishing for $M_0^2 \gg 1$. Thus, the error committed by the SSM is proportional to M_0^{-2}. The SSM solution in this case follows immediately, with $\tilde{n}_c$ given by Eq. (2.25):

$$\tilde{n}_c = 1/h^2, \tag{2.30}$$

and h being directly integrable from Eq. (2.27) (now $h^{2\gamma-1}h'' = C/M_0^2$), using the transformation $h'' = h'\mathrm{d}h'/\mathrm{d}h$:

$$(h')^2 - (h'(0))^2 = \frac{C}{M_0^2} \times \begin{cases} -\left(h^{2-2\gamma} - 1\right)/\left(\gamma - 1\right) & \text{for } \gamma > 1, \\ 2\ln h & \text{for } \gamma = 1. \end{cases} \tag{2.31}$$

Eq. (2.31) shows that the slope of h is unbounded in the isothermal case (although its growth is logarithmically slow), whereas for $\gamma > 1$, its asymptotic slope is given by:

$$(h')^2 \to (h'(0))^2 + 1/(\gamma - 1). \tag{2.32}$$

The final integration step can be carried out numerically (in the isothermal case the solution is analytical, in terms of $\mathrm{erf}(\zeta)$, the error function).

Lastly, the differential error from Eq.(2.28) can be written compactly in this case as:

$$\epsilon_l = \frac{C}{M_0^2}\frac{h'}{h^{2\gamma-1}}\left(4\eta\frac{\nu}{\nu'}+2\eta^2\right), \tag{2.33}$$

showing that ϵ_l is only zero for initial plasma profiles with $\nu \propto \eta^{-2}$, which gives a singular condition that cannot be extended down to $\eta = 0$.

Interestingly, it turns out that, by fully retaining pressure effects in the $\tilde{r}$ direction and neglecting them in the $\tilde{z}$ direction, the SSM approximation is very accurate even if globally it is only $O(1/M_0^2)$, as the role of pressure forces on the radial direction is far more important than in the axial direction, in a low-divergence plasma plume.

In Fig. 2.2 the streamlines and density contours for the SSM are plotted and compared against the MoC solution for an illustrative example. As it can be seen, except for low values of $\tilde{z}$ and high values of $\tilde{r}$ (for which the AEM yields a better result), the SSM has a solution that is as accurate or more than the 2nd order AEM, in spite of the $O(M_0^{-2})$ error in the $\tilde{z}$ equation.

The only degrees of freedom of the solution, besides the parameters M_0 and γ, are the value of $h'(0)$ (which dictates the initial divergence angle of the plasma plume) and the initial profile, for which only ν or υ can be freely fixed.

Parks and Katz [60], Korsun and Tverdokhlebova [84], and Ashkenazy and Fruchtman [61], following different approaches, reached independently three formulations of SSMs and initial profiles, which can be regarded as particularizations of the general SSM framework derived here. These SSMs have been successfully employed to propagate a known plume profile into the far-region, as done e.g. in Ref. [16].

In Ref. [60], a uniform axial velocity profile is chosen, leading to a Gaussian density profile:

$$\gamma = 1; \quad \nu = \exp\left(-C\eta^2/2\right); \quad \upsilon = 1. \tag{2.34}$$

The local differential error committed by this SSM cancels out for the streamline $\eta = \sqrt{2/C}$.

In Ref. [84] the choice is the following:

$$\nu = \left(1+C\frac{\eta^2}{2}\right)^{-1}; \quad \upsilon = \left(1+C\frac{\eta^2}{2}\right)^{-\gamma/2}, \tag{2.35}$$

which incidentally makes the differential momentum error independent of η.

Lastly, in Ref. [61] υ is defined in the isothermal case $\gamma = 1$:

$$\gamma = 1; \quad \nu = \left(1+k\eta^2\right)^{-C/(2k)}; \quad \upsilon = \left(1+k\eta^2\right)^{-1/2}, \tag{2.36}$$

where k is an arbitrary constant and $(h'(0))^2 = k$ to enforce an initially conical expansion. Observe that by choosing $k = C/2$, this profile coincides with the isothermal model of Korsun *et al*, and that for $k \to 0$, it tends to the profile of Parks *et al*. Like in the method of Ref. [60], the differential error cancels out for a single streamline. These initial profiles are compared graphically in Fig. 2.5.

It is important to note that the profile choice in SSM is not restricted to these three cases nor the condition $\tilde{u}_c = \text{const}$, and that therefore there is a certain freedom

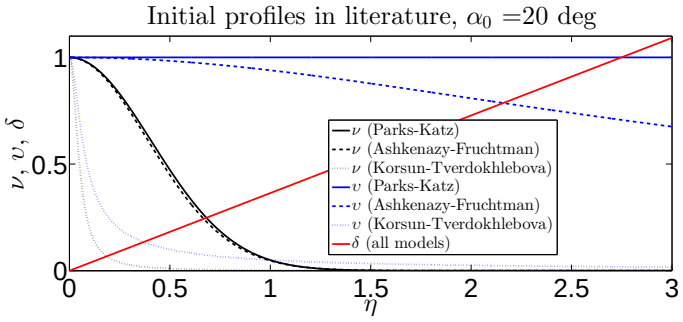

Figure 2.5: Initial SSM profiles, for normalized plasma density (black lines), axial velocity (blue lines), and divergence angle tangent (red lines), for Parks (solid lines), Ashkenazy (dashed lines), and Korsun (dotted lines)]. A common divergence angle $\alpha_0 = 20$ deg is considered, while Korsun profile features $\gamma = 1$.

(within the mentioned constraints) to better match the experimental data (see e.g. Ref. [16], where the plasma profile is defined from an experimental vector of data) or obtain greater accuracy in the regions of interest. As additional examples, we propose two generalizations to non-isothermal plumes of the $\upsilon = 1$ case, and of the Gaussian density profile case. In the first case, the corresponding profile is given by:

$$\gamma > 1; \quad \nu = \left[1 - (\gamma - 1) C \frac{\eta^2}{2}\right]^{1/(\gamma-1)}; \quad \upsilon = 1, \tag{2.37}$$

while, for a Gaussian density profile, we have:

$$\gamma > 1; \quad \nu = \exp\left(-C\eta^2/2\right); \quad \upsilon = \left[\exp\left(-\frac{C\eta^2}{2}\right)\right]^{\frac{\gamma-1}{2}}. \tag{2.38}$$

By comparing Eq. (2.38) with the isothermal Parks profile, Eq. (2.34), we observe that the axial velocity must decrease radially if $\gamma > 1$, as shown also in Fig. 2.6, representing this generalized Gaussian density profile, for different values of γ. The effects on the plasma density are, on the other hand, much smaller.

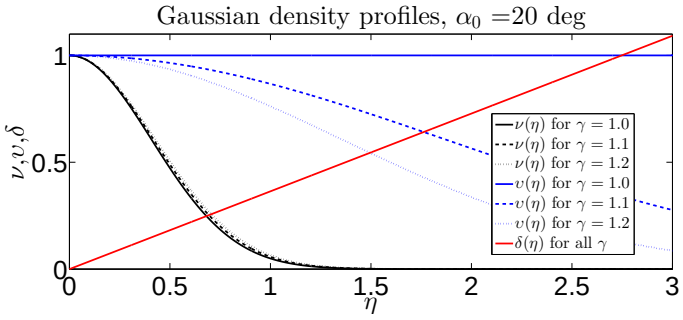

Figure 2.6: Initial plume density (black lines), axial velocity (blue lines), and divergence angle tangent (red lines) of the generalized Gaussian profile, for different values of γ: 1.0 (solid lines), 1.1 (dashed lines), and 1.2 (dotted lines).

Finally, it is worth discussing also SSMs where $\tilde{u}_c \neq 1$. An interesting alternative choice to the cases described in this section is the one given by:

$$\frac{1}{2}\left(\tilde{u}_c^2\right)' = -\frac{\tilde{n}_c^{\gamma-2}}{M_0^2}\tilde{n}_c', \tag{2.39}$$

which is the ion energy equation (see Eq. (2.28)) particularized on the axis of the plume, $\eta = 0$. This choice has the advantage that the local error committed by the SSM when ignoring the axial momentum equation is zero, at and near the axis, which is of particular importance for applications where the main concern is to study the core of the plume. Since the condition given by Eq. (2.26) is not affected by $\tilde{u}_c$, the same profiles discussed before can be used. As a drawback, in this case $\tilde{u}_c$, h and $\tilde{n}_c$ are coupled through Eqs. (2.25), (2.27) and (2.39), which complicates the solution procedure.

2.4 Comparison of the methods and error discussion

The MoC solution can be regarded as exact (except for the numerical truncation error), since it does not introduce any further simplification with respect to the model. However, the MoC necessitates full numerical integration, whereas the semi-analytical AEM and SSM require only minimal numerical work and are therefore markedly faster.

As it can be observed in Fig. 2.2, both the AEM (at first- and second-order) and the SSM follow closely the numerical solution of the MoC, with deviations only becoming visible far downstream. The AEM provides a better approximation than the SSM for short distances, especially for the higher-order AEM solutions, while the SSM is in general better suited than the AEM farther downstream. In return, the AEM can reach arbitrary accuracy by adding higher-order correction terms, and is more precise within a short distance from the initial plane. The region in which the AEM outperforms the SSM is larger the higher M_0 and γ. Note that the AEM solutions shown here do not restart the integration on intermediate planes (down-marching scheme), which would further improve their accuracy.

Figure 2.7 presents the relative error committed by each method at $\tilde{z} = 10$ and 50. The largest relative error is typically committed in the plasma density. Understandably, since the methods rely on $M_0 \gg 1$, the error depends on M_0 and vanishes for $M_0 \to \infty$ as we approach the cold beam limit.

AEM errors are lower than SSM errors at relatively low distances from the initial plane (e.g. $\tilde{z} = 10$), specially in the velocity. This trend is inverted further downstream (e.g. at $\tilde{z} = 50$).

The error also depends on γ, with a purely isothermal plasma (i.e., one that maintains a higher electron pressure downstream) yielding the largest error in both methods, as expected, and on the initial profile. Smoother initial profiles, in fact, lead in general to a smaller error downstream. A larger initial divergence angle α_0,

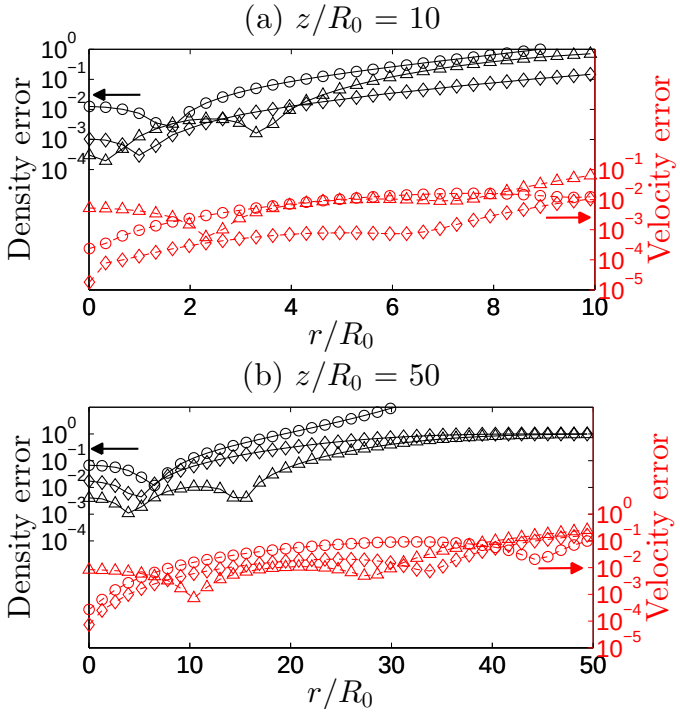

Figure 2.7: Relative density error (upper, black lines; left vertical axis) and relative velocity magnitude error (lower, red dashed lines; right vertical axis) with respect to the MoC numerical solution, for the AEM (1st order: circles; 2nd order: diamonds) and the SSM (triangles) at $\tilde{z} = 10$ (a) and 50 (b) for the same plasma plumes as in Fig. 2.2, with $\gamma = 1.2$.

improves the accuracy of the AEM, but decreases slightly that of the SSM (cf. Fig. 8 of Ref. [49]).

The main differences between the AEM and the SSM are as follows. Firstly, the AEM allows for more general initial plasma profiles, while the SSM sets stronger constraints on the permitted ν, υ and δ (Eqs. (2.24) and (2.26)). This points out that modeling 'exotic' plasma plumes with unconventional profiles (e.g., the plume with high-density wings observed in the HEMPT[17] and DCFT [113]) can only be approached with the AEM (or the MoC). Secondly, each semi-analytical method has a differing advantage: the SSM yields the $O(M_0^{-2})$ streamlines directly as part of the solution, whereas the correction terms of the AEM are independent of M_0 (facilitating, for example, parametric studies).

As a final comment, observe that the two methods are more adequate than the MoC at high Mach numbers, when the latter is geometrically ill-conditioned (the characteristic lines become near parallel), thereby complementing it in those cases.

2.5 Discussion of the plume expansion physics

The presented model and solution methods allow us to explore the fundamental magnitudes of the expansion of a plasma plume. This section discusses the im-

portance of the ambipolar electric field in the plume, its divergence angle, and the limitations of the model in the light of other physical effects.

2.5.1. Ambipolar electric field

As electrons with temperature T_e expand, the plasma generates an ambipolar electric field $-\nabla\phi \propto T_e$ that confines them both axially and radially. Simultaneously, the presence of this field accelerates ions downstream and raises their divergence angle, becoming a central ion transport mechanism in the plasma plume. The evolution of $\tilde{\phi} = e\phi/T_{e0}$ along the axis and along $\eta = 1$ is shown in Fig. 2.8.

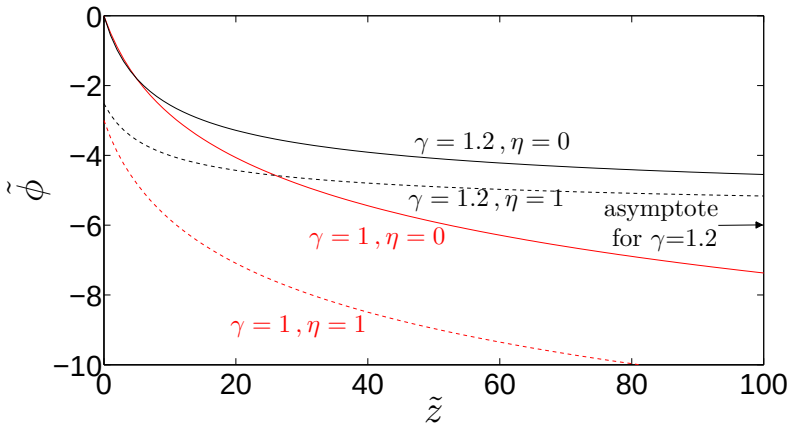

Figure 2.8: Ambipolar electric potential, $\tilde{\phi}$ along $\eta = 0$ (axis) and $\eta = 1$ (95% ion current tube), for $\gamma = 1$ and 1.2, and the same plasma plumes as in Fig. 2.2. The asymptotic value of the potential in the polytropic case is shown on the right side. The solution shown is the (exact) MoC solution.

A first observation, anticipated already in the derivation of the AEM and SSM above, is the modest value of $2e\phi/(m_i u_0^2) = 2\tilde{\phi}/M_0^2$ in a highly hypersonic plume ($M_0 \gg 1$). The resulting low axial electric field is responsible for the small axial ion acceleration, which allowed us to assume $\tilde{u}_c = \text{const}$ as a first approximation in the SSM. In spite of its moderate strength, the ambipolar electric field is the only mechanism in our model responsible for the radial ion acceleration and the increase of the plasma plume divergence angle.

Secondly, observe that the actual value of $\tilde{\phi}$ is determined by the full kinetic description of the electrons. It is noted that, while the *full* fluid equations are always satisfied in a collisionless plasma (as integral moments of Vlasov's equation), a closure is always needed in a fluid model with a finite number of equations, which affects the thermodynamics of electrons. In our model, this closure is carried out by assuming isotropic pressure and a polytropic or isothermal expansion, Eq. (1.4), leaving the effective cooling rate γ as an additional degree of freedom to match the experimentally observed behavior of a plume. The relevance of this unknown parameter is evidenced by the appreciable differences between the expansions with $\gamma = 1$ and 1.2 in Fig. 2.2. Observe that another simple closure, not explored here,

would be to retain the electron energy equation and introduce a Fourier law-like heat equation with a constant electron thermal conductivity [108]. Any of these two choices (or any similar approximation) is equally unjustified from a collisionless kinetic viewpoint, neglects the possible anisotropization of the electron population, and unavoidably means a loss of accuracy in the obtained electric field.

The isothermal limit in the model is equivalent to an infinite electron thermal conductivity and to the so-called Boltzmann relation, $\tilde{\phi} = \ln \tilde{n}$ (our Eq. (2.7)), widely used in more complex models of plasma plume expansions, as seen in Tab. 1.3 [87, 88, 96, 97, 98, 99, 100, 114]. In spite of its ample use, the $\gamma = 1$ limit has the inconvenience of yielding an unrealistic $\tilde{\phi} \to -\infty$ as $\tilde{n} \to 0$, which is approached as the plasma expands downstream. This unbounded decrease of $\tilde{\phi}$ brings the following unphysical consequences. Clearly, $\tilde{u}_i \to \infty$, so that ions appear to be continuously accelerated (albeit logarithmically slow). Secondly, sustaining the constant T_e everywhere (in spite of the expansion) and the unbounded ion acceleration requires an infinite supply of thermal power by the plasma source, in the form of infinite electron heat fluxes. This impedes the computation of the energy balance in a plasma thruster with an isothermal model. Lastly, $\Delta\tilde{\phi} = -\infty$ means that the spacecraft emitting the plume is floating at an infinite positive potential with respect to the ambient plasma. Hence, Boltzmann's relation (the isothermal limit) is not applicable to an infinite expansion.

This unphysical behavior at infinity is not present if the plasma is allowed to cool down at a rate $\gamma > 1$, for which the ambipolar potential exhibits an asymptotic value,

$$\tilde{\phi} \to \tilde{\phi}_\infty = -\frac{\gamma}{\gamma - 1}, \tag{2.40}$$

as $\tilde{n}, \tilde{T}_e \to 0$, defining an (asymptotic) complete expansion state where the electric field vanishes, and $\tilde{u}_i^2 \to \upsilon^2(1+\delta^2)+2\nu^{\gamma-1}/(M_0^2(\gamma-1))$. As stated in Section 2.1, the polytropic model is more consistent with the reported behavior in several laboratory plume experiments. Recent advances in the kinetic modeling of electrons (but in the case of a magnetized expansion [33]) do indeed predict the gradual cooling and anisotropization of electrons downstream, albeit not with a single value of γ for the whole plume domain. Moreover, the inadequacy of $\gamma = 1$ is already apparent in fully-kinetic simulations of the first instants of plume formation [77].

Finally, note that the $\eta = 0$ lines in Fig. 2.8 depart at about $z \simeq 10R_0$ in this example, a distance at which the isothermal and polytropic models start to yield different results in the central part of the plume.

2.5.2. Plume divergence angle

The divergence angle is a central figure of merit of a plasma plume. A practical convention to characterize the divergence angle of the plume and compare similar thrusters is to consider the angle of the streamtube $\tilde{R}(\tilde{z})$ containing 95% of the plasma current. Clearly, due to the continued radial expansion, the divergence angle does not remain constant in the far-region, but keeps increasing downstream

due to the effect of the residual thermal pressure and the ambipolar electric field. To discuss this behavior, we define an *equivalent* far-region divergence angle,

$$\alpha_F(\tilde{z}_F) = \arctan \frac{\tilde{R}(\tilde{z}_F) - 1}{\tilde{z}_F} \tag{2.41}$$

as the half-angle of the *cone* that contains 95% of the ion current at a chosen distance from the initial plane (shown in Fig. 2.1). Although α_F is a function of $\tilde{z}_F$, notice that (I) α_0 sets a lower boundary to α_F, and (II) this cone is a conservative boundary for that fraction of the ion current within the distance $\tilde{z} \in [0, \tilde{z}_F]$. Calculating the angle α_F allows a rapid estimation of the momentum transferred to a surface downstream (following, e.g., the formulation in Ref. [43]). Nevertheless, note that α_F does not fully characterize the divergence characteristics of the plume, it being necessary to know the details of the radial plasma profile to describe where the ion current (and momentum) is concentrated. This is particularly true for unconventional plumes such as those of the HEMPT[17] or DCFT[113] that can have a hollow central part and most of the current on the plume periphery.

Figure 2.9 displays the calculated value of α_F at $\tilde{z}_F = 50$ as a function of the two main parameters of the expansion M_0, α_0, and for two values of γ. Several conclusions can be drawn from this graph.

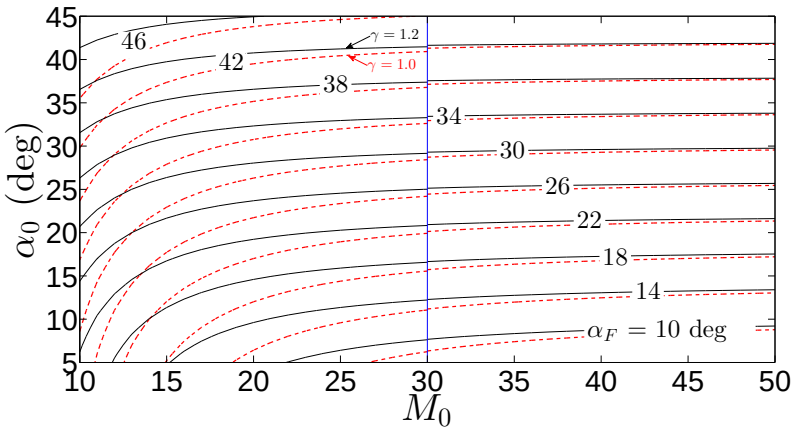

Figure 2.9: Equivalent far-region divergence angle α_F at $\tilde{z} = 50$, as a function of the initial Mach number M_0 and the initial divergence angle α_0. The initial profiles are those of Fig. 2.2, adapted to the value of α_0 used. Both the isothermal limit (red dashed lines) and a polytropic plume with $\gamma = 1.2$ (black lines) are shown. The contours have been calculated with the MoC for the lower Mach numbers ($M_0 < 30$), and with the SSM for the larger ones, where the MoC is geometrically worse conditioned (characteristic lines are nearly parallel at high M).

Firstly, at sufficiently large values of the initial Mach number M_0 (approximately $M_0 > 35$), the electron pressure effect becomes negligible, and α_F approaches asymptotically α_0, independently of the polytropic coefficient. Secondly, at moderate Mach numbers (say, $M_0 < 20$), α_F depends strongly on M_0, and increasing M_0 (whether by imparting a larger acceleration voltage to the ions or by reducing the electron

temperature in the plume with a careful neutralizer design) may be more effective to reduce the far-region plume divergence than reducing α_0, specially if the latter is already low. Thirdly, α_F is higher the lower the γ for a given M_0 and α_0, due to the electron pressure decaying more slowly closer to the isothermal limit. In fact, while unphysical, the isothermal limit $\gamma = 1$ provides a conservative value of $\alpha_F\,(\tilde{z}_F)$. Finally, α_F also has a small dependency on the initial density and velocity profile, which, in view of the SSM's evolution of the h function (Eq. (2.31)), is only second-order.

Note that, like for $\tilde{\phi}$, there is no asymptotic value for α_F as $\tilde{z}_F \to \infty$ in the isothermal limit. On the contrary, for $\gamma > 1$, the equivalent divergence angle is upper-bounded, and (in the SSM case) the tangent of the asymptotic α_F is given by Eq. (2.32).

2.5.3. Additional plume physics

While the fluid model has a clear set of assumptions that limit its range of application to collisionless, quasineutral plasma plumes, it is worth exploring, at least qualitatively, the effect and tendencies of other physical phenomena that may be relevant in the expansion, as those affecting the near-region, introduced in Sec. 1.3.

Near-region collisions are an important source for slow charge-exchange ions that may depart at large angles from the axis. Collisions of all types participate in the setting-up of the initial divergence and help homogenize the plume profile; however, they soon become negligible downstream. As a conservative estimate for a typical propulsive application, consider a 10 cm thruster that emits a xenon plasma with $n_0 = 10^{18}$ m^{-3}, $T_{e0} = 3$ eV, $u_0 = 30$ km/s, $\alpha_0 = 15$ deg, and a mild propellant utilization efficiency of 75%. Assuming that the remaining 25% of the massflow leaving the thruster are cold neutrals (~ 300 K) at their sonic velocity, we have an initial neutral density $n_n \simeq 7 \cdot 10^{19}$ m^{-3}. At this ion energy, the charge-exchange collision cross section is roughly [54] $1.6 \cdot 10^{-19}$ m^2; hence, the ion mean-free-path for charge-exchange collisions is already larger than 1 m initially, and increases rapidly downstream as n_n and n decrease. Observe that the temperature of neutrals, approximately the temperature of the propellant distributor, plays a minor role in this estimation (to double neutral density and halve the mean free path, the propellant injector has to be at 75 K). Similarly, recombination collisions are infrequent in the plume even in the case of a fast cooling rate, and can therefore be neglected for very large distances.

The presence of a sufficiently dense ambient plasma and neutrals can affect the plume expansion in two ways. First, the background plasma will start modifying the solution of the ambipolar potential as soon as its density becomes comparable to the beam density. This could result in (I) an effective cancellation of the expanding electric field, (II) a limitation to the acceleration of ions, (III) the entrainment of background plasma into the plume, and/or (IV) the induction of two-stream instabilities in the very far downstream region. Second, background species will slightly enhance collisions due to the additional density. The effects of background

plasma and neutrals are probably largest in vacuum chamber tests due to the limited dynamic pumping capacities, affecting the quality of the peripheral and far-region measurements that can be taken in the laboratory. In space operation, however, the main practical effect of the background plasma ($n \sim 10^{11}$ m^{-3} in low Earth Orbit) is probably to set a limit to the total $\Delta\phi$ along the plume, as ϕ_∞ must match the background potential, and the satellite cannot float very positive due to the negative charging produced by the ambient electrons. As such, this effect may work together with the plasma cooling described above to set the actual ϕ_∞.

Finally, the presence of an ambient magnetic field $\boldsymbol{B}$ such as the geomagnetic field ($\simeq 0.5$ G at low Earth orbit) can deform the shape of the plume by magnetizing and guiding the trajectories of the light electrons. Macroscopically, the external magnetic field induces electric currents $\boldsymbol{j}$ on the plume. Concurrently, these currents induce a plasma-generated magnetic field that opposes and tends to expel the external one from the core of the plasma (i.e., the currents are diamagnetic). The relative importance of the induced magnetic field compared with the external one is given by the total beta parameter [115], which relates the energy available in the plasma and the energy of the external magnetic field,

$$\beta_{tot} = \frac{n(T_e + m_i u_i^2/2)}{B^2/\mu_0}. \tag{2.42}$$

A value $\beta_{tot} \gg 1$ indicates dominant induced field effects and that the external field therefore only perturbs the thinner peripheral plasma. For the same numerical example as above with $n_0 = 10^{18}$ m^{-3}, we need to travel more than 20 m downstream before $\beta_{tot} < 1$, which suggests a strong expulsion of the external magnetic field from the core of the beam up to long distances. The electric currents in the plasma also receive the Lorentz force $\boldsymbol{j} \times \boldsymbol{B}$. This force distorts the plume expansion depending on the direction of the magnetic field with respect to the axis of the plume, possibly affecting its divergence. As suggested in Ref. [52], the magnetic field would flatten the plume in the direction perpendicular to both $\boldsymbol{B}$ and the axis of the plume, along which the transport is hindered, and stretch it in the plane defined by $\boldsymbol{B}$ and the axis. This behavior of the plume is of particular concern for spacecraft charging and contamination studies, where we are interested in determining precisely the ion flux to a given satellite surface.

Notwithstanding, a qualitative analysis shows that a uniform external magnetic field $\boldsymbol{B}_0$ can deform, but not deflect, a globally-current-free plasma plume. Indeed, assuming that no electrical currents flow in or out of the plasma domain or to infinity, the total magnetic force on the whole plasma domain Σ is zero, since the induced magnetic field forces are purely internal, and for the external field:

$$\boldsymbol{F}_{plume} = \int_\Sigma \boldsymbol{j} \times \boldsymbol{B}_0 d\Sigma = \left(\int_\Sigma \boldsymbol{j} d\Sigma \right) \times \boldsymbol{B}_0 = 0, \tag{2.43}$$

where the integral in parenthesis is zero since no current flows in or out of the volume (i.e., for each vector component of the integral, e.g. x, we have $\int j_x dydz = 0$ over a yz cross-section of the plume).

2.6 Fluid model validation against full-PIC simulations

In collisionless plasma plumes, all types of fluid closures appear to be equally unjustified, as commented in Sec. 1.5.3. Therefore, a natural question arises as to whether or not the fluid model introduced in this chapter is capable of retaining the essential physics of a plume expansion. For this reason, a comparison study between our fluid model (Sec. 2.1, solved with the AEM method of Sec. 2.2), and a full-PIC model, developed at the University of Southern California, has been carried out [62]. The AEM method has been preferred to the SSM, as it allows more flexibility in the choice of the initial plasma plume profiles.

In the following subsections, the plume geometry chosen for this comparison is introduced, and then a generalization of the AEM method to this different plume geometry is described. Finally, the comparison study results are shown and discussed.

2.6.1. Simulation geometry

The full PIC simulations feature a planar plume geometry like the one depicted in Fig. 2.10. The plume is a plasma slab, which is symmetric with respect to the (y, z) plane, extends to infinity along y and expands in the x and z directions. This choice, instead of the more usual axisymmetric configuration considered in the previous sections, is dictated by a present limitation in the full-PIC code, and allows to reduce the required number of simulated macro-particles and, hence, the computational cost. To allow for a direct comparison of the results, the fluid model solver must consider this plume geometry as well.

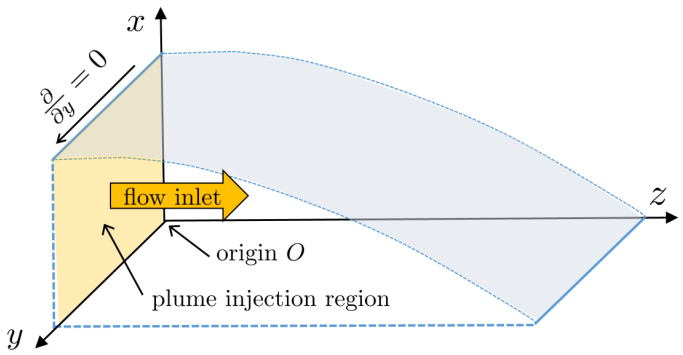

Figure 2.10: Simulation domain and plume geometry for the comparison study. The 2D planar plume is symmetric with respect to the (y, z) plane.

2.6.2. AEM model for a plasma plume slab

Although the fluid model presented in Sec. 2.1 is applied to an axially symmetric plume case, the stationary fluid equations derived there can be easily generalized

to the planar 2D geometry of Fig. 2.10, obtaining the following non-dimensional equations for mass conservation and momentum balance:

$$\tilde{u}_{zi}\frac{\partial \ln \tilde{n}}{\partial \tilde{z}} + \tilde{u}_{xi}\frac{\partial \ln \tilde{n}}{\partial \tilde{x}} + \frac{\partial \tilde{u}_{zi}}{\partial \tilde{z}} + \frac{\partial \tilde{u}_{xi}}{\partial \tilde{x}} = 0, \tag{2.44}$$

$$\tilde{u}_{zi}\frac{\partial \tilde{u}_{zi}}{\partial \tilde{z}} + \tilde{u}_{xi}\frac{\partial \tilde{u}_{zi}}{\partial \tilde{x}} = -\frac{\tilde{n}^{\gamma-1}}{M_0^2}\frac{\partial \ln \tilde{n}}{\partial \tilde{z}}, \tag{2.45}$$

$$\tilde{u}_{zi}\frac{\partial \tilde{u}_{xi}}{\partial \tilde{z}} + \tilde{u}_{xi}\frac{\partial \tilde{u}_{xi}}{\partial \tilde{x}} = -\frac{\tilde{n}^{\gamma-1}}{M_0^2}\frac{\partial \ln \tilde{n}}{\partial \tilde{x}}, \tag{2.46}$$

Note that the only difference is the missing axisymmetric term, with respect to Eqs. (2.9), (2.10), and (2.11). In this case, in the cold beam limit ($M_0 \to \infty$), the analytical solution for the density and velocity of the plasma, takes the form:

$$\tilde{n}^{(0)}(\tilde{x},\tilde{z}) = \frac{\nu(\eta)}{1+\delta'\tilde{z}} \tag{2.47}$$

$$\tilde{u}_{zi}^{(0)}(\tilde{x},\tilde{z}) = \upsilon(\eta) \tag{2.48}$$

$$\tilde{u}_{xi}^{(0)}(\tilde{x},\tilde{z}) = \upsilon(\eta)\delta(\eta), \tag{2.49}$$

where now $\eta = \tilde{x}$ at the initial plane. Such density solution differs from the one presented in Sec. 2.2 due to the absence of the axisymmetric term $(1+\tilde{z}\delta/\eta)$ in the denominator, which models the density decrease as the streamline radius increases. In this planar 2-D geometry, the density only decreases if the streamlines diverge from one another.

Finally, the down-marching scheme of Sec. 2.2.4 has been applied to extend the validity of this AEM method to arbitrary M_0 and α_0 values.

2.6.3. Full particle-in-cell simulator

The electrostatic full particle-in-cell model considered for this comparison study is described in detail in Refs. [76, 77, 116, 117, 118]. As in all full-PIC models, both the electrons and the singly-charged ions are modeled as macro-particles. The ion and electron dynamics, the space charge and the electric potential ϕ are solved self-consistently with Eqs. (2.50) and (2.51), with m, eZ representing respectively the elementary particles mass and charge, and $\boldsymbol{v}$,$\boldsymbol{r}$ the macro-particle position and velocity vectors:

$$\epsilon_0 \nabla^2 \phi = e\,(n_e - n_i) \tag{2.50}$$

$$\frac{d}{dt}\,(m\boldsymbol{v}) = eZ\boldsymbol{E}, \quad \boldsymbol{v} = \frac{d\boldsymbol{r}}{dt}. \tag{2.51}$$

The simulation setup is similar to that described in Refs. [77] and [116]. First of all, the simulation domain is initially a vacuum. At each step, macro-particles representing singly charged ions and electrons are emitted along the z direction into the simulation domain. The ions are sampled from a cold drifting Maxwellian

distribution and have a finite temperature T_{i0}. The electrons inside the plume source, on the other hand, are thermal and stationary. Simulations are run using the real mass ratio of proton to electron, $m_i/m_e = 1836$, with a temperature ratio of ion to electron at the source equal to $T_{i0}/T_{e0} = 0.01$, where the subscript 0 denotes the condition at the plume source plane ($0 < \tilde{x} < 10, z = 0$). This corresponds to a normalized ion thermal velocity of $v_{th,i0}/v_{th,e0} = 0.0023$. Two different macroscopic drifting velocity for the ion beam, $u_B/c_s = M_0 = 5$ and 15 have been considered, as shown in Tab. 2.1, with $c_s = \sqrt{T_{e0}/m_i}$ representing the ion sonic velocity at the plume source plane.

Regarding injection, a zero net current density has been assumed at the source plane, meaning that $\boldsymbol{j}_{e0} = \boldsymbol{j}_{i0}$. The cell size is taken to be the Debye length at this plane, λ_{D0}, with respect to which the coordinates are normalized. The simulation domain in the $\tilde{x} - \tilde{z}$ plane is 600 λ_{D0} $\times$1000 λ_{D0}, with a time step resolution of $\Delta t \times \omega_{pe} = 0.05$ ($\Delta t \times \omega_{pi} \simeq 1.16 \times 10^{-3}$), where ω_{pe} and ω_{pi} are the electron and ion plasma frequencies at the plume source plane. The initial plasma plume size along $\tilde{x}$ is taken to be $R_B = 10\lambda_{D0}$, as pointed out in Fig. 2.10.

For the $M_0 = 15$ case, the normalized simulation duration is $t\omega_{pe} = 856.8$ or $t\omega_{pi} \simeq 20$ (a total number of simulation steps equal to 17136). At each step, approximately 1000 simulation particles are injected. For the $M_0 = 5$ case, the simulation normalized duration is $t\omega_{pe} = 2570.4$ or $t\omega_{pi} \simeq 60$ (51408 total simulation steps). At each step, approximately 400 simulation particles are injected. Note that the simulations duration is much longer than the ion plasma period and that the beam transient length, $L_B = u_B t$ is much larger than the beam initial radius, R_B. Therefore, a steady state for both electrons and ions is well established behind the beam front (the farthest section that the ions have reached, located at $z \simeq u_B t$). Since the electrons oscillate back and forth many times around this front, it can be reasonably assumed that they reach a quasi-stationary condition. In the following, for the comparison with the stationary fluid simulations, we shall therefore consider a simulation region extending downstream to $\tilde{z} \sim 250$.

2.6.4. Comparison simulations set

For this comparison study, a set of 4 different plume cases has been taken into account, as reported in Tab. 2.1. The initial density profile for the plasma plume has been assumed to be uniform in the range $\tilde{x} \in [0, 10]$, while for the injection ion velocity components, the conical profile of Eq. (2.52) and (2.53) has been used:

$$\tilde{u}_{zi}\left(\tilde{x}, \tilde{z} = 0\right) = \left(1 + \left(\frac{\tilde{x}}{10}\tan\alpha_0\right)^2\right)^{-1}, \tag{2.52}$$

$$\tilde{u}_{xi}\left(\tilde{x}, \tilde{z} = 0\right) = \tilde{u}_{zi}\left(\tilde{x}, \tilde{z} = 0\right)\tan\alpha_0\frac{\tilde{x}}{10}. \tag{2.53}$$

The ion Mach number shown in Tab. 2.1 is computed by assuming $\gamma = 1$. This means that, if the electrons of the PIC simulation are injected with a thermal random

velocity corresponding to a temperature T_{e0}, the ion injection fluid velocity at the axis is computed as $u_{i0} = M_0\sqrt{T_{e0}/m_i}$.

Table 2.1: Simulation set parameters considered in the fluid-full PIC comparison

Parameter	**Sim. 1**	**Sim. 2**	**Sim. 3**	**Sim. 4**
Initial Mach number	15	15	5	5
Initial outermost streamline div. angle	0	10	0	10
Initial density profile	flat	flat	flat	flat

The initial density and velocity profiles are finally plotted for the Sim. 2 and Sim. 4 case in Fig. 2.11.

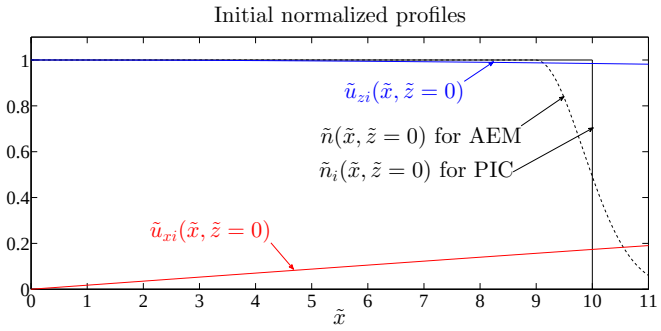

Figure 2.11: The initial normalized plume profiles at the beam injection: initial density profiles for the AEM (dashed black) and for the PIC (solid black), initial velocity profiles $\tilde{u}_{zi}(\tilde{x},0)$ (solid blue) and $\tilde{u}_{xi}(\tilde{x},0)$ (solid red) for both methods.

The Sim. 1 and Sim. 3 cases feature an identical density profile, but with a constant initial axial velocity $\tilde{u}_{zi}$ and a zero velocity component along $\tilde{x}$ ($\alpha_0 = 0$). Note that the AEM density profile has necessarily been smoothed for its correct implementation in the fluid solver, which requires a smooth transition to vacuum, while preserving the total mass flow in the $\tilde{z}$ direction. The PIC density profile, on the other hand, is provided for the ions only, since that of the electrons is slightly different and determined by the current flux condition $\boldsymbol{j}_{e0} = \boldsymbol{j}_{i0}$, as explained in Sec. 2.6.3.

2.6.5. AEM simulation results

The AEM fluid solution provides insight into the essential physical processes occurring in the plasma plume expansion. Fig. 2.12 shows the evolution of the density profiles and of the divergence profiles $\tilde{u}_{xi}/\tilde{u}_{zi}$ for the 4 simulation cases of Tab. 2.1 and at successive planes $\tilde{z}_i$, with the assumption of $\gamma = 2$. This γ value, allows to match well the fluid and PIC simulation results, as it will be shown in Sec. 2.6.6. The reported simulations have been carried out with the down marching scheme presented in Sec. 2.2.4 and a correction up to second order. Such initial

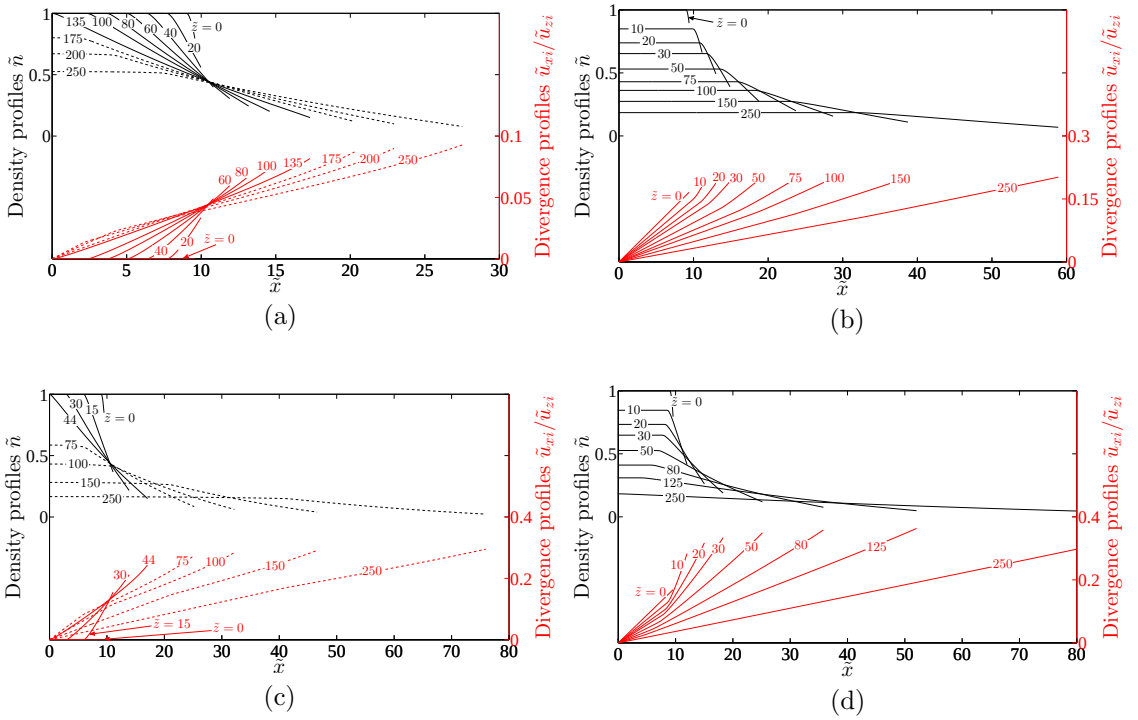

Figure 2.12: Density and divergence profiles at different $\tilde{z}$ sections in the AEM fluid model: (a) Sim. 1 case, (b) Sim. 2 case, (c) Sim. 3 case, (d) Sim. 4 case. The polytropic coefficient γ has been assumed equal to 2.0.

profiles are a subset of the input initial profiles, which are fed to the AEM fluid solver, at each re-start.

In Fig. 2.12 (a) and (c) (zero initial plume divergence and Mach number of respectively 15 and 5), the propagation of the expansion Mach line can be observed clearly. In fact, the density gradient and the related ambipolar electric field, generating at the plume edge $\tilde{x} = 9, \tilde{z} = 0$ (refer to Fig. 2.11), propagates inwards towards $\tilde{x} = 0$ along a line with a slope given by $-\arcsin(1/M_0)$ and reaches the axis after a certain axial distance, which is larger the higher the Mach number (bold lines in the plots). Once the expansion wave reaches the beam symmetry plane, the wave reflection effect is that of generating a density plateau in the x-direction, which extends further downstream. The generation of the expansion wave can be appreciated at the outer edge of the plasma plume, by observing the gradual onset with $\tilde{z}$ of a non-zero divergence angle (red curves), which propagates inwards. The plume develops a conical velocity field, or a divergence profile linear with $\tilde{x}$ at the expansion wave reflection, but not elsewhere. This conical divergence profile is the only admitted profile of the fluid models based on the self-similarity assumption [49, 50, 52, 60, 119]. After the expansion wave reflection, the divergence profile is no more completely self-similar (or linear in $\tilde{x}$).

Fig. 2.12 (b) and (d) show the evolution of the plume profiles for the Sim. 2 and 4 cases. Since the divergence angle is not zero in these cases, the density drops

since the beginning. For the Sim. 2 case ($M_0 = 15$), the expansion Mach line has a slope relative to the outermost streamline lower than $\alpha_0 = 10$ degrees. Therefore, it gradually gets farther away from the symmetry plane, producing an increasingly wider region with $\tilde{z}$, which is completely unaffected by the expansion and that expands conically, according to Eq. (2.47). Eventually, the expansion wave will reach the symmetry plane, as it crosses plume regions with a decreasing ion divergence angle, and this crossing is farther downstream the higher the γ coefficient and the M_0. For the Sim. 4 case ($M_0 = 5$), in fact, the lower Mach number makes the expansion wave approach the plume symmetry plane since the very beginning.

2.6.6. Comparison of the results and discussion

In order to match the full-PIC simulation results with those of the fluid model, an error figure of merit ϵ has been introduced. This is defined as the root mean square of the relative density error over a common AEM-PIC simulation domain, with a weight, for each common node (i, j), given by $w_{ij} = n_{AEMij} / \sum_{i,j} n_{AEMij}$:

$$\epsilon = \sqrt{\sum_{i,j} w_{ij} \cdot \left(\frac{n_{AEMij} - n_{PICij}}{n_{AEMij}} \right)^2}. \tag{2.54}$$

Referring to Fig. 2.13, the comparison domain extends from $\tilde{z} = 0$ to $\tilde{z} = 250$, the upper boundary being due to the PIC "stationary" region extension. In the $\tilde{x}$ direction, on the other hand, such domain is limited by the radius of the outermost AEM streamline solution.

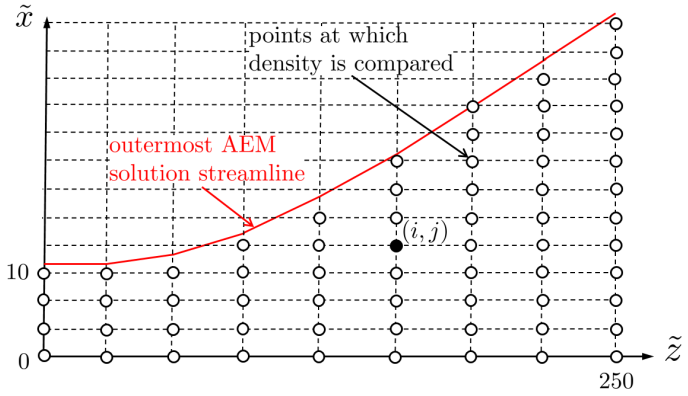

Figure 2.13: Common 2-D domain considered for the comparison between the full-PIC and the fluid model results

The fluid model parameters have then been tuned to minimize this figure of merit. This has been done by evaluating the fluid solution for a set of γ and M_0 values contained in a 2-D solution space. The results for the Sim. 1 case are shown in Fig. 2.14.

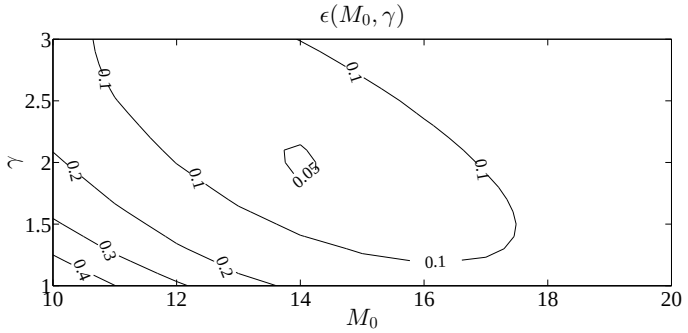

Figure 2.14: Error figure of merit as a function of the M_0 and γ parameters of the fluid model for the Sim. 1 case. The adiabatic γ limit is 2.

The R.M.S. relative density error ranges between a minimum of 3.4% for the $M_0 = 15$, $\alpha_0 = 10$ deg. case and a maximum of 7.5% for the $M_0 = 5$, $\alpha_0 = 0$ deg. case. The pairs of γ and M_0 that minimize the errors and the corresponding R.M.S. error are finally reported in Tab. 2.2, for all the simulation cases.

Table 2.2: Optimal γ and M_0 values

Parameter	**Sim. 1**	**Sim. 2**	**Sim. 3**	**Sim. 4**
M_0	14.0	15	4.5	4.0
γ	2.0	1.7	1.6	1.9
ϵ	5.0%	3.4%	7.5%	5.3%

The optimal γ coefficient (for density prediction) appears to be somewhere between 1.6 and 2, depending on the simulation case, with 2 representing the adiabatic value for the considered geometry. In fact, although ions and electrons have always 3 degrees of freedom (along x,y,z), it is clear that the degree of freedom in the infinite direction (y) does not participate at all in the expansion, thus remaining frozen. Therefore, in the computation of the adiabatic specific heat ratio, only two degrees of freedom should be taken into account, leading to an adiabatic value equal to $\gamma = 1 + 2/N_{DOF} = 2$. The fact that the optimal γ appears to be close to this adiabatic limit, seems to contradict the expectations from experimental measurements, where γ is found between 1.0 and 1.3 (being 1.67 the adiabatic limit of the axisymmetric case). Two reasons can explain these differences:

1. the considered case is a 2D plasma plume slab, which might yield to different results with respect to the axisymmetric plume case of experiments.

2. The optimal polytropic coefficient (minimizing the density error in the given domain) can be different from the global coefficient found in experiments, which is obtained by processing density and temperature measurements at different axial and radial coordinates. As suggested in Refs. [116], [117] and [118], the polytropic coefficient seems to vary from streamline to streamline and along their expansion. So, this optimal coefficient might reflect the value of the plasma region where most of the divergence increase takes place.

For what regards the optimal M_0, this is not very different from the full-PIC simulation one, computed with Eq. (1.5) and taking $\gamma = 1$. Again, two reasons may explain the observed differences. Firstly, the optimal Mach number should approach the value of the effective Mach number, which controls the real speed of density perturbations within the supersonic plume (in the full-PIC simulation). Such effective Mach number is lower than the Mach number of Tab. 2.1 because it depends on an effective coefficient $\gamma > 1$, through Eq. (1.5). Secondly, just like the optimal γ, also the optimal Mach number of the fluid simulation minimizes the error figure of merit and, therefore, it does not necessarily coincide with the effective Mach number.

With the optimal values for M_0 and γ of Tab. 2.2, the AEM solutions have finally been compared with those of the full-PIC model, in terms of density contours and ion streamlines, as shown in Fig. 2.15.

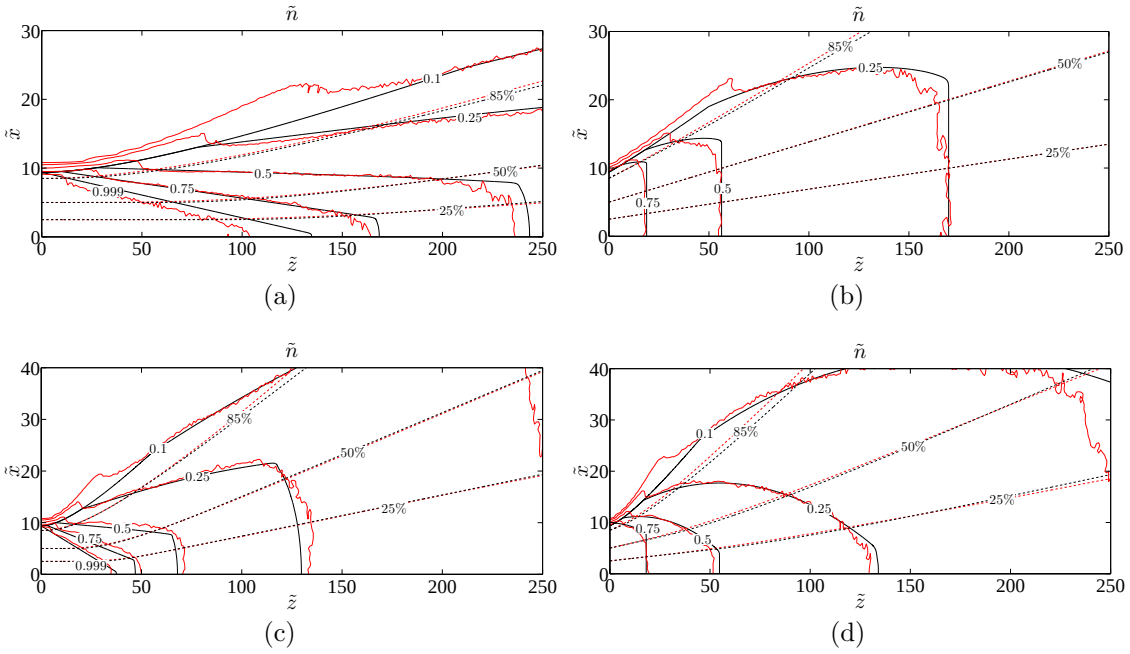

Figure 2.15: Density contour (solid lines) and streamlines (dashed lines) comparison (25, 50 and 85% ion current). Red lines refer to the PIC, while black lines to the AEM. (a) Sim. 1 case, (b) Sim. 2 case, (c) Sim. 3 case and (d) Sim. 4 case.

In all cases, the agreement is quite satisfactory, both in terms of the density contours and of the ion streamlines. Regarding the former, the iso-density lines only depart significantly at the outer periphery of the plume, where the difference between the initial profiles for AEM and PIC simulations is important (refer to Fig. 2.11). Regarding the latter, it can be noticed that the AEM slightly overestimates the divergence growth of the core streamlines (e.g. the 25% ion current streamlines), while underestimating the divergence growth of the outermost streamlines. This is clearly due to the assumption of a single polytropic coefficient for the fluid model, while the full-PIC simulations show that the effective γ value changes from streamline to streamline [116, 117, 118]. In particular, the outermost streamlines present a

lower γ value, thus retaining their thermal energy farther downstream and expanding more than the core streamlines. The AEM optimal solution thus assumes an average effective polytropic coefficient, that minimizes the overall error.

Finally, referring to Fig. 2.15 (a), the density perturbation (or the expansion Mach line), represented by the iso-density line with value 0.999, moves towards the plume symmetry plane more quickly in the PIC simulation than in the fluid one. This suggests that the effective initial Mach number (dictating the wave propagation velocity) is lower than the optimal initial Mach number, used for the fluid simulation.

The major conclusions that can be extracted from this comparative study are finally summarized below:

- The fluid model reproduces correctly the results of the full-PIC simulations in terms of plasma density and velocity at least down to a distance of 25 initial plume radii.

- A single value for the polytropic exponent ($\gamma \simeq 1.6 - 2$) appears to be reasonably good for all the 2D planar plume simulations considered. Although a detailed analysis [117, 118] suggests the existence of different γ regions, this is not particularly relevant for the prediction of the plume density. In fact, a near adiabatic γ seems to correctly model the plume divergence growth and hence the density field.

The above-mentioned conclusions, however, do not reduce the importance of kinetic simulations in the study of the plasma plume expansion. Firstly, they remain the only way to study the evolution of the electron and ion energy distribution functions, and their deviations from pure Maxwellian ones (due to collisions such as MEX or CEX). Secondly, they allow to properly study the electron cooling mechanism, which affects the electric potential drop, far downstream. In fact, this is strongly related to the local γ coefficient in the far region of the plume, whose value may be different from the optimal one obtained here.

2.7 Conclusions

The behavior of hypersonic plasma plumes has been studied with a two-fluid model, which has been integrated with two semi-analytic solution methods (AEM and SSM) and the MoC. The AEM and SSM methods both yield approximate solutions, and each has its own advantages. The AEM method enables to reach arbitrary accuracy in a limited region, can be used to set up a marching integration scheme, and provides more flexibility in the choice of initial density and velocity profiles, allowing the study of complex plumes. An additional advantage of the AEM is that the perturbation terms themselves are independent of M_0 and can be reused to explore the effect of different Mach numbers on the expansion without recalculating the solution each time (useful e.g. for parametric studies). The SSM, in contrast, is algebraically simpler, provides the ion streamlines directly as part of

the solution (h function) for a limited range of initial plasma profiles, and a relatively easier calculation with an accurate solution in a wider region.

The relative error of AEM and SSM in density and velocity, when compared with the MoC exact solution, is small in all the studied cases (10^{-2}–10^{-3} at 50 thruster radii downstream at the axis). Both methods are particularly accurate near the hypersonic limit where the MoC is geometrically ill-conditioned (Mach lines become near parallel at high M), thereby complementing it (which remains more appropriate for problems with $M_0 \gtrsim 1$).

The electron thermodynamics, through the effective cooling rate γ, have been shown to condition the plume expansion, the evolution of the ambipolar plasma potential, and the divergence angle growth rate. The isothermal limit, $\gamma = 1$, which yields the well-known Boltzmann's relation, leads to unphysical results at infinity, indicating that there must exist a collisionless cooling mechanism in the plume, and revealing the inadequacy of Boltzmann's relation for infinite expansions.

The equivalent divergence angle α_F at a given downstream section depends fundamentally on M_0^2 (conversely, on the ratio of beam accelerating voltage to electron temperature in the plume) and α_0. An important observation is that, in order to decrease α_F, it may be more advantageous to increase the ion Mach number M_0 (i.e., increase the voltage or limit the electron temperature in the plume) than to decrease the initial divergence angle α_0, which can be more challenging in certain thruster designs, specially at lower Mach numbers and already low divergence angles ($M_0 < 20$ and $\alpha_0 < 20$ deg). In regard to α_F, $\gamma = 1$ yields the upper bound for plume divergence angle.

Moreover, several physical aspects of plasma plumes not included in the fluid model have been briefly discussed and some of them (e.g. collisions effects) will be treated in the following chapter. Collisions and recombination have been shown to be negligible in the far plume, while electron kinetic effects can play a major role in the expansion and warrant detailed modeling. A dense ambient plasma or a neutral species could alter the expansion of the plume, while a background magnetic field can distort the expansion of the plasma profile, but—at least under certain assumptions—not its propagation direction.

Finally, in order to evaluate the applicability of a two-fluid model with a polytropic closure to a collisionless plume, a comparison study between the results of a full-PIC model (developed at the University of Southern California) and our fluid model based on the AEM method has been carried out. The AEM method has been adapted to a 2D plasma slab geometry (considered by the computationally expensive full-PIC code), with a down-marching scheme to ensure a sufficient accuracy, independently of the ion Mach number and plume divergence. Such a study has permitted to determine the optimal values of the free parameters of the fluid model, M_0 and γ, which allow to minimize the relative errors between the two models. The optimal Mach number appears to be close to the effective Mach number of the PIC simulations, while the optimal polytropic cooling coefficient assumes values close the adiabatic limit. These optimal parameters yield reasonably low density errors over a large domain, extending up to 25 initial plume radii downstream, thus demon-

strating that a good accuracy in the prediction of a plasma plume expansion can be reached even with a simple fluid model based on polytropic electrons.

Regarding future work, an extension of this comparison study to a 3-D axisymmetric plume geometry should be carried out, in order to investigate the existence of an optimal γ value, also in this more realistic case.

Chapter 3

The hybrid PIC-fluid model

This chapter presents the hybrid PIC-fluid model that has been developed to study the plasma plume interaction with a satellite and any nearby object. The code is named EP2PLUS, and has already been presented in Ref. [94]. Here, the detailed modeling aspects of the PIC model, of the electron model, and of the fluid closure algorithms, for both quasineutral and non-neutral plasma regions, are presented [1]

[1] The contents of this chapter are based on a conference paper [94], and primarily on two journal publications, submitted at the time of this thesis defense [120, 121]

3.1 EP2PLUS: Extensible Parallel Plasma PLUme Simulator

3.1.1. Motivation for a three-dimensional hybrid code

The simulation of the plasma plume interaction with the satellite and with any downstream object is a three-dimensional problem, except for very rare scenarios, featuring axisymmetric satellites (with respect to the plasma plume axis). Moreover, as discussed in Sec. 1.5.6, the hybrid approach permits saving a large computational power, with respect to full-PIC and fully-kinetic codes, while being more flexible than fluid ones, when dealing with the heavy particles distribution functions (which are arbitrary). For these reasons, a three-dimensional hybrid code has been developed, and named EP2PLUS, acronym for "*Extensible Parallel Plasma PLUme Simulator*". Although a first phase has been completed within the LEOSWEEP project, which requested the capability of simulating an ion beam shepherd mission scenario, the developed code can be employed to study a large variety of plasma plume applications.

3.1.2. Development methodology and overall code structure

EP2PLUS has been developed following strict development and validation standards. A test driven design (TDD) development has permitted validating new modules by designing, in the first place, dedicated validation tests. In this way, new code functions have been added only when validated, while the functionality of old functions has been continuously checked throughout the development phase by running the existing tests suite. The Appendix C can be consulted for a detailed description of the existing functional and integration tests.

Moreover, as suggested by its acronym, the code is scalable and highly modular, with industry level input/output formats, like HDF5. The physical unit, which actually performs the simulation, is called CORE and is coded in Fortran, while the pre-processing (PRE) and post-processing (POST) units are coded in Python. As clearly stated by the code acronym, parallelization has been implemented with Open-MP, to take the advantage of large shared memory workstations. A schematic representation of the overall code is given in Fig. 3.1, while a brief description of the three units is given hereafter:

- SET: coded in Python, it is in charge of the pre-processing tasks, including the generation of the necessary input files for the CORE. The simulation settings are specified by a dedicated input file, "set.inp", editable by the user. The outputs are "sim_params.inp" (text file), which contains the simulation parameters, and "SimState.hdf5" (HDF5 format), which contains the minimum set of variables to start or re-start the simulation (particle data, mesh data, fields data, etc...).

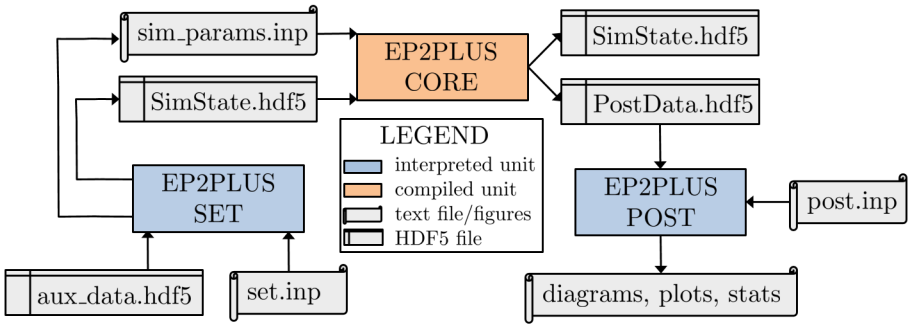

Figure 3.1: Overall structure of the EP2PLUS code, featuring a SET, a CORE, and a POST unit.

- CORE: coded in Fortran, it represents the simulation core unit, which carries out the plasma physics simulation. Taking as inputs both "sim_params.inp" and "SimState.hdf5", it runs the simulation and generates the "PostData.hdf5" output file, which contains the plasma plume properties at given time steps, and an updated version of the "SimState.hdf5" file, at the last simulation time step.

- POST: coded in Python, it reads the CORE output files and produces different graphical results (plots and diagrams) as required by the user, through a dedicated POST input file, named "post.inp".

This chapter shall focus exclusively on the CORE unit algorithms.

3.1.3. Main characteristics and capabilities of the code

Being a hybrid PIC-fluid code, EP2PLUS presents a PIC sub-model to deal with the heavy particles (ions and neutrals), an electron sub-model for the fluid electrons, and dedicated fluid closure algorithms that update the electric field self-consistently.

The PIC sub-model features the following:

- Use of a 3D structured mesh, which can be either Cartesian or non-uniform, thus adapting to the geometric plume expansion.

- Sub-division of heavy particles in dedicated particle populations, depending on their charge state, mass, and energy content.

- Use of a population control algorithm that permits controlling the macro-particles number at those cells adjacent to injection surfaces, or where collisional effects are important.

- Use of Direct Simulation Monte-Carlo (DSMC), Monte Carlo Collisions (MCC), or deterministic algorithms for the simulation of heavy particles collisions.

- Simulation of the interaction between macro-particle and simulation objects, with different wall types: particles injection, ion recombination, neutral reflection, and sputtering.
- Bohm's condition forcing on quasineutral material boundaries.

The electron fluid model and the corresponding fluid closure algorithms, on the other hand, represent the most innovative contribution, in this work. Their main features are briefly summarized below:

- Electron fluid model for an unmagnetized plasma, based on a kinetic closure for the electron pressure tensor (polytropic electrons), and retaining a collisional term, in order to compute the electron current streamlines.
- Dynamic division of the simulation domain into quasineutral and non-neutral sub-domains. In the former, the electron momentum equation directly yields the electric potential, while in the latter it is coupled with Poisson's equation (non-linear Poisson's solver).
- Computation of boundary conditions for both the electric potential and electric current density, through a dedicated plasma sheath model and an equivalent circuit that model the interaction between the plasma and dielectric/conductive objects.

The above defined characteristics permit simulating the following physics:

- Interaction of heavy particles with conductive (iso-potential) or dielectric objects.
- Electric charging of conductive objects.
- Backscattering ion flux estimation. Slow ions are generated mostly by near-region collisions, such as ionizations of different degrees and resonant symmetric CEX reactions.
- Backsputtering flux estimation, when a sputtered target is considered. This is useful for studying the satellite-plasma-debris interaction, in the context of an IBS mission, as reported in Sec. 5.3.
- Simulation of the electric current loop within the plasma, as done in the simulations of Chapter 4.
- Proper characterization of non-neutral regions, such as the lateral plume regions (where ions are deflected towards the spacecraft), and the wake behind a debris object, in the context of the IBS scenario, without having to generate complex meshes, locally adapting to the Debye length.

3.2 The particle-in-cell model for heavy species

The PIC model simulates both ions and neutrals as macro-particles and its simplified scheme is shown in Fig. 3.2.

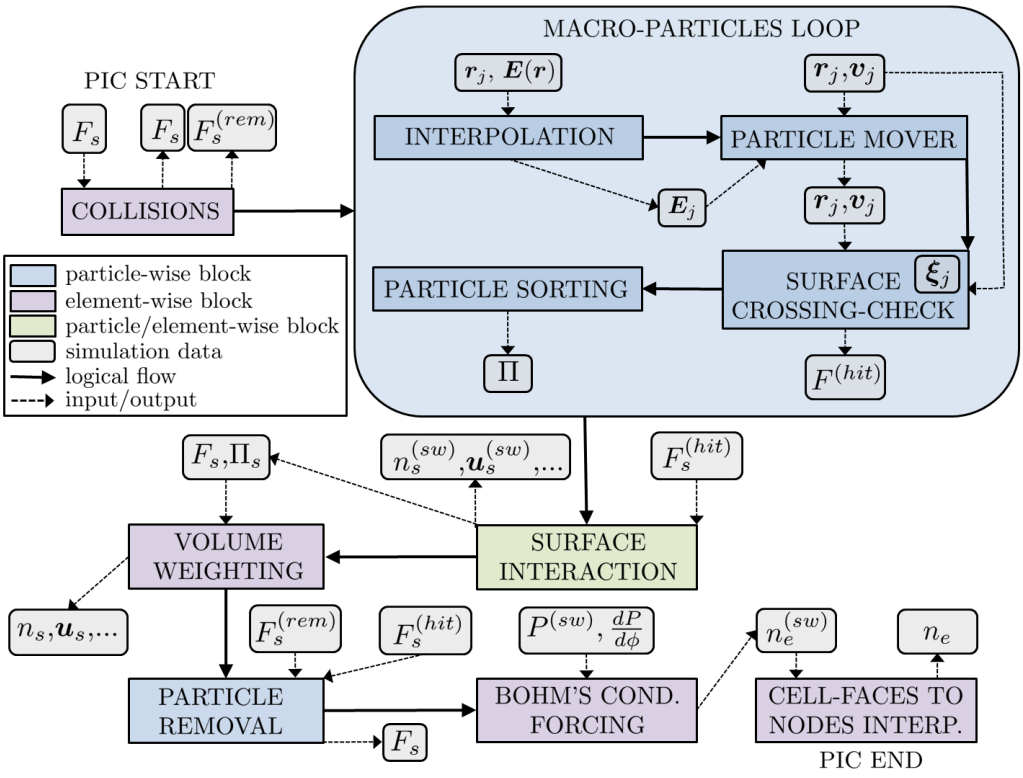

Figure 3.2: Scheme of the PIC model for the heavy species. F_s represents the distribution function of the s^{th} particle population, or equivalently a list containing the position, velocity and weight of the macro-particles of the s^{th} population. $F_s^{(hit)}$, $F_s^{(rem)}$ are respectively the list of macro-particles that have hit a non-transparent surface and the list of macro-particles to be removed due to collisional events, in the current time step, for the s^{th} particle population. Finally, Π_s is the particle track, which contains the IDs of the s^{th} population macro-particles that are contained in each PIC cell (used for weighting purposes).

Referring to the above figure, this module is responsible for:

- Simulation of macro-particles collisions (and removal of to-be-removed macro-particles).
- Macro-particles moving loop. For each macro-particle, this includes: (I) interpolating the known electric and magnetic fields to the particle position, (II) moving the macro-particle self-consistently with the known fields (Sec. 3.2.3), (III) checking for material surface crossing (Sec. 3.2.6.1), thus updating a list $F^{(hit)}$ of hitting macro-particles, and, finally, (IV) sorting the macro-particle into the corresponding PIC cell (a particle track structure Π is updated).

- Simulation of the interaction between the macro-particles and the material surfaces (Sec. 3.2.6). This includes (I) the simulation of the effects on macro-particles (injection of new particles, reflection, re-injection, sputtering, etc...), and (II) the surface weighting of emitted or colliding macro-particles (to update the plasma properties at the corresponding cell-faces centers).
- Volume weighting of sorted macro-particles (Sec. 3.2.4) to obtain plasma properties at the mesh nodes.
- Macro-particles removal. All particles that have crossed an external boundary or an absorbing surface have to be removed from the simulation.
- Bohm's condition forcing (Sec. 3.2.7), in which the surface weighted plasma density, if need be, is corrected to yield supersonic ion conditions, followed by an interpolation of this corrected density at the cell-faces centers $n_e^{(sw)}$ to the cell nodes (the fluid closure algorithms, in fact, only make use of plasma properties known at the mesh nodes).

3.2.1. PIC mesh: computational and physical coordinates

As shown in Tab. 1.3, hybrid codes can make use of either unstructured or structured meshes. In this work, a structured mesh is used, given its higher computational efficiency in terms of macro-particles sorting algorithms, at the cost of a lower flexibility when dealing with complex object geometries.

In a structured mesh, each position vector is identified by a set of 3 computational coordinates $\boldsymbol{\xi} = (\xi, \eta, \zeta)$, which have a bijective relation with the corresponding physical coordinates $\boldsymbol{r} = (x, y, z)$, as shown in Fig. 3.3. If N_ξ, N_η, N_ζ are the numbers of nodes along the three coordinate directions, then the computational coordinates vary respectively in the ranges $[0, N_\xi - 1]$, $[0, N_\eta - 1]$ and $[0, N_\zeta - 1]$.

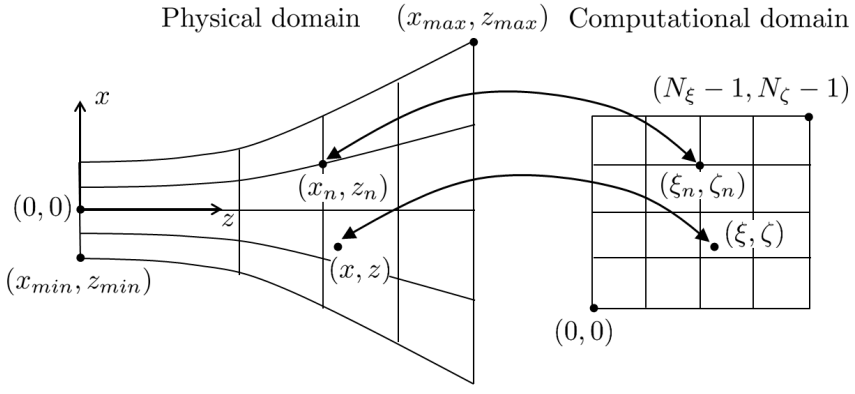

Figure 3.3: Physical and computational domains, associated to the PIC mesh. For the sake of clarity, a 2-dimensional x, z plane slice of the domain is shown.

Given the physical coordinates of the nodes x_n, y_n and z_n, it is straightforward to compute, at their location, the inverse Jacobian matrix of the transformation from

computational to physical coordinates:

$$\mathcal{J}_i = \frac{\partial(x,y,z)}{\partial(\xi,\eta,\zeta)} = \frac{\partial \boldsymbol{r}}{\partial \boldsymbol{\xi}}, \tag{3.1}$$

where the elements of $\mathcal{J}_i$ are evaluated with a centered difference scheme of the 2nd order, and a simple matrix inversion provides $\mathcal{J} = \mathcal{J}_i^{-1}$.

The transformation from computational to physical coordinates is then a simple trilinear interpolation of the physical coordinates of the occupied cell nodes to the macro-particle position. In a structured mesh, the occupied cell is identified by the 3 indices corresponding to the integer part of the particle computational coordinates $\boldsymbol{\xi} = (\xi, \eta, \zeta)$. If $\boldsymbol{\xi}_0$ are the computational coordinates of the lower left node of this cell, then the relative macro-particle computational coordinates are

$$\boldsymbol{\xi}' = \boldsymbol{\xi} - \boldsymbol{\xi}_0, \tag{3.2}$$

and the physical coordinates are finally obtained by interpolating the physical coordinates of the cell nodes to the particle position, using the 8 trilinear weights defined below:

$$\begin{cases} w_{000} = (1-\xi')(1-\eta')(1-\zeta'), \\ w_{001} = (1-\xi')(1-\eta')\zeta', \\ w_{010} = (1-\xi')\eta'(1-\zeta'), \\ w_{011} = (1-\xi')\eta'\zeta', \\ w_{100} = \xi'(1-\eta')(1-\zeta'), \\ w_{101} = \xi'(1-\eta')\zeta', \\ w_{110} = \xi'\eta'(1-\zeta'), \\ w_{111} = \xi'\eta'\zeta', \end{cases} \tag{3.3}$$

where, for example, w_{110} is the weight corresponding to the cell node with computational coordinates $(\xi_0 + 1,\, \eta_0 + 1,\, \zeta_0)$.

For what concerns the inverse transformation, that is from physical to computational coordinates, it requires an initial guess and the use of the Jacobian matrix. The initial guess can be either a point in the middle of the simulation domain, or the previous time step computational coordinates (if the macro-particle already existed). Let $\boldsymbol{\xi}^{(0)} = \left(\xi^{(0)}, \eta^{(0)}, \zeta^{(0)}\right)$ be this initial guess, and $\boldsymbol{r}^{(0)}$ the corresponding physical coordinates. Then, an initial estimation error is computed as:

$$\boldsymbol{\epsilon}^{(0)} = \boldsymbol{r} - \boldsymbol{r}^{(0)}, \tag{3.4}$$

and, if the error magnitude is above a maximum tolerance, a correction loop is entered in which, at each iteration k, the computational coordinates are corrected by an amount $\Delta\boldsymbol{\xi}^{(k)}$ provided below:

$$\Delta\boldsymbol{\xi}^{(k)} = \mathcal{J}^{(k-1)}\big|_{\boldsymbol{\xi}^{(k-1)}}\, \boldsymbol{\epsilon}^{(k-1)}. \tag{3.5}$$

In this expression, the Jacobian matrix is evaluated at the previously computed computational coordinates $\boldsymbol{\xi}^{(k-1)}$, through a trilinear interpolation with the same weights of Eq. (3.3), and the error $\boldsymbol{\epsilon}^{(k-1)}$ is the $(k-1)^{\text{th}}$ step reconstruction error.

3.2.1.1. The PIC mesh types

EP2PLUS can use three different types of mesh, as shown in Fig. 3.4:

- Cartesian type: all nodes are aligned with the x, y and z axes, although the spacing may be different along each coordinate direction.
- Conical mesh type: all nodes are aligned with the straight trajectories of the ions of a cold beam (zeroth order ion streamlines, described in Sec. 2.2.1). In order to fully define this mesh, it is necessary to define a characteristic initial plume radius R_0, and the divergence angle α_0 of the corresponding ion streamline.
- Generic structured mesh.

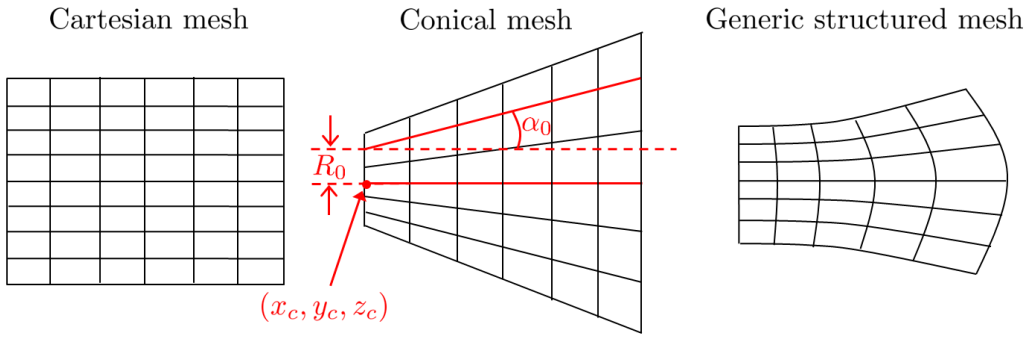

Figure 3.4: The different available mesh types in EP2PLUS. For the sake of clarity, only two-dimensional slices of the domain are shown.

The algorithms described in the previous section are applicable to all meshes, however, for the Cartesian and conical meshes, the following simplified approaches are followed.

In a Cartesian mesh, the physical coordinates are directly retrieved as:

$$\begin{aligned} x &= x_{min} + \xi \Delta x, \\ y &= y_{min} + \eta \Delta y, \\ z &= z_{min} + \zeta \Delta z, \end{aligned} \tag{3.6}$$

where x_{min}, y_{min} and z_{min} represent the minimum coordinates values, and Δx, Δy, Δz are the nodes spacing along the coordinate directions. The computational coordinates, on the other hand, are obtained from the knowledge of x, y, z, by simply inverting Eq. (3.6).

In a conical mesh, featuring a plume origin at (x_c,y_c,z_c) on an initial $z = z_c$ plane, and a divergence angle α_0 at a radius R_0, the following approach is followed.

Regarding the physical coordinates, these are obtained as:

$$\begin{aligned} x &= x_c + x^O \left[1 + \frac{z}{R_0}\tan(\alpha_0)\right], \\ y &= y_c + y^O \left[1 + \frac{z}{R_0}\tan(\alpha_0)\right], \\ z &= z_c + \zeta \Delta z, \end{aligned} \tag{3.7}$$

where Δz is constant throughout the domain, and x^O, y^O are given by:

$$\begin{aligned} x^O &= \xi \Delta x_0 + x_{min0} - x_c, \\ y^O &= \eta \Delta y_0 + y_{min0} - y_c. \end{aligned} \tag{3.8}$$

In this equation, $\Delta x_0 = \left.\frac{\partial x}{\partial \xi}\right|_{z=z_c}$ and $\Delta y_0 = \left.\frac{\partial y}{\partial \eta}\right|_{z=z_c}$ are the x and y node spacings at the initial plume plane $z = z_c$ (constant by construction), and (x_{min0}, y_{min0}) the minimum x and y coordinates at this plane. In what regards the computational coordinates, they are retrieved by first evaluating x^O, y^O:

$$\begin{aligned} x^O &= \frac{(x - x_c)}{1 + \tan\alpha_0 \dfrac{(z - z_c)}{R_0}}, \\ y^O &= \frac{(y - y_c)}{1 + \tan\alpha_0 \dfrac{(z - z_c)}{R_0}}, \end{aligned} \tag{3.9}$$

and then:

$$\begin{aligned} \xi &= \frac{x_c + x^O - x_{min0}}{\Delta x_0}, \\ \eta &= \frac{y_c + y^O - y_{min0}}{\Delta y_0}, \\ \zeta &= \frac{z - z_c}{\partial z / \partial \zeta}. \end{aligned} \tag{3.10}$$

3.2.1.2. The PIC cell-faces and the definition of objects

In the PIC model, macro-particles can interact with "special" cell-faces (or surface elements) that represent material, injection or sink surfaces. The use of a structured mesh allows to identify each cell-face with a set of 3 indices, and store their corresponding surface types in a 3-D matrix. The available cell-face types are summarized in Tab. 3.1, each one being uniquely identified by an integer number in this cell-face types matrix. The indices (i_f, j_f, k_f) of each cell-face are a simple function of the computational coordinates of the cell-face center (ξ_c, η_c, ζ_c):

$$\begin{aligned} i_f &= 2\xi_c + 1, \\ j_f &= 2\eta_c + 1, \\ k_f &= 2\zeta_c + 1, \end{aligned} \tag{3.11}$$

where, for convention, indices start from 1.

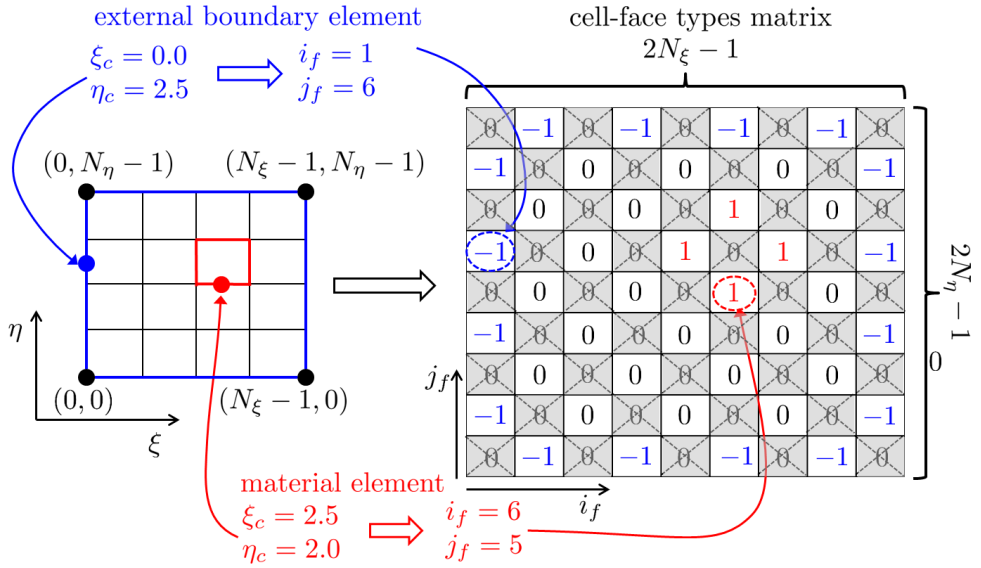

Figure 3.5: Indexing logic of PIC cell-faces into a cell-face types matrix. For the sake of clarity, a 2-dimensional x, y plane slice of the domain is shown. The shaded matrix elements refer to non-existing cell-faces. External boundary cell-faces feature a -1 type, the material cell-faces a $+1$ type, and the transparent cell-faces a 0 type.

Fig. 3.5 shows how the external simulation domain (blue lines) and the surface of a rectangular object map into the cell-face types matrix, for a two-dimensional x, y slice of the domain. Some matrix entries refer to non-existing cell-faces, while the dimensions of the cell-face types matrix are $(2N_\xi - 1) \times (2N_\eta - 1) \times (2N_\zeta - 1)$. Given the large number of zero elements (the non-existing and the transparent types, which represent no special surface), this matrix can be allocated in sparse format. However, since it is continuously accessed by the surface-crossing check algorithm, the quickest solution is to store it in dense format, so that memory access is quickest.

Finally, objects can be added to the simulation, as shown in Fig. 3.5 (for a square object), by storing in dedicated lists, the indices (i_f, j_f, k_f) of their boundary cell-faces.

3.2.2. Particle populations

In the PIC model, ion and neutral macro-particles are grouped into L different populations, in terms of:

- their atomic mass m, which determines the atomic species,
- their charge number Z (singly charged ions have $Z = 1$, neutrals have $Z = 0$), and
- their origin or energy content.

The division of macro-particles of the same type and charge in terms of the last property is used to achieve better statistics. The clearest example is that of the CEX collision, in which the slow ions and the fast neutrals produced by this event are stored into dedicated "slow ions" and "fast neutrals" populations, which are treated independently from the others by the population control algorithm (Sec. 3.2.9).

3.2.3. Particle mover

The interpolation of the electric and magnetic field to the j^{th} macro-particle position $\boldsymbol{r}_j$ is accomplished through a trilinear interpolation from the occupied cell nodes, with weights given by Eq. (3.3). Once the fields $\boldsymbol{E}_j$ and $\boldsymbol{B}_j$ have been obtained, the macro-particle is advanced in time by a dedicated particle mover. In order to maintain the stability of the integration scheme, every macro-particle has to cross less than one cell per time step [74]. So, in this hybrid PIC context (in which we are not interested in plasma oscillations), it is the macro-particles maximum velocity and the cell size that set the upper threshold to the integration Δt. The particle mover is based on Boris' CYLRAD algorithm [69], a generalization of the second order leap frog integration, and hence with velocity and position of the macro-particles referring to interleaved time points (separated by $\Delta t/2$). In particular, the macro-particle position is known at time k and the velocity at time $k-1/2$, and they are updated respectively to times $k+1$ and $k+1/2$.

The equation of motion for the j^{th} macro-particle is given by Eq. (1.19), in which relativistic terms are neglected because heavy particles in plasma plumes never reach relativistic velocities: $v \ll c$. From inspection of Eq. (1.19), it is noticed that neutral macro-particles simply move in straight trajectories (the right hand side, in fact, is zero), so that their velocity remains unaltered. For ion macro-particles, on the other hand, the velocity changes. Neglecting the sub-index j in the following, and introducing the Larmor motion angular velocity vector $\boldsymbol{\omega}_B = eZ\boldsymbol{B}/m$, the ion macro-particle velocity is first advanced to time k, with the sole effect of the electric field:

$$\boldsymbol{v}^{(k),1} = \boldsymbol{v}^{(k-1/2)} + C_f \frac{eZ}{m} \boldsymbol{E}^{(k)} \frac{\Delta t}{2}, \tag{3.12}$$

where C_f is a correction factor, equal to 1 when $B = 0$, and given by the expression below, when $B > 0$:

$$C_f = \frac{\tan\left(\omega_B \Delta t/2\right)}{\omega_B \Delta t/2}. \tag{3.13}$$

This updated velocity $\boldsymbol{v}^{(k),1}$ is then rotated around the magnetic field vector as:

$$\boldsymbol{v}^{(k),2} = \boldsymbol{v}^{(k),1} + \frac{C_f}{1 + \left(\dfrac{\tan\left(\omega_B \Delta t\right)}{2}\right)^2} \left(\boldsymbol{v}^{(k),3} \times \boldsymbol{\omega}_B\right) \Delta t, \tag{3.14}$$

where another auxiliary velocity $\boldsymbol{v}^{(k),3}$ is computed as:

$$\boldsymbol{v}^{(k),3} = \boldsymbol{v}^{(k),1} + C_f \left(\boldsymbol{v}^{(k),1} \times \boldsymbol{\omega}_B\right) \frac{\Delta t}{2}. \tag{3.15}$$

Finally, $\boldsymbol{v}^{(k),2}$ is advanced to time $(k+1/2)$ by considering only the electric field effect:

$$\boldsymbol{v}^{(k+1/2)} = \boldsymbol{v}^{(k),2} + C_f \frac{eZ}{m} \boldsymbol{E}^{(k)} \frac{\Delta t}{2}. \tag{3.16}$$

Once the velocity has been advanced to time $k+1/2$, the particle position is simply updated as:

$$\boldsymbol{r}^{(k+1)} = \boldsymbol{r}^{(k)} + \boldsymbol{v}^{(k+1/2)} \Delta t. \tag{3.17}$$

The above described algorithm has been validated with the test case described in Sec. C.1.

3.2.4. Particle volume weighting

After moving a macro-particle, if this has not crossed any special surface (external boundary, material surface, etc...), it is assigned or sorted to the corresponding cell. Once all macro-particles have been moved, a volume weighting algorithm assigns the sorted macro-particles (stored within a dedicated particle track structure Π) to the mesh nodes.

Regarding the sorting step, performed during the macro-particle loop of Fig. 3.2, this is particularly simple in a structured mesh. In fact, as already commented in Sec. 3.2.1, the occupied cell indices (i, j, k) are efficiently obtained from the knowledge of the macro-particles computational coordinates (ξ, η, ζ). In particular the integer part of these coordinates coincide with those of the lower left node of the occupied cell $\boldsymbol{\xi}_0$.

For each cell and particle population, the volume weighting consists in a loop over the sorted macro-particles, in which their computational coordinates $\boldsymbol{\xi}'$ relative to the lower left node are first evaluated, and their total weight W is then assigned to the 8 neighboring nodes, with weights given by Eq. (3.3). This is equivalent to assuming a macro-particle shape function in the computational domain, that belongs to the first order cloud-in-cell method (CIC) [122].

For a generic node of the mesh, with computational coordinates $\boldsymbol{\xi}$, the weighted density then assumes the expression:

$$n = \frac{1}{\Delta V} \sum_{j=1}^{N} S(\boldsymbol{\xi}_j - \boldsymbol{\xi}) W_j, \tag{3.18}$$

where ΔV is the volume associated to the PIC mesh node, N is the number of macro-particles, with a non-zero weight to the considered node (i.e. belonging to adjacent cells), $\boldsymbol{\xi}_j = (\xi, \eta, \zeta)$ are the computational coordinates of the macro-particle, and S is the macro-particle shape function, to be evaluated at the node:

$$S(\boldsymbol{\xi}'_j) = (1 - |\xi'_j|)(1 - |\eta'_j|)(1 - |\zeta'_j|), \tag{3.19}$$

where $(\xi'_j, \eta'_j, \zeta'_j) = (\xi_j - \xi, \eta_j - \eta, \zeta_j - \zeta)$ are the computational coordinates of the j^{th} macro-particle, relative to the considered node.

Regarding the volume ΔV associated to the mesh node, this is generally computed from the knowledge of the inverse Jacobian matrix $\mathcal{J}_i$ as:

$$\Delta V = \iiint S(\xi', \eta', \zeta') \left|\mathcal{J}_i(\xi', \eta', \zeta')\right| d\xi' d\eta' d\zeta', \tag{3.20}$$

where the integral extends over the applicable computational weighting volume for the node (where to-be-weighted macro-particles are located, i.e. a maximum of 8 cells), and (ξ', η', ζ') are the relative computational coordinates (as considered above). In Cartesian meshes, this integral turns out to be equal to the physical cell volume for inner nodes and to a specific fraction of it for boundary nodes (which feature a smaller applicable volume). For non-uniform meshes, in this work, an approximation of the volume ΔV is considered, that is the sum of the physical volumes of the neighboring applicable cells, divided by 8 (the expected number of neighboring cells in a 3D geometry).

3.2.5. Macro-particles collisions

Although a plasma plume is weakly collisional, a large variety of collisional processes can affect the heavy particles, especially in the near-region. At present, the following have been included:

- Ionization collisions:
  $\mathrm{A} + e \rightarrow \mathrm{A}^+ + 2e$
  $\mathrm{A} + e \rightarrow \mathrm{A}^{++} + 3e$
  $\mathrm{A}^+ + e \rightarrow \mathrm{A}^{++} + 2e$

- Symmetric and pure CEX collisions:
  $\mathrm{A}^+(\mathrm{fast}) + \mathrm{A}(\mathrm{slow}) \rightarrow \mathrm{A}^+(\mathrm{slow}) + \mathrm{A}(\mathrm{fast})$
  $\mathrm{A}^{++}(\mathrm{fast}) + \mathrm{A}(\mathrm{slow}) \rightarrow \mathrm{A}^{++}(\mathrm{slow}) + \mathrm{A}(\mathrm{fast})$

Regarding the former, higher ionization degrees have not been considered, given their increasing ionization energies and hence decreasing reaction rates. For what concerns the CEX, the considered ones are the resonant-symmetric reactions, with no momentum exchange. Such reactions are the dominant collisions in a plasma plume and have the highest cross sections, as shown in Refs. [50],[54],[55], and [123]. The assumption of a zero momentum exchange is a good approximation for resonant CEX, made even by more complex ion-neutral collision models, like that of Ref. [123], in which the collision outcome is either a pure CEX or an elastic momentum exchange collision (MEX).

MEX collisions have generally little importance in a plasma plume. Ion-ion MEX collisions, due to Coulomb interaction, modify the affected particles relative velocity (for an ion species emitted by a plasma thruster, this amounts to fractions of eV in terms of energy), which is much smaller than their absolute velocity (corresponding to thousands of eV), so that their effect is clearly negligible. MEX collisions between ions and neutrals, or between ions of different charge, on the other hand,

can have larger effects. However, their importance with respect to that of the CEX is still small, as shown in Refs. [124, 125], especially when it comes to determine the backscattering ion flux towards the satellite, almost entirely constituted by slow CEX ions.

Although excitation collisions are an important factor of energy loss inside a plasma thruster, their effect in the dynamics of a plasma plume is also negligible. From a PIC point of view, these collisions create a macro-particle belonging to a different excited population, with possibly different collision cross sections, but with the same charge number Z. This is clearly a second order effect, since only the collision properties (but not the trajectory) of those few macro-particles that suffer an excitation collision are affected. Finally, recombination collisions are also neglected, given their low frequency in a cold rarefied plasma plume.

In the following, the collision algorithms for the considered collisions are presented. As already indicated in Fig. 3.2, these are cell-wise algorithms.

3.2.5.1. Ionization collisions.

The approach considered is similar to that of the HP-HALL code, described in detail in Ref. [126]. All the macro-particles of the input particle population being ionized, are sampled to be affected by ionization (deterministic sampling).

Then, an ionization rate $R_i(T_e)$ is evaluated at the cell center, by using existing literature models that are based on two assumptions: a Maxwellian electron distribution function with temperature T_e, and an electron thermal velocity much larger than the heavy particles bulk velocity $T_e \gg mu^2$. In particular, Drawin's model [127] is used for the ionization reactions of neutrals, while Bell's model [128] is considered for the ionization of singly charged ions. Once the generation rate $R_i(T_e)$ has been evaluated, for the ionization of neutrals, the new ion mass Δm_i to be generated in the cell is computed as:

$$\Delta m_i = n_e n_n m R_i(T_e) \Delta V \Delta t, \tag{3.21}$$

where n_e is the electron density, n_n is the density of the input neutral population, and ΔV is the physical cell volume. The same formula can be applied for the second ionization of an ion population by substituting n_n with the corresponding ion number density. The average number of new ion macro-particles is then obtained as $\Delta N = \frac{\Delta m_i}{m W_{gen}}$, where W_{gen} is the generation weight associated to both the cell and the output ion population (refer to Sec. 3.2.9). The decimal part of this ratio, is taken into account by producing one additional macro-particle with probability $\Delta N - \text{int}(\Delta N)$. Regarding the distribution of the generated macro-particles, the velocity is sampled from a Maxwellian, with mean velocity and temperature equal to those of the input population, while the position is uniformly distributed across the cell. Finally, the weights of the macro-particles in the cell of the input population (e.g. neutrals) are updated by reducing them proportionally to their values, with a total reduction given by: $\sum_j \Delta W_j = -\frac{\Delta m_i}{m}$.

The validation of the above described algorithms has been carried out with a dedicated test, described in Sec. C.8.

3.2.5.2. CEX collisions.

Given the two input populations (e.g. fast ions and slow neutrals), the first step is to sample the macro-particles that undergo a CEX collision. Two approaches can be followed:

1. Direct Simulation Monte Carlo (DSMC) sampling: macro-particles are checked in pairs (one for each input population), and each pair collides if a random number U is lower than the collision probability $p_{c,pair}$ of the pair:

$$p_{c,pair} = \frac{1 - \exp\left(-\sigma(v_{rel}) n_n v_{rel} \Delta t\right)}{N_n}, \tag{3.22}$$

   where σ is the collision cross section, v_{rel} is the relative velocity between the macro-particles of the pair, n_n is the elementary number density of the neutral population, N_n the number of neutral macro-particles inside the cell, and Δt must not be larger than the expected collision time $(1/(\sigma n_n v_{rel}))$. It is noted that the probability that an ion macro-particle collides with any of the neutral macro-particles, that is $p_{c,pair} N_n$, is equal to the elementary particle collision probability. This makes sense in a PIC code, in which the macro-particles must behave like the elementary particles they represent, and therefore must be subject to the same collision probabilities. The number of pairs to be checked is given by $N_i N_n$, and it can be particularly large. In order to reduce the computational cost of the DSMC sampling, a more efficient version [73] has then been adopted, which limits this number of collision checks to $p_{c,max} N_i N_n$, with $p_{c,max} = p_{c,pair}\left(|v_{rel}\sigma(v_{rel})|_{max}\right)$ representing the maximum expected collision probability for the pair. The random number U is then compared to the ratio $p_{c,pair}/p_{c,max}$, thus resulting into a more efficient macro-particles sampling (e.g. less collision checks, with a higher acceptance probability).

2. Monte Carlo Collisions (MCC) / deterministic sampling: in this case, the macro-particles of the fast ion population are sampled with a probability:

$$p_c = 1 - \exp\left(-\sigma(v_{rel}) n_n v_{rel} \Delta t\right), \tag{3.23}$$

   which represents the elementary particle collision probability (with any of the neutrals). The relative velocity v_{rel} now refers to the relative velocity with respect to the average motion of the neutral population, which means that $\boldsymbol{v}_{rel} = \boldsymbol{v}_i - \boldsymbol{u}_n$, where $\boldsymbol{v}_i$ is the ion macro-particle velocity, and $\boldsymbol{u}_n$ is the fluid velocity of the slow neutrals population. For what concerns the neutral population, on the other hand, all macro-particles are affected by the collision outcomes, so that they are deterministically sampled (just like in the ionization collisions).

The CEX cross section for both types of CEX reactions (singly and doubly charged ions with neutrals) is provided, for Xenon gas, by Miller's model [55]:

$$\sigma(v_{rel}) = C_1 - C_2 \log_{10}\left(\frac{1/2 m v_{rel}^2}{1\text{eV}}\right), \tag{3.24}$$

where the argument of the logarithm represents the relative kinetic energy of the impacting elementary particles, expressed in eV. The constants depend on the type of reaction:

- $\text{Xe}^+(\text{fast}) + \text{Xe}(\text{slow}) \rightarrow \text{Xe}^+(\text{slow}) + \text{Xe}(\text{fast})$: $C_1 = 87.3\text{Å}^2$, $C_2 = 13.6\text{Å}^2$
- $\text{Xe}^{++}(\text{fast}) + \text{Xe}(\text{slow}) \rightarrow \text{Xe}^{++}(\text{slow}) + \text{Xe}(\text{fast})$: $C_1 = 45.7\text{Å}^2$, $C_2 = 8.9\text{Å}^2$

Another available model, valid only for the singly-charged ion CEX reaction, is Rapp's model [54]:

$$\sigma(v_{rel}) = \sigma_0 \left(1 - C \ln\left(\frac{v_{rel}}{1\text{km/s}}\right)\right)^2, \tag{3.25}$$

where $C = 0.1$, and σ_0 generally depends on the atomic type. For Argon $\sigma_0 = 65\text{Å}^2$, while, for Xenon, $\sigma_0 = 81\text{Å}^2$.

After the sampling step, new macro-particles have to be generated in the slow ion and fast neutral populations. This generation step can follow two different approaches:

1. Random generation: referring to Fig. 3.6, new macro-particles are uniformly distributed within the cell and have the generation weight of the corresponding cell and output population. Regarding their velocities, these are sampled from a local Maxwellian distribution with mean velocity and temperature given by the corresponding input population. This means that the slow ions feature a fluid velocity and temperature equal to that of the slow neutrals, while the fast neutrals have the same fluid properties of the fast ions. This approach permits controlling the number of generated macro-particles in the cell, although the linear momentum is not exactly conserved, but only conserved on average.

2. Deterministic generation: referring to Fig. 3.7, the new macro-particles feature the exact positions and velocities of the corresponding sampled macro-particles. This means that slow ions will have the positions and velocities of the sampled slow neutrals, while fast neutrals will have the positions and velocities of the sampled fast ions. Regarding their weights, both slow ions and fast neutrals share the weight of the sampled ion macro-particles. In case the slow neutrals population is deterministically sampled (in the MCC/deterministic approach), the corresponding slow ion macro-particles are generated at the positions of the sampled ion macro-particles, but with a random velocity that resembles the fluid properties of the slow neutrals population. The

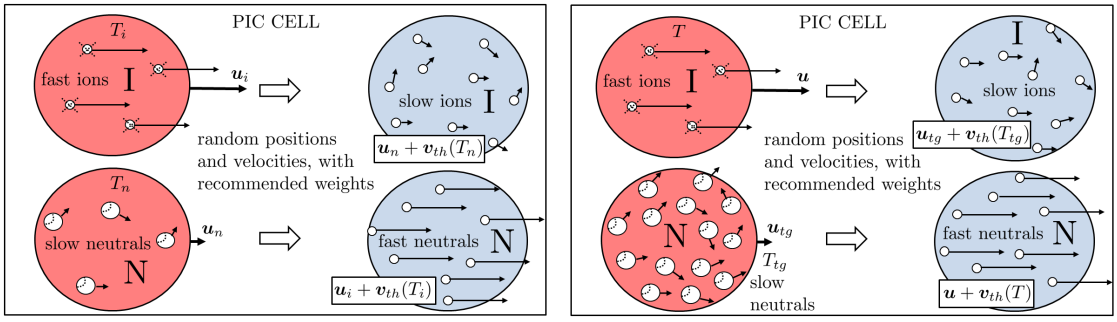

(a) (b)

Figure 3.6: Random CEX generation for (a) DSMC sampling, and (b) MCC sampling

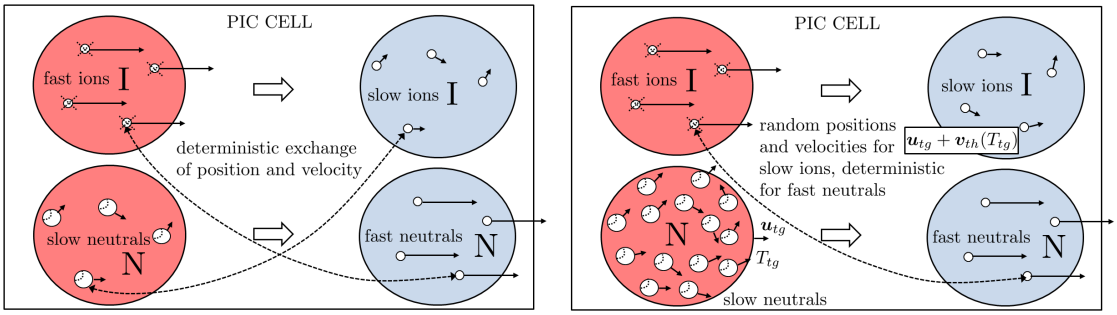

(a) (b)

Figure 3.7: Deterministic CEX generation for (a) DSMC sampling, and (b) MCC sampling

deterministic generation approach with DSMC sampling permits conserving exactly the linear momentum and energy of the macro-particles, although the macro-particles number is not actively controlled.

The input particle populations are finally updated with a scheme that depends on the sampling type:

- DSMC sampling: the update is done pair by pair, meaning that the weight of the heavier macro-particle is updated by subtracting the weight of the lighter macro-particle, which is removed from the simulation. An acceptance-rejection scheme prevents the algorithm from producing very small residual macro-particles when the input weights are very similar, while preserving mass on average.

- MCC/deterministic sampling: the weights of the deterministically sampled population (slow neutrals) are reduced proportionally to their values, with a total weight reduction equal to the number of collided elementary ions. The macro-particles of the fast ions, on the other hand, are simply removed from the simulation.

The validation of the above described algorithms has been carried out with a dedicated test, described in Sec. C.7.

3.2.6. Macro-particles surface interaction

As anticipated in Sec. 3.2.1.2, the PIC mesh presents different types of cell-faces, some of which interact actively with the macro-particles. The considered cell-face types are summarized in Tab. 3.1.

Table 3.1: Existing surface types. The effects of the injection type refer to the macro-particles that happen to cross an injection element from within the simulated plasma.

Element type	**Effects on ions**	**Effects on neutrals**
Transparent	none	none
Particle sink	removal	removal
Injection	re-injected as neutrals	re-injected as neutrals
Standard material wall	recombination	reflection
Sputtered material wall	recombination + sputtering emission	reflection + sputtering emission

Each cell-face type features a dedicated algorithm to simulate the produced effects on the macro-particle, summarized in Sec. 3.2.6.3. By monitoring the variations of the integer part of the macro-particles computational coordinates, a surface crossing detection algorithm verifies if it has crossed a non-transparent cell-face. If this happens, the macro-particle undergoes surface interaction, which consists of the following steps:

1. Sorting and surface-weighting of impacting macro-particles (from the plasma to the cell-faces).

2. Simulation of the surface-interaction effects on macro-particles, including direct injection of new macro-particles into the domain.

3. Sorting and surface-weighting of the emitted macro-particles (from the cell-faces to the plasma).

3.2.6.1. Surface crossing detection and check

The algorithm dedicated to surface crossing-detection monitors the integer part of each macro-particle computational coordinates. If any change is detected (from the previous time step), the indices of the crossed cell-faces are identified and the corresponding types are read. If any of these types is not of the "transparent" type, then the macro-particle is stored for surface interaction in a dedicated hit list $F^{(hit)}$, as shown in Fig. 3.2. A different hit list per particle population is considered.

Fig. 3.8 shows a macro-particle trajectory between two successive PIC times (in 2D for the sake of clarity), with (i_0, j_0) being the indices of the initial occupied

cell and (i_F, j_F) the final ones. Since the occupied cell has changed, the crossing-detection and check algorithm is activated. In the example, the macro-particle crosses several cells, a rare condition if Δt is small enough, although possible for cell-face crossings that happen to be very close to one of the cell vertices.

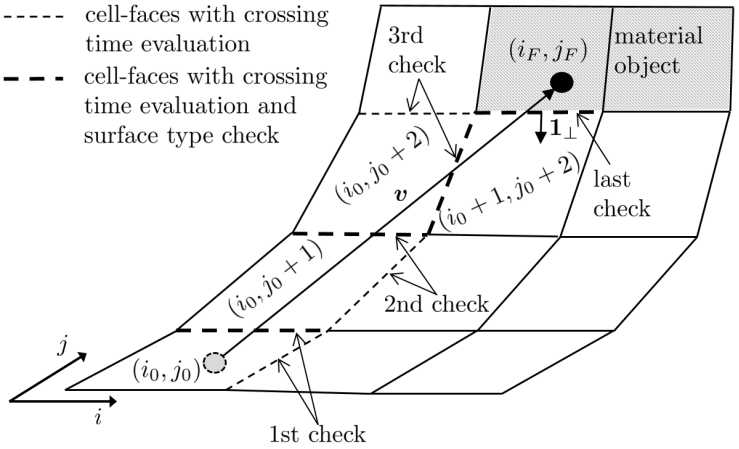

Figure 3.8: Surface crossing-detection and check algorithm. The macro-particle moves from a cell with indices i_0, j_0 to a final one with indices i_F, j_F.

Depending on the change of the initial/final cell indices (+1 along ξ and +3 along η, in the provided example), a certain number of cells are crossed (4 in the example). For each crossed cell, the algorithm computes the times of the possible crossings with the cell-faces as:

$$\Delta t_{cross} = \frac{\mathbf{1}_\perp \cdot (\boldsymbol{r}_n - \boldsymbol{r}_0)}{\mathbf{1}_\perp \cdot \boldsymbol{v}}, \tag{3.26}$$

where $\mathbf{1}_\perp$ is the corresponding cell-face normal (known from the knowledge of the mesh), $\boldsymbol{r}_0$ is the initial macro-particle position vector, $\boldsymbol{r}_n$ is the position vector of an arbitrary node of the cell-face, and $\boldsymbol{v}$ is the macro-particle velocity vector. The surface type of the cell-face with the lowest crossing time is then read and checked. If this is transparent, the process continues with the next crossed cell ($(i_0, j_0 + 1)$ in the example), otherwise, the macro-particle is sorted for surface interaction (as it occurs at the last check, in Fig. 3.8).

3.2.6.2. Macro-particles injection

Some cell-faces of the simulation domain are dedicated to inject new particles into the simulation domain. More specifically, a drifted Maxwellian injection is simulated, which is defined by the injected particle flux g_{inj}, the injection fluid velocity $\boldsymbol{u}_{inj}$, and the injection temperature T_{inj}. In order to better represent smoothly changing injection profiles, these injection properties can vary linearly across the injection cell-faces, and are provided at the 4 vertices of each one of them. The number N_{inj} of injected macro-particles, per cell-face and per time step, is obtained as:

$$N_{inj} = \frac{\bar{g}_{inj} \Delta S \Delta t}{W_{gen}}, \tag{3.27}$$

where $\bar{g}_{inj}$ is the average particle flux of the injection cell (e.g. evaluated at the cell-face center), ΔS is the injection cell-face area, and W_{gen} is the generation weight at the injection cell, for the injected particle population.

Then, the injection algorithm generates a stochastic sample of N_{inj} macro-particles per cell-face. Their injection positions are uniformly distributed across the cell-face, while their weight is given by:

$$W_{inj} = W_{gen} \frac{g_{inj}(\boldsymbol{r}_{inj})}{\bar{g}_{inj}}, \tag{3.28}$$

where $g_{inj}(\boldsymbol{r}_{inj})$ is the particle flux interpolated to the macro-particle position. The generation of a stochastic injection velocity then requires also the interpolation of the injection velocity $\boldsymbol{u}_{inj}(\boldsymbol{r}_{inj})$ and temperature $T_{inj}(\boldsymbol{r}_{inj})$ to the macro-particle position, and is based on the algorithms of Ref. [73]. The probability distribution function is proportional to the normal component $v_\perp$ (with respect to the cell-face) of the macro-particle velocity $\boldsymbol{v}$:

$$f_{inj}(\boldsymbol{v}) \propto v_\perp \exp\left(-\frac{m\left|\boldsymbol{v}-\boldsymbol{u}_{inj}\right|^2}{2T_{inj}}\right). \tag{3.29}$$

The direct proportionality on $v_\perp$ models the fact that the particles reservoir (region of space, upstream of the injection surface, that the injected macro-particle has crossed in the last time step) extends linearly with this velocity. A random normal velocity is then generated with the "acceptance-rejection" method: a minimum and a maximum normal velocities $v_{\perp\,min}$ and $v_{\perp\,max}$ are first defined as $u_\perp \pm 4\sqrt{T_{inj}/m}$, with $u_\perp$ representing the normal component of the injection fluid velocity. Then, a normalized probability distribution function is introduced:

$$\tilde{f}_{v_\perp} \propto \frac{f_{inj}(v_\perp)}{f_{inj}(\hat{v}_\perp)}, \tag{3.30}$$

with $\hat{v}_\perp$ the normal velocity that maximizes the injection probability, Eq. (3.29):

$$\hat{v}_\perp = \frac{u_\perp + \sqrt{u_\perp^2 + 4T_{inj}/m}}{2}. \tag{3.31}$$

A uniformly distributed normal velocity $v_\perp \in [v_{\perp\,min}, v_{\perp\,max}]$ is then accepted only if a random number $U \in [0,1]$ (again, uniformly distributed) is lower (or equal) than $\tilde{f}_{v_\perp}$:

- $U \leq \tilde{f}_{v_\perp}(v_\perp) \rightarrow v_\perp$ is accepted.
- $U > \tilde{f}_{v_\perp}(v_\perp) \rightarrow$ the generation process is repeated until a random $v_\perp$ is accepted.

Once the normal component of the injection velocity has been generated, the tangential velocity components are directly obtained from a 2D Maxwellian distribution.

This means that the probability distribution function for the tangential velocity vector is given by:

$$f_{v_\parallel}(v_{\parallel 1}, v_{\parallel 2}) \propto \exp\left(-\frac{m\left[(v_{\parallel 1}-u_{\parallel 1})^2+(v_{\parallel 2}-u_{\parallel 2})^2\right]}{2T_{inj}}\right), \tag{3.32}$$

where $v_{\parallel 1}$,$v_{\parallel 2}$ are the tangential components of the macro-particle velocity and $u_{\parallel 1}$,$u_{\parallel 2}$ are the tangential components of the injection fluid velocity, again evaluated at the macro-particle position. This probability distribution function can be directly integrated and inverted, so that a direct method for generating random 2D Maxwellian samples is readily available, as described in the Appendix C of Ref. [73]. This method consists in generating a first random number $U \in [0,1]$, which determines the magnitude of the thermal component of the tangential velocity:

$$\left|\boldsymbol{v}_{th,\parallel}\right| = \sqrt{v_{th,\parallel 1}^2 + v_{th,\parallel 2}^2} = \sqrt{-\frac{2\ln(U)T_{inj}}{m}}, \tag{3.33}$$

and then a random angle $\theta \in [0, 2\pi]$, which determines the two tangential thermal components:

$$\begin{cases} v_{th,\parallel 1} = \left|\boldsymbol{v}_{th,\parallel}\right| \cos\theta, \\ v_{th,\parallel 2} = \left|\boldsymbol{v}_{th,\parallel}\right| \sin\theta. \end{cases} \tag{3.34}$$

The stochastic injection velocity is finally obtained as:

$$\boldsymbol{v} = v_\perp \mathbf{1}_\perp + (v_{th,\parallel 1} + u_{\parallel 1})\mathbf{1}_{\parallel 1} + (v_{th,\parallel 2} + u_{\parallel 2})\mathbf{1}_{\parallel 2}, \tag{3.35}$$

where $\mathbf{1}_{\parallel 1}$ and $\mathbf{1}_{\parallel 2}$ are the cell-face tangential unit vectors (normal to each other).

In order to simulate a continuous injection and avoid undesired discretization effects, each injected macro-particle is finally advanced (in straight line, along its velocity direction) from a random injection time, uniformly distributed between $t^{(k)}$ and $t^{(k+1)}$ to the end of the PIC time step $t^{(k+1)}$.

The above described injection algorithms have finally been validated with the test case of Sec. C.5.

3.2.6.3. Surface interaction effects on impacting macro-particles

Depending on the surface type, different effects have to be simulated, as described in this section.

3.2.6.3.1. Particle sink

When a macro-particle crosses a particle sink cell-face, such as the external boundary elements of the simulation domain, or a total absorption surface, it is simply removed from the domain.

3.2.6.3.2. Injection cells

For what concerns the macro-particles that cross an injection cell-face from within the plasma, they are re-injected as additional neutrals with the algorithms described in Sec.3.2.6.2. This means that all ions that cross the injection cells are assumed to recombine there.

3.2.6.3.3. Standard material wall cells

When crossing a material wall surface, ion macro-particles recombine into neutrals, while neutral macro-particles suffer either a specular or a diffuse reflection, with a user's defined probability. While the neutral specular reflection is simply simulated by inverting the normal velocity component of the macro-particle, the neutral re-injection due to both ion recombination or neutral diffuse reflection, is carried out independently for each impacting population.

For each cell-face, a dedicated counter accumulates the amount of mass to be re-injected Δm_{reinj}, due to each impacting population. If W_{gen} represents the generation weight of the recombined neutrals population, and m their atomic mass, then two conditions arise:

- $\Delta m_{reinj} \geq W_{gen} m$: a number $N_{reinj} = \text{int}\left[\Delta m_{reinj}/(W_{gen} m)\right]$ of neutral macro-particles (each one of weight W_{gen}) is re-injected. The accumulated mass is then updated by subtracting the re-injected mass.

- $\Delta m_{reinj} < W_{gen} m$: the mass to be re-injected keeps accumulating, for the next time steps.

When $\Delta m_{reinj} < W_{gen} m$, the above approach is equivalent to a re-injection with probability given by the ratio $\Delta m_{reinj}/(W_{gen} m) < 1$, with no accumulation, as considered by the HP-HALL code, [126]. However it gives the advantage of conserving mass exactly on the long-term (and not on average, every time step). Regarding the re-injected neutrals velocity distribution, this depends on the mean impacting energy $\bar{E}_{imp}$ of the impacting population, the mean re-injected atom energy being

$$\bar{E}_{reinj} = 2 A_W T_W + (1 - A_W) \bar{E}_{imp}, \tag{3.36}$$

where T_W is the wall temperature (in energy units), A_W is a wall accommodation coefficient, and $\bar{E}_{imp}$ is evaluated as the time-averaged wall-impact kinetic energy of the impacting population elementary particles. The factor 2 that multiplies T_W takes into account that the emission is semi-maxwellian, and hence the average emission energy is twice the temperature of the thermalized source. Regarding the angular distribution of the emission, a thermal cosine emission law is assumed for the injection probability distribution function, which is equivalent to using Eq. (3.29), with $\boldsymbol{u}_{inj} = \mathbf{0}$, and $T_{inj} = \bar{E}_{reinj}/2$.

The algorithms used for these standard material walls have been validated with the test described in Sec. C.9.

3.2.6.3.4. Sputtered material wall cells

When crossing a sputtered wall surface, apart from the recombination/reflection effects considered for the material wall surface, sputtered macro-particles are generated as well. In fact, when a hypersonic macro-particle hits such surfaces, it knocks out a certain average number of material surface atoms. The sputtering response can be modeled, in general, by defining:

- The sputtering yield Y: number of sputtered atoms per impacting particle.
- The particle backscattering probability p_{bks}: probability that an impacting particle is reflected backwards. In the case of an ion, this means that it does not recombine.
- The emission mean energy $\bar{E}_{emi}$ for the sputtered atoms.

These parameters are functions of the impacting particle species, of the surface material (e.g. the binding energy), and of the impacting particle kinetic energy E_{imp} and angle α_{imp} (with respect to the surface normal). For a given impacting species and target material, Y, $\bar{E}_{emi}$, and p_{bks} are 2D functions of the sole impact energy and angle. These properties can be obtained with SRIM/TRIM [129], a dedicated plasma-matter interaction software. Alternatively they can be obtained from simplified empirical models, like those described in Refs. [130] and [131].

In the PIC model context, the sputtering effects are considered to be the same independently of the impacting particle charge (be it singly-charged, doubly-charged or neutral). Each impacting macro-particle produces a population of sputtered atoms with a total mass $m_{sput} = m_{tg}WY$, where m_{tg} is the atomic mass of the target material, W is the weight of the impinging macro-particle, and Y the corresponding sputtering yield (that depends on the specific particle impacting energy and angle). As considered also for the diffuse neutrals reflection or ions recombination, the number of sputtered macro-particles is given by the population control algorithm of Sec. 3.2.9, which controls their number per cell by dictating their generation weight W_{gen}. Regarding the velocity distribution of the sputtered atoms, this is assumed to be given by a thermal emission, like that of Eq. (3.29), where $T_{inj} = \bar{E}_{emi}/2$. This is a clearly a simplifying assumption, because the distribution can be asymmetric with respect to the surface normal, and generally depends on both the incidence angle and the principal directions of the sputtered material lattice [130, 131].

Finally, the impinging macro-particle can undergo backscattering. This is a different process with respect to the accommodation process described above (based on the accommodation coefficient A_W), since it represents a very quick reflection, occurring within the first atomic layers of the target material. In order to deal with this, a random number U is compared with $p_{bks}\left(E_{imp}, \alpha_{imp}\right)$. If $U < p_{bks}$, the macro-particle is backscattered along the specular reflection direction, but with a lower kinetic energy (that is deterministically modeled as a function of the impact angle, impact energy, and backsputtered atoms properties). More specifically, the backscattered particle kinetic energy is computed as:

$$E_{bks} = \left(1 - C_{\parallel}\right) \bar{E}_{emi} + C_{\parallel} \left(E_{imp} - Y \bar{E}_{emi}\right), \tag{3.37}$$

with

$$C_{\parallel} = \left[\frac{\alpha_{imp} - \alpha_{min}}{\pi/2 - \alpha_{min}} \right]^{\beta_s}, \tag{3.38}$$

where β_s is an empirical coefficient, and α_{min} is the minimum impact angle that yields a non-zero backscattering probability (in the simulations of Sec. 5.3, $\beta_s = 4$, and $\alpha_{min} \approx 50$ deg.). Eq. (3.37) contains the most important dependencies of the backscattered particle energy. As $\alpha_{imp} \to \pi/2$ (parallel incidence), and hence $C_{\parallel} \to 1$, the particle tends to conserve most of its kinetic energy E_{imp}, since it barely enters in the material lattice. Nevertheless, it loses some energy due to the collisions with the sputtered atoms, that is $Y\bar{E}_{emi}$. Secondly, as $\alpha_{imp} \to \alpha_{min}$, the particle tends to be backscattered with the same energy as the rest of the sputtered atoms, since it gradually loses memory of its impacting kinetic energy.

The above described approach is another simplification of the real physics for two reasons: (I) the real backscattering direction does not coincide exactly with the specular reflection direction (but it is rather distributed around it), and (II) the backscattered particles, of a given impact energy and angle, have a distribution of energy, rather than a precise energy, as considered here.

The test of Sec. C.11 has finally been considered to validate the above algorithms.

3.2.6.3.5. Computation of the wall-impact energy

In order to evaluate both the re-injection atoms energy $\bar{E}_{reinj}$, the sputtered atoms mean energy $\bar{E}_{emi}$, and the energy flux to the walls, it is necessary to compute the macro-particles kinetic energy E_{imp}, at wall-impact. If the macro-particle is neutral, the wall-impact energy coincides with its kinetic energy at the cell-face crossing. For positive ions and quasineutral cell-faces (see description in Sec. 3.3.3), on the other hand, the crossed cell-face represents only the plasma sheath edge, so that the analysis is more complex. If ϕ_S is the sheath edge potential, ϕ_W the wall potential, and $E_{\perp} = \frac{1}{2}mv_{\perp}^2$ the kinetic energy (per elementary particle) in the normal direction (with respect to the cell-face), the following cases are considered:

- $\phi_W < \phi_S$: the macro-particle hits the wall, and its wall-impact kinetic energy (per elementary ion) is $E_{imp} = \frac{1}{2}mv^2 + eZ\,(\phi_S - \phi_W)$.
- $\phi_W > \phi_S$ and $eZ\,(\phi_W - \phi_S) > E_{\perp}$: the macro-particle does not hit the wall and is specularly reflected inside the sheath. The specular reflection algorithms are thus employed.
- $\phi_W > \phi_S$ and $eZ\,(\phi_W - \phi_S) \leq E_{\perp}$: the macro-particle hits the wall and its wall-impact kinetic energy (per elementary ion) is $E_{imp} = \frac{1}{2}mv^2 - eZ\,(\phi_W - \phi_S)$.

3.2.6.4. Surface-weighting

Every time a macro-particle crosses a non-transparent cell-face in both directions (e.g. for impacting macro-particles, but also for emitted or reflected ones), it is sorted for surface weighting. This is carried out with the Extended Surface Weighting

algorithm introduced in Refs. [132] and [133], as this permits achieving more accurate and less noisy results than volumetric weighting at the boundaries. The surface weighted density and particle flux vector are obtained, for each population, as:

$$n^{(sw)} = \frac{1}{\Delta t \Delta S}\left(\sum_{j=1}^{N_{hit}} \frac{W_j}{|v_{\perp,j}|} + \sum_{j=1}^{N_{emi}} \frac{W_j}{|v_{\perp,j}|}\right), \tag{3.39}$$

$$\boldsymbol{g}^{(sw)} = (n\boldsymbol{u})^{(sw)} = \frac{1}{\Delta t \Delta S}\left(\sum_{j=1}^{N_{hit}} \frac{W_j \boldsymbol{v}_j}{|v_{\perp,j}|} + \sum_{j=1}^{N_{emi}} \frac{W_j \boldsymbol{v}_j}{|v_{\perp,j}|}\right), \tag{3.40}$$

where ΔS is the cell-face area, and $|v_{\perp,j}|$ is the absolute value of the j^{th} macro-particle perpendicular velocity (with respect to the cell-face). The summation extends over the N_{hit} impacting macro-particles from within the plasma (identified by the hit list $F^{(hit)}$ of Fig. 3.2), and the N_{emi} macro-particles that are emitted or reflected from the cell-face, both referring to the current time step. It is noticed that a specularly reflected macro-particle thus appears twice in the summation, with the same normal velocity magnitude. Therefore, it counts twice for what regards the density (otherwise this would be given by the density of particles moving only in one direction), while its total contribution to the particle flux vector is parallel to the cell-face.

A similar process is also considered for computing the fluxes of other specific properties, at the cell-faces centers. Of particular interest are the total particle flux and the total energy flux, related to impacting particles, from the plasma to the walls:

$$g_{imp}^{(sw)} = \frac{1}{\Delta t \Delta S}\sum_{j=1}^{N_{hit}} W_j, \tag{3.41}$$

$$e_{imp}^{(sw)} = \frac{1}{\Delta t \Delta S}\sum_{j=1}^{N_{hit}} W_j E_{imp}, \tag{3.42}$$

where E_{imp} is the wall-impact kinetic energy, computed as shown in the previous section. The average wall-impact kinetic energy, for each population, is then obtained as:

$$\bar{E}_{imp} = \frac{e_{imp}^{(sw)}}{g_{imp}^{(sw)}}. \tag{3.43}$$

Finally, in order to compute the transmitted force to the wall, the transferred linear momentum vector flux is obtained as:

$$\dot{\boldsymbol{p}}^{(sw)} = \frac{1}{\Delta t \Delta S}\left(\sum_{j=1}^{N_{hit}} W_j m \boldsymbol{v}_j - \sum_{j=1}^{N_{emi}} W_j m \boldsymbol{v}_j\right), \tag{3.44}$$

where the summation extends over both the impacting and emitted/reflected macro-particles, and the macro-particle velocity refers to the simulation boundary (sheath

edge for quasineutral boundaries, material wall for non-neutral ones). The minus sign for the emitted or reflected macro-particles models the fact that they contribute to the force transmission with a recoil effect.

Finally, in order to reduce the statistical noise of the above defined variables, a time-averaged version at the time step k, is actually considered, meaning that:

$$\bar{n}_{(sw)}^{(k)} = \frac{(\Delta k_{avg} - 1)\, \bar{n}_{(sw)}^{(k-1)} + n_{(sw)}^{(k)}}{\Delta k_{avg}} \tag{3.45}$$

for the density, and similarily for other variables. In Eq. (3.45), Δk_{avg} represents the averaging number of time steps. This averaging scheme permits saving storage memory with respect to a standard moving average scheme (which would require to store all Δk_{avg} previous values).

3.2.7. Bohm's condition forcing

In all quasineutral material cell-faces (refer to Sec. 3.3.3.1), which feature a wall potential ϕ_W lower than the sheath edge potential ϕ_S, it is necessary to force Bohm's condition, which means to impose that ions reach them with sonic/supersonic conditions.

The algorithm considered for this Bohm's condition forcing (BCF) is the one presented in Refs. [132] and [133], and considers the kinetic Bohm criterion, firstly introduced by Harrison in 1959 [134]. As shown there, the supersonic conditions at the domain boundaries of quasineutral codes are not automatically met, and must be forced by applying a correction δn_e in the weighted plasma density. This density correction has the effect of generating an additional accelerating electric field towards the PIC cell-face. As the ion flow adapts self-consistently to this electric field and sonic conditions are progressively approached, the density correction tends to zero and Bohm's condition is consistently self-sustained.

If electrons are assumed Maxwellian at the sheath edge, a monotonic, non-oscillating plasma potential solution across the sheath requires that:

$$P(\delta\phi) = \sum_{s=1}^{L} \int_0^{\infty} \left(\frac{Z_s}{T_e} - \frac{Z_s^2}{m_s v_\perp^2(\delta\phi)} \right) F_s(v_\perp) dv_\perp \geq 0, \tag{3.46}$$

where L is the total number of heavy particle populations, F_s and m_s are respectively the heavy particles distribution function at the sheath edge and the elementary mass of the s^{th} population, $\delta\phi$ is the electric potential drop (≥ 0) applied in a virtual pre-sheath region (not simulated by the PIC), and $v_\perp(\delta\phi)$ is the corresponding perpendicular velocity, which can be obtained from the energy conservation equation (through the virtual pre-sheath region) as:

$$v_\perp(\delta\phi) = \sqrt{v_\perp^2(\delta\phi = 0) + 2\frac{Z_s e}{m_s}\delta\phi}. \tag{3.47}$$

If $P(0) < 0$, the BCF algorithm looks for the $\delta\phi$ yielding $P(\delta\phi) = 0$. In particular, $P(\delta\phi)$ can be evaluated by surface-weighting the macro-particles that hit the surface element as:

$$P(\delta\phi) = \frac{1}{\Delta t \Delta S} \sum_{s=1}^{L} \sum_{j=1}^{N_{hit}} \left(\frac{W_j Z_s}{T_e \left| v_{\perp,j}(\delta\phi) \right|} - \frac{W_j Z_s^2}{m_s \left| v_{\perp,j}(\delta\phi) \right|^3} \right). \tag{3.48}$$

By expanding P in terms of $\delta\phi$, the BCF algorithm obtains the required $\delta\phi$ to achieve $P = 0$. Since the computation of the electric potential is a prerogative of the fluid closure algorithms, the electric potential correction must be translated into a correction of the weighted plasma density δn_e (which is the real input of these algorithms). As shown in Ref. [133], the ordinary derivative $dn_e/d\delta\phi$, at first order in $\delta\phi$, can be computed as the following surface weighted variable:

$$\frac{dn_e}{d\delta\phi} = -\frac{1}{\Delta t \Delta S} \sum_{s=1}^{L} \sum_{j=1}^{N_{hit}} \frac{W_j e Z_s^2}{m_s \left| v_{\perp,j}(\delta\phi = 0) \right|^3}. \tag{3.49}$$

Notice that, for positive potential drops $\delta\phi > 0$ (if this is negative, there is no need of enforcing Bohm's condition as $P > 0$ already), this derivative is always negative. The electron density correction, for each quasineutral boundary cell-face, is finally obtained as:

$$\delta n_e = \frac{dn_e}{d\delta\phi} \delta\phi. \tag{3.50}$$

The above described algorithms have been validated with the test case described in Appendix C, Sec. C.14.

3.2.8. Interpolation from cell-faces centers to mesh nodes

As shown in Fig. 3.2, the corrected electron density at the quasineutral material boundary refers to the centers of the cell-faces (Bohm's correction considers, in fact, surface-weighted variables). Therefore, since the fluid closure algorithms of Sec. 3.3.2 and 3.3.3 consider plasma properties at the mesh nodes (gradients and other differential operators are better defined there), it is necessary to interpolate the "corrected" electron density to the mesh nodes.

Each node of the PIC mesh belongs to a given number N_f of material cell-faces. Typically, this number is 4, although there are some situations in which it can be smaller, like in the case of a 3D object vertices, for which $N_f = 3$. In all cases, the density at each mesh node is computed as a simple average of the surface-weighted variable on the applicable N_f cell-faces:

$$n_e = \frac{1}{N_f} \sum_{f=1}^{N_f} n_{e,f}^{(sw)}, \tag{3.51}$$

where $n_{e\,f}^{(sw)}$ is the surface weighted electron density (corrected), at the center of the f^{th} applicable cell-face. The same interpolation is also applied to all heavy particle

population properties (density and particle fluxes), and to other surface-weighted variables (mostly for post-processing needs).

3.2.9. The PIC population control

In PIC codes, controlling the macro-particle number is a fundamental task. In fact, a low number of macro-particles per cell produces a large statistical noise, while too large numbers may yield excessive computational costs. Moreover, the macro-particle weight dispersion within each cell has to be controlled as well, as too large dispersions affect negatively the performance of different algorithms, such as the collision sampling algorithms (that work best with homogeneous weights within each involved population and cell), and the statistical noise.

The goals of PIC population control algorithms are therefore to (I) ensure that the number of macro-particles per cell be within a desired interval $[N_{min}, N_{max}]$, and (II) to minimize the weights dispersion within each cell. The possible solutions to achieve such goals are:

- Active control of macro-particle number in collision and surface interaction algorithms.
- Use of a weight re-normalization algorithm, which either splits or groups existing macro-particles, while conserving their overall momentum and energy [135, 136].
- Use of a non-uniform mesh that expands as the expected number density drops.

The present code implements the first solution, described hereafter, while the other two approaches are left for future work. Nevertheless, it is worth mentioning that an expanding mesh, that follows the conical expansion of the plasma plume, can reduce dramatically the numerical noise downstream, as shown in Appendix C, Sec. C.13, and in Ref. [94], where a plume expansion test with a conical mesh is considered and compared with the solutions obtained with either a Cartesian mesh or with the SSM method (based on the fluid model of Chapter 2).

As noted in Secs. 3.2.5 and 3.2.6, collision and surface interaction algorithms make use of a generation weight $W_{gen} = W_{gen}(\boldsymbol{r})$, which depends on both the cell and the particle population. A dedicated algorithm updates such a generation weight in all cells, by monitoring the current number of macro-particles per cell N, its time steps evolution dN/dk, and the average weight of the existing macro-particles $\bar{W}$ in the cell. Let N_{tg} be a targeted number of macro-particles per cell, within the interval $[N_{min}, N_{max}]$. Then, if at least one macro-particle has been generated or injected in the considered cell in the latest time step, the generation weight is updated only if:

1. $N \in [N_{min}, N_{max}] \ \cap \ \frac{d\bar{N}}{dk} < \frac{1}{\Delta k_{avg}}$: stationary within the control interval,
2. $N < N_{min} \ \cap \ \frac{dN}{dk} \leq 0$: below the minimum and not increasing,
3. $N > N_{max}$: above the maximum,

where $\bar{N}$ is the time-averaged number of macro-particles per cell. In the first two cases, the generation weight is updated as $W_{gen} = \bar{W}\bar{N}/N_{tg}$, using the time-averaged number of macro-particles per cell. In the third case, on the other hand, in order to avoid large overshoots in the macro-particle number, the instantaneous value N is used, and the generation weight updated as $W_{gen} = \bar{W}N/N_{tg}$. Thus, W_{gen} dynamically adapts to the different conditions of each individual cell, allowing to actively control the macro-particle number for the injected or re-injected populations (from a contiguous injection or material cell-face) or the generated population (due to non-negligible collisional effects). A functional test for this population control algorithm is presented in Sec. C.10.

3.3 The electron fluid and electric field closures

In this hybrid code context, the electric potential and hence the electric field required by the PIC sub-model are obtained by solving the electron conservation equations, coupled in some cases, with Poisson's equation for the electric potential. Since the solution for the electron properties (density, velocity, and temperature) is generally coupled with that of the electric potential, this section deals with the "fluid and electric field closures" together. First, the electron fluid model is derived in Sec. 3.3.1, and then, the algorithms necessary to update both the electron properties and the electric potential are presented, for both quasineutral (Sec. 3.3.2) and non-neutral plasma regions (Sec. 3.3.3).

3.3.1. Electron fluid model derivation

The fluid model for electrons, complemented with Poisson's equation for the electric potential ϕ, permits computing their density n_e, temperature T_e, and current density $\boldsymbol{j}_e = -en_e\boldsymbol{u}_e$. As commented in Sec. 1.5.3, since electrons are weakly-collisional, local thermodynamic equilibrium cannot be invoked and the closure of the fluid equations is delicate. If collisions are introduced through standard resistive terms, the main concern is in the expressions for the pressure tensor $\mathcal{P}_e$ (in the momentum equation) and for the heat flux (in the energy equation), in the collisionless limit. Both should be derived from a kinetic approach, and several attempts are under progress in this regard, both for magnetized and unmagnetized plumes [33, 77, 116, 137] and even for anisotropic temperature plasmas [138], showing a combination of near-isothermal and quasi-polytropic behaviors.

A key point is that, if an auxiliary kinetic model is used (and collisions are weak), a closure of the fluid equations at the level of the momentum equation is the most advantageous. Thus, the proposed electron fluid model consists of electric current continuity and inertialess electron momentum equations,

$$\frac{\partial \rho_c}{\partial t} + \nabla \cdot \boldsymbol{j} = 0, \tag{3.52}$$

$$0 = -\nabla \cdot \mathcal{P}_e - en_e(-\nabla\phi + \boldsymbol{u}_e \times \boldsymbol{B}) - \sum_{s=1}^{L} \nu_{es} m_e n_e \left(\boldsymbol{u}_e - \boldsymbol{u}_s\right), \tag{3.53}$$

plus Poisson's equation:

$$\nabla^2\phi = -\frac{\rho_c}{\epsilon_0} \quad \text{with} \quad \rho_c = e\left(\sum_{s=1}^{L} Z_s n_s - n_e\right). \tag{3.54}$$

Here n_s and $\boldsymbol{u}_s$ are the fluid velocity of the s^{th} population, obtained from the PIC model, ν_{es} is the electron momentum transfer collision frequency with population s (refer to Sec. 3.3.1.1 for more details), and ρ_c is the electric charge density. Adding for

all heavy populations, we define the ion current density, the "quasineutral electron density", and the total electron collision frequency,

$$\boldsymbol{j}_i = e\sum_{s=1}^{L} n_s Z_s \boldsymbol{u}_s, \quad n_e^* = \sum_{s=1}^{L} Z_s n_s, \quad \nu_e = \sum_{s=1}^{L} \nu_{es}, \tag{3.55}$$

respectively. Notice that, in general, ν_{es} depends on electron properties too (density and temperature).

For the purposes of the present work, we will limit the fluid model to an unmagnetized plume ($\boldsymbol{B} = 0$) and to the simple polytropic electron closure:

$$\mathcal{P}_e = p_e \mathcal{I} \quad \text{with} \quad p_e(n_e) = n_e T_e, \quad T_e = T_{e0}\left(\frac{n_e}{n_{e0}}\right)^{\gamma-1}, \tag{3.56}$$

where γ is the constant polytropic coefficient, and n_{e0}, T_{e0} are the electron density and temperature at the plume location where we set $\phi = 0$.

In terms of the electric current density $\boldsymbol{j} = \boldsymbol{j}_i + \boldsymbol{j}_e$, Eq. (3.53) simplifies to:

$$0 = -\nabla p_e + e n_e \nabla\phi + \frac{m_e \nu_e}{e}\left(\boldsymbol{j} - \boldsymbol{j}_d\right), \tag{3.57}$$

where

$$\boldsymbol{j}_d = \boldsymbol{j}_i - \frac{e n_e}{\nu_e}\sum_{s=1}^{L} \nu_{es}\boldsymbol{u}_s \tag{3.58}$$

is a "driving" current density (for the special case of one population of ions and neutrals, some authors call this term "ion slip"). Solving the momentum equation for $\boldsymbol{j}$, the generalized Ohm's law is finally obtained:

$$\boldsymbol{j} = \frac{\sigma_e}{e}\nabla H_e + \boldsymbol{j}_d, \tag{3.59}$$

where $\sigma_e = e^2 n_e/\nu_e m_e$ is the electron conductivity,

$$H_e = h_e - e\phi \tag{3.60}$$

is the Bernoulli's function, and

$$h_e(n_e) = \begin{cases} T_{e0}\ln\left(\frac{n_e}{n_{e0}}\right) & \text{for } \gamma = 1 \\ -\frac{\gamma T_{e0}}{(\gamma-1)}\left[1 - \left(\frac{n_e}{n_{e0}}\right)^{\gamma-1}\right] & \text{for } \gamma > 1 \end{cases} \tag{3.61}$$

is the barotropic function, satisfying $\nabla h_e = \nabla p_e/n_e$. Notice that we have set $h_e, H_e = 0$ at the location where $\phi = 0$ and $n_e = n_{e0}$.

Introducing now Eq. (3.59) into Eq. (3.52), an elliptic differential equation for H_e is obtained:

$$\nabla^2 H_e + \nabla \ln\sigma_e \cdot \nabla H_e = -\frac{e}{\sigma_e}\left(\nabla\cdot\boldsymbol{j}_d + \frac{\partial\rho_c}{\partial t}\right). \tag{3.62}$$

Therefore, the fluid model reduces basically to solving two coupled elliptic equations: the above one for H_e and Poisson's equation for ϕ. Typical conditions at different boundaries set either these magnitudes or the derivatives perpendicular to the walls. In the case of the Bernoulli's function, the perpendicular derivative is indeed a condition on the electric current density:

$$\frac{\partial H_e}{\partial \mathbf{1}_\perp} = \frac{e}{\sigma_e}\left(\boldsymbol{j} - \boldsymbol{j}_d\right)\cdot \mathbf{1}_\perp, \tag{3.63}$$

where $\mathbf{1}_\perp$ is the unit vector normal at the boundary and directed towards the plasma.

3.3.1.1. Computation of the electron collision frequency

In order to compute the electron momentum transfer collision frequency with the s^{th} particle population ν_{es}, only elastic collisions are here taken into account. The electron-ion collision frequencies are then obtained as [139]:

$$\nu_{es} = \frac{2^{1/2} n_s Z_s^2 e^4 \ln\Lambda}{12\pi^{3/2}\epsilon_0^2 m_e^{1/2} T_e^{3/2}}, \tag{3.64}$$

where n_s is s^{th} population number density, and the parameter $\ln\Lambda \approx 10$ (for typical plasma plumes). For the neutrals, on the other hand, the collision frequency is computed by integrating the elastic collision cross section $\sigma_{es}(v_e)$ over a Maxwellian electron distribution function [140, 141]:

$$\nu_{es} = n_s\sqrt{\frac{2T_e}{9\pi m_e}}\int_0^\infty (x)^5\,\sigma_{es}(x)\exp\left(-\frac{x^2}{2}\right)dx, \tag{3.65}$$

where $x = v_e/v_{th,e}$ represents the normalized electron velocity with respect to the electron thermal velocity $v_{th,e} = \sqrt{T_e/m_e}$, and $\sigma_{es}(x)$ depends on the s^{th} population atomic type, and follows the model of Ref. [142] (for xenon). It is noticed, that Eqs. (3.53), (3.64) and (3.65) are only valid if the electron thermal velocity $v_{th,e}$ is much larger than the fluid velocity of both the heavy particle population u_s and of the electrons u_e.

3.3.2. The quasineutral closure

Let us consider first the zero Debye length limit, for which the whole plume can be considered quasineutral. The mathematical structure of the problem changes and simplifies. First of all, Poisson's equation reduces to

$$n_e = n_e^* \quad (\text{i.e.} \quad \rho_c = 0), \tag{3.66}$$

which determines the electron density and, subsequently, the electron temperature $T_e^* = T_e(n_e^*)$, the barotropic function $h_e^* = h_e(n_e^*)$, the conductivity $\sigma_e^* = \sigma_e(n_e^*)$, and the driving current density $\boldsymbol{j}_d^* = \boldsymbol{j}_d(n_e^*)$. Notice that all these quantities are

functions of the PIC model solution. The uncoupled equation for the Bernoulli's function then simplifies to:

$$\nabla^2 H_e + \nabla \ln \sigma_e^* \cdot \nabla H_e = -\frac{e}{\sigma_e^*} \nabla \cdot \boldsymbol{j}_d^*. \tag{3.67}$$

Once the solution for H_e is obtained, $\boldsymbol{j}$ is given by the generalized Ohm's equation, Eq. (3.59), and the electric potential from Eq. (3.60), that is:

$$\phi = \frac{h_e - H_e}{e}. \tag{3.68}$$

Notice that the widely-used isothermal and polytropic quasineutral models (like those presented in Sec. 2.1) correspond to setting $H_e \equiv 0$ in the above equation. Indeed $H_e = 0$ is the solution of Eq. (3.67) in the collisionless limit $\sigma_e^* \to \infty$. Therefore, H_e provides the electric potential correction due to collisional effects. Being the plasma weakly collisional, such a correction is generally small: for a typical scenario, featuring an NSTAR ion thruster and the corresponding neutralizer, as considered in the study of Chapter 4, the potential corrections are of the order of 10^{-2} V (see Fig. 4.6). However, what matters for the computation of the electric current is the gradient of H_e multiplied by the electron conductivity σ_e, which can be very large in nearly collisionless plumes, thus yielding non-negligible electric currents in the near region of the plasma plume, as shown in Fig. 4.7 (a).

In the collisionless limit $\sigma_e^* \to \infty$, on the other hand, the electric current in the generalized Ohm's law becomes indefinite, which is a severe limitation, especially when studying the plasma plume-SC interaction.

3.3.2.1. The sheath model

In the fully quasineutral closure, infinitely-thin Debye sheaths are postulated between the quasineutral solution and the walls, in order to accommodate potentials and electric currents there. Thus, at such boundaries, we must distinguish between the wall potential ϕ_W, and the potential at the sheath edge ϕ_S (of the quasineutral solution). The sheath model then establishes a relation between these two potentials and the perpendicular current density to the wall $j_W = \boldsymbol{j} \cdot \mathbf{1}_\perp = j_{i,W} + j_{e,W}$ (positive if emitted by the wall, since the unit vector is oriented towards the plasma).

In the most common case of a "negative" sheath, it is $\phi_W < \phi_S$, in order to confine electrons, while letting ions circulate free. The well-known solution for that (collisionless) sheath, assuming a Maxwellian-like electron distribution at its edge, yields:

$$\phi_W = \phi_S - \frac{T_e}{e} \ln \left(\frac{(j_W - j_{i,W})}{e n_e} \sqrt{\frac{2\pi m_e}{T_e}} \right), \tag{3.69}$$

where the ion current density, the electron density n_e and temperature T_e refer to the sheath edge.

In the case of a dielectric wall, the net-current free condition $j_W = 0$ yields ϕ_W locally. This is also the case of current-emitting walls (by thermoemission,

photoemission, ion bombardment), where j_W is known locally from the PIC model solution (or from known wall heating/illumination conditions).

For conductive walls (emissive or not), the problem is more complex, since there is no local condition setting either the wall potential ϕ_W or the total electric current through a certain region of the boundary. In fact, the electric potential of conductive objects depends on a global current balance, as described in Sec. 3.3.2.2, and, therefore, Eq. (3.69) is considered only to obtain the electric current j_W as a function of the wall potential ϕ_W:

$$j_W = j_{i,W} + j_{e,W} = j_{i,W} + en_e\sqrt{\frac{T_e}{2\pi m_e}}\exp\left(\frac{e\left(\phi_S - \phi_W\right)}{T_e}\right). \tag{3.70}$$

The computation of the electric current j_W to conductive walls is necessary to (I) obtain the boundary conditions for the computation of H_e (see Eq. (3.63)), and (II) to compute the total electric current to the conductive objects (needed by the equivalent circuit), assuming a given electric potential ϕ_W.

Finally, in the case of "positive" sheaths, $\phi_W > \phi_S$, the boundary electric current j_W is obtained from Eq. (3.70), by assuming a unitary exponential term, or equivalently, a thermal electron current contribution: $j_{e,W} = en_e\sqrt{T_e/(2\pi m_e)}$. It is then the PIC model, which must take into account the deceleration and the eventual reflection of the low energy ions within the sheath, as already discussed in Sec. 3.2.6.3.

3.3.2.2. The equivalent circuit solver

The conductive objects potentials (and hence their walls potential ϕ_W), are obtained from a global plasma current equilibrium, and hence, not from a local equilibrium, as considered for dielectric walls. For each conductive object, a total current from the plasma I_W is first computed by integrating the electric current density to its material wall boundaries. For a given object potential ϕ_W, j_W is obtained from Eq. (3.70), so that:

$$I_W = -\sum_f j_{W,f}\Delta S_f, \tag{3.71}$$

where the summation extends over the cell-faces of the object material boundary, and the minus sign is considered because j_W is positive if emitted by the object. Once this plasma current is obtained, an equivalent circuit like the one shown in Fig. 3.9 is considered. Each conductive object l is assumed to be an iso-potential node, it receives a current from the plasma $I_{W,l}$, and it can be connected arbitrarily to another node m by means of both a resistance R_{lm}, and a forced voltage difference V_{lm}. The electrical connections (either through a resistance or a power supply) split the whole circuit into sub-circuits, each one represented by an ensemble of electrically connected nodes (both directly and indirectly). Fig. 3.9 shows an example with two sub-circuits, a spacecraft sub-circuit (with 5 conductive objects, or nodes), and a target debris sub-circuit.

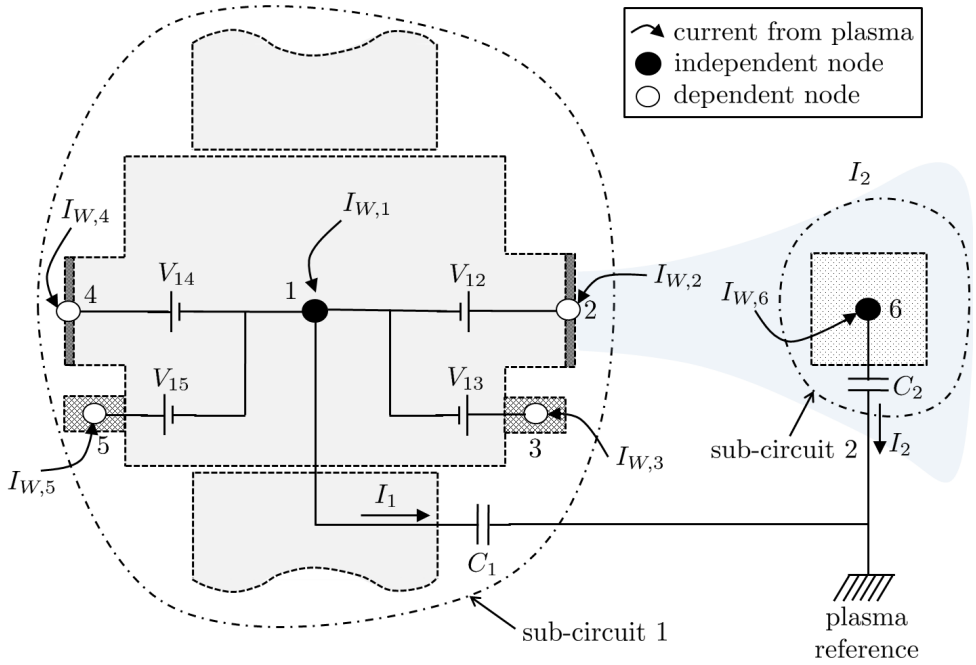

Figure 3.9: Scheme of the equivalent circuit, for a simulation featuring 6 conductive objects, and 2 independent sub-circuits

Each sub-circuit j is composed by independent and dependent nodes. The floating potential of each sub-circuit, or of the independent node, is obtained as the time evolution of the voltage of a capacitor C_j, which connects the j^{th} sub-circuit to the plasma:

$$\frac{d\phi_j}{dt} = \frac{I_j}{C_j} \tag{3.72}$$

The charging current I_j for the j^{th} sub-circuit is obtained as the sum of the plasma currents to the sub-circuit nodes:

$$I_j = \sum_l I_{W,l} \tag{3.73}$$

where the summation extends to the nodes of the sub-circuit. The value of the capacity C_j only affects the transient and not the stationary value of the independent node potential.

In order to compute the dependent nodes potentials and inter-node currents I_{lm} of each sub-circuit, a linear system is solved (derived from Kirchhoff's laws). This system consists of a current continuity equation for each dependent node, and an electric potential variation equation for each electrical connection (in the figure, 4 dependent nodes and 4 electrical connections are considered for the first sub-circuit):

$$\begin{cases} \text{current continuity at node } l: & I_{W,l} + \sum\limits_{m \neq l} I_{ml} = 0, \\ \text{potential across connection } lm: & \phi_l - I_{lm} R_{lm} + V_{lm} - \phi_m = 0. \end{cases} \tag{3.74}$$

3.3.3. The non-neutral closure

Once the quasineutral solution for the electron density n_e^*, the electric potential ϕ^*, and the electron temperature T_e^* are known at the instant $t^{(k)}$, the simulation domain is dynamically split into quasineutral and non-neutral subdomains, and the solution at time $t^{(k)}$ is recomputed in the non-neutral subdomain. In the following, the subdivision of the simulation domain is first introduced in Sec. 3.3.3.1, while the non-neutral solver is described in Sec. 3.3.3.2.

3.3.3.1. The quasineutral and non-neutral sub-domains

First of all, the quasineutral subdomain, constituted by quasineutral nodes and material boundary faces, must be defined. We will consider that cells and boundary faces are quasineutral if their level of non-neutrality is below a maximum value, called ε_{max}. For inner cell nodes, non-neutrality is measured by

$$\varepsilon_n = \left| \frac{\epsilon_0 \nabla^2 \phi^*}{e n_e^*} \right|^{1/2} = \left| \frac{n_e^* - n_e}{n_e^*} \right|^{1/2}, \tag{3.75}$$

and the cell node is part of the non-neutral subdomain when $\varepsilon_n > \varepsilon_{max}$. The square of ε_n thus represents the relative electric charge density. In the simulations of Chapter. 4 and Sec. 5.3, the chosen threshold value is $\epsilon_{max} = 0.032$, corresponding to a relative electric charge density of $1‰$.

For material boundary faces, non-neutrality is measured by the ratio between the local Debye length and the cell size Δl, in the direction normal to the surface:

$$\varepsilon_f = \frac{1}{\Delta l} \sqrt{\frac{\epsilon_0 T_e^*}{e^2 n_e^*}}. \tag{3.76}$$

Depeding on the value of ε_f, material faces are then sorted into quasineutral, if $\varepsilon_f \leq \varepsilon_{max}$, and non-neutral if $\varepsilon_f > \varepsilon_{max}$. A typical subdivision of the simulation domain nodes and material boundary faces is shown in Fig. 3.10.

The value of ϵ_f thus determines whether or not a discontinuity in the electric potential has to be postulated between the material wall W and the simulation boundary S. Numerical convergence for the transition between a quasineutral to a non-neutral sheath, then demands to add an intermediate case, so that three different cases are considered:

- if $\varepsilon_f \geq 1$: the boundary face is non-neutral, no sub-grid sheath exists (it is spatially resolved) and the boundary face is the wall, i.e. $\phi_S = \phi_W$,
- if $\varepsilon_f \leq \varepsilon_{max}$: the boundary face is quasineutral, there is a sheath discontinuity, and the potential at S is the quasineutral sheath edge potential ϕ_S^*,
- if $\varepsilon_{max} < \varepsilon_f < 1$, a partial sheath is added and the considered potential at the simulation domain boundary is:

$$\phi_S = \phi_W + \frac{1 - \varepsilon_f}{1 - \varepsilon_{max}} (\phi_S^* - \phi_W), \tag{3.77}$$

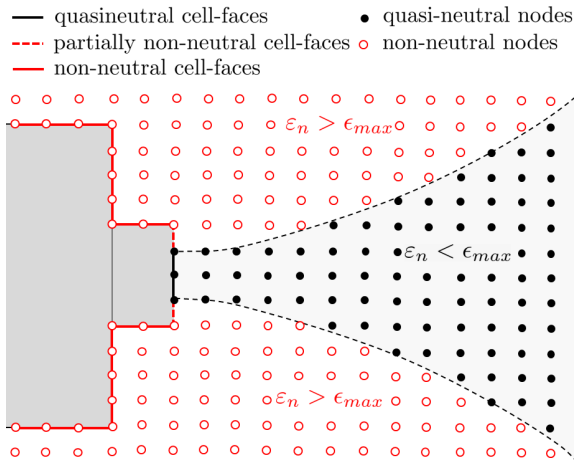

Figure 3.10: Sketch of a typical sub-division of the simulation domain into quasi-neutral and non-neutral nodes/cell-faces

where ϕ_S^* and ϕ_W are known from respectively the quasineutral electric potential solution and the current wall potential. The applied potential at S, for transition nodes like these, is shown in the sketch of Fig. 3.11.

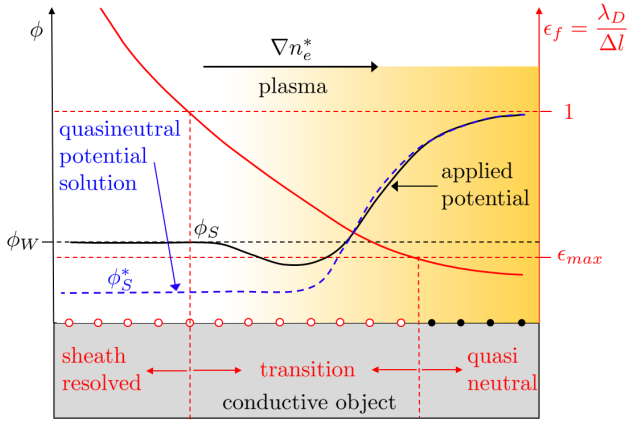

Figure 3.11: Applied potential at the simulation boundary ϕ_S (black line), versus the quasineutral electric potential solution ϕ_S^* (blue dashed line), and the Debye length to cell size ratio ϵ_f, at a material surface featuring a transition from a quasineutral sheath to a spatially resolved sheath. Quasineutral nodes are indicated by black dots, while non-neutral nodes by white dots.

3.3.3.2. The non-neutral solver

While in quasineutral regions the PIC solution provides all the necessary inputs for the computation of σ_e and $\boldsymbol{j}_d$ and hence for H_e and ϕ, in non-neutral regions the electron density n_e and temperature T_e are not known a priori, and the charge density ρ_c is not identically zero. Therefore, Eq. (3.62) is coupled with Poisson's

equation for the electric potential, repeated here for the sake of clarity:

$$\nabla^2\phi = -\frac{e}{\epsilon_0}\left(n_e^* - n_e\right), \tag{3.78}$$

where we remind that en_e^* is the ion electric charge. The iterative solution of the system composed by Eqs. (3.62) and (3.78) can be particularly costly, so that a different approach is proposed here. Since we are primarily interested in the stationary solution, the time derivative of the charge density appearing in Eq. (3.62) is neglected, while the electron conductivity and driving current vector, at the time step k, are substituted by their values at the previous time step:

$$\sigma_e \to \sigma_e^{(k-1)}, \qquad \boldsymbol{j}_d \to \boldsymbol{j}_d^{(k-1)}. \tag{3.79}$$

With this assumption, the Bernoulli's function H_e is solved for, and a functional dependence $n_e(H_e, \phi)$ is obtained explicitely by inverting Eq. (3.60), with the use of Eq. (3.61). For the sake of clarity, this functional dependence is shown for the isothermal and polytropic cases:

$$\begin{cases} n_e = n_{e0}\exp\left(\dfrac{H_e + e\phi}{T_{e0}}\right) & \text{for } \gamma = 1, \\ n_e = n_{e0}\left[1 + \dfrac{(H_e + e\phi)(\gamma - 1)}{\gamma T_{e0}}\right]^{\frac{1}{\gamma-1}} & \text{for } \gamma > 1. \end{cases} \tag{3.80}$$

Eq. (3.78) then becomes a non-linear differential equation in the unknown ϕ, which can be solved numerically, as shown in Appendix B, with the following boundary conditions:

- $\phi = 0$ at a reference plasma node (where $n_e = n_{e0}$, $T_e = T_{e0}$).
- $\phi = \phi^*$ at all quasineutral nodes of the domain (including those on the external boundary).
- $\phi = \phi_W$ at non-neutral material boundary nodes.
- $\phi = \phi_S$ at the transition material boundary nodes, with ϕ_S given by Eq. 3.77.
- $\dfrac{\partial\phi}{\partial\mathbf{1}_\perp} = 0$ at non-neutral external boundary nodes.

The non-linear solver has finally been validated with a dedicated test case, described in Sec. C.12.

3.3.3.3. Sheath conditions for non-neutral boundaries

While the electric circuit shows no difference with respect to the one described in Sec. 3.3.2.2, the sheath solver requires some clarifications, for what concerns the non-neutral boundaries. At dielectric walls, the electric current density is still 0,

while the wall potential ϕ_W (to be applied by the non-linear Poisson's solver) is now updated with Eq. (3.69), in which ϕ_S does not represent the sheath edge potential (which is now within the computational domain), but simply the electric potential at the computational boundary. Similarily, at conductive walls, the same approach can be followed to compute the electric current density, provided that ϕ_S now represents the electric potential at the computational boundary.

In both cases, if $\varepsilon_f > 1$, the non-linear Poisson's solver shall force $\phi_S \to \phi_W$ (sheath solved within the simulation domain), while, if $\varepsilon_{max} < \varepsilon < 1$, ϕ_S shall tend to an intermediate value between ϕ_W and ϕ_S^*, with a finite sheath discontinuity. This discontinuity is always taken into account when dealing with the interaction between macro-particles and material surfaces, just like considered for quasineutral boundaries.

3.4 The overall simulation loop

A generic step of the overall simulation loop is shown in Fig. 3.12, for a general non-neutral simulation. The particle push represents several PIC algorithms and generates updated fluid properties at times $k+1$ (quasineutral electron density n_e^*, and heavy particle densities n_s) and $k+1/2$ (heavy particle fluid velocities $\boldsymbol{u}_s$, current densities $\boldsymbol{j}_s$, and surface weighted variables at material boundaries). The quasineutral electron density and the surface weighted P variable are then fed to the Bohm's condition forcing algorithm, which corrects, if need be, the value of the electron density at the quasineutral material boundaries, thus completing the PIC sub-step.

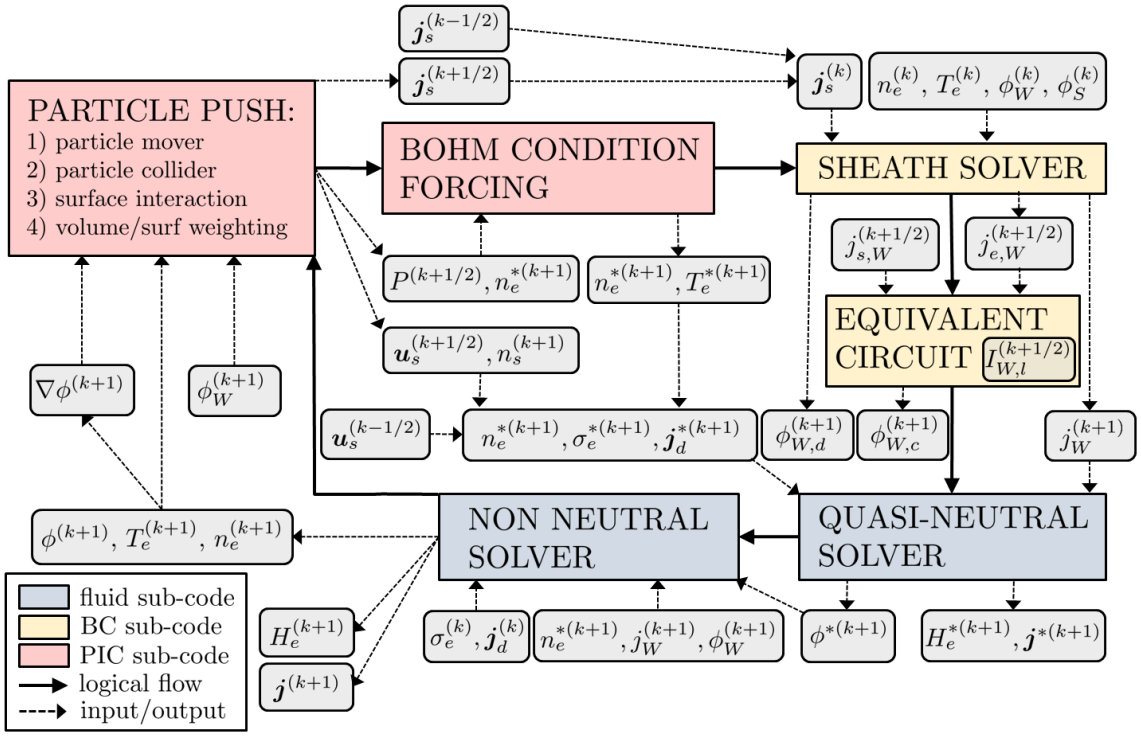

Figure 3.12: The hybrid-particle code simulation loop, at the time step $k+1$ (from time $t^{(k)}$ to time $t^{(k+1)}$)

Then, boundary conditions for the fluid closure at this new time $k+1$ need to be updated. First, the sheath solver updates the electron current density $j_{e,W}$ at conductive walls, and the dielectric walls potential $\phi_{W,d}$ both at time k, since its inputs (wall potential, sheath edge potential, electron density, temperature, and ion current) are known at this time step. The electron current density is then extrapolated to time $k+1/2$ and passed together with the ion current density to the wall $j_{i,W}$ (at time $k+1/2$) to the equivalent circuit solver. This obtains the electric current $I_{W,l}^{(k+1/2)}$ to the conductive objects and updates their potentials to time $k+1$, with a second-order leap-frog scheme. The sheath solver also extrapolates

the dielectric walls potential and the total electric current density to the wall $j_W = j_{e,W} + j_{i,W}$ to time $k+1$, as needed by the fluid closure algorithms.

This is then fed, together with the quasineutral electron density n_e^*, conductivity σ_e^*, and driving current density $\boldsymbol{j}_d^*$, all at time $k+1$, to the quasineutral solver, which solves for the quasineutral electric potential ϕ^*, the Bernoulli's function H_e^*, and the electric current density $\boldsymbol{j}^*$ at time $k+1$. The non-neutral solver then receives as input the quasineutral potential ϕ^*, the wall potential ϕ_W, and the quasineutral density n_e^* at time $k+1$, and assumes the latest step values for σ_e and $\boldsymbol{j}_d$. Its outputs are the electric potential ϕ, the electron temperature T_e, density n_e and Bernoulli's function H_e at the time step $k+1$. These, together with the updated wall potentials at time $k+1$ are fed back to the PIC model and the next time step is finally initiated.

The exact time consistency described above is important if we are interested in a second-order time integration scheme. In the simulations of Chapters 4 and 5, however, a less consistent approach has been followed in which the surface variables and hence the currents to the objects, are time-averaged over $\Delta k_{avg} = 100$ time steps, in order to minimize unwanted oscillations (due to PIC noise). This solution, clearly motivated in non-oscillating stationary problems, is valid in all those scenarios, in which the time scale of the object potentials variation is large compared with the Δk_{avg} averaging time steps.

Chapter 4

Simulation of the spacecraft-plume interaction

This chapter presents a study of the spacecraft-plasma plume interaction featuring both an ion thruster and a neutralizer. The simulations are carried out with the EP2PLUS code, and serve as a benchmark simulation for demonstrating the capabilities of the developed code, as well as for assessing the effects of non-neutral plasma regions, and of the electron thermodynamics. The electron model introduced in Chapter 3 allows to analyze the electric currents in the near region of the plasma plume, and the process by which the plasma plume gradually becomes current-free, as expected to be in the far-region of the expansion [1]

[1] The simulation results of this chapter have been presented in one journal publication [120]

4.1 Simulation geometry and settings

The plume-S/C interaction scenario considered here features a cubic S/C with an ion thruster, a hollow cathode neutralizer, and two solar arrays, as shown in Fig. 4.1 (a) and (b), while the corresponding equivalent circuit is shown in Fig. 4.2.

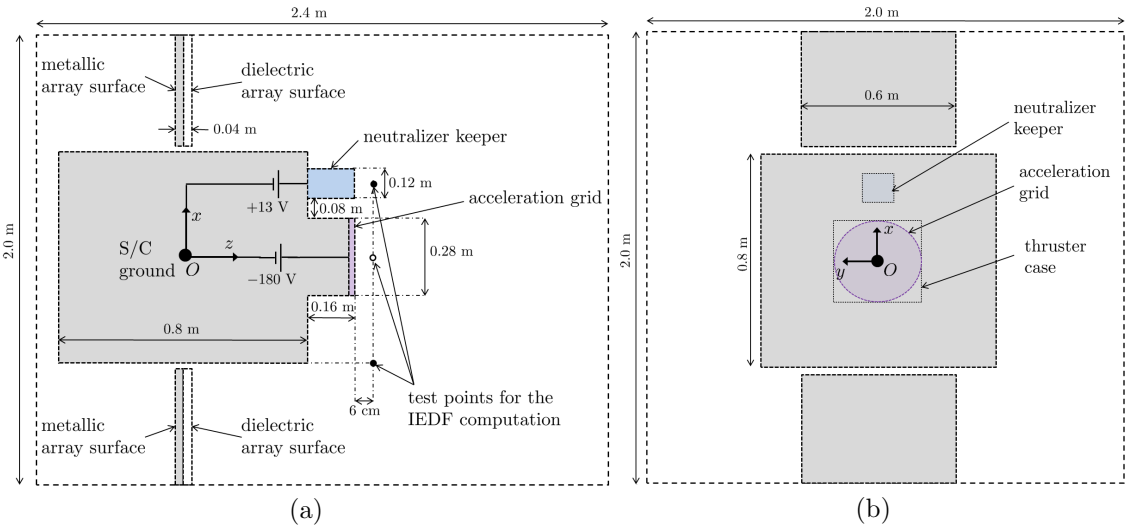

Figure 4.1: Simulation domain for the spacecraft-plume interaction simulation: (a) $x-z$ cross-section, and (b) $x-y$ cross-section, both through the satellite center. The PIC mesh is Cartesian, with a number of nodes along x, y, and z of $101 \times 101 \times 121$ (2 cm side cells). The white dot on the thruster symmetry axis is the reference point for the electron properties, the electric potential, and the Bernoulli's function. Two additional points on the thruster side and on the neutralizer axis are considered for the computation of the ion energy distribution function.

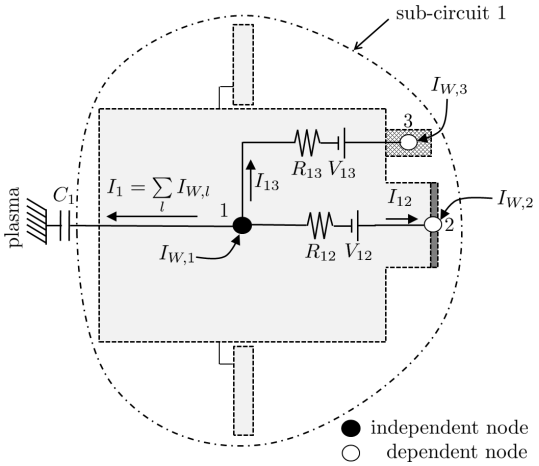

Figure 4.2: Scheme of the equivalent circuit, for the considered scenario. Although a small physical gap is considered (that let some particles through), the metallic face of the solar arrays is electrically short-circuited with the metallic cubic body.

Three conductive objects are considered: the satellite ground (including cubic body, thruster case and the back-face of the solar arrays), the neutralizer keeper external surface, and the most external grid of the thruster. The resistances between S/C ground and acceleration grid and neutralizer keeper are assumed to be zero ($R_{12} = R_{13} = 0$). The front face of the solar arrays, as shown in Fig. 4.1 (a), is modeled as a dielectric object (i.e. the wall potential is determined locally from current equilibrium). The values of some simulation parameters are summarized in Tab. 4.1.

Table 4.1: Considered parameters for the plasma-plume satellite interaction simulation. Applied voltages refer to the spacecraft ground. All considered objects are conductive, except for the front surface of the solar arrays, which is dielectric.

Simulation parameter	**Units**	**Values**
Neutralizer keeper voltage	V	+13
Acceleration grid voltage	V	−180
Thruster mass flow rate	sccms	27.13
Thruster mass utilization efficiency	%	90.0
Doubly to singly charged ion current ratio	%	9.1
Injected Xe^{+} profile (thruster)	n/a	SSM [2]
Injected Xe^{++} profile (thruster)	n/a	SSM [3]
Injected Xe^{+} energy (thruster)	eV	1040
Injected Xe^{++} energy (thruster)	eV	2080
Injected Xe^{+} temperature (thruster)	eV	0.1
Injected Xe^{++} temperature (thruster)	eV	0.2
Injected neutrals profile (thruster)	n/a	Flat
Injected neutral velocity (thruster)	m/s	247 (sonic)
Injected neutral temperature (thruster)	eV	0.05
Neutralizer mass flow rate	sccms	3.59
Injected neutrals profile (neutralizer)	n/a	Flat
Injected neutral velocity (neutralizer)	m/s	247 (sonic)
Injected neutral temperature (neutralizer)	eV	0.05
Neutralizer ion flow percentage	%	5.0
Injected Xe^{+}, Xe^{++} profile (neutralizer)	n/a	thermal, Gaussian [4]
Injected Xe^{+} temperature (neutralizer)	eV	0.2
Injected Xe^{++} temperature (neutralizer)	eV	0.4
Electron temperature at thruster exit	eV	3.5
Electron polytropic cooling coefficient	n/a	$[1.0, 1.3]$

The considered thruster simulates the NASA's NSTAR ion thruster [143, 144], while the applied voltages to the acceleration grid and neutralizer keeper are kept constant to respectively $V_{12} = -180$ and $V_{13} = +13$ V. The negative grid potential prevents most of electrons from backstreaming towards it, while the neutralizer keeper is biased positive with respect to the spacecraft ground [144].

[2] with outermost streamline radius $R_0 = 14$ cm and divergence angle $\alpha_0 = 20.5$ deg
[3] with outermost streamlines radius $R_0 = 14$ cm, and divergence angle $\alpha_0 = 30$ deg
[4] with outermost streamlines radius $R_0 = 4$ cm

The injection areas for both the thruster and neutralizer are circular with radii of respectively 14 and 4 cm. Neutrals are injected axially with sonic conditions and with a flat density profile from both the thruster and neutralizer injection cells. Regarding the thruster ions, these are injected following the Ashkenazy-Fruchtman Self Similar profile [50, 61], with an outermost streamline divergence angle $\alpha_0 = 20.5$ deg (at the radius $R_0 = 14$ cm from the thruster centerline). This divergence profile corresponds to a divergence efficiency of 0.98, as considered in Ref. [144]. An already developed divergence angle is considered because the mesh is not fine enough to simulate the effects of beamlets injection and coalescence into a single beam, so that the injection surface is actually simulated as a quasineutral surface, with a thin sheath (across which the potential drops from its value at the quasineutral plasma to that of the acceleration grid). For what concerns the neutralizer ions, past studies [145] have shown that a significant ion current is also emitted. Here we have considered that 5% of the total mass flow of the neutralizer is emitted in the form of singly or doubly charged ions from a thermal reservoir (with temperature of respectively 0.2 and 0.4 eV). Finally, a ratio between doubly and singly charged ion current of 9.1% [146] has been considered for both the thruster and the neutralizer emissions.

Regarding the electron thermodynamics, a peak electron temperature of 3.5 eV, consistent with existing experimental measurements for similar thrusters [59], is assumed at a node located 6 cm downstream from the thruster exit (which represents the reference plasma point for potential, Bernoulli's function and electron barotropic function), while four different values for γ are considered: 1.0 (isothermal), 1.1 (reference case), 1.2 and 1.3.

For what concerns the applied fluid closure, the simulations are run with the sole quasineutral solver between $t = 0$ and $t = 1$ ms, and, starting from $t = 1$ ms, the non-neutral solver is activated. The required time for a slow CEX ion (with an energy content of 5 eV) to cross the entire simulation domain is around 1 ms, so that the considered simulation time is expected to be sufficient to reach stationary conditions.

The boundary conditions for the computation of the Bernoulli's function H_e, in this simulation setup, are:

- Current free condition $\boldsymbol{j} \cdot \mathbf{1}_\perp = 0$ at the external boundaries and at the dielectric walls of the solar arrays front surface, thus yielding:

$$\frac{\partial H_e}{\partial \mathbf{1}_\perp} = -\frac{e}{\sigma_e} \boldsymbol{j}_d \cdot \mathbf{1}_\perp$$

- Fixed electric current $j_W = j_W(\phi_W)$ to the other conductive walls:

$$\frac{\partial H_e}{\partial \mathbf{1}_\perp} = \frac{e}{\sigma_e} \left(j_W - \boldsymbol{j}_d \cdot \mathbf{1}_\perp \right)$$

- Dirichlet conditions $H_e = \text{const}$, at the emissive surface of the neutralizer, equivalent to leaving a free electron current to balance the electron current lost to the boundaries, and generated inside the domain (e.g. due to ionization).

Regarding the electric potential, the boundary conditions are:

- Dielectric or conductive wall potential $\phi = \phi_W$ at the non-neutral material boundary nodes.
- Transition conditions $\phi = \phi_S$ (refer to Eq. 3.77) at the transition material boundary nodes.
- Quasineutral electric potential $\phi = \phi^*$ at all quasineutral nodes (including those on the external boundary).
- $\phi = 0$ at the reference node for the electron properties (6 cm downstream from the thruster exit area, on the plume axis).
- Neumann conditions on ϕ at the non-neutral external boundary nodes:

$$\frac{\partial \phi}{\partial \mathbf{1}_\perp} = 0.$$

This is clearly an approximation, but it turns out to be good enough for simulation purposes, if the external boundary is sufficiently far from regions characterized by steep plasma density gradients. Moreover, from Gauss' theorem, if this boundary condition is applied to the entire external boundary, it ensures that the total electric charge inside the domain be zero. Finally observe that, if the external boundary is locally quasineutral (because a dense plasma crosses it), then the local normal electric field is not constrained to be zero and is given by the quasineutral solution.

4.2 Simulation results and discussion

The electric potential, and the corresponding electric field intensity (and streamlines) are shown respectively in Fig. 4.3 (a) and (b), at the $y = 0$ cross section, for the reference $\gamma = 1.1$ case. In this case, the S/C is floating at a potential of -38 V with respect to the neutralized plasma plume (more precisely with respect to the white dot of Fig. 4.3 (a)), so that the iso-potential lines adapt to this value close to the cubic S/C body, through spatially resolved plasma sheaths. The sheath electric field is then always oriented towards the S/C surfaces. For what concerns the emitted plasma plume, the ambipolar electric field is always oriented radially outwards with a small component along the z axis, along the plume expansion. The effect of the CEX ions is clearly visible on the left of the main plasma plume, while the neutralizer creates a plasma bridge with the thruster (necessary for the plume neutralization) and alters substantially the symmetry of the plasma properties.

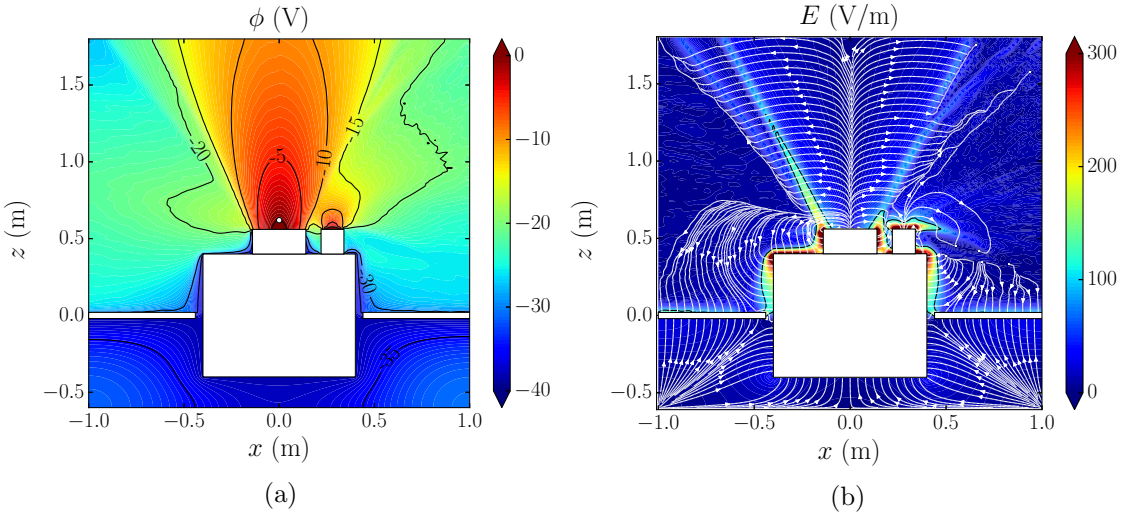

Figure 4.3: Reference case results at $y = 0$: (a) electric potential, and (b) electric field intensity (with streamlines). The reference point for the electric potential is shown in the sub-figure (a) with a white dot.

The electron density, the total ion and neutral density, and the relative electric charge density for the reference case are shown respectively in Fig. 4.4 (a), (b), (c), and (d). The electron density follows closely the evolution of the electric potential, with densities rapidly dropping to zero as the very negative S/C surfaces are approached. The CEX ion density (sum of both the singly and doubly charged ion density) reaches values of 10^{11} m^{-3} close to the solar array, and between 10^{12} m^{-3} and 10^{13} m^{-3} on the sides of the thruster, a result which is very similar to past simulations of this NASA ion thruster, like those of Refs. [147], [148], and [149]. Regarding the neutral density, this drops quickly from 10^{18} m^{-3} to 10^{14} m^{-3} as we move downstream and laterally from the thruster and neutralizer exit surfaces, while it is much lower close to the S/C lateral walls where neutrals are produced by ion recombination (and values between 10^{11} and 10^{13} are found). Finally, the

electric charge density, normalized with respect to the electron charge density, shows a negative region just on the right of the neutralizer, where ions are almost absent, and positive regions close to the other S/C surfaces.

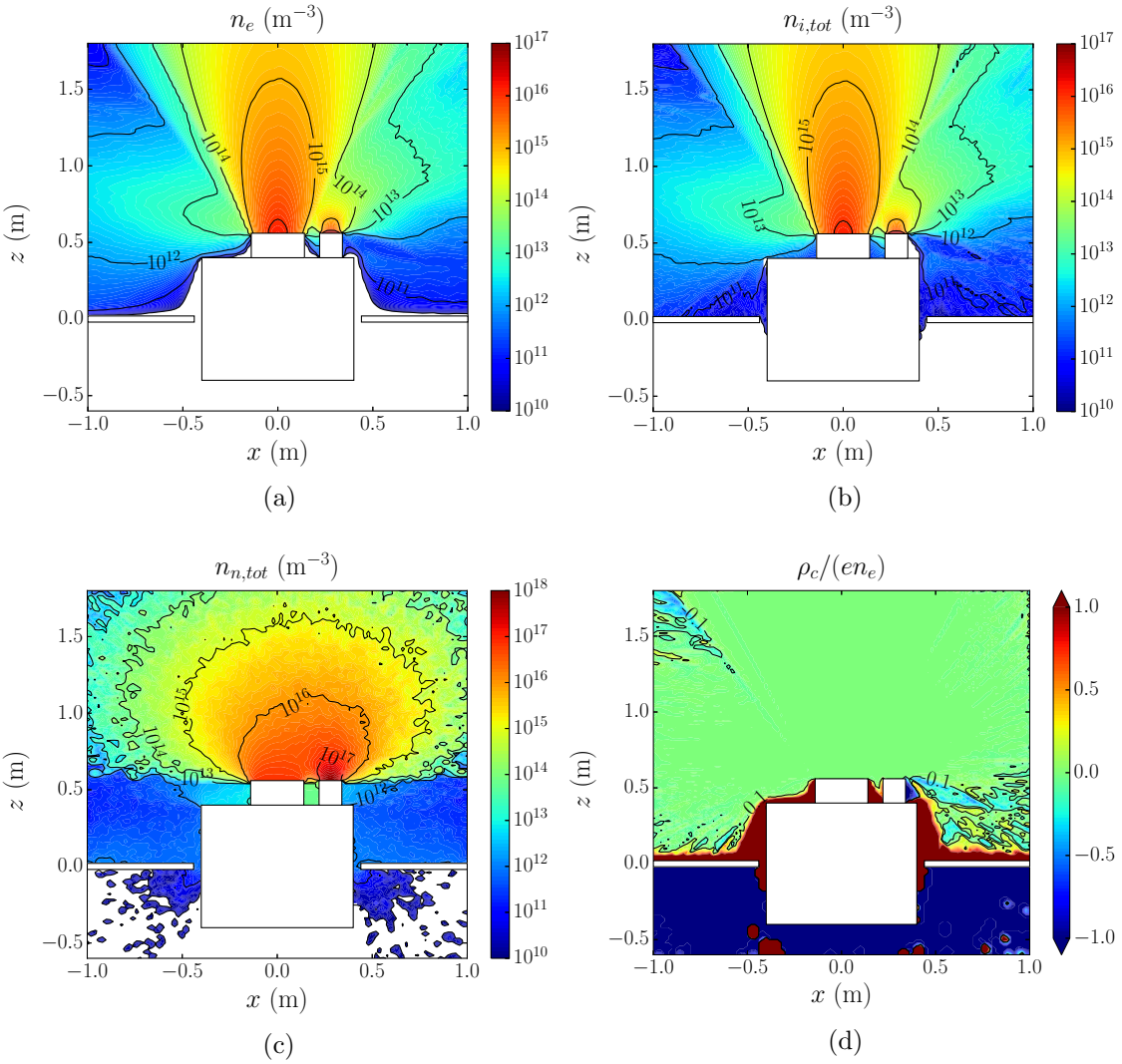

Figure 4.4: Reference case results at $y = 0$: (a) electron density, (b) total ion density (sum of the ion populations densities), (c) total neutral density, and (d) relative charge density, normalized with the local electron charge density.

The electron conductivity σ_e and the total ion current density are shown respectively in Fig. 4.5 (a) and (b). Regarding the former, this is highest inside the main thruster plume (up to 3000 Ω^{-1}m^{-1}) and features a lateral peak on the left of the thruster, where the ratio between the CEX ion and neutral densities is highest, and a second peak at the neutralizer exit, where both the quasineutral plasma and the neutral densities are high. The total ion current density is practically conical inside the main plume and diverts towards the S/C in the lateral plume regions.

The solution for the Bernoulli's function H_e is shown in Fig. 4.6. The electric potential correction due to collisional effects is negligible for the present case, in the

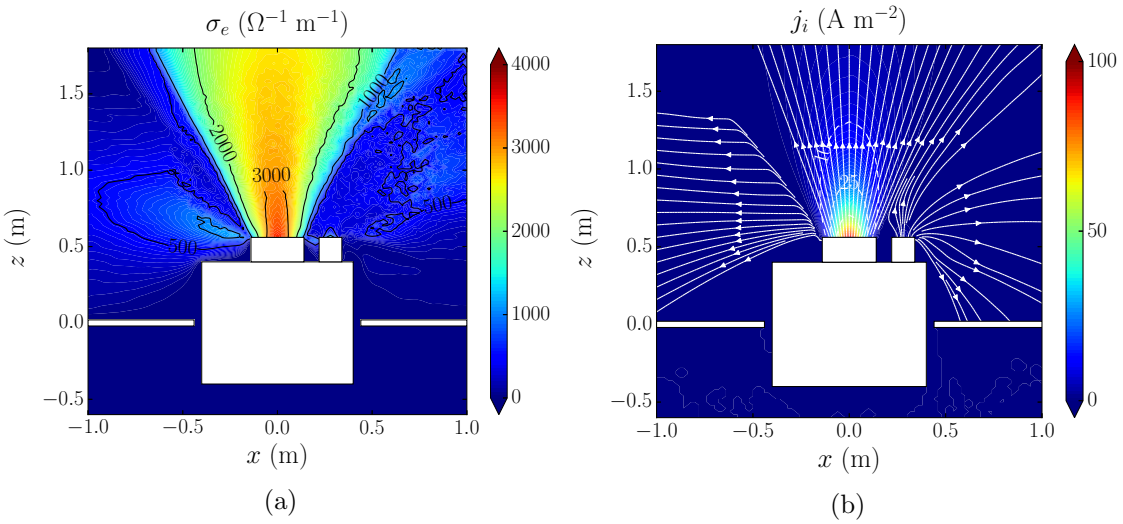

Figure 4.5: Reference case results at $y = 0$: (a) electron conductivity, and (b) total ion current density.

order of a few mV, reaching the largest values, around 10 mV, at the neutralizer exit (where collisional effects are largest).

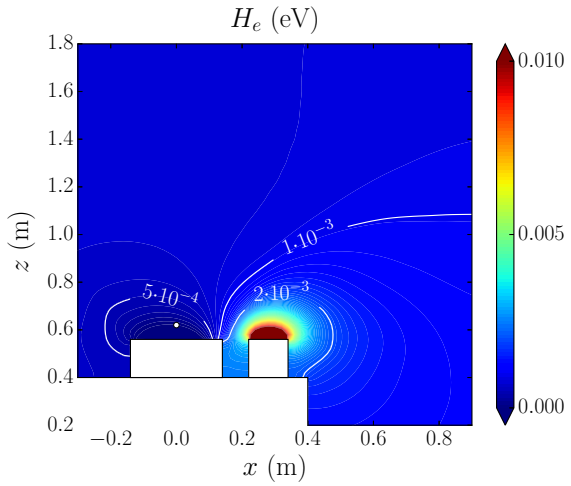

Figure 4.6: Solution for the Bernoulli's function at the $y = 0$ plane. The reference point ($H_e = 0$) is shown with a white dot.

However, although the absolute potential correction is small, the electric current density is not negligible in the near region of the plume, as shown in Fig. 4.7 (a), and presents values around 100 A/m^2 at the thruster exit and even larger ones at the neutralizer exit (given the lower emission area of the latter).

A virtually current-free plasma plume is achieved just $30 - 40$ cm downstream from the thruster exit, which is consistent with the assumption that the far-region plasma is essentially current free. All electric current streamlines originate at the thruster exit (due to the emitted ions) and reach the neutralizer emission surface

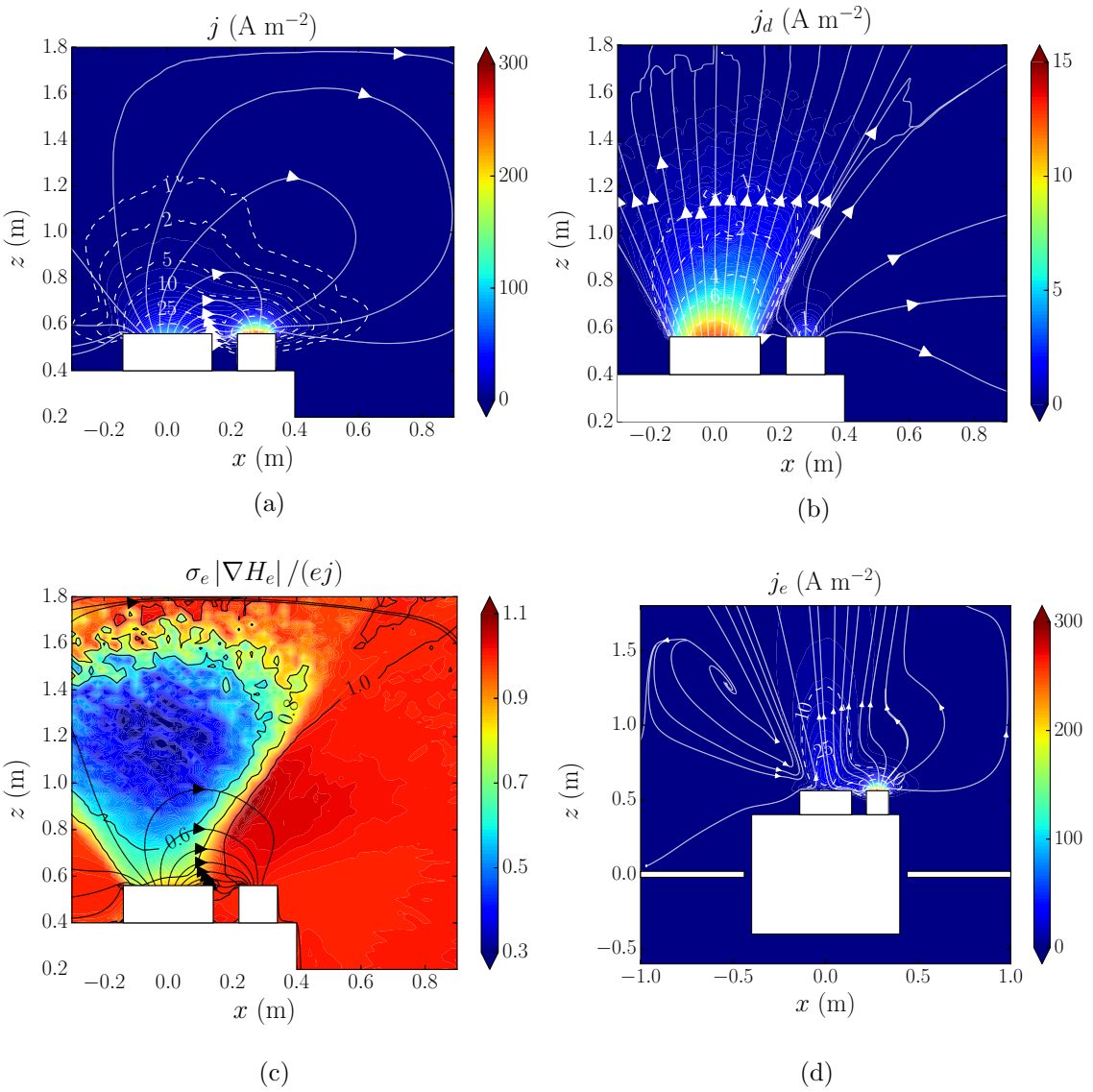

Figure 4.7: Reference case results: (a) total electric current density (with streamlines), (b) driving current density (with streamlines), (c) relative contribution of $\sigma_e \nabla H_e / e$ (with streamlines) to the total electric current density, and (d) electron current density (with streamlines), at $y = 0$.

(due to emitted electrons) just as expected (no electric current sources exist inside the domain). We remind the reader that the total electric current is given by Ohm's law, Eq. 3.59, and presents two different contributions: the product $\sigma_e \nabla H_e / e$ and the driving current $\boldsymbol{j}_d$. The latter is shown in Fig. 4.7 (b) and presents a shape similar to that of the ion current, although it decays much more rapidly as the plume expands. In fact, from its very definition in Eq. (3.58), the driving current tends to zero in a quasineutral plasma plume, composed of only singly charged ions and electrons (and no neutrals). The relative magnitude and streamlines of the

$\sigma_e \nabla H_e/e$ term are then shown in Fig. 4.7 (c). The observed values and streamlines clearly indicate that this term is the predominant one in determining the electric current in large portions of the domain, with the exception of the central region of the main plasma plume, where the contribution of the driving current term is comparable.

Finally, Fig. 4.7 (d) shows the electron current density and streamlines at the $y = 0$ cross section. It would appear as though some electrons that neutralize the plume are actually separated electrically from the neutralizer. However, the 3D electron streamlines, shown in Fig. 4.8, have a complex three dimensional structure, and the farthest (from the neutralizer) conical plume streamlines are neutralized by electrons that circle around the dense region of the plume. It is noticed that such an electric path may be justified by the local peaks of electron conductivity, due to the CEX ions, found around the main core of the plume, as shown in Fig. 4.5 (a). In any case, all streamlines originate inside the neutralizer, because $\nabla \cdot \boldsymbol{j}_e \approx 0$ inside this weakly collisional plasma (ionization effects are almost negligible).

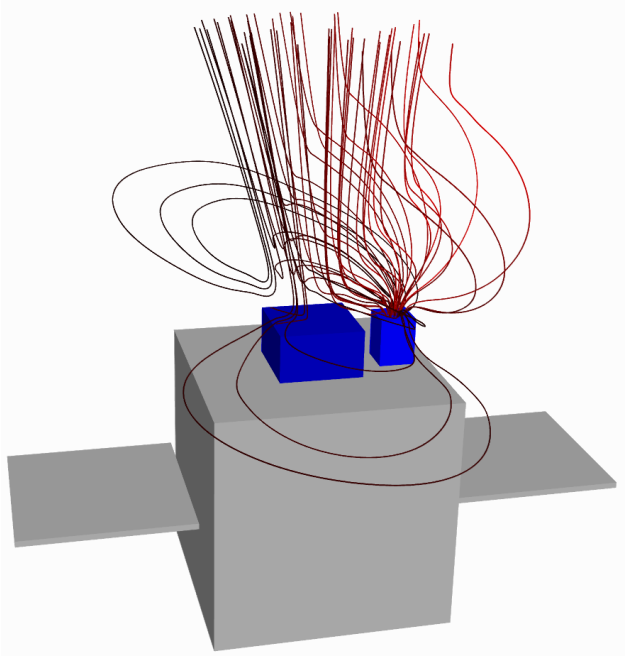

Figure 4.8: Three-dimensional electron current streamlines emanating from the neutralizer and merging with the ion plume. The farther (from the neutralizer) the ion streamline to be neutralized, the darker the color of the corresponding electron streamline.

An important capability of a S/C-plasma interaction tool is to predict the ion flux and the mean wall-impact energy of ions on the S/C surfaces, in order to evaluate the effects of sputtering and deposition. Fig. 4.9 (a) and (b) show respectively the backscattered CEX ion flux and their average wall-impact energy at the S/C surfaces. The flux on the cubic S/C surfaces is between 10^{15} and $5 \cdot 10^{15}$ $\mathrm{m^{-2}s^{-1}}$, while it decreases to approx. $2 - 5 \cdot 10^{14}$ $\mathrm{m^{-2}s^{-1}}$ on the solar array surfaces. Regarding

their energy, since CEX ions are mainly created at the center of the thruster plume (where $\phi \approx 0$), and the S/C floats at -38 V, the average wall-impact kinetic energy is between 30 and 40 eV, being larger at the S/C edges. At the solar array, this impact energy decreases to less than 30 eV.

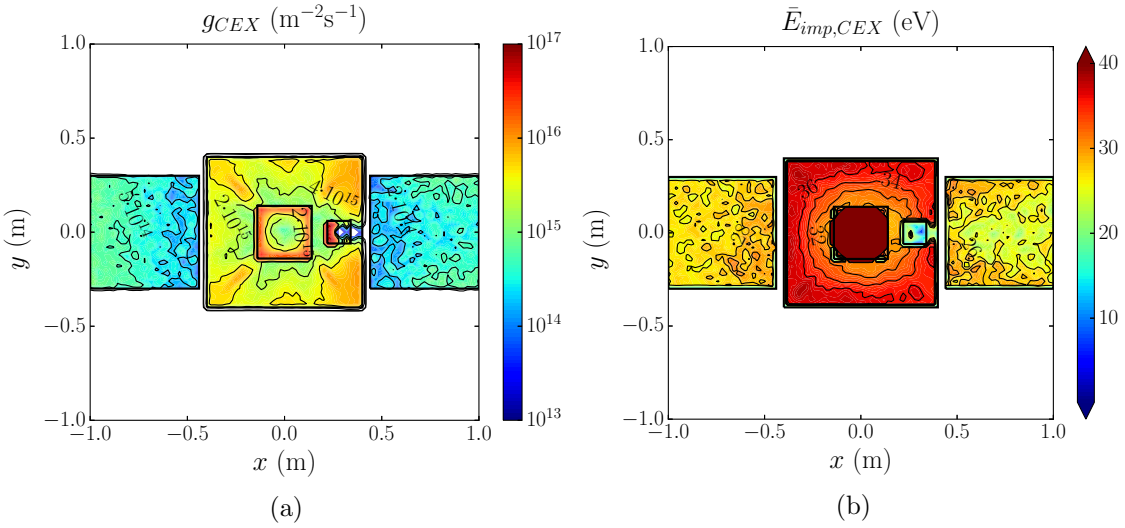

Figure 4.9: Reference case results at the S/C surfaces: (a) CEX ion flux, (b) average wall-impact kinetic energy of backscattered CEX ions.

Fig. 4.10 then shows the ion current density reaching the S/C front surfaces.

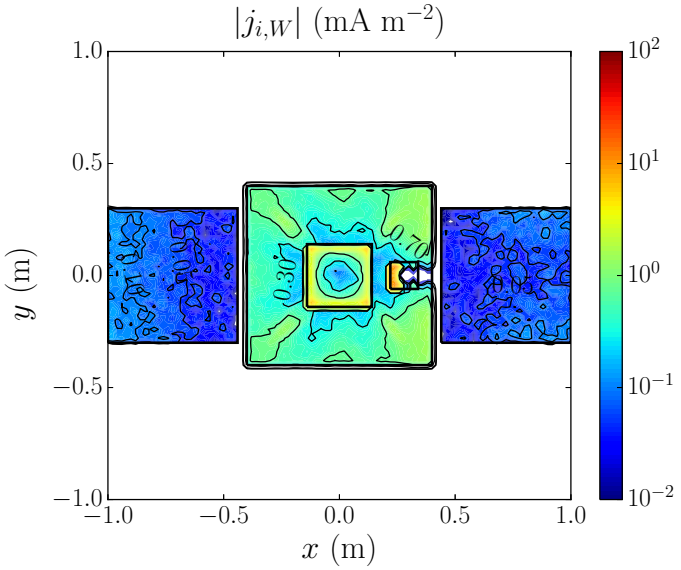

Figure 4.10: Ion current density to the S/C walls.

Clearly the same behavior of Fig. 4.9 (a) is resembled. A maximum ion current density of up to 10 mA m^{-2} is reached at the corners of the thruster case and on one side (the one closer to the thruster) of the neutralizer keeper. The average current

density to the S/C cubic body is around 0.5 mA m^{-2}. The current density to the solar array, on the other hand, is generally lower than 0.1 mA m^{-2}.

The ion energy distribution function [150] is finally plotted at the three different test points of Fig. 4.1 (a), in Fig. 4.11 (a). Close to the thruster exit (black solid line), three well defined populations of ions can be identified: the emitted doubly charged ions (with energies around 2080 eV), the emitted singly charged ions (with energies around 1040 eV), and the slow CEX ions (including both singly and doubly charged ions), which feature energies that are generally below 3 eV. On the thruster side (dotted blue line), on the other hand, only CEX ions are present, and the singly and doubly charged ions populations can be distinguished again in terms of energy content. In fact the energy of these ions depends directly on the potential difference between the location where they are generated (dense plume region, with $\phi \in [0, -5]$V) and the considered test point potential ($\phi \approx -20$V). Finally, at the neutralizer axis, the emitted singly and doubly charged ions can be clearly distinguished from CEX ions generated in the plume: the two well definite peaks at energies of approx. 15 and 30 eV are indeed caused by the acceleration of the emitted ions, due to the ambipolar electric field at the neutralizer exit (characterized by a steep potential drop). Finally, a zoom of the ion energy distribution function at the thruster axis is shown in Fig. 4.11 (b), which also provides the separate contributions of singly and doubly charged ions. The disparity of energies and distributions of the different ion populations shown in Fig. 4.11 (a) and (b) clearly makes the use of multiple fluids for the ion species quite troublesome.

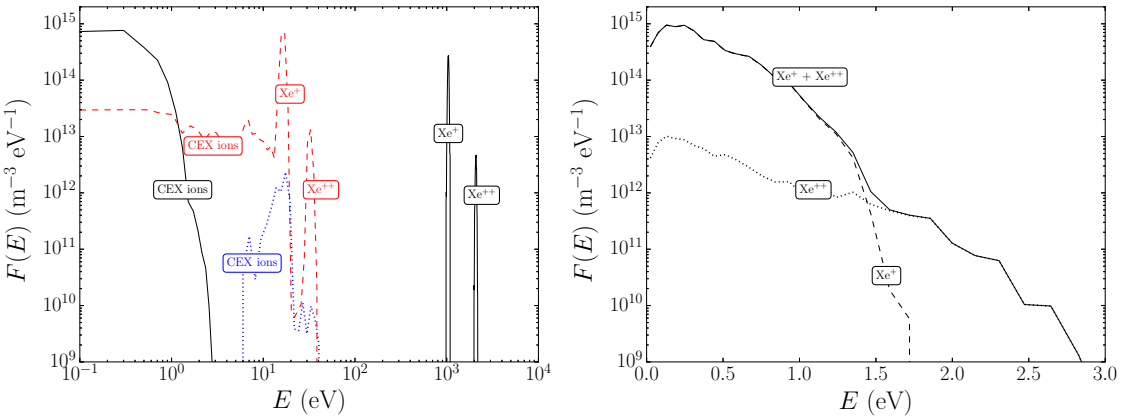

(a) (b)

Figure 4.11: (a) Ion energy distribution function at three different locations, shown in Fig. 4.1 (a): thruster axis (black solid line), neutralizer axis (red dashed line), and 40 cm off the thruster axis, opposite to the neutralizer position (blue dotted line). (b) Zoom on the slow CEX ions distribution function at the thruster axis: total (solid line), singly charged (dashed line), and doubly charged (dotted line) ions contributions. All results are instantaneous and not time averaged.

4.2.1. Effects of the electron thermodynamics

The interaction between the plasma plume and the satellite is strongly affected by the electron thermodynamics, which is here modeled with a polytropic cooling law. Fig. 4.12 (a) and (b) show respectively the S/C potential and the ion/electron current to the S/C walls (including also the currents to neutralizer, thruster grid and solar arrays), for the 4 γ-cases considered. After a short transient, the electric potential of the S/C reaches a stationary value, which means that the total current to the S/C node approaches zero or fluctuates dimly around it. Moreover, the floating potential is quite stable for all γ cases (the chosen value for the charging capacity C is 20 nF).

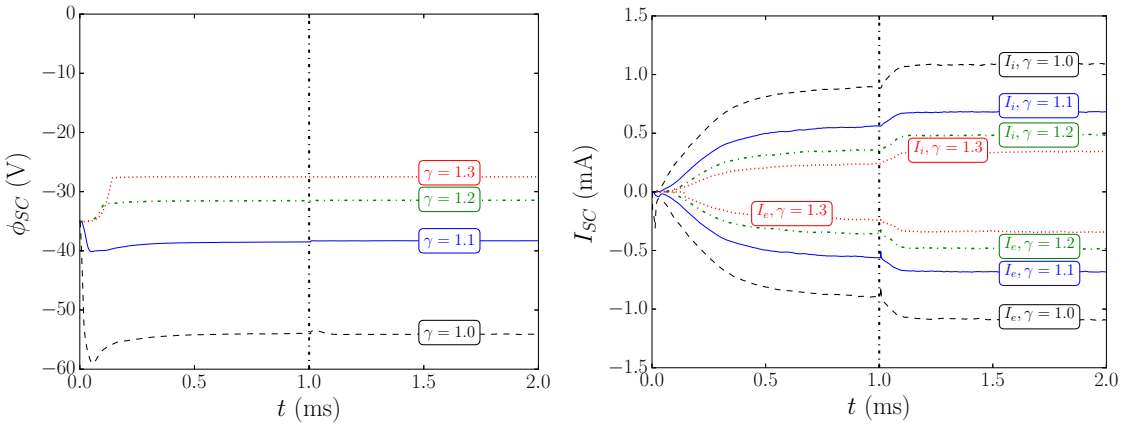

Figure 4.12: Time evolutions for $\gamma = 1$ (black dashed line), $\gamma = 1.1$ (blue solid line), $\gamma = 1.2$ (green dash-dot line), and $\gamma = 1.2$ (red dotted line) of (a) electric potential, and (b) ion and electron currents. The electric potential refers to the S/C with respect to the plasma reference node potential (6 cm downstream from the thruster exit), while the ion and electron currents refer to sum of all currents to the S/C walls, including the neutralizer, the last thruster grid, and the solar arrays. A vertical dash-dot line indicates when the non-neutral solver is activated ($t = 1$ ms).

The higher the polytropic coefficient, the more positive the S/C floats, as suggested by the limit to which the electric potential tends when the electron density goes to zero, which is $-\gamma T_{e0}/(\gamma-1)$, as shown in Sec. 2.5. Clearly, since the collected electron current is affected by this limit, the floating potential of the S/C also adapts to it. Moreover, the closer to isothermal the electrons, the larger the collected ion and electron currents, because of the larger electric fields that are capable of deviating a larger fraction of slow ions towards the spacecraft. From these results, it is then apparent that the S/C floating potential is strongly affected by the polytropic cooling coefficient of the electrons. A precise prediction of this potential thus requires a good knowledge of γ. Alternatively, by measuring the potential difference between the S/C and the plasma plume, important information can be obtained on the effective value of this coefficient.

The electric potentials for $\gamma = 1.1$ and $\gamma = 1.2$ are compared in Fig. 4.13 (a),

while the slow CEX ion density is compared in Fig. 4.13 (b). The larger the γ, the larger the electric potential, with the largest differences close to the S/C surface. The lower electric fields for $\gamma = 1.2$ yield a slightly higher CEX ions concentration downstream (+20%), and a lower one close to the solar array (−20/50%).

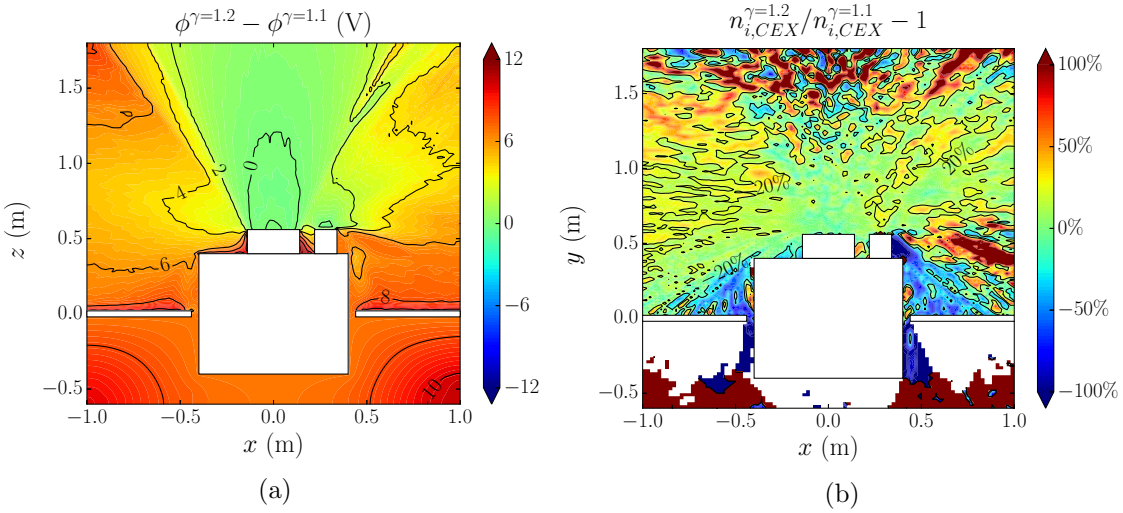

Figure 4.13: Comparison, at $y = 0$, of the $\gamma = 1.1$ and $\gamma = 1.2$ cases: (a) electric potential difference $\phi^{\gamma=1.2} - \phi^{\gamma=1.1}$, and (b) relative difference in the slow ion number density $n_{i,CEX}^{\gamma=1.2}/n_{i,CEX}^{\gamma=1.1} - 1$.

Finally, Fig. 4.14 (a) and (b) show respectively the relative differences in CEX ion flux and wall-impact energy at the S/C surfaces, between the $\gamma = 1.1$ and the $\gamma = 1.2$ cases.

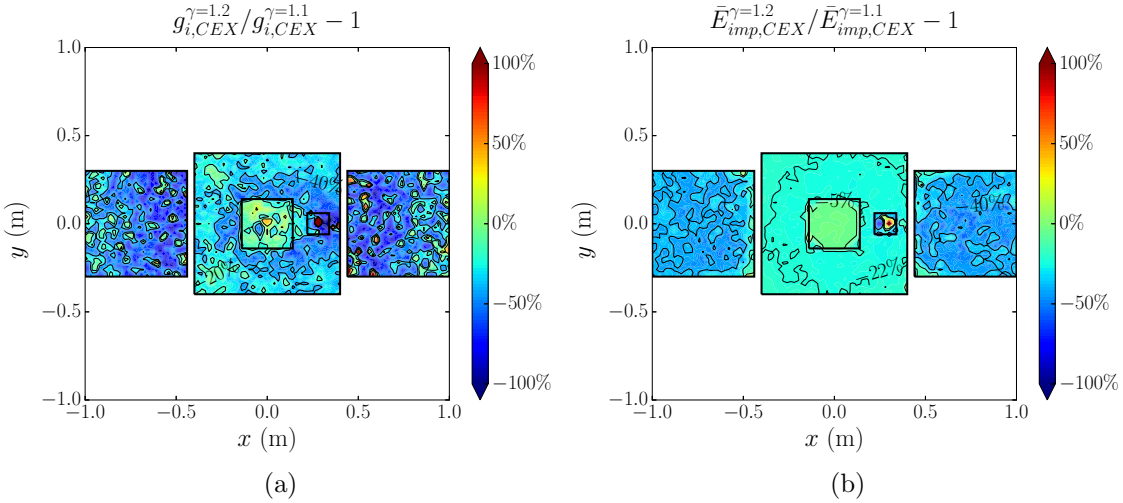

Figure 4.14: Comparison, at the S/C surfaces, of the $\gamma = 1.1$ and $\gamma = 1.2$ cases: (a) relative difference in the CEX ion backscattering flux $g_{i,CEX}^{\gamma=1.2}/g_{i,CEX}^{\gamma=1.1} - 1$, (b) relative difference in the wall-impact energy per ion $\bar{E}_{imp,CEX}^{\gamma=1.2}/\bar{E}_{imp,CEX}^{\gamma=1.1} - 1$.

As commented above, the ion flux is lower for the higher γ case (−20/40% on the

front S/C surface), because of the smaller electric fields. Regarding the wall-impact energy, on the other hand, this is lower in the $\gamma = 1.2$ case, mainly because of the higher floating potential of the S/C (-31 versus -38 V).

4.2.2. Effects of non-neutral plasma regions

As already explained in Sec. 3.3.3, EP2PLUS considers an automatic sub-division of the simulation domain into quasineutral and non-neutral regions. In this regard, Fig. 4.15 (a) and (b) show the square of ε_n (refer to Eq. 3.75), or equivalently the relative charge density (with respect to the quasineutral electron charge density), at respectively $y = 0$ and $x = 0$, indicating whether the material boundary faces are assumed to be quasineutral or non-neutral. The quasineutrality criterion for the inner plasma nodes ($\varepsilon_n < 0.032$ or a relative charge density lower than 1‰) is only met inside the thruster and neutralizer plumes, while the S/C boundaries are generally non-neutral, except for the quasineutral injection surfaces. As already commented in Sec. 4.1, a finer mesh would give the possibility of simulating the thin non-neutral region at the exit of the acceleration grid, however, a proper characterization would require a mesh adapting to the thruster grid holes (to simulate beamlets coalescence into a single beam profile), and this is beyond the objectives of this study.

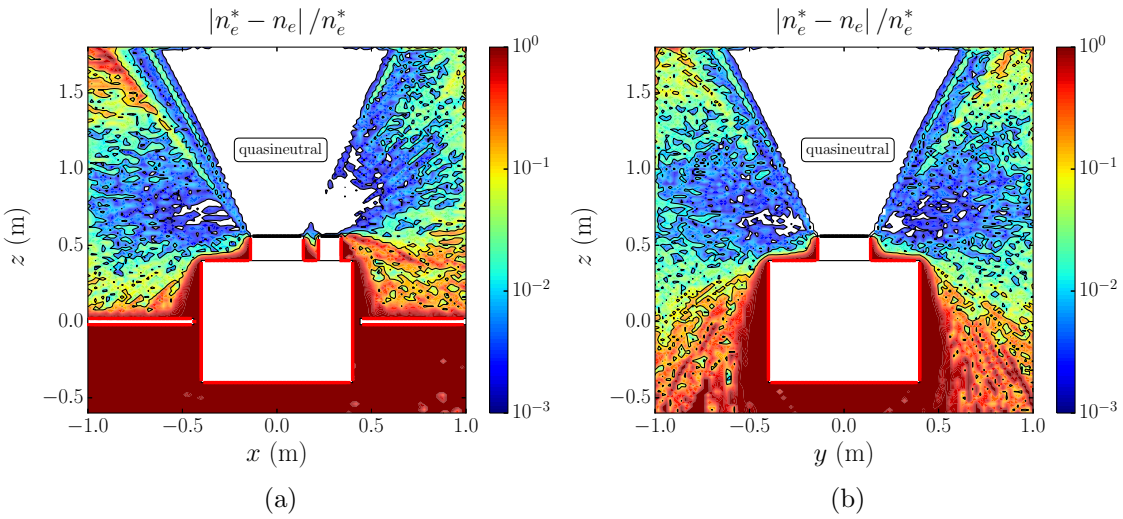

Figure 4.15: Reference case results: square of the non-neutrality ratio at (a) $y = 0$ and (b) $x = 0$. In both pictures, the non-neutral and quasineutral boundary cell-faces are highlighted respectively with a red and black line, respectively. The white areas correspond to quasineutral regions, in which $\varepsilon_n^2 < 10^{-3}$.

For what concerns the satellite floating potential, and the collected ion/electron current, let us refer to Fig. 4.12 (a) and (b). As mentioned in Sec. 4.1, the non-neutral solver is only activated at $t = 1$ ms. While the S/C potential is not affected significantly by this activation (variations of tenths of V are observed), the collected plasma current increases importantly, indicating that solving for a finite plasma sheath (with the correct boundary conditions) yields a larger attraction region for

the slow CEX ions. The relative increase in the collected plasma current is around 20% for all simulated γ cases.

The reference case electric potential and slow CEX ion density, obtained with a fully quasineutral simulation and with the non-neutral simulation considered above, both referring to the same final time $t = 2$ ms, are compared in Fig. 4.16 (a) and (b). Regarding the electric potential, the largest differences are concentrated close to the S/C surfaces, with the non-neutral solution featuring generally lower potentials (the potential at the S/C surface is up to 10 V more negative in the non-neutral case, due to the spatial resolution of the sheath). Regarding the CEX ion density, the differences downstream are mainly due to the statistical noise (CEX collisions are very rare downstream), while the non neutral solution generally shows larger densities close to the S/C surfaces (with the exception of the right side of the neutralizer).

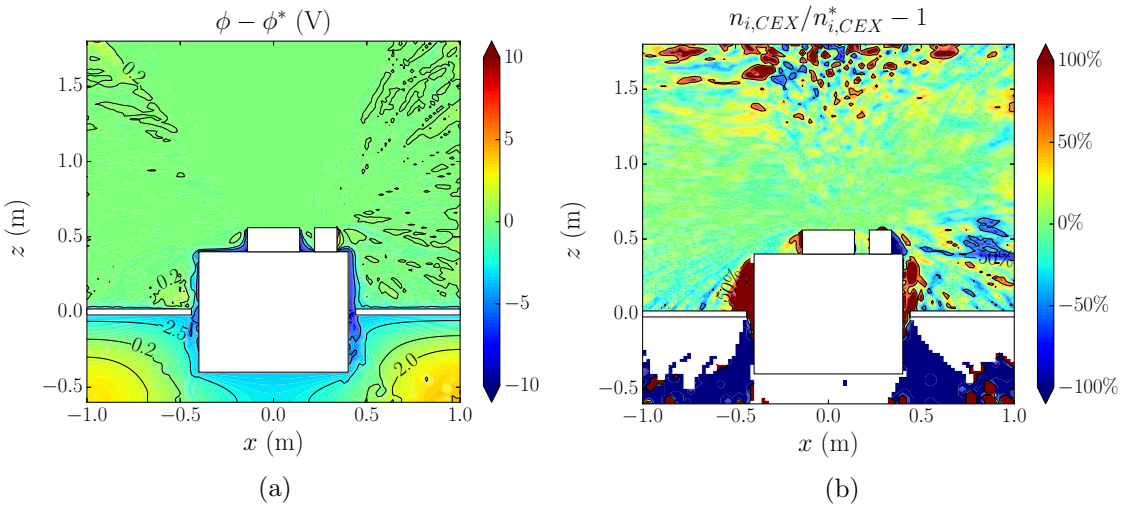

Figure 4.16: Reference case comparison, at $y = 0$, between non-neutral and quasineutral simulation results: (a) electric potential difference $\phi - \phi^*$, (b) relative difference in the CEX ion number density $n_{i,CEX}/n^*_{i,CEX} - 1$.

Fig. 4.17 (a) and (b) show the relative difference in the CEX ion flux and average impact energy, between the non-neutral and the quasineutral solutions. The ion flux increase (from quasineutral to non-neutral) at the S/C cubic body is around 20%, with peaks above 100%, with a similar behavior shown by the left solar array. The asymmetry introduced by the neutralizer makes the CEX flux change on the right solar array quite different, with a significant portion of it presenting a moderate decrease in the flux (−10/20%). The variation in the average impact energy, on the other hand, is much smaller, between 0 and 5%, since the S/C floating potential does not vary much when switching from the quasineutral to the non-neutral solution, as shown in Fig. 4.12 (a).

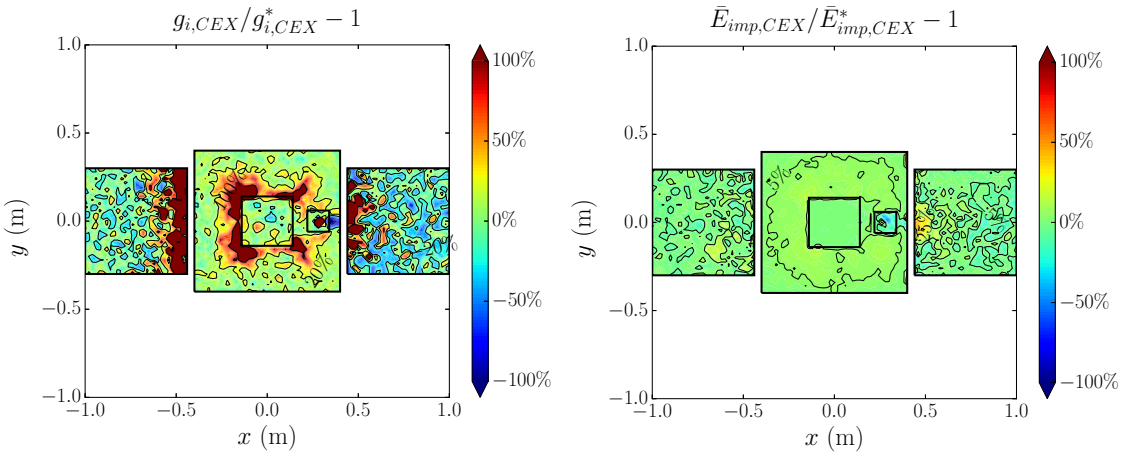

(a) (b)

Figure 4.17: Reference case comparison, at $y = 0$, between non-neutral and quasineutral simulation results: (a) relative difference in the CEX ion flux $g_{i,CEX}/g^*_{i,CEX} - 1$, (b) relative difference in the wall-impact energy per ion $\bar{E}_{imp,CEX}/\bar{E}^*_{imp,CEX} - 1$.

4.3 Conclusions

This study has permitted demonstrating the hybrid code capabilities as a whole, obtaining consistent results. In particular, the predicted CEX ion density appears to be definitely consistent with the available data in the literature, for the same thruster type. Moreover, the new electron model has permitted evaluating the electric current loop between the neutralizer and the ion thruster exit surface. An interesting result is that approximately half of the conical ion beam is neutralized by electrons that circle around the denser region of the plume, following a favorable conductivity path (partially due to the CEX ions) and avoiding the generation of extremely large electric currents in front of the thruster. Moreover, a virtually current free plume is achieved after $20 - 30$ cm from the thruster exit, thus validating our assumptions for the fluid model of the plasma plume far-region (Chapter 2).

The simulation has also highlighted that both the electron thermodynamics and the solution of non-neutral plasma regions have a non-negligible role in determining the backscattered CEX ion flux, the collected currents and the S/C floating potential.

Regarding the electron thermodynamics, the closer to isothermal are the electrons, the higher the backscattered CEX ion flux, the average wall-impact energy, and the lower (more negative) the spacecraft floating potential, as already suggested by the polytropic limit of the electric potential, identified in Chapter 2.

For what concerns the simulation of non-neutral plasma regions, the floating S/C potential is weakly affected, whereas a significant increase (up to 20%) in the backscattered CEX ion flux has been observed, when switching from a quasineutral solution to a non-neutral one, which takes into account the finite plasma sheaths that naturally appear around the S/C.

Regarding future work, the following features should be added to improve the simulation and its predictions:

- New heavy particles collisions, such as the momentum exchange collisions between ions and neutrals (MEX).
- Effects of new types of electron emission (photo-emission, ion bombardment emission, secondary electron emission, etc...) on the floating S/C potential.
- Study of the sputtering of affected S/C surfaces (especially the acceleration grid of the thruster).
- Effect of the ionosphere ambient plasma on the S/C floating potential (not treated here).

Chapter 5

Application to the ion beam shepherd scenario

This chapter presents two different studies, which focus on the ion beam shepherd mission scenario. The first is an optimization study of the whole electric propulsion subsystem of an IBS spacecraft, carried out with the use of the fluid model of Chapter 2 and a simplified plasma plume-target interaction model. The second is a detailed study of the spacecraft-plasma-target interaction, the so-called plasma bridge interaction, carried out with the EP2PLUS hybrid code of Chapter 3, with the goal of assessing quantitatively some of the most important operational issues affecting the performance of an IBS mission [1]

[1] The contents of this chapter are based on two journal publications [151, 121] and a conference paper [152]

5.1 Introduction and study goals

The space debris problem is gradually becoming a serious threat for the future exploitation of certain types of Earth orbits [153, 154, 155, 156], such as the sunsynchronous, polar or geostationary orbits. In the absence of active removal actions, the space debris density might reach a critical point, beyond which a cascade effect in the inter-objects collisions would cause an uncontrolled population growth, thus endangering the human space exploration for generations (Kessler's syndrome). In any case, the actual space debris population is already causing a non-negligible impact on operational mission costs, as more frequent collision avoidance maneouvres are becoming necessary. In order to tackle this serious issue, two remediation strategies can be followed: (I) mitigation and (II) active debris removal (ADR) or relocation.

Regarding mitigation, it is necessary to define common and international disposal strategies at the end of life of both commercial and scientific satellites. This represents an extra cost to be added to the mission budget (e.g. extra propellant to transfer the satellite from its operative orbit to a disposal orbit) and it ought to be common to all space competitors in the international scene. While being strictly necessary, this mitigation approach is not enough to prevent the debris population from growing indefinitely, as suggested by recent research [153, 155], according to which, even if all new launches respected the most recent legislation on spacecraft postmission disposal strategies (e.g. a final disposal to a 25-year decay orbit), at least 5 debris objects per year need to be actively de-orbited in order to prevent the debris number from growing, due to collisions and explosions in the already existing population. This can be clearly observed in Fig. 5.1, showing the predicted space debris population, under three different future scenarios.

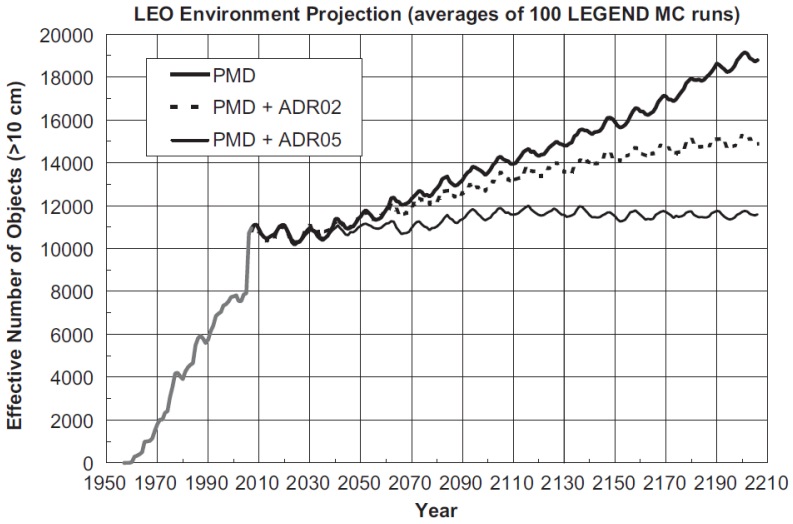

Figure 5.1: Predicted space debris objects population, under three different scenarios: simple post-mission disposal (PMD), post-mission disposal + 2 removed objects per year, post-mission disposal + 5 removed objects per year. Figure taken from Ref. [153].

For the above reasons, the international community interest in ADR techniques is

rapidly growing. The ion beam shepherd [42, 43, 44, 45] is one of such techniques, in which the space debris object is progressively relocated to a different orbit, through the slowly pushing action of a hypersonic plasma plume, generated by a plasma thruster onboard a shepherd spacecraft. Referring to Fig. 1.2, two thrusters are then required: an impulse transfer thruster (ITT), and an impulse compensation thruster (ICT), located on the other side of the spacecraft to maintain formation flying with the debris. This technique is contactless (a security distance is maintained from the debris), and uses electric propulsion, thus being very efficient from a propellant point of view. This makes the IBS particularly appealing, when compared with other ADR techniques that involve capturing physically the debris object and/or using chemical propulsion (e.g. the space tug), as it avoids a docking maneuver with an uncooperative body.

However, because of the thruster plume divergence, the operating distances are limited to a few times the debris size (with the current plasma propulsion technologies). The effective force transferred to the debris is thus only a fraction of the total ITT thrust, F_{ITT}, as shown in Eq. (5.1), with η_B representing the momentum transfer efficiency of the beam:

$$F_{TG} = \eta_B F_{ITT}. \tag{5.1}$$

Formation flying between the spacecraft and the debris then demands that the accelerations on both the IBS and the space debris be equal, meaning that the ICT thrust, F_{ICT}, is generally higher than that of the ITT [43], as dictated by the thrust ratio equation:

$$F_{ICT} = \left(1 + \eta_B \frac{m_{IBS}}{m_{TG}}\right) F_{ITT} > F_{ITT}, \tag{5.2}$$

where m_{IBS} and m_{TG} are respectively the IBS and target debris masses.

At system level, it is extremely important to identify the operational points of both thrusters (e.g. the operating voltage and the mass flow rate) that yield the lowest possible system mass, while complying with a vast set of constraints, ranging from overall power availability to size and cost of the required components. Such optimal points strongly depend on the distance between the IBS and the debris object, on the thruster types and characteristics, and on the mission specifications. The main goal of the study of Sec. 5.2 is to propose an approach for the optimization of the ITT thruster alone and of the overall electric propulsion subsystem (EPS), considering a realistic IBS mission scenario.

Sec. 5.3, on the other hand, focuses on specific technical issues of this technique. Although the IBS is a relatively simple concept, the evaluation of some operational issues requires an advanced study of the plasma plume interaction between the S/C and the debris object. In particular, the following phenomena appear to be particularly critical, especially for long duration IBS missions (i.e. aiming at relocating a large number of debris objects):

- The ion backscattering flow: charge-exchange collisions at the thruster exit produce a low energy ion population that is deflected back towards the satellite by the local electric fields. This ion backscattering can produce erosion

and/or contaminate sensitive spacecraft surfaces, such as the solar array or some optical sensors, required by the formation control GNC.

- The sputtered atoms backflow from the target debris: the hypersonic plume ions are energetic enough to knock out atoms of the space debris object towards the spacecraft. This clearly represents an additional source of contamination.
- Electric charging effects: apart from the clearly dominating effect of the emitted plume ions, which connect electrically the spacecraft and the debris object (plasma bridge), other sources of electric charging are the backscattered ions (from CEX), the photoemission due to the incident light on the objects, the secondary electron emission, the ion bombardment emission, and the ambient ions and electrons.

Sec. 5.3 then aims at evaluating quantitatively the above described phenomena with the hybrid code of Chapter 3, for the optimal mission scenario identified in Sec. 5.2. Moreover, the force and torque transmission to the target debris is evaluated precisely and compared with the results obtained using a Self-Similar fluid model, like those of Chapter 2.

5.2 Optimization of the electric propulsion subsystem

This section is based on the journal publication of Ref. [151], and is organized as follows. The mission specifications and the IBS power constraints and assumptions are described in Sec. 5.2.1. The ITT and ICT performance models are introduced in Sec. 5.2.2. Then, the simplified models for the plasma plume expansion and interaction with the space debris are presented in Sec. 5.2.3. The independent optimization of the ITT is described and discussed in Sec. 5.2.4. Sec. 5.2.5 then presents the results of the overall propulsion subsystem optimization, including both the ITT and ICT. Finally, the conclusions of the study are reported in Sec. 5.2.6.

5.2.1. Mission specifications and propulsion subsystem constraints

An IBS mission generally consists of two phases: a rendezvous phase with the target debris object, out of the scope of this study, and a shepherding phase, in which the orbit change is carried out with the use of electric propulsion. The specifications of a realistic de-orbiting IBS mission are summarized in Tab. 5.1.

Table 5.1: De-orbiting mission specifications and assumptions

Mission requirements and assumptions	**Values**	**Units**
IBS spacecraft mass, m_{IBS}	500	kg
Target debris mass, m_{TG}	$\simeq 1.5$	tons
Target debris characteristic diameter	2.5	m
Orbit altitude change	300	km
Orbit altitude change per day	~ 2	km/day
Daylight fraction in orbit, f_l	67	%
Shepherding phase duration, Δt_{IBS}	170	days
Achieved target delta-V	0.190	km/s
Required force on the debris, F_{TG}	30	mN
Operational distance, d, between ITT and target debris	≥ 7	m

A de-orbiting manoeuvre of approximately 300 km in 170 days, or equivalently a de-orbit rate of approx. 2 km/day, has been considered as the baseline mission goal. The debris object weighs 1.5 metric tons and currently orbits in a nearly-polar low Earth orbit. Considering an average 67% orbit daylight fraction (thrusters cannot operate on battery power alone, due to a S/C design choice), the above defined specifications on the debris mass and orbit decay rate are equivalent to constraining the transmitted force to the debris, F_{TG}, to 30 mN. Moreover, the operational distance between the ITT exhaust plane and the debris object must not be lower than 7 m. This threshold corresponds to the half span of the S/C solar array and has been chosen due to collision safety considerations in case of a failure of the relative attitude control. Finally, the IBS wet mass, m_{IBS}, is expected to be around 500 kg.

The electric propulsion subsystem, which is in charge of transmitting the required force to the target, must comply with stringent power constraints at platform level. Referring to Tab. 5.2, the total input power to the power processing units (PPUs) of the EPS is limited to 3 kW. This means that, assuming a PPU energy conversion efficiency of 85% (a conservative value), this power limit corresponds to 2.6 kW at thruster level. Finally, regarding the power generation subsystem, a value of 13.3 kg/kW has been considered for the specific mass of the dedicated solar arrays. This value is representative of the current available technology.

Table 5.2: IBS power constraints and assumptions

EPS constraints and assumptions	**Values**	**Units**
Input power to the EPS PPUs	≤ 3	kW
PPUs efficiency, η_{PPU}	85	%
Input power to both thrusters	≤ 2.6	kW
Specific mass of the power generation subsystem, ρ_{pwr}	13.3	kg/kW

5.2.2. Characterization of the ITT and ICT

In this study, both the ITT and the ICT are assumed to be radio-frequency ion thrusters (RIT). This is a particular type of gridded ion thruster, in which the ionization process is achieved through the inductively-coupled RF antenna, wrapped around the thruster chamber, as shown in Fig. 5.2. The generated ions are accelerated through a grid system to a kinetic energy given by $q_i \Delta\phi_B$, with q_i representing the ion charge and $\Delta\phi_B$ the effective acceleration beam voltage. As shown in Fig. 5.2, this beam voltage is the effect of various contributions: the plasma voltage drop within the chamber (a few tens of volts), $\Delta\phi_{chamber}$, the voltage drop between screen and acceleration grids (several kilovolts) and a final voltage increment, $\Delta\phi_{neut}$, that brings the potential to a value slightly higher than the potential of the neutralizing hollow cathode common [1] (a few tens of volts) and that is necessary to attract the neutralizing electrons. Since the hollow cathode is grounded, the effective beam acceleration voltage is well approximated by the screen grid potential:

$$\Delta\phi_B = \Delta\phi_{chamber} + (\phi_{screen} - \phi_{acc}) - \Delta\phi_{neut} \simeq \phi_{screen}. \tag{5.3}$$

For this optimization study, a thruster performance model is needed to explore the behavior of various thruster figures of merit as a function of some design parameters. The details and the justification of such a performance model can be found in Ref. [157]. Hereafter, only a summary of the main characteristics of the model is provided. Referring to Fig. 5.3, the required input variables (or design parameters) are the beam voltage, $\Delta\phi_B$, and the thrust force, F. The model then provides as output the thruster plume divergence angle, α_0, the necessary beam current, I_B, the thruster radius, R_{thr}, the mass utilization efficiency, η_m, and the RF input power, P_{RF}, necessary to sustain the discharge. These performance figures follow

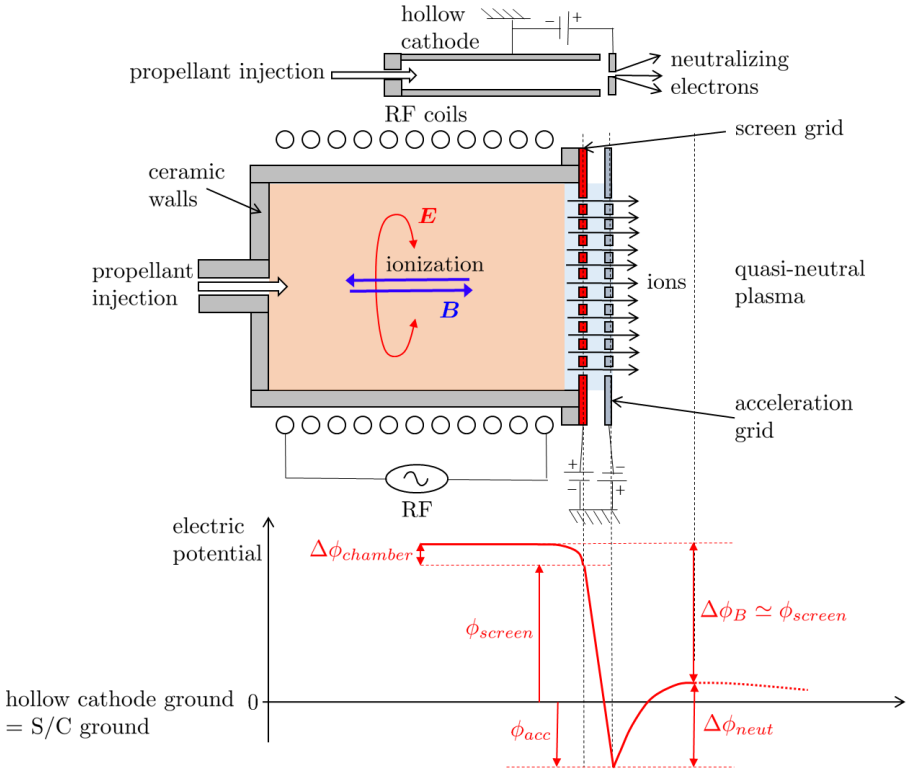

Figure 5.2: Generic working principle of a RIT thruster and electric potential evolution across the thruster symmetry axis. Voltage drops and lengths are not to scale.

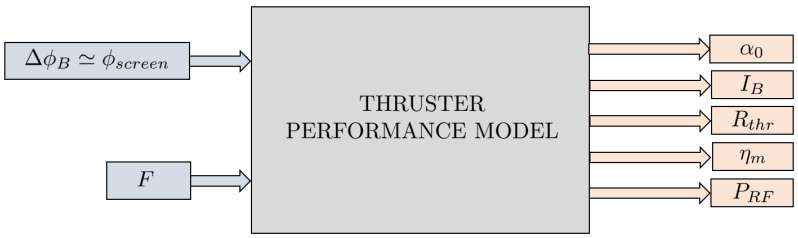

Figure 5.3: Block diagram of the performance model used for both the ITT and the ICT.

the dependencies shown in Eqs. (5.4) to (5.8):

$$\alpha_0 \propto \Delta\phi_B^{-\beta_1}, \tag{5.4}$$

$$I_B \propto F\Delta\phi_B^{-1/2}, \tag{5.5}$$

$$R_{thr} \propto I_B^{1/2}, \tag{5.6}$$

$$\eta_m \propto \ln(R_{thr}), \tag{5.7}$$

$$P_{RF} \propto R_{thr}^{\beta_2}. \tag{5.8}$$

First of all, the thruster divergence angle, α_0, is modeled as a decreasing power law of the beam voltage, with a coefficient $\beta_1 > 1$, as shown in Eq. (5.4). The beam current is then proportional to the ratio between the thrust and the ion exhaust velocity

(which scales as $\Delta\phi_B^{1/2}$), as shown in Eq. (5.5). Since the required ion extraction area is proportional to the beam current and grows with the square of the thruster radius, R_{thr} is proportional to the square root of I_B, as dictated by Eq. (5.6). The mass utilization efficiency, η_m, increases logarithmically with the thruster radius according to Eq. (5.7), as a larger thruster requires a lower neutral gas pressure to sustain the RF discharge and hence features a lower neutral outflow fraction. The required RF input power is also modeled as a function of the thruster radius, and more precisely as a power law with coefficient $\beta_2 > 1$, so that a larger thruster requires a higher RF input power, as shown in Eq. (5.8).

With the performance figures computed above, it is then straightforward to obtain the beam power, P_B, and hence the total thruster input power, $P = P_B + P_{RF}$, the mass flow rate, $\dot{m}$, the specific impulse, I_{sp}, and the total thrust efficiency, η_T, following their classical definitions, provided in Eqs. (5.9) to (5.13).

$$P_B = I_B \Delta\phi_B, \tag{5.9}$$

$$P = P_{RF} + P_B, \tag{5.10}$$

$$\dot{m} = \frac{m_i}{q_i}\frac{I_B}{\eta_m}, \tag{5.11}$$

$$I_{sp} = \frac{F}{\dot{m} g_0}, \tag{5.12}$$

$$\eta_T = \frac{F I_{sp}}{2P}. \tag{5.13}$$

The models for the ITT and for the ICT only differ in terms of the proportionality constants and power law coefficients in Eqs. (5.4) to (5.8), as discussed in Ref. [157].

5.2.3. Momentum transfer efficiency

5.2.3.1. Simplified plume expansion and debris interaction models

A detailed description of the physical phenomena taking place in a plasma plume expansion has already been provided in Sec. 1.3. Fig. 5.4 shows the near and far-region of a plasma plume, in the context of an ion beam shepherd mission, and includes a spherical target debris. Please also observe that the far region divergence angle, introduced in Sec. 2.5.2, is particularized to the distance of the target debris center of mass. As done in Chapter 2, we begin by defining a reference frame based on an initial plane located within the far region, at a distance d_0 from the thruster exit. The plume is then modeled here with the Parks-Katz initial profiles, given by Eq. (2.34) and shown in Fig. 2.5. This means that it features a Gaussian density profile, a constant axial velocity and a linearly increasing radial velocity. As considered in Chapter 2, the streamtube containing 95% of the ion current has a radius R_0 and a half-cone angle given by the thruster divergence angle, α_0, as shown in Fig. 5.4.

Given the impossibility to obtain experimental near region data at this design stage, we shall further assume that our far region starts at the exit plane of the

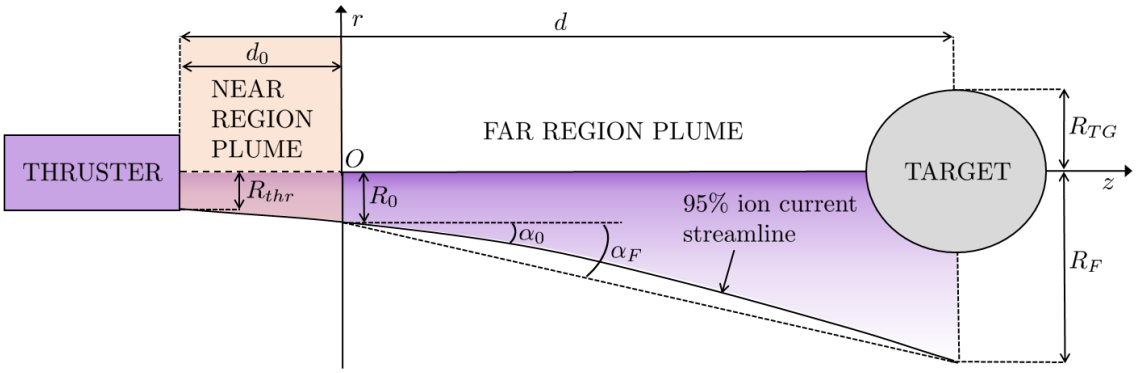

Figure 5.4: Sketch of the plasma plume near and far regions, the plasma streamtube containing 95% of the ion current, and the target debris.

thruster (i.e. we take $d_0 = 0$), where the ITT performance model provides the corresponding plume divergence angle, α_0. To cover for the potential divergence increase in the near-region, a +10% margin on this initial divergence angle (or thruster divergence angle) is included in the following analyses.

The SSM method then allows to compute the plasma density and velocity through a self-similar expansion function h, which obeys Eq. (5.14) and can be obtained through numerical integration with the initial condition $h(0) = 1$. In this differential equation, $\tilde{z} = z/R_0$ is the normalized axial coordinate and M_0 is the initial ion Mach number, whose square represents the ratio between the ion kinetic energy and the electron thermal energy, and is shown in Eq. (5.15) as a function of the beam voltage, where m_i and q_i are the ion mass and charge (we assume here singly charged xenon ions) and T_{e0} is the electron temperature at the origin O of the reference frame of Fig. 5.4, expressed in energy units (equal to the product of the Boltzmann's constant and the classical temperature):

$$\frac{dh}{d\tilde{z}} = \sqrt{\tan^2\alpha_0 + 12\frac{\ln h}{M_0^2}} \quad ; \quad h(0) = 1, \tag{5.14}$$

$$M_0 = \sqrt{\frac{m_i u_{i0}^2}{T_{e0}}} = \sqrt{\frac{2q_i\Delta\phi_B}{T_{e0}}}. \tag{5.15}$$

The 95% ion current streamtube radius, $R(z)$, the axial and radial plume velocity, $u_z(r,z)$ and $u_r(r,z)$, and the plume density, $n(r,z)$, are finally obtained with Eqs. (5.16) to (5.19). Here n_0 and u_{i0} represent the plasma density and ion velocity

at the origin O:

$$R(z) = R_0 h(\tilde{z}), \tag{5.16}$$

$$u_z(r,z) = u_{i0}, \tag{5.17}$$

$$u_r(r,z) = u_{i0}\frac{dh}{d\tilde{z}}(\tilde{z})\frac{r}{R(z)}, \tag{5.18}$$

$$n(r,z) = \frac{n_0}{h^2(\tilde{z})}\exp\left(-3\frac{r^2}{R^2(z)}\right). \tag{5.19}$$

It is worth mentioning that the self-similar solution of Eq. (5.14) and Eqs. (5.16) to (5.19) is valid only for isothermal electrons. Other thermodynamic models for the electrons can be easily employed, such as polytropic electrons. However, as shown in Sec. 2.5.2, the isothermal limit is conservative, in the sense that it causes the largest increase of plume divergence and hence, in the context of an IBS mission, the lowest momentum transfer efficiency [49, 50]. The electron temperature appearing in Eq. (5.14) (through M_0) assumes values around $2-3$ eV [58, 92] in Hall Effect thrusters and between 1 and 3 eV in ion thrusters [11]. Therefore, we have assumed the conservative value of $T_{e0} = 3$ eV, as shown in Tab. 5.3. In fact, the higher the electron temperature and their thermal energy, the higher the increase of divergence in the plume. On the contrary, if we progressively decrease the electron temperature to 0, we get the limit of $M_0 \to \infty$, for which the self similar function can be easily solved as $h(\tilde{z}) = 1 + \tilde{z}\tan\alpha_0$, corresponding to a perfectly conical plume expansion.

With the plume solution of Eq. (5.14) and Eqs. (5.16) to (5.19), and following the approach of Ref. [43], a simplified formula for the fraction of plume momentum intercepted by the debris can be obtained. Firstly, to simplify the analysis, the debris is modeled as an equivalent sphere of radius $R_{TG} = 1.25$ m (half of the characteristic diameter of the target debris, given in Tab. 5.1) and its center is located at a distance d from the thruster exit plane. At this distance, assumed equal to 7 m (the minimum operational distance of Tab. 5.1), the radius of the plasma tube carrying 95% of the ion current is R_F, which allows us to define an equivalent conical divergence angle at the debris, α_F, as:

$$\alpha_F = \arctan\left(\frac{R_F - R_0}{d}\right) > \alpha_0. \tag{5.20}$$

Note that α_F is *not* the local slope angle of the 95% ion current streamline, as clearly shown in Fig. 5.4. Integrating the plasma momentum over the surface of the sphere, we can finally compute the momentum transfer efficiency as:

$$\eta_B = 1 - \exp\left(-\frac{3R_{TG}^2}{R_F^2 - \left(\tan\alpha_F R_{TG}\right)^2}\right). \tag{5.21}$$

Please note that a generalization of the force transmission to a generic target shape (and hence not a spherical target) has been considered in a related study [158].

The assumptions described so far for the characterization of the momentum transfer efficiency are finally summarized in Tab. 5.3.

Table 5.3: Parameters affecting the plume expansion and target interaction

Plume and debris interaction parameters	**Values**	**Units**
Electron temperature, T_{e0}, at the origin O	3.0	eV
Equivalent spherical radius, R_{TG}, of the debris	1.25	m
Near region axial length, d_0	0.0	m
Distance between thruster exit and debris centre, d	7.0	m
Margin on α_0 to account for near region effects	10.0	%
Ion mass m_i (xenon)	$2.18 \cdot 10^{-25}$	kg
Ion charge, q_i	$1.6 \cdot 10^{-19}$	C

5.2.3.2. Equivalent conical divergence angle at the debris and momentum transfer efficiency

In this section, the effect of the ITT beam voltage on α_F and η_B is assessed and discussed. With the use of the plume model described in Sec. 5.2.3, and with the parameters of Tab. 5.3, we can obtain a 2-D map of the equivalent conical divergence angle and of the momentum transfer efficiency as a function of $\Delta\phi_B$ and α_0 for 2 different values of R_0 (7 and 25 cm), whose range should include the design radius of the ITT thruster.

Referring to Fig. 5.5 (a), as the beam voltage, $\Delta\phi_B$, or the initial divergence angle, α_0, increase, the difference between the near and equivalent conical divergence angles becomes smaller. Asymptotically, α_F tends to α_0 for both increasing beam voltage and near region divergence angle. Regarding the initial plume radius effect, the higher plume radius yields a lower equivalent divergence angle at the debris, because the radial electron pressure gradients at the initial plume plane are lower, thus yielding a lower divergence increase.

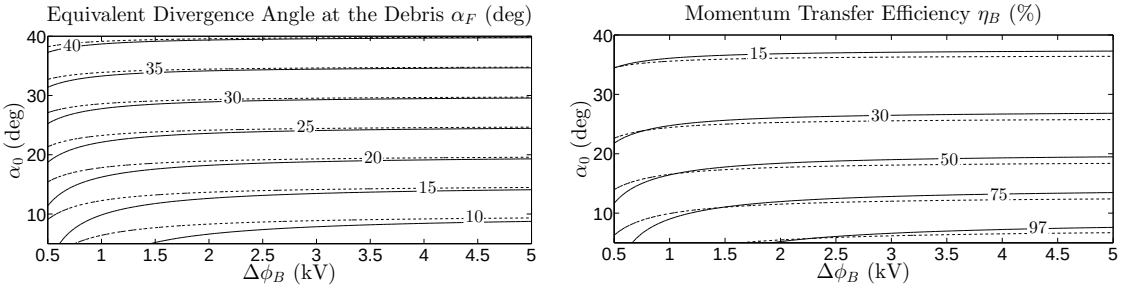

(a) (b)

Figure 5.5: Representations of (a) equivalent conical divergence angle and (b) momentum transfer efficiency, for $R_0 = 7$ cm (solid line) and 25 cm (dashed line).

Fig. 5.5 (b) shows the corresponding dependence of the momentum transfer efficiency on $\Delta\phi_B$ and α_0 for the two initial radius cases. The momentum transfer efficiency increases substantially for decreasing divergence angles, and, for a given α_0, it shows a weak dependence on the beam voltage, except at very low voltage and small initial divergence angle. The effect of the initial plume radius, on the other

hand, is twofold. At a sufficiently high beam voltage or divergence angle, when the electron pressure effects are negligible, a higher initial plume radius R_0 yields automatically a higher radius R_F at the target debris, and hence a lower momentum transfer efficiency (through Eq. (5.21)). At small initial divergence angles and beam voltages, on the other hand, the increase in divergence angle plays a more important role than the initial plume radius, so that a lower initial radius also yields a lower momentum transfer efficiency.

In our ITT performance model, the near region divergence angle, α_0, is a direct function of the beam voltage, as given by Eq. (5.4), so that the momentum transfer efficiency (and the equivalent conical divergence angle at the debris) is indeed a function of $\Delta\phi_B$ and R_0.

In order to evaluate the real effect of the initial plume radius R_0 on the momentum transfer efficiency for our ITT, η_B has been evaluated again for the two different initial radius cases (7 and 25 cm). The use of the thruster performance model of Sec. 5.2.2 has been limited to Eq. (5.4) to model the dependence of the initial divergence angle on $\Delta\phi_B$ (Eq. (5.6) has not been considered here). The momentum transfer efficiency evolution with $\Delta\phi_B$ is shown in Fig. 5.6. At low beam voltages (below 2.5 kV), the momentum transfer efficiency increases almost linearly with $\Delta\phi_B$, while at higher voltages (above 2.5 kV) the increase becomes weaker, saturating at almost 100% for voltages above 4.5 kV.

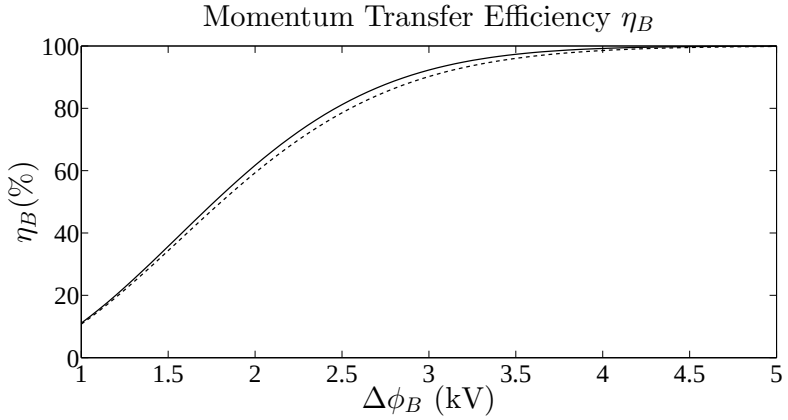

Figure 5.6: Momentum transfer efficiency versus $\Delta\phi_B$, for $R_0 = 7$ cm (solid line) and 25 cm (dashed line).

Although the differences between the two R_0 cases are small (always lower than 5%), the worst case scenario is clearly represented by the higher initial radius case (25 cm). The 25 cm case has then been considered to model conservatively the dependence of η_B on $\Delta\phi_B$ in the optimization study described in the following sections.

Before proceeding with it, however, it is worth to further discuss the plume expansion effects on the momentum transfer efficiency. Referring to Fig. 5.5 (a), it is apparent that the more hypersonic (the higher M_0 or $\Delta\phi_B$) and the more divergent (the higher α_0) the plume is, the closer to conical its expansion. This conical-like

expansion is the major source of momentum transfer efficiency loss, as shown in Fig. 5.5 (b), where the iso-η_B lines are almost horizontal and show a weak dependence on the beam voltage. Under a purely "geometrical" expansion, the plume density decreases with the square of its streamline radius, which is proportional to both the operational distance and $\tan(\alpha_0)$. Therefore, it is paramount to minimize α_0, which generally requires operating at a high beam voltage (Fig. 5.6).

Secondly, even if the initial divergence angle is small, the residual electron pressure makes the plume expand further, meaning that the slope of the ion streamlines increases away from the thruster [49, 50]. This effect is small in our case, except at very low $\Delta\phi_B$ and α_0 (where the iso-α_F and iso-η_B lines of Fig. 5.5 (a) and (b) deviate from horizontal lines), and can always be mitigated by increasing the operating Mach number, M_0, provided by Eq. (5.15). For a fixed propellant atom mass, this can be achieved by either increasing the beam voltage, $\Delta\phi_B$, or reducing the residual electron temperature, T_{e0}, in the plume.

5.2.4. Optimization of the ITT

Before proceeding with the optimization of the overall EPS, it is useful to firstly optimize the ITT independently. This means to identify the operating beam voltage of the ITT that maximizes some specific figure of merit. As explained in Ref. [157], a key figure of merit for the ITT is the ratio between transmitted force to the debris and input power to the thruster. Referring to Fig. 5.6, if we operate at a constant ITT thrust, the transferred thrust to the debris grows linearly with $\Delta\phi_B$ at low beam voltages (Fig. 5.6), while the required input power grows with $\Delta\phi_B^{1/2}$ (Eqs. (5.9) and (5.5) with F constant). The transferred thrust to power ratio thus increases with $\Delta\phi_B$ until the momentum transfer efficiency begins to saturate and its increase is equal to the increase in input power. The voltage corresponding to this maximum transferred thrust to power ratio represents the optimal ITT operational condition.

A method to maximize the above defined figure of merit is described hereafter. By fixing the transmitted force on the target to the required 30 mN value (see Tab. 5.1), we shall look for the operational voltage that minimizes the required ITT input power. First, we compute the required ITT thrust as a function of $\Delta\phi_B$, with the conservative curve of Fig. 5.6 to express the momentum transfer efficiency:

$$F_{ITT}(\Delta\phi_B) = \frac{30 \text{ mN}}{\eta_B(\Delta\phi_B)}. \tag{5.22}$$

Then, once $\Delta\phi_B$ and F_{ITT} are fixed, with the use of the performance model of Sec. 5.2.2, all the thruster performance figures can be obtained, including the input thruster power, P_{ITT}. This power is finally plotted in Fig. 5.7 as a function of $\Delta\phi_B$. As expected, a minimum operating power is found at a $\Delta\phi_B = 3.3$ kV (black dot in the figure), with a corresponding thrust force of 31.9 mN and a momentum transfer efficiency of 94.1%.

The choice of the design voltage of the ITT, however, cannot be determined solely by the maximization of the transferred force to power ratio. A key figure of merit of

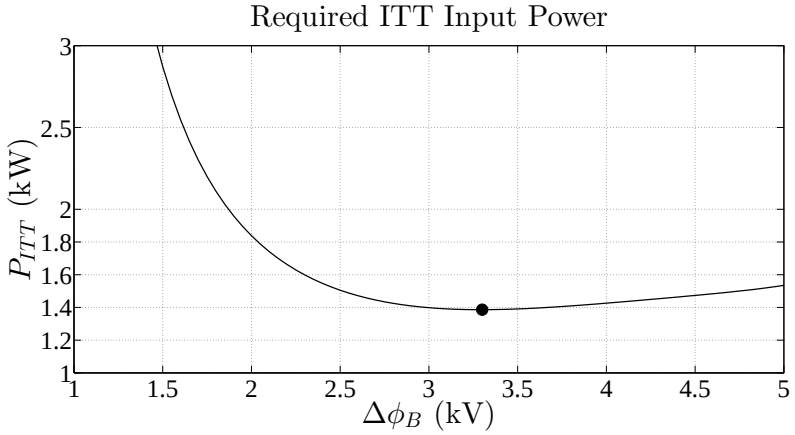

Figure 5.7: ITT input power required to transfer a force of 30 mN to the debris.

the ITT is, in fact, the mass utilization efficiency, η_m, which should be high. In fact, a low η_m can cause a high number of charge-exchange collisions between ions and neutral atoms in the near region, and hence a large ion backflow towards sensitive S/C surfaces, which could potentially endanger the mission, or increase the initial plume divergence, α_0, beyond the values assumed here. These effects are further investigated in Sec. 5.3.

At the optimal ITT point discussed above, the mass utilization efficiency turns out to be 72.2% (according to the ITT performance model). Although it is out of the scope of this paper to assess the effects of such efficiency, it is a key aspect to model when designing a real mission.

Finally, in order to get an idea of how an already existing technology would perform as ITT, we have chosen the NASA Solar Technology Application Readiness (NSTAR) thruster [11, 159, 160] as a representative candidate. At its throttle level N.9 (out of 15), this thruster features a total input power of 1.57 kW, a beam voltage of 1.1 kV, a thrust force of 62.5 mN, and a 95% ion current divergence angle of 28.5 deg.

Assuming an initial plume radius of 15 cm (equal to the NSTAR thruster radius), and a 10% margin on the initial divergence angle, the NSTAR would feature a momentum transfer efficiency equal to 20.1%, with a transmitted force on the target equal to 12.5 mN. This means that, at a power level close to the minimum of Fig. 5.7, the NSTAR thruster would achieve the mission in approximately 400 days (versus the 170 days requirement). This illustrates clearly the central importance of a low plume divergence to increase the IBS efficiency and reduce the debris removal time.

5.2.5. Optimization of the electric propulsion subsystem

5.2.5.1. Major assumptions

The optimization described in Sec. 5.2.4 provides very valuable inputs for the choice of the operational point of the ITT alone. Nevertheless, from an overall

subsystem perspective, what needs to be minimized are the input power to the two thrusters, $P^\star$, and the fraction of the EPS dedicated mass that can be optimized, $m^\star$. In this section, we shall describe the approach we have followed to define the optimal operational points (or beam voltages) of the two thrusters that minimize $P^\star$ and $m^\star$.

The total thruster input power to be optimized, $P^\star$, is simply given by:

$$P^\star = P_{ITT} + P_{ICT}, \tag{5.23}$$

while the definition of $m^\star$ is less straightforward. The total EPS dedicated mass can be split into several contributions: the two thrusters mass, $m_{ITT} + m_{ICT}$, the total dedicated power generation subsystem mass, m_{pwr} (solar arrays fraction dedicated to the generation of the PPUs input power), the total propellant mass, m_{prop}, and the power processing units mass, m_{PPU}. In this study, however, we have considered for $m^\star$ only a part of the above defined EPS dedicated mass, as shown in Eq. (5.24):

$$m^\star = m_{pwr} + m_{prop}. \tag{5.24}$$

In fact, the mass contributions of the thrusters and of the PPUs have not been included, as their variations with the operational beam voltage are expected to be quite small. The former (thruster units masses) would slightly depend on the operating conditions, as a higher voltage yields a lower mass flow rate and hence a smaller and lighter thruster [157]. However, a thruster unit weighs only a few kg (at these power levels) and hence, its mass variation can be neglected with respect to the major mass contributions: m_{pwr} and m_{prop}. Regarding the PPUs, on the other hand, their mass can hardly be modelled as a linear function of $\Delta\phi_B$ and their mass variation is expected to be small (in the considered range of beam voltages). The remaining mass contributions are modeled as given by Eqs. (5.25) and (5.26):

$$m_{prop} = f_l \Delta t_{IBS} \left(\dot{m}_{ITT} + \dot{m}_{ICT} \right), \tag{5.25}$$

$$m_{pwr} = \frac{\rho_{pwr} P^\star}{\eta_{PPU}}, \tag{5.26}$$

where f_l and Δt_{IBS} are respectively the orbital period fraction in daylight conditions and the shepherding phase duration, $\dot{m}_{ITT}$ and $\dot{m}_{ICT}$ are the mass flow rates of the ITT and ICT, and ρ_{pwr}, η_{PPU} are respectively the solar array specific mass and the PPUs energy conversion efficiency.

The values of all the parameters required by the EPS optimization study are listed in Tabs. 5.1 and 5.2.

5.2.5.2. Overall optimization method

The electric propulsion subsystem optimization consists of studying the evolution of figures of merit such as the total thruster input power, $P^\star$, the optimizable EPS mass, $m^\star$, the total required propellant mass, m_{prop}, and the equivalent shepherding delta-V, ΔV_{eq}, as 2-D functions of $\Delta\phi_{B,ITT}$ and $\Delta\phi_{B,ICT}$. For any ITT beam voltage, $\Delta\phi_{B,ITT}$, the following applies:

1. The ITT thruster parameters are computed following the approach of Sec. 5.2.4 with the model of Ref. [157] (described in Sec. 5.2.2).

2. Given the ITT thrust, F_{ITT}, the required ICT thrust is obtained through Eq. (5.2).

3. For a varying ICT beam voltage in a range between 0.5 and 5 kV, the following parameters are computed:

   a) The ICT thruster performance figures, with the model of Ref. [157] (described in Sec. 5.2.2); b) the overall (ITT+ICT) thruster input power, $P^\star = P_{ICT} + P_{ITT}$; c) the overall required propellant mass, m_{prop}, using Eq. (5.25); d) the overall power subsystem dedicated mass, m_{pwr}, using Eq. (5.26); e) the equivalent shepherding phase delta-V, ΔV_{eq}. An equivalent propulsion subsystem specific impulse is first obtained as follows:

$$I_{sp,eq} = \frac{\dot{m}_{ITT} I_{sp,ITT} + \dot{m}_{ICT} I_{sp,ICT}}{\dot{m}_{ITT} + \dot{m}_{ICT}}, \tag{5.27}$$

   where $I_{sp,ITT}$ and $I_{sp,ICT}$ are respectively the ITT and ICT specific impulses. Then, through Tsiolkovsky's equation, ΔV_{eq} is computed as:

$$\Delta V_{eq} = I_{sp,eq} g_0 \ln\left(\frac{m_{IBS}}{m_{IBS} - m_{prop}}\right), \tag{5.28}$$

   where g_0 is the standard gravity acceleration constant.

5.2.5.3. Overall optimization results

Following the procedure described in the previous paragraph, the 2-D contours of Fig. 5.8 have been obtained. Fig. 5.8 (a) shows the total thruster input power, $P^\star$. For a given ITT voltage, the total power presents a minimum at an ICT voltage of approx. 1000 V. Then, it starts to increase again because, for a given ICT thrust, the required ICT power grows with the ICT specific impulse (or beam voltage). The lowest total power is 2.54 kW, achieved at the ITT-ICT voltages point (3.58, 1.01) kV. At this point, $F_{ITT} = 31.1$ mN and $F_{ICT} = 40.6$ mN. It is important to underline that small changes in the ITT voltage around this optimal point produce no significant variation in the total thruster power.

Fig. 5.8 (b) shows the optimizable EPS dedicated mass, $m^\star$. The optimal point now shifts to higher voltages for both the ITT and the ICT with respect to that of Fig. 5.8 (a), because the total propellant mass decreases for increasing voltages. The optimal voltages (corresponding to a total mass of 56.6 kg) are (4.01,1.56) kV. At this point, $F_{ITT} = 30.5$ mN and $F_{ICT} = 40.1$ mN. Observe that, for a wide region around the optimal point, variations in both the ITT and ICT voltage produce no significant changes in $m^\star$. Moreover, the total mass savings that an optimized design yields are quite small ($10 - 15$ kg), when compared to the total expected IBS mass (500 kg).

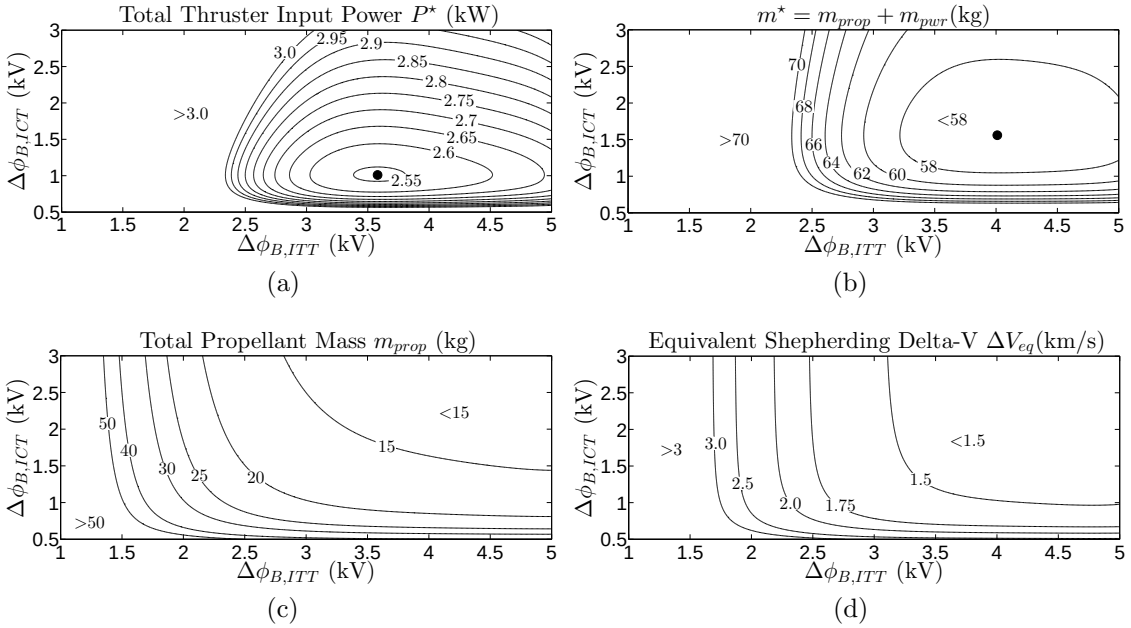

Figure 5.8: Representations of (a) total thrusters input power, (b) optimizable EPS dedicated mass, (c) total propellant mass, and (d) equivalent shepherding delta-V.

Fig. 5.8 (c) shows the total propellant mass of the shepherding phase as a function of both the ITT and the ICT beam voltages. Clearly, the higher these voltages, the lower the overall propellant mass. However, the propellant mass savings of an optimized design are, again, quite small. For example, at $\Delta\phi_B = 3.5$ kV, increasing the ICT voltage from 1 to 2 kV only yields a mass saving of 5 kg.

Finally, Fig. 5.8 (d) shows the equivalent shepherding delta-V, ΔV_{eq}. As expected, for an ICT voltage above $1 - 1.5$ kV, the delta-V depends essentially on the momentum transfer efficiency and hence on the ITT voltage alone: the higher the ITT voltage, the lower the ΔV_{eq}. At low ICT voltages however, the divergence losses of the ICT become important and this means that the ICT mass flow necessary to achieve the required thrust increases as the voltage decreases. For this reason, the equivalent shepherding delta-V increases substantially as the ICT voltage becomes smaller. It is also pointed out that ΔV_{eq} does not represent the inertial velocity change of either the target or the IBS (shown in Tab. 5.1), but rather the propulsion delta-V of a thruster, which is equivalent (in terms of mass consumption) to the ITT-ICT system.

The main conclusion that can be extracted from the presented results is that the optimal points for the ICT and ITT beam voltage are very different. The need to guarantee a sufficiently high momentum transfer efficiency drives the optimal ITT voltage to higher values. For the ICT, on the other hand, as long as the thruster efficiency is not strongly affected, a lower voltage allows to keep the required power low, at the expense of a higher propellant consumption. This results into an ICT optimal beam voltage, which is generally quite lower than that of the ITT.

The optimal design choice may be either based on the total dedicated mass or on

the total thruster power, depending on the specific mission constraints. For example, for missions featuring a well defined limit for the total platform power, minimization of the total thruster power should be pursued (Fig. 5.8 (a)). For other missions not featuring such a stringent constraint, the total dedicated mass would represent a more adequate figure of merit for the overall electric propulsion subsystem (Fig. 5.8 (b)). Nonetheless, as seen in this analysis for a single de-orbiting mission, $m^\star$ is quite small with respect to the total IBS wet mass (10%), and therefore the dedicated mass optimization has only a small impact on the total mass budget.

5.2.6. Conclusions

This section has presented a dedicated study of the optimization of the electric propulsion subsystem of an ion beam shepherd mission, a novel technique for contactless debris de-orbiting/relocation that requires two electric thrusters: an impulse transfer thruster and an impulse compensation thruster. The optimal operational points of the ITT alone and of the two thrusters considered simultaneously, expressed in terms of their beam voltages, have been identified and the corresponding optimization method described.

Dedicated design performance models [157] have been used to model the effects of changes in the operational conditions of both thrusters (beam voltage and thrust) on their performance figures.

Then, simplified plasma plume and target interaction models have been used to characterize numerically the momentum transfer efficiency, and it has been found that, for the given mission scenario, the plume physics clearly affects the design choice. First of all, the thruster must guarantee a small initial divergence angle, as the conical beam expansion is the major factor that reduces the momentum transfer to the target and hence the efficiency of the IBS technique. Secondly, a high operational voltage also reduces the increase of the beam divergence due to electron thermal effects.

From the point of view of the ITT alone, it is found that an optimal beam voltage exists that maximizes the transmitted force to power ratio, or equivalently that minimizes the required power for a given force on the target.

The optimization study for the whole electric propulsion subsystem has permitted to identify the optimal operational points of both thrusters simultaneously, finding that the minimum total dedicated mass or power are minimized for two different beam voltages of ITT and ICT, being that of the ITT much higher. The choice on whether to minimize the total dedicated mass or the total thruster power depends on the individual mission specifications.

The study presented in this paper can be further refined in the future, by introducing additional effects in the total EPS mass budget, such as the influence of the mass of the thruster units and of the dedicated PPUs.

In addition, although both thrusters have been considered of the same type (radio-frequency ion thrusters) to reduce the system complexity, using a different technology for the ICT, like a Hall Effect thruster, is also envisaged and should be further

investigated. In fact, such thrusters generally feature a better thrust to power ratio than ion thrusters, thus turning out to be very promising for missions with stringent constraints on the available platform power.

An important study to be addressed in future work is also the optimization of a multiple debris removal mission. In fact, the IBS is clearly re-usable, a characteristic that makes it particularly appealing, compared to other ADR techniques. Such an optimization should take into account the time required by the rendezvous phases with each of the successive debris objects, as well as the corresponding delta-V. For what concerns the latter, its value is fixed by the mission orbital parameters and, apart from driving upwards the S/C wet mass, it only affects the mass optimization, favoring a higher specific impulse for the rendezvous thruster (ITT or ICT). On the other hand, the rendezvous phases duration affects both the mass and power optimizations, because it determines, together with the number and mass of the debris objects, the minimum force to be transmitted to the debris, for a given mission duration.

Finally, future work should also address the effects of an off-center plume impact on the debris, which consist in a momentum transfer efficiency loss, but also in an induced angular acceleration of the debris object. Recent research [45], suggested the use of a dedicated control strategy, even though the associated fragmentation risk is estimated to be quite small.

5.3 Spacecraft-plasma-debris interaction study

This study is based on the journal publication of Ref. [121], and is structured as follows. Sec. 5.3.1 introduces the main modeling aspects, and the simulation setup. Then, Sec. 5.3.2 describes and discusses the corresponding results, while Sec. 5.3.3 summarizes conclusions and future work.

5.3.1. Spacecraft-plasma-target model and simulation setup

The study of the spacecraft-plasma-target interaction in an IBS mission requires modeling some aspects that have not been fully covered in Chapter 3.

First of all, in order to evaluate the backsputtering contamination from the target debris, the sputtering properties have to be properly characterized (yield, sputtered atoms energy, backscattering probability). This is dealt with in Sec. 5.3.1.1.

Secondly, the equivalent circuit of Fig. 3.9 is considered to model the plasma plume interaction with both the IBS and the target. In this scheme, the spacecraft sub-circuit is composed of the last grids of both ion thrusters (ITT and ICT), the neutralizers keepers, and the S/C ground, with the latter consisting of a cubic body, the ITT and ICT cases, and the bottom face of the solar arrays. The top face of the solar arrays, on the other hand, is considered to be dielectric and directly illuminated by the Sun. For what concerns the space debris sub-circuit, it only features the debris body.

Thirdly, the forces and torques transferred to the space debris are modeled following the approach described in Sec. 5.3.1.2.

Finally, the simulation setup is presented in Sec. 5.3.1.3.

5.3.1.1. Modeling the target debris sputtering

When a hypersonic particle hits the target debris surface, apart from the neutral reflection and ion recombination phenomena, treated in Sec. 3.2.6.3, it can also cause sputtering, which means that it knocks out a certain number of material surface atoms. As already explained in Sec. 3.2.6.3, the sputtering response can be modeled, in general, by defining: (I) the sputtering yield Y (number of sputtered atoms per impacting particle), (II) the particle backscattering probability p_{bks} (probability that an impacting particle is reflected backwards), and (III) the emission mean energy $\bar{E}_{emi}$ for the sputtered atoms. While the sputtering effects in the PIC model are simulated with the algorithms of Sec. 3.2.6.3, here it is important to adequately characterize the above mentioned sputtering properties. For a target debris made of aluminium and a xenon ion species, the resulting sputtering properties (obtained with SRIM/TRIM [129]) are shown in Fig. 5.9. The yield presents a maximum value at oblique incidence angles (around 75 deg.) and grows with the impacting particle energy (since more collisions are capable of knocking out a lattice atom). For what concerns the sputtered atoms energy, this grows monotonically with both the particle energy and incidence angle, as expected. Finally, the backscattering

probability is practically independent of the impacting particle energy and grows with the incidence angle, being maximum at grazing incidence and null for $\alpha_{imp} < 45$ degrees. For instance, the values of the yield and of the mean sputtered atoms energy for the ITT singly charged ions at 3500 eV of energy (refer to Tab. 5.4) and impacting at normal incidence, are respectively 2 and 14 eV, while the backscattering probability is zero.

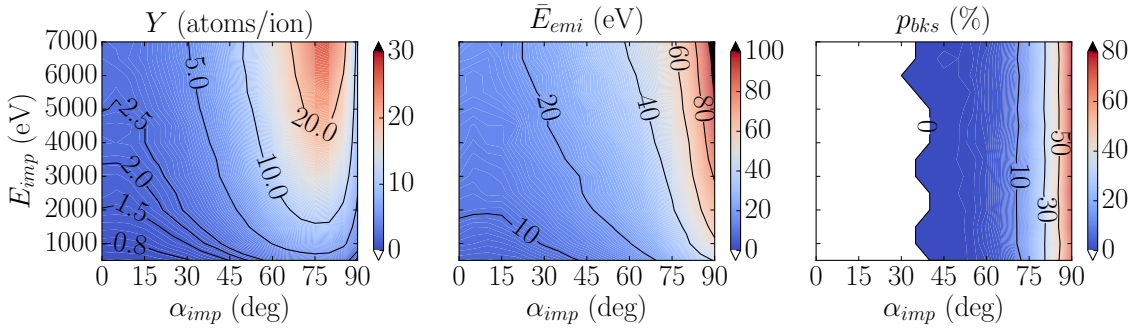

Figure 5.9: Sputtering properties for a hypersonic flow of Xe ions/atoms on an Al target, showing (a) the particle yield (i.e. the average number of sputtered atoms per incident particle), (b) the mean sputtered atoms emission energy, and (c) the incident particle backscattering probability.

5.3.1.2. Transmitted force and torque to the debris

The estimation of the total force and torque transmitted to the target debris is of fundamental importance in the context of an IBS mission. While the former determines directly the momentum transfer efficiency η_B, the latter can be used to estimate the angular acceleration of the space debris. In fact, angular momentum build-up should be watched out to avoid fragmentation risk [45]. The present model is able to refine former calculations of the thrust and torque [42, 43, 44, 45, 151, 152], considering the contributions from (I) linear momentum of impacting and emitted macro-particles (the latter contributing with a recoil effect), (II) electron pressure, and (III) electric forces effect. Therefore, the total transmitted force assumes the form:

$$\boldsymbol{F}_{TG} = \int_S (\dot{\boldsymbol{p}} - p_e \mathbf{1}_\perp + \sigma_s \boldsymbol{E})\, dS \tag{5.29}$$

where $\dot{\boldsymbol{p}}$ represents the linear momentum vector flux of the impacting and emitted macro-particles, obtained with Eq. (3.44), $p_e = n_e T_e$ is the electron pressure, and the last term is the electric force effect, with σ_s representing the surface charge density. From Poisson's equation and Gauss's theorem, this can be evaluated as:

$$\sigma_s = \epsilon_0 \boldsymbol{E} \cdot \mathbf{1}_\perp \tag{5.30}$$

The integral of Eq. 5.29 extends over the debris simulation boundary (sheath edge for quasineutral regions, material wall for non-neutral ones), and is simply evaluated numerically as a sum over the debris cell-faces that discretize it.

Finally, from the knowledge of the elementary force $d\boldsymbol{F}_{TG}$ acting on each cell-face, the elementary torque with respect to the TG center of mass is computed as

$$d\boldsymbol{\tau}_{TG} = \boldsymbol{r} \times d\boldsymbol{F}_{TG}, \tag{5.31}$$

with $\boldsymbol{r}$ the radius vector from the target center of mass to the cell-face center.

5.3.1.3. Simulation setup

The nominal scenario considered for this study is similar to that of Sec. 5.2, whose mission facts are summarized in Tab. 5.1. The simulation geometry is described in Fig. 5.10 (a) and (b), while the most relevant simulation parameters are summarized in Tab. 5.4.

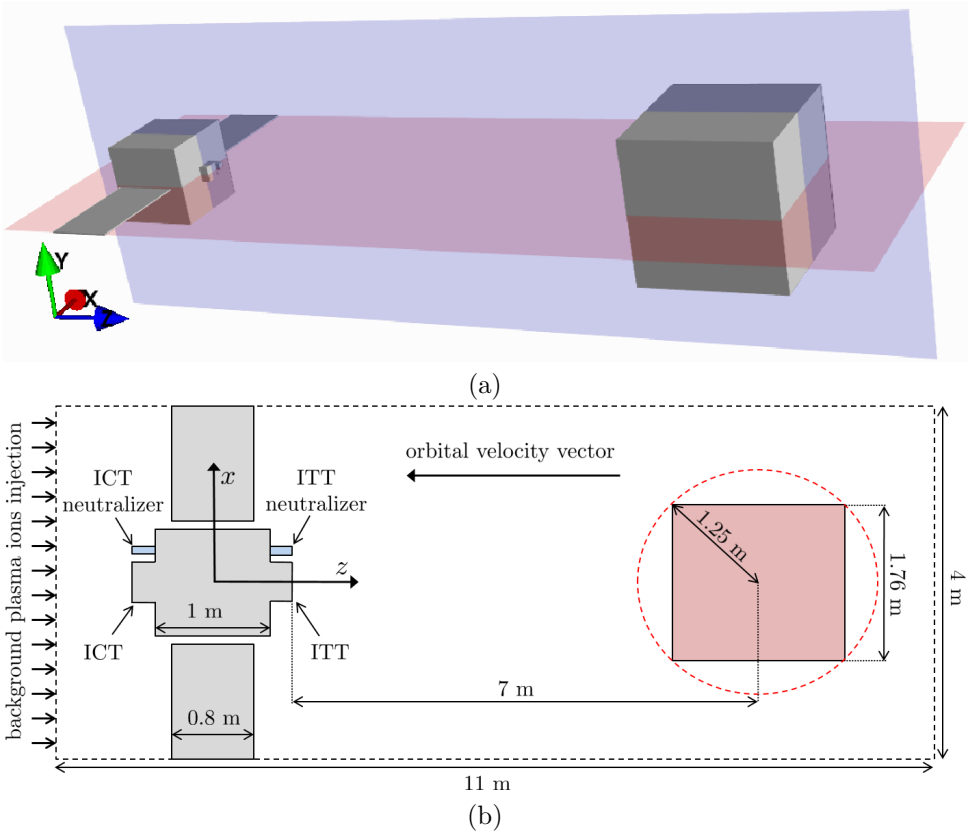

Figure 5.10: Simulation geometry for the IBS-plasma plume-debris interaction: (a) 3D rendering showing two important cross sections through the satellite center, $y = 0$ (in red) and $x = 0$ (in blue). (b) Schematic view of the $y = 0$ cross section showing the simulation objects size and the ambient ions injection direction. The width of the solar arrays along the y direction (towards the reader) is 4 cm, while the Sun is along the $+y$ direction. The cell size is 2 cm along x and y, and 4 cm along z. The number of nodes is 201 along both x and y, and 276 along z.

Xe neutrals are emitted by the thrusters and neutralizers with sonic conditions ($M = 1$), assuming a polytropic coefficient equal to 5/3 (adiabatic), and a temperature of 0.05 eV.

Table 5.4: IBS simulation parameters. Applied voltages refer to the spacecraft ground. The thrusters injection surfaces are circular with radius $R_0 = 8$ cm. The injection profiles for the thruster ions are self-similar profiles (as described in the footnotes). The ITT and ICT data corresponds to the optimal operational points (for minimum power consumption) identified in Sec. 5.2, and is obtained with the performance models of Sec. 5.2.2.

Simulation parameter	**Units**	**Values**
Neutralizers keeper voltage	V	10
ITT/ICT last grid voltages	V	-100
ITT/ICT beam voltage	V	3500/1000
ITT/ICT thruster mass flow rate	mg/s	0.566/1.293
ITT/ICT mass utilization efficiency	%	75/85
Doubly charged to total ion current ratio	%	9.1
ITT injected Xe^+ profile	n/a	SSM [2]
ICT injected Xe^+ profile	n/a	SSM [3]
ITT injected Xe^{++} profile	n/a	SSM [4]
ICT injected Xe^{++} profile	n/a	SSM [5]
ITT/ICT injected Xe^+ temperature	eV	0.1
ITT/ICT injected Xe^{++} temperature	eV	0.2
ITT/ICT injected neutrals profile	n/a	flat
ITT/ICT inj. neutral axial velocity	m/s	247
ITT/ICT injected neutral temperature	eV	0.05
ITT/ICT neutralizers mass flow rate	mg/s	0.0565
Neutralizers inj. neutrals profile	n/a	flat
Neutralizers inj. neutral axial velocity	m/s	247
ITT/ICT neutralizers inj.neutral temperature	eV	0.05
Neutralizers ion flow percentage	%	5.0
Neutralizers injected Xe^+, Xe^{++} ions profile	n/a	thermal, Gaussian [6]
Neutralizers injected Xe^+ temperature	eV	0.2
Neutralizers injected Xe^{++} temperature	eV	0.4
Electron temperature at ITT thruster exit	eV	3.0
Electron polytropic cooling coefficient	n/a	1.15
Background plasma density (O^+ ions)	m^{-3}	$5 \cdot 10^{10}$
Background plasma temperature (O^+ ions)	eV	0.15
Background O^+ ion velocity	km/s	7.5
Target debris material	n/a	Al
Material walls accommodation coefficient	n/a	0.98

Regarding the thrusters ions, both singly and doubly charged ions are emitted, with a kinetic energy provided by their corresponding beam voltage (respectively 3500 and 1000 eV for the singly charged ions emitted by the ITT and ICT thrusters). The injection profiles are based on the Ashkenazy-Fruchtman initial profile [61], while the values for R_0 and α_0 are provided in the table footnotes. The neutralizers

[2] with outermost streamline radius $R_0 = 8$ cm and divergence angle $\alpha_0 = 7$ deg
[3] with outermost streamline radius $R_0 = 8$ cm and divergence angle $\alpha_0 = 35$ deg
[4] with outermost streamline radius $R_0 = 8$ cm and divergence angle $\alpha_0 = 15$ deg
[5] with outermost streamline radius $R_0 = 8$ cm and divergence angle $\alpha_0 = 40$ deg
[6] with outermost streamline radius $R_0 = 2$ cm and zero divergence

ions, on the other hand, are emitted as a thermal flux with temperatures of 0.2 and 0.4 eV for respectively the singly and doubly charged ions, and represent 5% of the total emitted particle flow (the remaining part being neutrals). Finally, a background population of O ions is assumed to be moving along the positive z direction, with a velocity comparable to the LEO orbital velocity (7.5 km/s), a temperature of 0.15 eV, and a density of $5{\cdot}10^{10}$ m^{-3}, which corresponds to an average plasma density at an altitude of 600 km over the Sun activity cycle. The direction of the injected ions is typical of a de-orbiting scenario, in which the shepherd spacecraft is ahead of the space debris along the orbit direction. Finally, the solar panels are oriented with their normal at 90 degrees with respect to the orbit plane, a typical operational condition in sun-synchronous orbits with a local solar time at the ascending node equal to either 6 AM or 6 PM.

Regarding the heavy particle collisions, the considered model includes (I) resonant symmetric CEX collisions between the emitted Xe ions and neutrals (both $Xe^{+} + Xe$ and $Xe^{++} + Xe$), and (II) ionization collisions of different degrees, again only for the Xe species ($Xe \rightarrow Xe^{+}$, $Xe \rightarrow Xe^{++}$ and $Xe^{+} \rightarrow Xe^{++}$). Collisions within the oxygen ambient ions population, the sputtered Al atoms population, and the cross-species collisions between these two species and the emitted Xe species, are not considered as their effect is clearly negligible. In fact, a rough estimation of the mean free path for the cross-species collisions involving Xe shows that: (I) Xe-O collisions have a mean free path $\lambda_c = O(10^6)$ km, and (II) Xe-Al collisions, at the very surface of the target debris (where Al density is highest), have a mean free path $\lambda_c = O(10)$ km. Comparing these values with the simulation domain size (≈ 10 m), we can reasonably assert that their effect is negligible.

For what concerns the sputtering effect of the ambient ions on both the target debris and on the spacecraft, this is also negligible (with respect to the impinging Xe ions), because (I) their density is $3-4$ orders of magnitude lower (at the target debris surface), and (II) the corresponding yield at their low energy (tens of eVs at most) is almost negligible.

Additional simulations are finally considered to investigate the effect of different physical phenomena:

- Electron cooling: one simulation with $\gamma = 1.25$ (versus the nominal $\gamma = 1.15$).
- Ambient plasma: one simulation with a perfect vacuum.
- CEX and ionization collisions: one simulation without them.
- Space debris attitude and position: one simulation with an off-axis target debris.

5.3.2. Simulation results

5.3.2.1. Nominal scenario

Fig. 5.11 (a) and (b) show the electric potential at the $y = 0$ and $x = 0$ cross sections. The reference point ($\phi = 0$), where the electron temperature is fixed to 3.0 eV, is located 8 cm downstream of the ITT exhaust plane, on the axis. The effects of CEX ions and emitted plume of the neutralizers are clearly visible in Fig. 5.11 (a), while Fig. 5.11 (b) shows more symmetric results. The electric potential close to the metallic objects (SC cubic body, neutralizer, thruster cases, target debris) adapts locally to their electric potential, except at the quasineutral material boundaries of the thruster and neutralizer exit surfaces and of the front surface of the debris (the one facing the S/C).

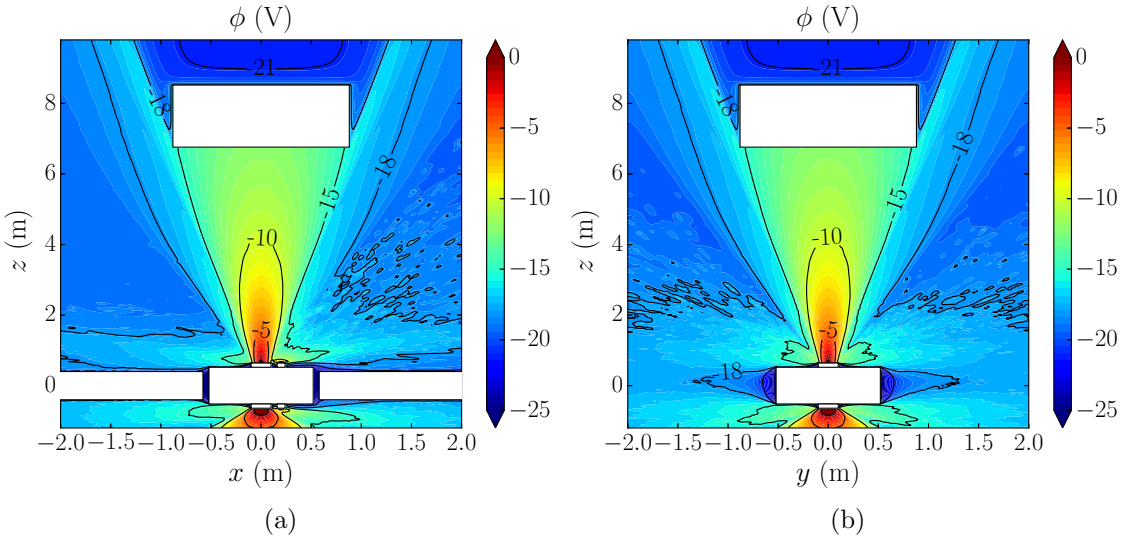

Figure 5.11: Nominal scenario results: electric potentials at (a) $y = 0$, and (b) $x = 0$. Both cross sections pass through the geometric center of the satellite cubic body. The potentials refer to a plasma location, 8 cm downstream from the ITT thruster exit plane, at its axis. The horizontal and vertical axes scales are different.

The total Xe ion and neutral densities are shown in Fig. 5.12 (a) and (b), while the electron density and the resulting charge density are shown in Fig. 5.12 (c) and (d). The neutral density is quite symmetric with respect to the ITT plume axis, with peak values of almost 10^{18} m^{-3} at the thruster exits, and above 10^{14} m^{-3} at the target debris surface (due to ion recombination). The plume of the neutralizer, on the other hand, introduces a larger asymmetry in both the ion and electron densities close to the spacecraft. The peak plasma density of the ITT is slightly above 10^{15} m^{-3}, a quite low value corresponding to the combined effect of a low mass flow rate and a large acceleration voltage (3500 V). The peak density of the ICT thruster, which features a beam voltage of 1000 V, is above 10^{16} m^{-3}. Moreover, no ions hit the lateral sides of the target debris, while the electron density is not identically zero there, and presents a value corresponding to the target potential (≈ -16 V).

Finally, the charge density shows extended non-neutral regions on the sides of the ITT plume, in the resolved plasma sheaths close to the S/C surfaces, and in the wake regions behind the target. In particular, the front surface of the target debris is quasineutral with a thin sheath drop smaller than the typical floating potential (with respect to the plasma potential), because the ions enter it with hypersonic velocities (the local Mach number is around 50 at the target debris). On the other hand, inside the wake region behind the target, the charge density is negative, since ions cannot deflect rapidly enough to fill it.

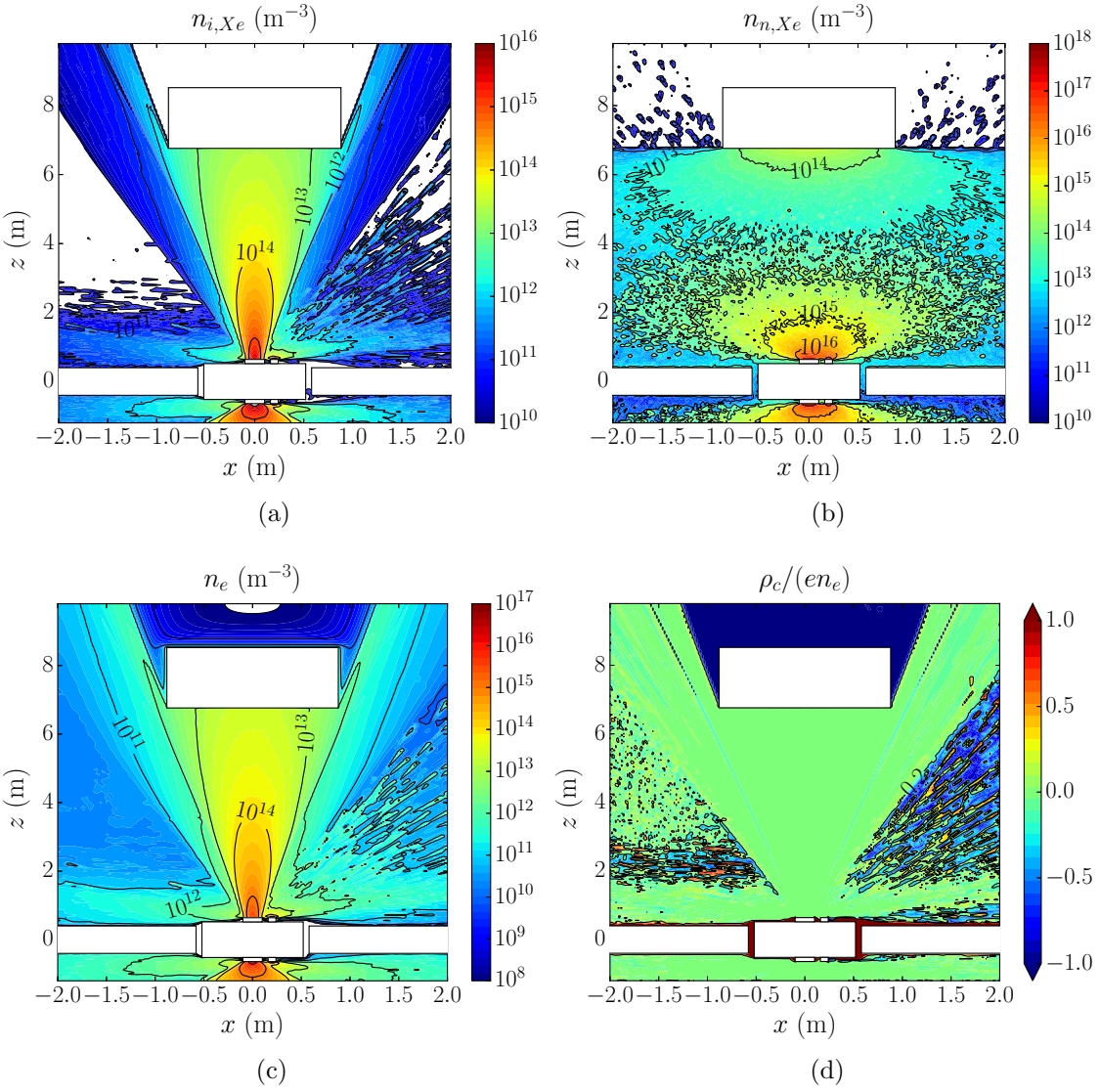

Figure 5.12: Nominal scenario results at $y = 0$: (a) Xe ion density, (b) total Xe neutral density, (c) electron density, and (d) electric charge density.

Of particular interest are the plots of the slow Xe ion density and vector particle flux (not including emitted ions of thrusters and neutralizers). These are shown respectively in Fig. 5.13 (a) and (b), for a simulation region close to the S/C. The

ions emitted by the neutralizer generate a potential barrier that prevents the slow Xe ions (mostly produced by CEX collisions, with a minor contribution of ionization) from crossing over to the right solar array (at least in the $y = 0$ plane). Moreover, the slow ion velocity progressively turns towards the S/C, as shown in the flux vector plot.

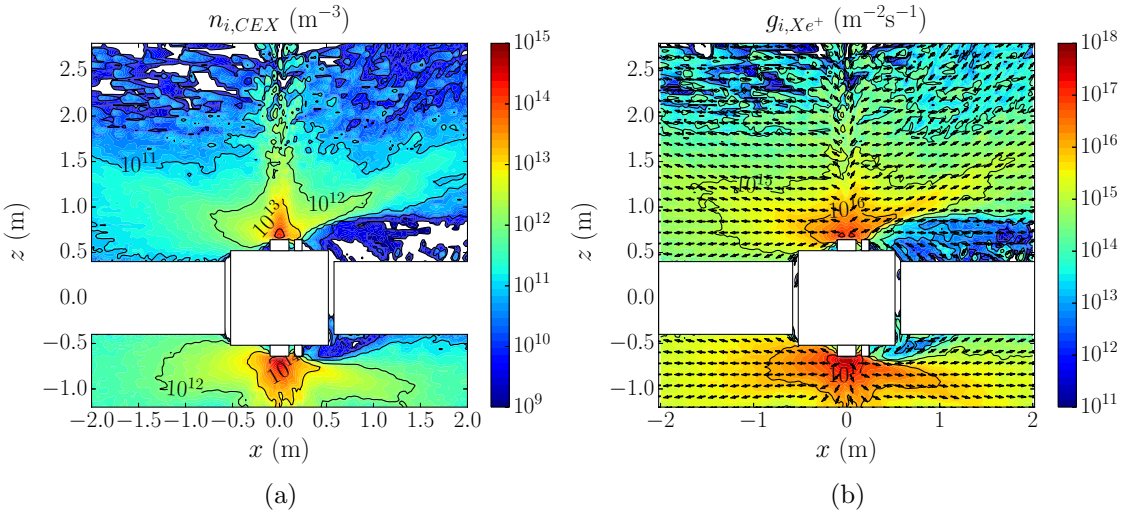

Figure 5.13: Nominal scenario results at $y = 0$: (a) slow Xe ion density (for both Xe^+ and Xe^{++}), and (b) slow Xe^+ particle flux. Only slow ions from CEX and ionization are taken into account (injected ions from the thrusters and neutralizers are not included). Regarding the vector flux, its direction is shown by the arrows.

The fast neutral density, on the other hand, is shown in Fig. 5.14. CEX neutrals are generated at the thrusters and neutralizers exits, and being very fast with a small divergence, they reach the target with a moderate drop in density (a factor of 10), with values around 10^{11} m^{-3} at the debris surface.

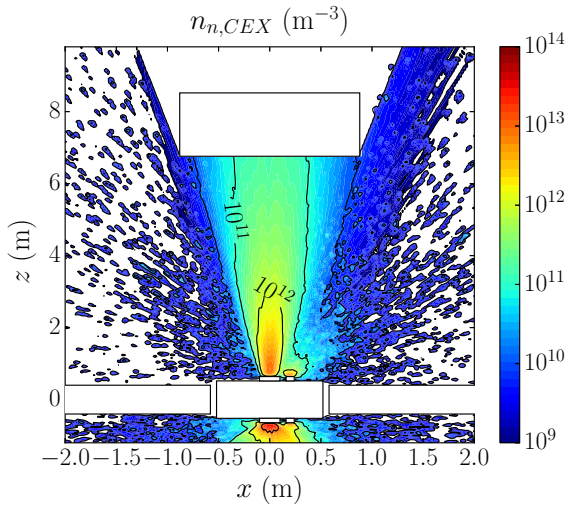

Figure 5.14: Nominal scenario results at $y = 0$, for the fast CEX neutral density.

The slow Xe ion backscattering flux towards the S/C front surface (the side facing the debris), and on the solar arrays, are then shown in Fig. 5.15 (a), and in Fig. 5.16 (a) and (b), while the corresponding wall-impact energies are shown in Fig. 5.15 (b), and Fig. 5.17 (a) and (b).

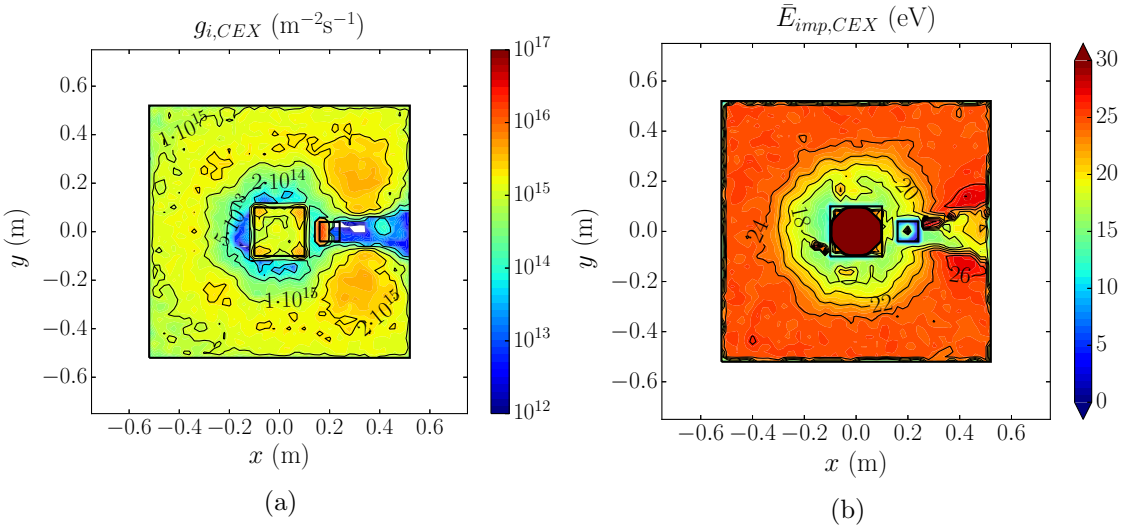

Figure 5.15: Nominal scenario results at the S/C front surface: (a) slow Xe ion flux, and (b) slow Xe ions mean wall-impact energy. Only slow ions from CEX and ionization are taken into account.

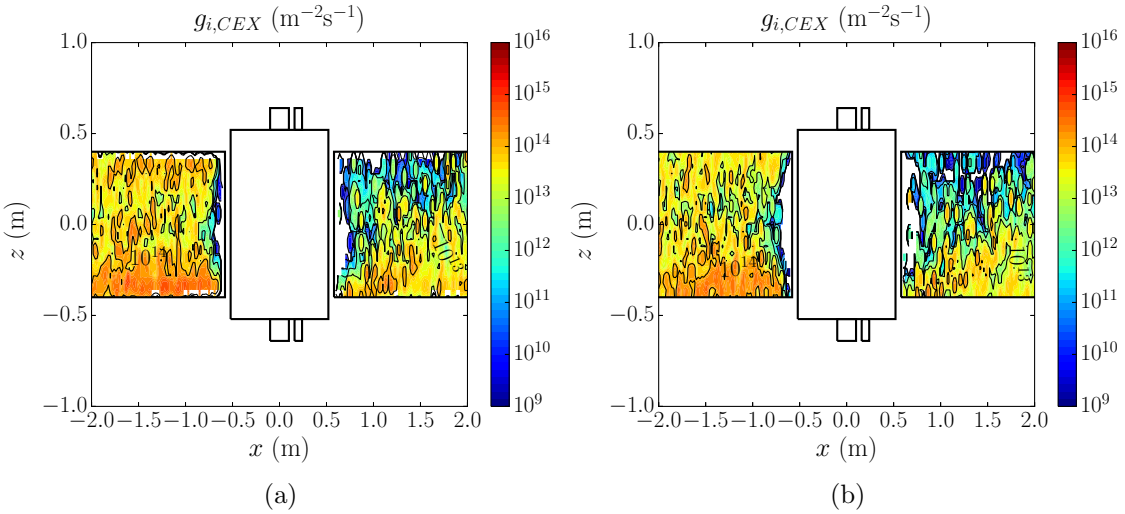

Figure 5.16: Nominal scenario results at the solar arrays surface for the slow Xe ion flux at (a) the conductive faces, and (b) at the dielectric faces. Only slow ions from CEX and ionization are taken into account.

The regions on the S/C surface with the largest CEX ion flux are located close to the sides of the neutralizer, with values as high as $2 \cdot 10^{15}$ m^{-2}s^{-1}, with peak wall-impact energies around 26 eV. The CEX ion flux on the solar arrays is negligible

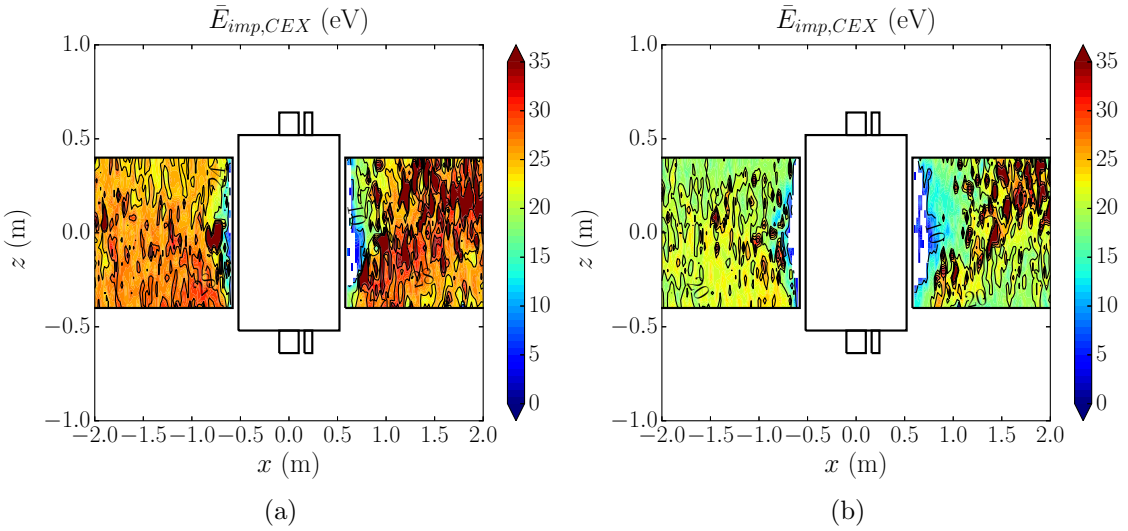

Figure 5.17: Nominal scenario results at the solar array surfaces for the slow Xe ions wall-impact energy at (a) the conductive faces, and (b) at the dielectric faces. Only slow ions from CEX and ionization are taken into account.

very close to the S/C body, and reaches values close to 10^{15} m^{-2}s^{-1} at the arrays side close to the ICT. The wall-impact energies, on the other hand, are around $25 - 30$ eV for the conductive face, and $15 - 20$ eV for the dielectric face.

The difference in the ion impact energy on the two faces of the arrays can be explained by observing the electric potential distribution at the $z = 0$ cross section, shown in Fig. 5.18. The electric potential at the conductive face ($y < 0$) is lower than at the dielectric face, meaning that it draws a net positive current (the dielectric face draws no net current). This yields a wider sheath region and a larger impact energy of the slow CEX ions, at the conductive face.

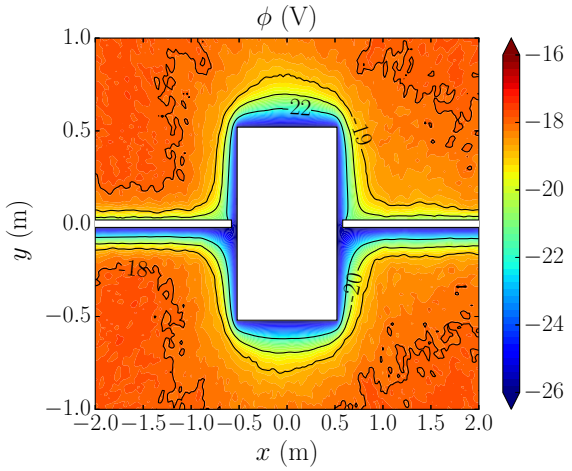

Figure 5.18: Nominal scenario results at $z = 0$, for the electric potential. The conductive face of the arrays is the one at $y < 0$, while the dielectric face is at $y > 0$. The scales are different along x and y.

Regarding the backsputtering contamination, Fig. 5.19 (a) and (b) show the sputtered Al atoms density and vector flux. The density decreases from a peak value of almost 10^{15} m^{-3} at the debris to much lower values around 10^{13} m^{-3} close to the S/C surface, where the density increases again due to the atoms diffuse reflection. The sputtered atoms vector flux follows the same trend with the distance from the target, and drops rapidly to zero very close to the S/C, due to the diffuse reflection.

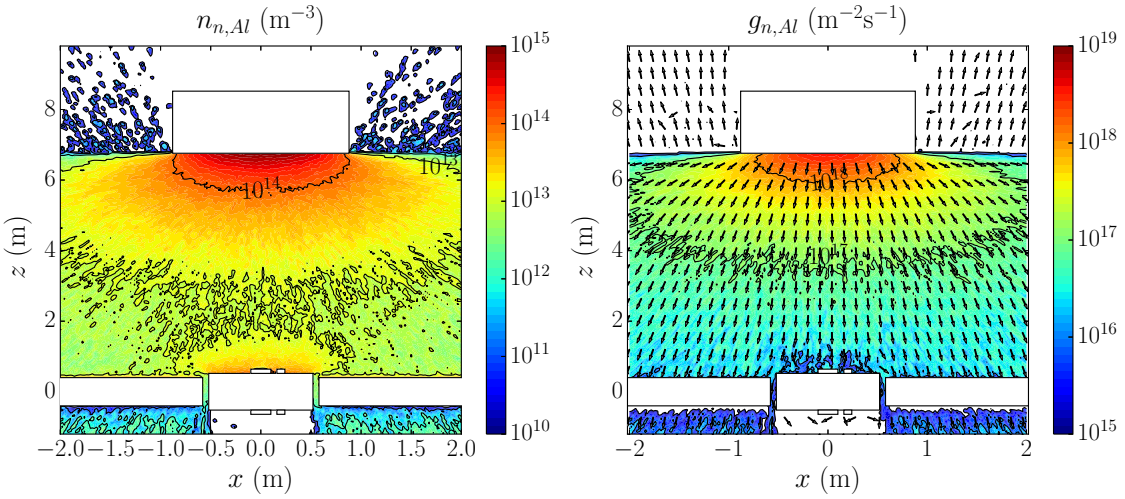

Figure 5.19: Nominal scenario results at $y = 0$ for the sputtered atoms (a) density, and (b) vector flux. The direction of the vector flux is shown by the arrows.

The sputtered Al flux on both the S/C front surface and the solar arrays dielectric face (here equivalent to the conductive face) is shown in Fig. 5.20 (a) and (b).

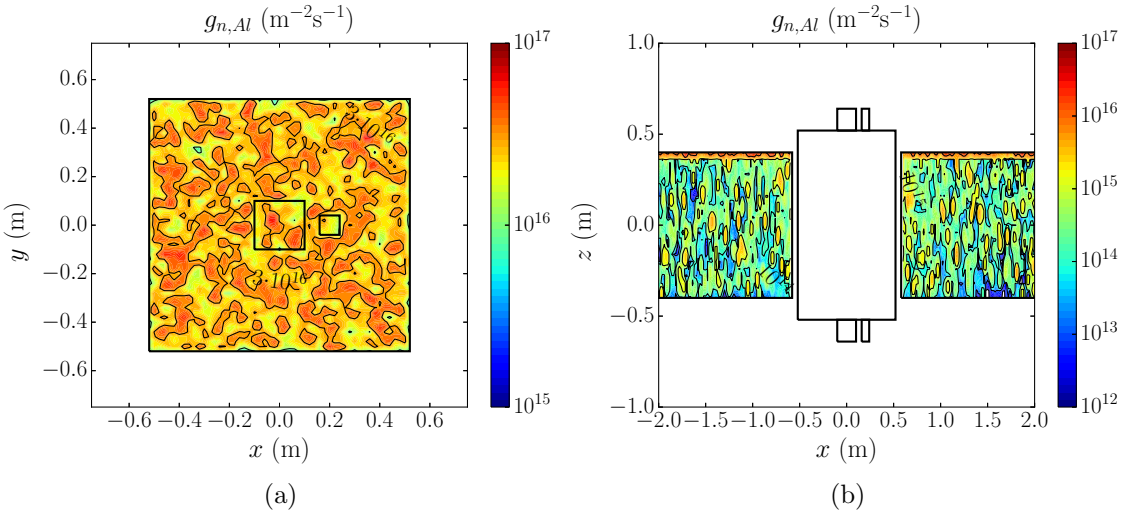

Figure 5.20: Nominal scenario results at $y = 0$ for the sputtered atoms flux on (a) the S/C front surface, and on (b) the dielectric face of the solar arrays.

Values between 1 and $4 \cdot 10^{16}$ $m^{-2}s^{-1}$ are found on the S/C front surface, while much lower fluxes impact on the solar arrays, given their orientation (lower, on average, than 10^{15} $m^{-2}s^{-1}$). Assuming no reflection of Al atoms (worst case for contamination), an average flux of $2 \cdot 10^{16}$ $m^{-2}s^{-1}$, an IBS mission duration of 170 days with a sunlight orbit fraction of 67% (IBS is not active during solar eclipses), then a contamination layer with a thickness of 3.2 μm would form on all surfaces with a normal oriented along the z direction. This could affect the solar arrays efficiency, if they were oriented with a normal along z (in the considered case, on the other hand, they would suffer a much smaller contamination). Please observe that the ambient O^+ flux for the considered scenario is, at normal incidence, $3.75 \cdot 10^{14}$ $m^{-2}s^{-1}$, approx. 2 orders of magnitude smaller than the above considered flux.

The mean wall-impact energy of the sputtered atoms on the S/C front surface and on the dielectric face of the solar arrays are finally shown in Fig. 5.21 (a) and (b). Values between 10 and 16 eV are found on the S/C front surface, as expected from the knowledge of the sputtered atoms mean emission energy of Fig. 5.9 (b) (for $\alpha_{imp} \approx 0$ and $E_{imp} = 3500$ and 7000 eV for respectively Xe^+ and Xe^{++} ions). The lower average impact energy of Al atoms on the solar arrays, on the other hand, is due to the contribution of reflected atoms from the S/C cubic body, which have a lower energy than the impacting ones (the accommodation coefficient is $A_W = 0.98$).

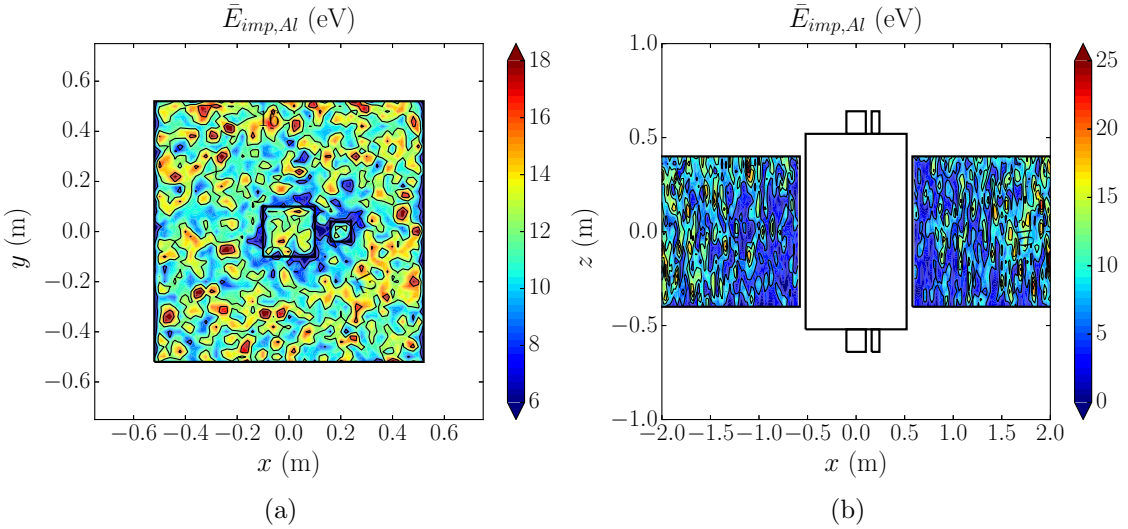

(a) (b)

Figure 5.21: Nominal scenario results for the mean wall-impact kinetic energy of sputtered atoms on (a) front S/C surface, and (b) solar arrays dielectric face.

The ambient ion density and vector flux are finally shown in Fig. 5.22 (a) and (b). The emitted plume of the ICT acts as a potential barrier ($5-10$ V, as shown in Fig. 5.11) that prevents most of the ambient ions (with kinetic energies of approx. 5 eV) from reaching the S/C cubic body. Moreover, even if they tend to flow around the thin solar arrays, the main plasma plume core of the ITT also rejects them. As a consequence of the S/C wake, only a negligible fraction of ambient ions finally hits the target debris.

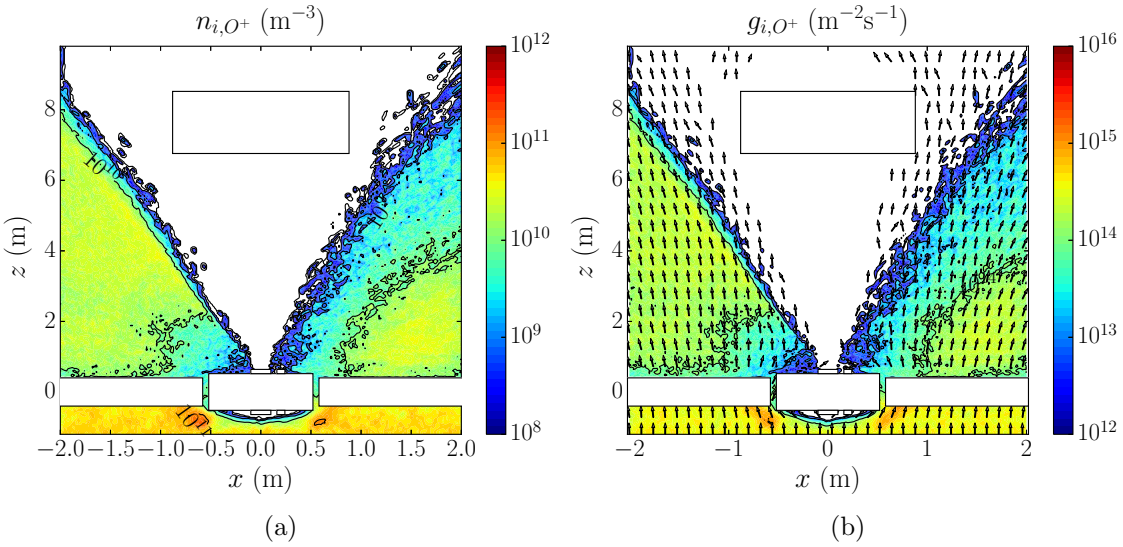

Figure 5.22: Nominal scenario results: (a) oxygen ion density and (b) oxygen ion flux, at the $y = 0$ cross section . The direction of the vector flux is shown by the arrows.

The evolution with time of the electric potential and collected ion currents of the S/C and of the target debris are finally reported in Fig. 5.23 (a) and (b).

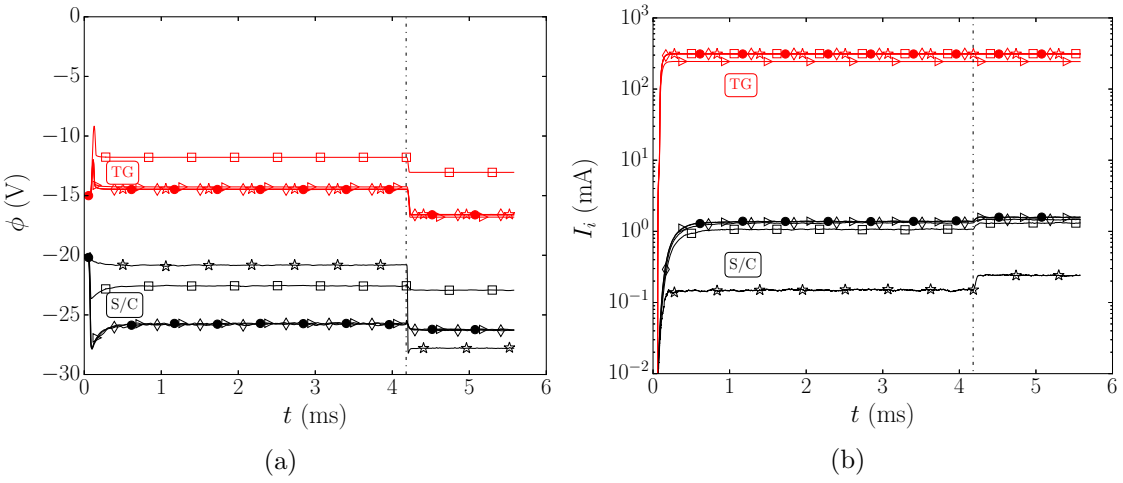

Figure 5.23: Time evolutions of (a) electric potentials and (b) collected ion currents for both the S/C (black lines) and the target (red lines). The nominal case is shown with filled circles, the $\gamma = 1.25$ case with empty squares, the off-axis debris case with triangles, the no-CEX collisions case with empty stars, and the no ambient ions case with empty diamonds. The potentials refer to a plasma location, situated 8 cm downstream of the ITT thruster exit plane, at its axis, while the collected S/C ion currents include the currents to neutralizers, thrusters and both faces of the solar arrays. The sudden changes in electric potentials and currents, that occur at $t \simeq 4.18$ ms as indicated by the vertical line, are due to the activation of the non-neutral solver.

As explained in Chapter 3, the code features both a quasineutral and a non-neutral solver. To speed up the simulation, thus quickly filling the simulation domain

with particles, the first 15000 steps (corresponding to a simulation time $t = 4.18$ ms) are run with the quasineutral solver alone, while the non-neutral solver is activated afterwards and produces a change in the electric potentials and collected ion currents evolutions (for both the S/C and the TG). In the nominal scenario, featuring $\gamma = 1.15$, the target debris finally charges positively with respect to the S/C, with a constant difference of approx. 10 V. Regarding the ion currents, on the other hand, the debris collects approx. 0.3 A, while the S/C approx. 1.5 mA (mostly due to CEX ions).

Finally Tab. 5.5 shows the transferred force to the debris along the plume axis and its partial contributions, for the considered simulation cases.

Table 5.5: The different contributions to the transferred force along z to the target debris, for the considered simulation cases. The contribution of the injected Xe^+ ions for the nominal and off-axis target cases is compared with an SSM plume model prediction (given in parenthesis).

	Transferred force (mN) along z, for the different cases				
Contributions	**nominal**	$\gamma = 1.25$	**no coll.**	**no amb.**	**off-axis TG**
Injected Xe^+	28.8(27.7)	29.0	28.9	28.8	22.4(21.2)
Injected Xe^{++}	1.07	1.11	1.07	1.07	0.903
Recombined Xe	2.67	2.70	2.66	2.67	2.08
Fast CEX Xe	0.170	0.173	0.0	0.173	0.147
Sputtered Al	0.934	0.941	0.934	0.933	0.739
O^+ ions	$1.2 \cdot 10^{-8}$	$1.4 \cdot 10^{-6}$	$2.1 \cdot 10^{-9}$	0.0	$6.3 \cdot 10^{-7}$
Electron pressure	$1.1 \cdot 10^{-8}$	$3.1 \cdot 10^{-9}$	$1.1 \cdot 10^{-8}$	$1.1 \cdot 10^{-8}$	$9.1 \cdot 10^{-9}$
Electric field	$-6.6 \cdot 10^{-10}$	$-2.1 \cdot 10^{-10}$	$-6.7 \cdot 10^{-10}$	$-6.6 \cdot 10^{-10}$	$-9.4 \cdot 10^{-10}$
Total	33.6	34.0	33.6	33.6	26.3

The predicted contributions for injected singly charged ions is compared with the prediction of the Parks-Katz Self-Similar model, generalized with $\gamma = 1.15$ (Eq. 2.38). A particularly good match is found, with the SSM underestimating slightly the transferred force (1 mN less). In the nominal case, the backsputtered atoms contribution is around 3% of the total transmitted force, while the effect of recombined Xe neutrals is around 8% (this depends greatly on the wall accommodation coefficient, here $A_W = 0.98$). The contributions of oxygen ions, surface electric fields and electron pressure are all negligible. The achieved total force transferred to the debris is above the requirement of 30 mN (it is actually 33.6 mN), which, for a total ITT simulated thrust of 31.5 mN, corresponds to a momentum transfer efficiency of 107% (above 100% because of the recoil effect of recombined Xe neutrals and sputtered Al atoms). Finally, the torque is negligible in the nominal case, being $(1.51, 4.55, 0.08)$ μN m.

5.3.2.2. Effects of the electron cooling

The comparison of the nominal scenario, featuring $\gamma = 1.15$, with the non-nominal $\gamma = 1.25$ case, provides important information on the effects of the electron cooling in the plume.

Referring to Tab. 5.5, a larger polytropic coefficient yields a slightly larger transferred force to the target (+0.4 mN), since the divergence angle of the emitted ions increases less due to the smaller ambipolar electric fields in the plume. Therefore a slightly larger fraction of emitted ions hits the target debris.

Fig. 5.24 (a) and (b) show the changes with respect to the nominal case of respectively the electric potential, at $y = 0$, and the slow Xe ion flux on the S/C front surface.

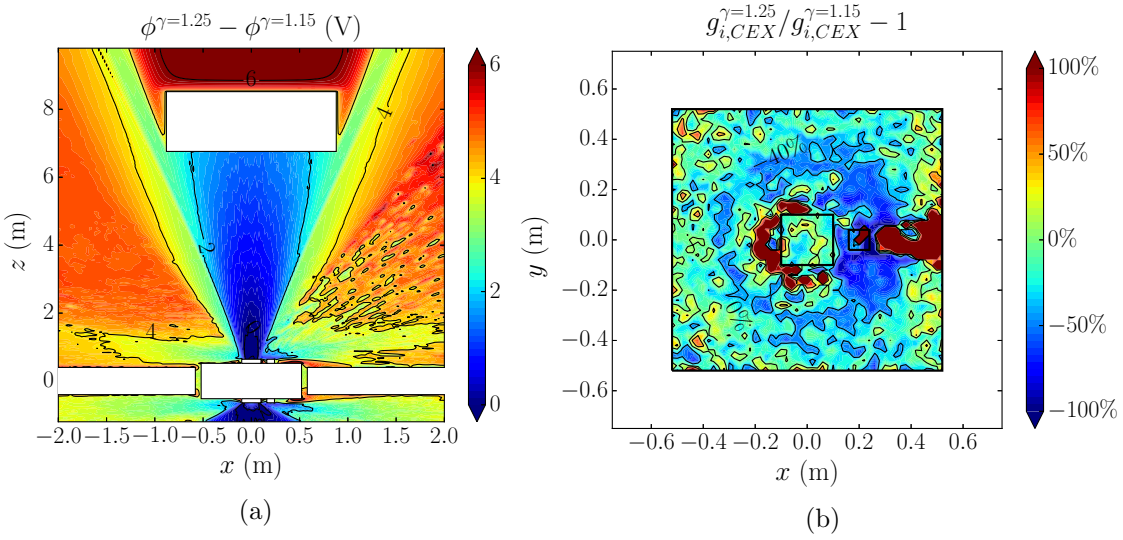

Figure 5.24: Electrons cooling effects: (a) electric potential change $\phi^{\gamma=1.25} - \phi^{\gamma=1.15}$, at $y = 0$, and (b) relative change in the slow Xe ions flux on the S/C front surface $g_{i,CEX}^{\gamma=1.25}/g_{i,CEX}^{\gamma=1.15} - 1$. Only ions generated by CEX and ionization are taken into account.

In general, a larger electron cooling yields a larger electric potential in both the core and lateral plume regions (up to 6V higher inside the plasma plume wake of the target debris). Therefore, both the target and the S/C potentials increase by approx. 3 V with respect to the nominal case, as shown in Fig. 5.23 (a) (squares versus filled circles). The electric potential difference between S/C and TG, on the other hand, presents approximately the same value as in the nominal case ($\approx$ 10V).

The lower ambipolar electric fields of the non-nominal case yield to a smaller fraction of slow ions backscattered towards the S/C, as shown in Fig. 5.24 (b), where the average change is clearly negative with reduction peaks of more than 50%. This is also patent in Fig. 5.23 (b) where the S/C collected ion current clearly reduces (black squares versus black filled circles). The effects of the electron cooling on the TG collected ion current, on the other hand, are almost negligible.

5.3.2.3. Effects of the ambient plasma

As shown in Fig. 5.22 (a) and (b), the S/C emitted plumes act as potential barriers for the ambient plasma ions, so that a negligible fraction of them actually reach the target debris. For this reason, the simulation with no ambient ions present the same transferred force to the debris, as shown in Tab. 5.5. Referring to Fig. 5.23 (b), the collected ion current (black diamonds) of the no-ambient plasma case is slightly lower than that of the nominal case. In fact, approximately 0.2 mA of current are due to ambient O^+ ions, versus approx. 1.5 mA of current due to slow Xe ions (due to CEX and ionization). This small difference in electric current yields an almost negligible effect, however, on the S/C potential.

Finally, the electric potential change from the nominal simulation to the one without ambient ions injection is shown in Fig. 5.25 (a). The effect of ambient ions is small throughout the simulation domain, as expected, except for the left side of the ITT plume, where the potential of the nominal case is slightly larger (up to 2 V). On the right side of the ITT plume, on the other hand, the oxygen ion density is smaller (refer to Fig. 5.22 (a)) and the ITT neutralizer ions represent the dominating species, so that the potential difference between the two simulations is smaller and caused by statistical noise.

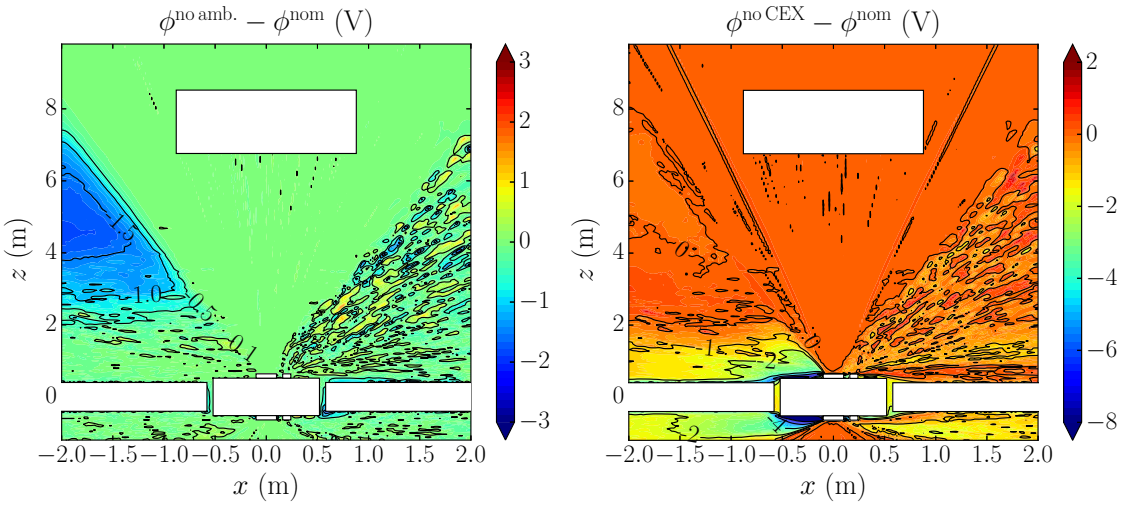

Figure 5.25: CEX and ambient plasma effects on the electric potential at $y = 0$: (a) electric potential change from the nominal simulation to the simulation with no ambient ions $\phi^{\text{no amb.}} - \phi^{\text{nom}}$, and (b) electric potential change from the nominal simulation to the simulation with no collisions $\phi^{\text{no CEX}} - \phi^{\text{nom}}$.

To conclude, ambient ions only have a minor importance: their effect is negligible for what concerns the S/C floating potential and the transferred force to the TG, while their total flow to the S/C is approximately 10% of that of the CEX ions, and is almost negligible with respect to the contamination flux of sputtered Al atoms.

5.3.2.4. Effects of CEX and ionization collisions

The backscattered slow Xe ions, generated by CEX or ionization, represent, by far, the most important contribution to the S/C collected ion current. In particular their contribution is one order of magnitude larger than that of the ambient ions, as shown in Fig. 5.23 (a) and (b), in which the simulation with no collisions is shown by star markers. The collected ion current decreases by more than 1 mA, being given only by the ambient plasma ions, while the S/C potential at the end of the simulation is 1.5 V lower than in the nominal case. Among the slow Xe ions, CEX ions represent the clearly dominant contribution, being 2-3 orders of magnitude denser than ions from ionization.

The comparison between the electric potential of the nominal case and the case without collisions is finally shown in Fig. 5.25 (b). Differences of up to 8 V are found on the left side of both the ITT and ICT thrusters, while the emitted ions of the neutralizers mitigate the differences on the right sides.

Finally, collisions don't affect significantly the target properties, such as the transferred force, the collected ion current or the electric potential, just as expected.

5.3.2.5. Effects of the space debris position

The off-axis target simulation presents a target center of mass displaced by +0.44 m along the x direction, and −0.44 m in the y direction. Therefore, the symmetry of the backsputtered atoms flux with respect to the z axis is lost, as shown in Fig. 5.26 (a). Nevertheless, by comparing these results with Fig. 5.19 (b), the changes are quite small at the S/C position. This is also confirmed in Fig. 5.26 (b), which shows the relative change in the sputtered atoms flux on the S/C front surface.

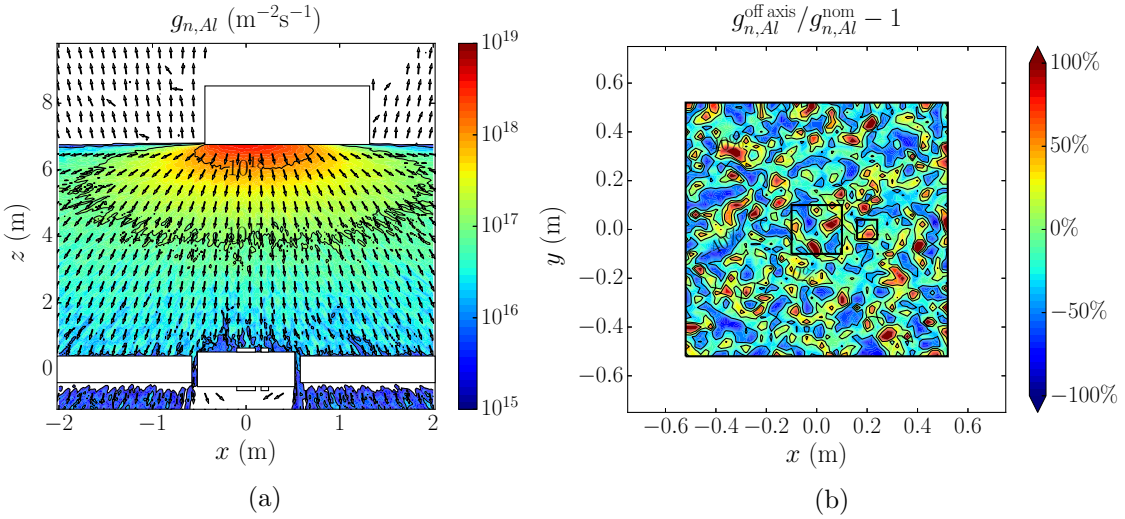

Figure 5.26: Effects of an off-axis target debris: (a) backsputtered Al atoms vector flux (with the direction shown by the arrows), at y = 0, and (b) relative change in the backsputtered Al atoms flux on the S/C front face, from the nominal to the off-axis target simulation $\phi^{\text{off axis}} - \phi^{\text{nom}}$.

Finally, regarding the transferred force along z to the debris, this clearly reduces from 33.6 to 26.3 mN, since a larger fraction of plume ions misses the target. This corresponds to a momentum transfer efficiency of 83.5%. Moreover, the transferred force presents non-negligible components along x and y, being $F_{TG,x} = 0.358$ mN and $F_{TG,y} = -0.362$ mN. Finally, the transferred torque to the target debris is no more negligible (except around the z axis): $(-2.82, -2.82, -6.73 \cdot 10^{-4})$ mN m. This yields to an angular momentum build-up in 1 day of approx. 250 kg m^{2}s^{-1} per axis, which corresponds, for the considered target debris mass and shape, to an angular velocity of approx. 0.3 rad/s.

5.3.3. Conclusions

The study presented in this section is a detailed analysis of the S/C-plasma plume-debris interaction, which has permitted evaluating the effects of some of the most problematic phenomena affecting an IBS spacecraft. In particular the following has been found:

- The backscattering ion flux on the S/C surface is around 10^{15} m^{-2}s^{-1} on average, whereas on the solar arrays, this flux is around 10^{14} m^{-2}s^{-1}, and is different on the conductive and dielectric faces. Regarding the mean ion impact energy, this is around $20 - 30$ eV, a value which should produce negligible surface sputtering, although the confirmation of this statement is left to future studies.

- The backsputtering neutral flux on the S/C front surface is above 10^{16} m^{-2}s^{-1}, and, depending on the mission duration, it might have non-negligible contamination effects (a contamination layer of approx. 3 μm thickness forms during the de-orbiting phase in surfaces whose normal is aligned with the TG direction). The mean kinetic energy of backsputtering atoms is between 10 and 16 eV. Obviously, this contamination flux would reduce for larger operational distances (at the cost of a lower momentum transfer efficiency).

- The stationary difference of potential that builds up between the S/C and the target is around 10 V, with the target positive with respect to the S/C.

- The electron thermodynamics affect the stationary potentials of S/C and TG, but not their difference. Moreover, a larger polytropic coefficient yields a slightly larger transferred force to the TG, and a lower backscattered slow ion flux to the S/C.

- Ambient plasma ions present a minor contribution to the total ion current collected by the S/C (approx. 10%), while the ITT plume prevents most of the ambient ions from hitting the debris.

- CEX ions represent the dominant contribution to the S/C collected ion current, and are an important factor in determining the stationary electric potential of the S/C.

- An off-axis target position affects only slightly the backsputtered flux on the S/C, although it also causes a significant reduction of the momentum transfer efficiency and a non-negligible torque acting on the debris. A recent study [43] has also shown that the lateral forces that originate due to an off-axis target position have a destabilizing effect, to be counteracted by the relative position GNC.

Finally, regarding future work, the following is envisaged:

- Deformed meshes for non-rectangular and non-aligned objects.
- Use of a re-normalization algorithm, in order to reduce the PIC noise.
- Study of the effects of the Earth's magnetic field in the plasma plume expansion, requiring a more complex electron model (with a tensor conductivity).
- Study of the sputtering effects on the S/C surfaces, requiring a low-energy study of the sputtering between the Xe and Al ions/atoms and the S/C surface material.

Chapter 6

Experimental study of the PEGASES plasma plume

Ion thrusters based on the alternate acceleration of positive and negative ions are receiving an increasing attention in the electric propulsion community, as they can work in steady state with no external neutralizer, a critical element for most ion thrusters. PEGASES (Plasma propulsion using Electronegative GASES) is one of these thrusters and, given its low maturity level, it still requires some fundamental investigation of its working physical principles. This chapter describes the results of an experimental campaign, carried out during my visit to the Laboratoire de Physique des Plasmas, which aimed at characterizing the plasma plume, both in space and time, thus trying to provide a better explanation of the physics behind an alternate ions plume expansion and neutralization. My personal contributions include, apart from the plume measurements and their post-processing and interpretation, the building of the Langmuir probes and of an innovative plasma potential sensor to study the oscillating potential inside the plume. The evolution with distance of time averaged plume parameters has been obtained and evidence of localized travelling beam packets has been found [1]

[1] The contents of this chapter are based on a conference paper [161]

6.1 Introduction

The alternate extraction and acceleration of positive and negative ions for propulsion is a new concept, proposed and validated experimentally at the Laboratoire de Physique des Plasmas (LPP), as shown in Refs. [34, 35, 36, 37, 38]. This innovative thruster concept is named PEGASES, acronym for *Plasma propulsion using Electronegative GASES*, and achieves the alternate acceleration of positive and negative ions with the use of an ion optics system, that switches its potential in time.

As explained more in detail in the next section, a square voltage waveform with a frequency of hundreds of kHz is applied to the screen grid, while the acceleration grid is grounded. By controlling the duty cycle (ratio between the positive voltage and the total wave periods), an overall neutral beam can be extracted, as shown in Ref. [37], thus requiring no further neutralization. The resultant plasma plume is composed only of positive and negative ion beam packets with (theoretically) no electrons, a characteristic which makes this thruster concept interesting for several reasons.

Firstly, since no neutralizer is needed, this thruster would not suffer from hollow cathode lifetime limitations, which affect other, more mature thruster technologies. Moreover, this cathode-less design allows to scale down the thruster, both in size and power, without important propellant utilization efficiency losses (a neutralizer, on the contrary, would require a minimum neutral gas flow to work, regardless of the thruster size). Finally, an electron-less plasma plume presents several advantages for the ion beam shepherd technique, treated in detail in Chapter 5, and which largely benefits from very low divergence plasma plumes at relatively large distances from the thruster ($10 - 20$ m). In fact, the absence of light electrons makes the plume expansion almost insensitive to the Earth's magnetic field (which might distort or affect the expansion of a plasma plume containing electrons in non-trivial ways) and, at the same time, the divergence growth due to the residual electron pressure (the major source of divergence increase in electric thruster plumes, as shown in Chapter 2), is effectively cancelled.

While the working principle of PEGASES has already been demonstrated by testing a prototype at LPP, some phenomena still need to be further investigated. While some advances in the modeling of an alternate ions plume have been recently achieved, especially for what concerns the near region, as shown in Ref. [162], from an experimental point of view, this field remains almost completely unexplored. This chapter then describes the most recent experimental activities carried out to characterize the PEGASES plasma plume, both in space and in time. In Sec. 6.2, the thruster elements and its working principles are presented. In Sec. 6.3, the experimental setups are described. In Sec. 6.4, the results of respectively the spatial and time resolved characterization campaigns are presented and discussed, while the conclusions are summarized in Sec. 6.5.

6.2 PEGASES elements and working principles

Fig. 6.1 shows a vertical cross section of the PEGASES thruster. This has an external metal housing, 12 cm long with a rectangular cross section, of dimensions 8 × 12 cm. An internal metal source tube is coupled inductively to an RF antenna through a ferrite core and a ceramic window. The plasma is generated close to the ceramic window through an inductive discharge, by injecting propellant through 8 injection holes, distributed axially along the thruster length. The internal metal housing, in contact with the plasma, is electrically insulated from the external grounded one by means of a Teflon piece.

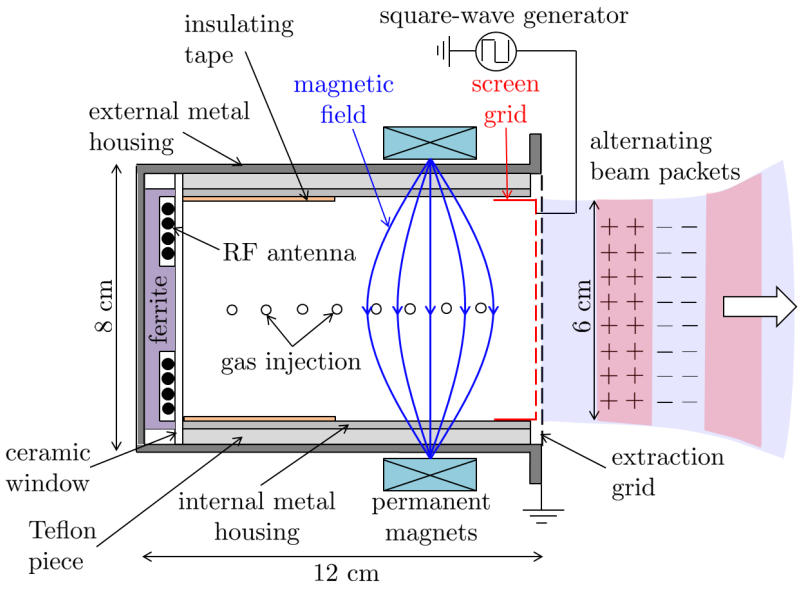

Figure 6.1: Schematic of the PEGASES thruster.

A transversal magnetic field, generated by external permanent magnets allows to reduce the electron temperature downstream by approximately a factor of 10, as shown in Ref. [163]. If an electro-negative gas is used as propellant, the resulting low energy electrons, instead of crossing the magnetic field lines through collisions, tend to be captured by the gas atoms and form negative ions, which can traverse easily the magnetic field barrier, together with the positive ions, thus maintaining the plasma quasi-neutrality.

Thus, an ion-ion plasma with a very high electronegativity (ratio between negative ion and electron number densities) can be achieved close to the screen grid. Such plasma is electrically insulated from the electron plasma close to the RF antenna, where the electron density is not negligible, by means of an insulating tape. In this way, the ion-ion plasma potential can follow more freely the applied screen grid voltage, avoiding some problems encountered in a previous thruster design, as shown in Refs. [35] and [164].

By applying a square voltage waveform of a sufficiently high frequency (hundreds of kHz) to the screen grid, in order to prevent the formation of an excessive space

charge region and hence beam stalling, it is finally possible to alternatively extract positive or negative ions, thus forming a plume made of alternated beam packets, as shown in Fig. 6.1. For the experimental campaign described here, a frequency of 250 kHz was considered with a duty cycle of 0.5 (negative and positive voltage half periods are equal). These conditions are very close to the optimal frequency for current extraction, as shown in Ref. [37].

While ideally no electrons should be extracted, in reality, some of them reach the screen grid region and are extracted during the negative voltage half period. In fact, as observed in Ref. [165], one lateral surface of the thruster presents a relative geometry between the plasma sheath electric field and the transversal magnetic field, that yields an $\boldsymbol{E} \times \boldsymbol{B}$ drift towards the screen grid, as shown in Fig.6.2. For this reason, in the following experiments, in order to minimize the amount of co-extracted electrons, the screen grid half surface close to this lateral thruster surface was blocked. So, the active screen grid area or the initial plume cross section is a 6×6 cm square.

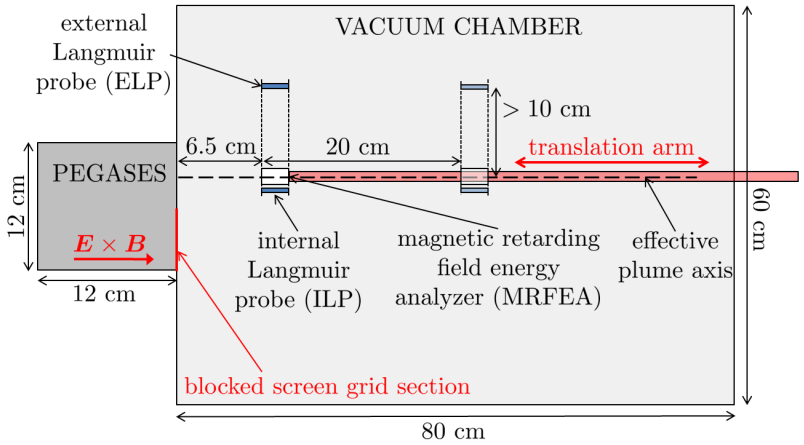

Figure 6.2: Spatial characterization campaign setup. Horizontal cross section of the vacuum chamber and thruster.

6.3 The experimental setup

The vacuum chamber used for the experimental campaign is a cylindrical chamber of 60 cm diameter and 80 cm length. The PEGASES thruster is connected to one side of this chamber, through a dedicated flange, as shown in Fig.6.2. The vacuum is achieved through a rotative primary pump and a magnetic levitated turbo-molecular pump, which permit achieving a downstream pressure as low as $2 \cdot 10^{-6}$ mbar, with zero mass flow rate. With the thruster on, the downstream pressure was always higher than $6 \cdot 10^{-5}$ mbar, reaching a maximum value around $2 \cdot 10^{-4}$ mbar, for the highest tested mass flow rate.

6.3.1. Spatial diagnostics

The spatial characterization campaign had the major goals of determining:

- the amount of electrons downstream, identifying their major source,
- the time-averaged profiles of ion density, electron temperature and plasma potentials along the plume centerline, and
- any evidence of downstream recombination.

The experimental setup is schematically shown in Fig. 6.2, while Fig. 6.3 shows a photo taken inside the vacuum chamber with an active plume.

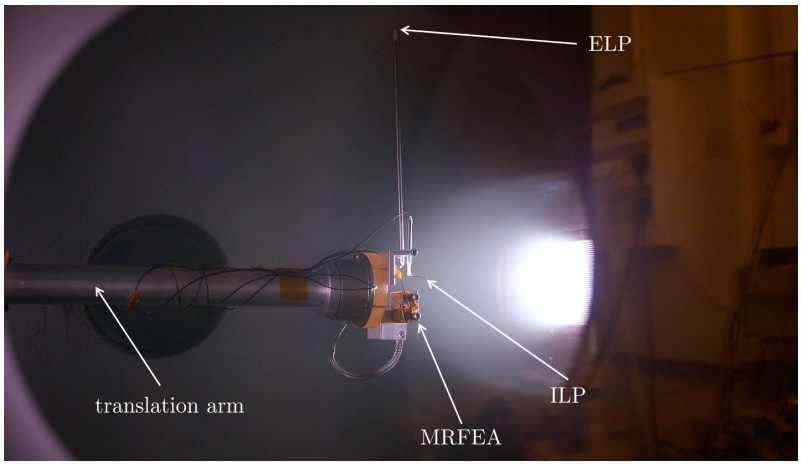

Figure 6.3: Photo of the PEGASES plume during the spatial characterization campaign.

As previously mentioned, one half of the screen grid was blocked to prevent the extraction of the electrons from the thruster lateral surface that was characterized by the $\boldsymbol{E} \times \boldsymbol{B}$ drift (right side lateral surface in Fig. 6.2). The diagnostics were then aligned with the centerline of the effective plume, of initial size 6×6 cm. Such diagnostics consisted of two Langmuir probes and a Magnetic Retarding Field Energy Analyzer (MRFEA), fully described in Ref. [166]. The Langmuir probes consist of a tungsten wire and an insulating alumina tube. One probe is located at the plume centerline (internal Langmuir probe or ILP), and another is located out of the main plume at a distance higher than 10 cm from the beam centerline (external Langmuir probe or ELP).

Regarding the MRFEA, this is a retarding field energy analyzer, with one grounded grid, a varying voltage collector and a magnetic system generating a homogeneous transversal magnetic field in the entrance slit. Such field prevents electrons from being collected, while letting the ions (positive and negative) flow through. As shown in Ref. [166], the MRFEA grid transparency above ion energies of 200 eV can be considered almost constant and equal to 30%.

Table 6.1: Properties of the spatial characterization diagnostics.

Diagnostic properties	**Units**	**Values**
ILP tip length	mm	81.8
ELP tip length	mm	13.0
ILP and ELP diameter	mm	0.5
ILP and ELP material	n/a	tungsten
MRFEA collector area	cm^2	1.0
MRFEA transparency	%	30.0

The properties of the above described diagnostics are summarized in Tab. 6.1. Referring to Fig. 6.2, the diagnostics could be moved axially by 20 cm with the use of a translation arm.

All experimental cases were run with a constant power from the RF generator of 200 W. Four different mass flow rates were tested, as summarized in Tab. 6.2, and corresponding to either 3 or 6 SCCMs of Ar or SF_6. Argon was also considered for cases 1 and 2, as it is the gas currently used to ignite the thruster (a direct ignition with the electronegative SF_6 cannot be achieved). For each of the 4 cases, 2 different screen grid square voltage amplitudes were considered (250 and 350 V).

Table 6.2: Experimental cases of the spatial characterization campaign.

Case N.	**Voltage Amplitudes (V)**	**SF_6 mass flow rate (mg/s)**	**Ar mass flow rate (mg/s)**
1	250, 350	0.652	0.178
2	250, 350	0.326	0.089
3	250, 350	0.652	0.000
4	250, 350	0.326	0.000

The downstream chamber pressure and the ion mean free paths corresponding to the above defined experimental cases, are finally reported in Tab. 6.3. The latter have only been roughly estimated, as the real plasma is a mixture of many ionic types (as it is typically the case for SF_6) and limited collisional data is available.

Table 6.3: Plume and vacuum parameters for the 4 considered spatial characterization cases.

Case N.	**Downstream pressure (mbar)**	**Downstream ion mean free path (cm)**	**Ion mean free path at thruster exit (cm)**
1	$2.00 \cdot 10^{-4}$	140	37
2	$1.06 \cdot 10^{-4}$	270	75
3	$1.13 \cdot 10^{-4}$	250	57
4	$6.00 \cdot 10^{-5}$	480	114

6.3.2. Time-resolved diagnostics

The time resolved characterization campaign had the major goals of determining:

- whether the beam packets are localized in space and if this changes with the distance from the thruster, and
- the peak to peak and time averaged values of the plasma potential in the plume.

The experimental setup, modified for this time characterization campaign, is shown in Fig. 6.4, while Fig. 6.5 shows a photo of the plume taken during this campaign.

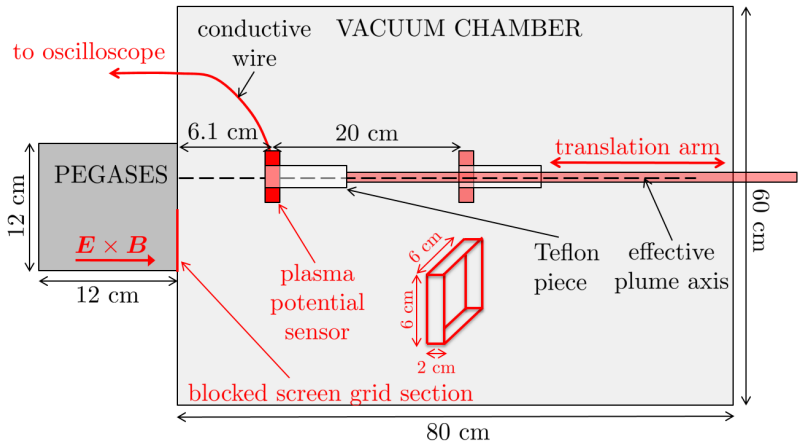

Figure 6.4: Time resolved campaign setup. Horizontal cross section of vacuum chamber and thruster.

In order to measure the plasma potential inside the plume as a function of both space and time, a special capacitive potential sensor was designed for this campaign, consisting of a copper square ring of cross section 6×6 cm, equal to the initial beam size, and with a depth of 2 cm. Such a sensor was aligned with the PEGASES plume, as shown in Fig. 6.4, and its distance from the source could be changed with a translation arm by as much as 20 cm. This ring was connected to the arm through an insulating Teflon piece. In short, such a sensor should follow closely the evolution in time of the plasma potential, provided that its coupling capacity with the plume is sufficiently high. To better understand this concept, refer to Fig. 6.6.

The alternating ion beam packets act as a source of alternating voltage ϕ_p, coupled to the sensor through the plasma sheath capacity C_{ring}, which depends on the total lateral surface of the ring and on the sheath depth (unknown a priori). Of course, a proper modeling of the conduction current to the ring also requires adding a parallel resistance to the model. However, at the frequencies considered here, the contribution of the conduction current can be neglected and, in any case, by doing so, we are considering a worst case scenario (the conduction currents have the effect of improving the quality of the measured signal). Other important elements of the circuit are the feedthrough capacity C_{feed} and the oscilloscope equivalent circuit, consisting of a resistance R_{osc} in parallel with a capacity C_{osc}.

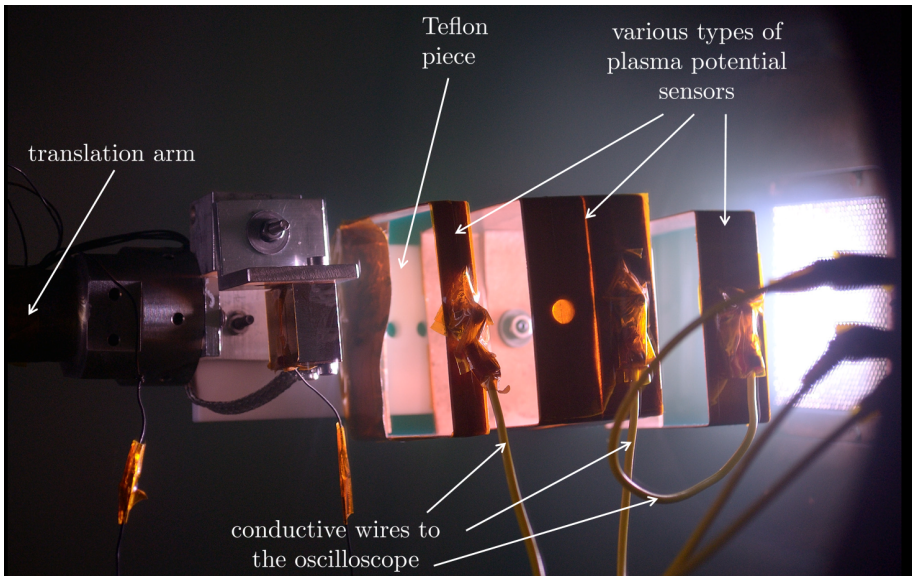

Figure 6.5: Photo of the PEGASES plume during the time characterization campaign. Different shapes of potential sensors were tested, although the results shown here have been obtained with the sensor to the right.

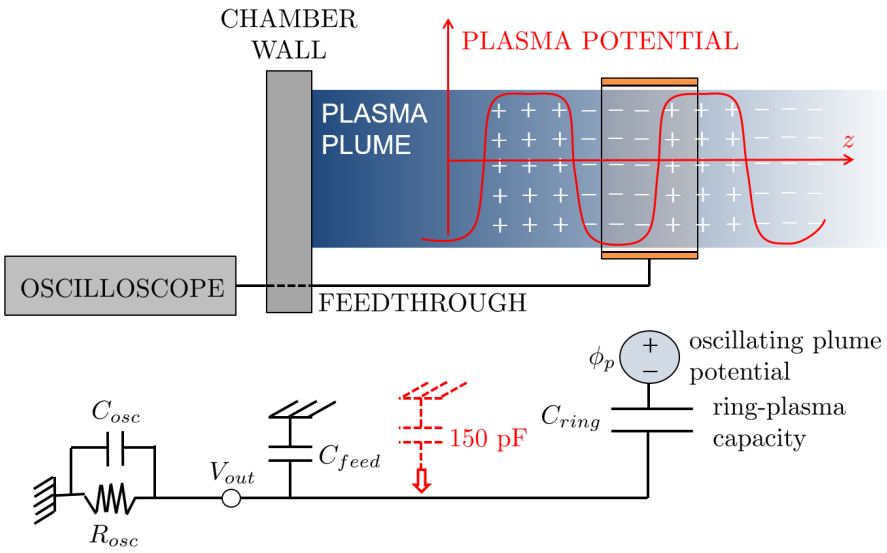

Figure 6.6: Schematic and equivalent circuit of the plasma potential sensor.

A rough estimation for the depth of the sheath forming between the sensor and the plasma can be obtained by inverting the Child Langmuir's space charge formula and assuming some rough estimations for the voltage drop $\Delta\phi_s$ and the current density j_i across the sheath, as shown in Eq. (6.1), where m_i is the ion mass and ϵ_0 is the dielectric constant of a vacuum:

$$d_s = \left(\frac{4}{9}\epsilon_0\sqrt{\frac{2e}{m_i}}\frac{\Delta\phi_s^{3/2}}{j_i}\right)^{1/2}. \tag{6.1}$$

By assuming $\Delta\phi_s = 10$ V, and $j_i = c_s n_i e = 19$ mA/m^2, where c_s is the expected ion sound velocity (or Bohm's velocity), n_i is the expected plasma density and e is the electronic charge, the sheath depth is approximately 3 mm, so that the coupling capacitance can be roughly estimated as:

$$C_{ring} = \frac{2\epsilon_0 \Delta S_{ring}}{d_s} \approx 28\text{pF}, \tag{6.2}$$

where ΔS_{ring} is the lateral surface of the sensor in contact with the plasma. According to the equivalent circuit of Fig. 6.6, if we assume that the oscilloscope series resistance is very large and that we can neglect the current flowing through it, then the measured potential V_{out} is given by:

$$V_{out} = \phi_p \left(1 - \frac{C_{feed} + C_{osc}}{C_{feed} + C_{osc} + C_{ring}}\right). \tag{6.3}$$

So, if $C_{ring} \gg C_{osc} + C_{feed}$, the output voltage measured by the oscilloscope would coincide with the plasma potential inside the plume. The value of the oscilloscope input capacitance is a manufacturer provided value, 9.5 pF for the oscilloscope probes used here, while the feed-through capacity can be generally neglected (lower than 1 pF). By connecting in parallel to the oscilloscope a known capacity of 150 pF, as shown in Fig. 6.6, it was then straightforward to obtain an indirect measurement of the ring capacity. In fact, it turns out that the ratio between the output voltage amplitude V_0 measured without this capacitance and the output voltage amplitude V_1 measured with it, is a direct function of the ring-plasma mutual capacitance, as shown by Eq. (6.4):

$$\frac{V_0}{V_1} = \frac{C_{osc} + C_{ring} + 150\text{pF}}{C_{osc} + C_{ring}}. \tag{6.4}$$

In this way, we estimated it to be 20.5 pF, a value which is not very different from the one previously obtained. Since the oscilloscope input capacitance is 9.5 pF, the measured voltage should correspond to approx. 70% of the real plasma potential. For the purposes of this characterization, this was considered enough to get representative electric potential evolutions in space and time. Finally, for the time-resolved characterization campaign, we considered only the case N.4 of Tab. 6.2: 0.326 mg/s of pure SF_6, with applied voltages of either 250 or 350 V. The distance between the sensor center and the thruster exit was initially 6.1 cm and it could be extended, once again, up to 26.1 cm with the use of the translation arm.

6.4 Experimental results and discussion

Before, proceeding with the presentation of the results, it is paramount to say that the observed measurements were dominated by electrons. Therefore, no ion-ion plasma theory has been used here to post-process the measurements. Moreover, as mentioned before, the plasma is a mixture of many different types of ions (both positive and negative), due to the use of SF_6 as electronegative propellant. Therefore,

in the following, we have assumed an average ion mass $m_i = 100$ AMUs (atomic mass units) as a first approximation for the considered SF_6-Ar mixture.

6.4.1. Spatial characterization campaign

From the Langmuir probe measurements, it was observed that the probe current first derivative was very noisy close to the plasma potential and that, in general, it did not reach a saturation value. So, computing the plasma potential as the maximum of the collected current first derivative or as the first zero (after the floating potential point) of the second derivative, produced large errors. For this reason, we followed a different approach. First of all, the floating potential ϕ_f was determined as the probe voltage for which a zero current was measured, and, secondly, the electron temperature was obtained from the portion of the I-V characteristic where the $\ln T_e$ vs $\ln n_e$ was rectilinear. Here n_e and T_e represent respectively the electron density and temperature. Then, the plasma potential ϕ_p was computed by assuming a Maxwellian population of electrons as:

$$\phi_p = \phi_f + T_e \left[0.5 + \ln \left(\frac{m_i}{2\pi m_e} \right) \right]. \tag{6.5}$$

This approach is also justified by the fact that the Langmuir probe characteristics showed a positive voltage saturation region clearly dominated by electrons, either extracted from the PEGASES or created downstream by secondary processes (ionizing collisions of ions against neutral gas atoms or ion bombardment secondary emissions with the chamber walls). The evolution of the floating potential with the distance from the thruster exit d, for an applied voltage of 250 V and 350 V, is respectively shown in Fig. 6.7 (a) and (b).

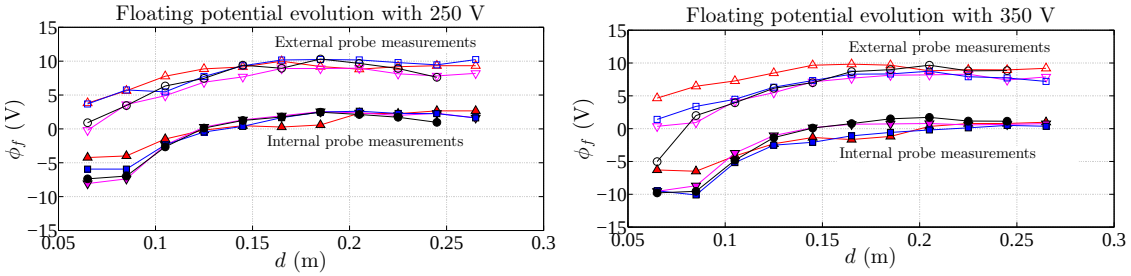

Figure 6.7: Time-averaged floating potential Vs distance from the thruster for (a) 250 V of grid voltage, and (b) 350 V of grid voltage. Filled markers refer to the internal probe, empty markers to the external one. Case N.1 is shown with red upwards triangles, case N.2 in magenta downwards triangles, case N.3 in blue squares and case N.4 in black circles.

The time-averaged floating potential is slightly negative (as low as -10 V) close to the thruster exit, meaning that the negative ion current density should be slightly higher than the positive ion current density. This implies that the 50% duty cycle used here, seems to favour the extraction of negative ions. As we get farther

away from the thruster, however, the floating potential approaches 0, meaning that the plume eventually neutralizes. Moreover, the floating potential seems to depend weakly on both the mass flow rates and the applied voltage magnitude and it is always higher for the external Langmuir probe, by approximately 10 V. This behaviour suggests that the main source of surface charging inside the plume is represented by negative ions, absent for the external Langmuir probe, which thus requires a higher voltage to draw no net current. The time-averaged electron temperature evolution with the distance, on the other hand, is shown in Fig.6.8 (a) and (b), for respectively the 250 and 350 V cases. The electron temperatures are generally higher inside the main plume than outside and they are between 4 and 5 eV very close to the thruster exit. The electron temperature inside the plume tends to decrease with the distance from the thruster, reaching a value around 3 eV, at a distance of 25 cm. The external probe electron temperature is less dependent on the distance from the thruster and it varies between 3 and 3.5 eV.

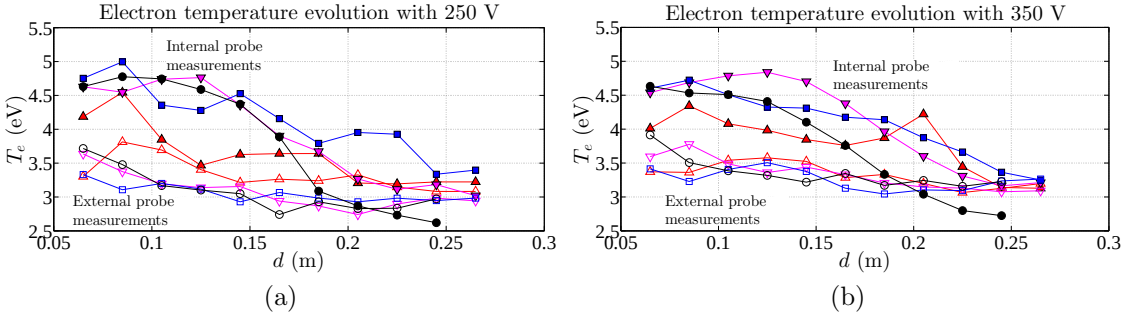

(a) (b)

Figure 6.8: Time-averaged electron temperature Vs distance from the thruster for (a) 250 V of grid voltage, and (b) 350 V of grid voltage. Filled markers refer to the internal probe, empty markers to the external one. Case N.1 is shown with red upwards triangles, case N.2 in magenta downwards triangles, case N.3 in blue squares and case N.4 in black circles.

With the time-averaged floating potential and electron temperature evolutions, we could then determine the plasma potential, shown in Fig. 6.9 (a) and (b).

The plasma potential behaves differently inside and outside of the main plume. For the outside ambient plasma, the plasma potential increases slightly at the beginning to reach a plateau around 25 V, for both voltage cases. The plasma potential inside the plume, on the other hand, increases at the beginning, probably due to some ion focusing (which makes the plasma density increase with the distance), to later start decreasing monotonically, as for a standard diverging plasma plume. The peak plasma potential is reached at a distance of approximately 15 cm from the thruster exit. The fact that the plasma potential is higher outside of the main plume is hard to explain and should be further tested and investigated in future work. A possible explanation could be that a high negative ion density inside the plume, bigger than the positive ions density for the considered thruster operational point, results in an inwards ambipolar electric field, which is opposite to the one normally found in a conventional neutral plasma plume (directed outwards).

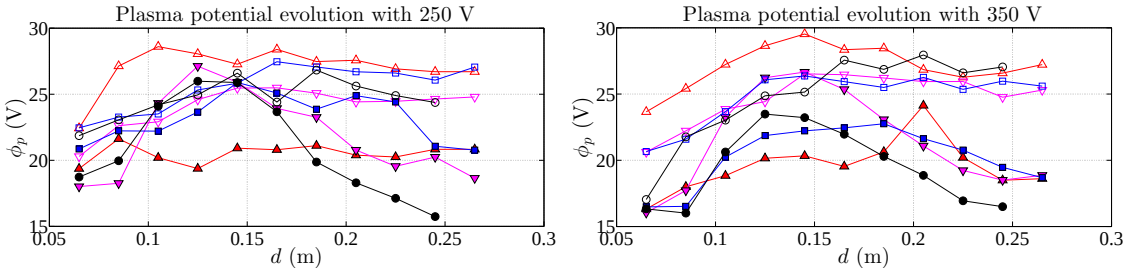

Figure 6.9: Time-averaged plasma potentials Vs distance from the thruster for (a) 250 V of grid voltage, and (b) 350 V of grid voltage. Filled markers refer to the internal probe, empty markers to the external one. Case N.1 is shown with red upwards triangles, case N.2 in magenta downwards triangles, case N.3 in blue squares and case N.4 in black circles.

From the knowledge of the plasma potential and the Langmuir probes geometry, we then computed the electron density inside and outside of the plume. This is shown in Fig. 6.10 (a) and (b).

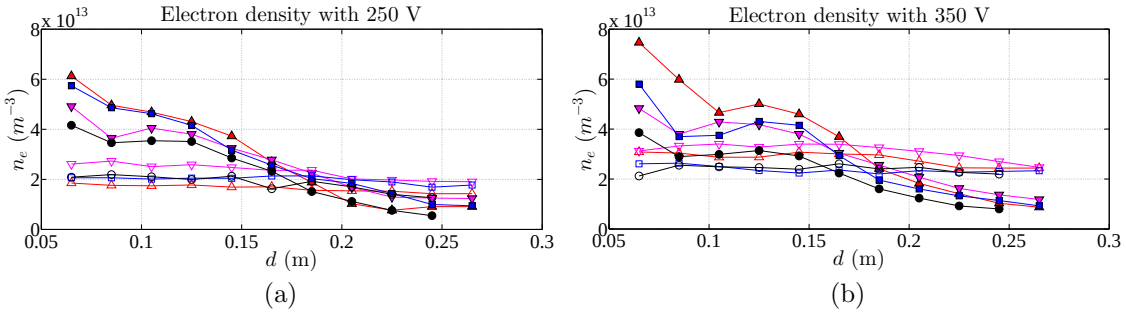

Figure 6.10: Time-averaged electron densities Vs distance from the thruster for (a) 250 V of grid voltage, and (b) 350 V of grid voltage. Filled markers refer to the internal probe, empty markers to the external one. Case N.1 is shown with red upwards triangles, case N.2 in magenta downwards triangles, case N.3 in blue squares and case N.4 in black circles.

Once again, for the external probe, the electron density does not vary much with the distance and is around $2 \cdot 10^{13}$ m^{-3} (for 250 V) and $3 \cdot 10^{13}$ m^{-3} (for 350 V). Inside the plume, on the other hand, the electron density rapidly decreases with the distance. This means that electrons are drawn towards the center of the plume to compensate, on average, the total space charge and this compensation is higher, the denser the plume. In all cases, at a distance between 15 and 20 cm, the electron density inside the plume drops below its value outside of the plume, as dictated by the fact that the electric potential inside the plume is lower than the one outside. Regarding the effect of the mass flow rate, the cases with the highest total mass flow rates (cases N.1 and 3, respectively in red and blue) also present the highest electron densities, as clearly expected.

The electron densities and temperatures can be plotted in a log-log plot to verify if a polytropic law is applicable. This is done in Fig. 6.11, for the experimental case

N.3.

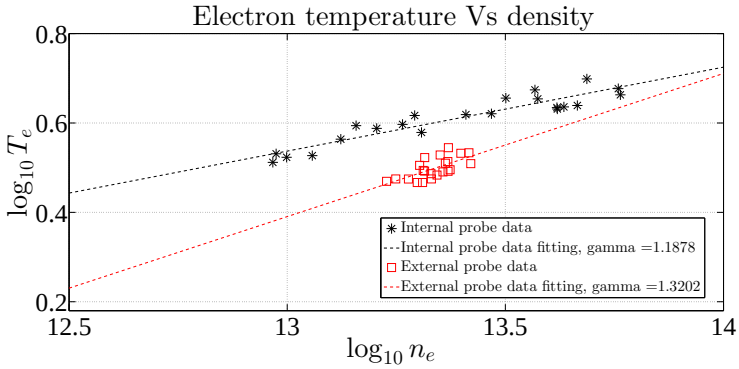

Figure 6.11: Time-averaged electron temperature Vs density in a log-log plot. T_e is in eV, while n_e is in m^{-3}. The corresponding polytropic coefficients, which are the slopes of the linear fittings, are shown as well. Data for the 250 and 350 V cases has been merged together.

The effective polytropic coefficients for the other experimental cases are summarized in Tab. 6.4. The reported values are compatible with electropositive plume values found in literature, which are between 1 and 1.3, as shown in Refs. [16, 56, 57, 58]. Moreover, it seems that the lower the SF_6 mass flow rate (cases N.2 and 4, featuring 3 SCCMs), the higher the γ for the internal electrons. This suggests that some phenomenon strictly correlated with the mass flow rate of SF_6, is taking place. The lower this mass flow rate, the faster the electrons cool down (a higher polytropic coefficient means faster cooling).

Table 6.4: Polytropic coefficients for the different experimental cases.

Case N.	**Polytropic coefficient for the external electrons**	**Polytropic coefficient for the internal electrons**
1	1.05	1.12
2	1.32	1.34
3	1.32	1.19
4	1.28	1.35

Let us now consider the results obtained with the MRFEA. Some difficulties were encountered when trying to characterize the ion energy distribution function for the positive ions, as some films due to SF_6 deposition were constantly forming on the collector. The positive voltage sweep of the MRFEA then induced constantly a breakdown of this film, thus contaminating the quality of the measurements. An example of an experimental ion energy distribution function for the case N.4 is shown in Fig. 6.12. The ion energy distribution function can be simply computed as the derivative of the collected MRFEA current with respect to the voltage. The mentioned film formation/destruction effects make the positive ion energy distribution function reach much higher peaks than that of the negative ions. Given this difficulty, we have opted to analyze only the IEDF of the negative ions.

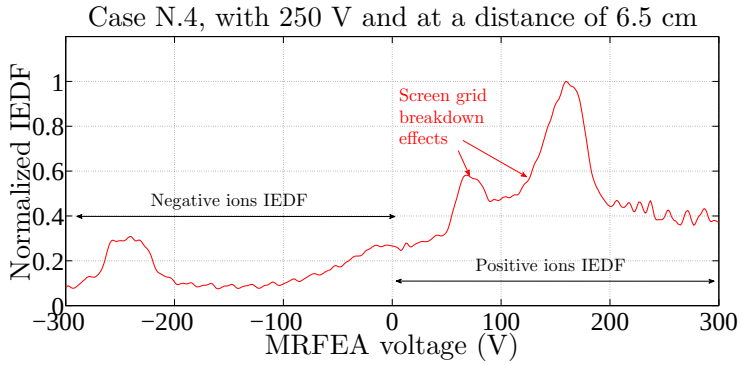

Figure 6.12: Normalized ion energy distribution function for the experimental case N.4, with 250 V of grid voltage amplitude, and at a distance from the thruster exit of 6.5 cm.

The evolution of the time-averaged negative ion energy distribution function with the distance is shown in Fig. 6.13, for a 300 V grid voltage case with 0.326 mg/s of pure SF_6.

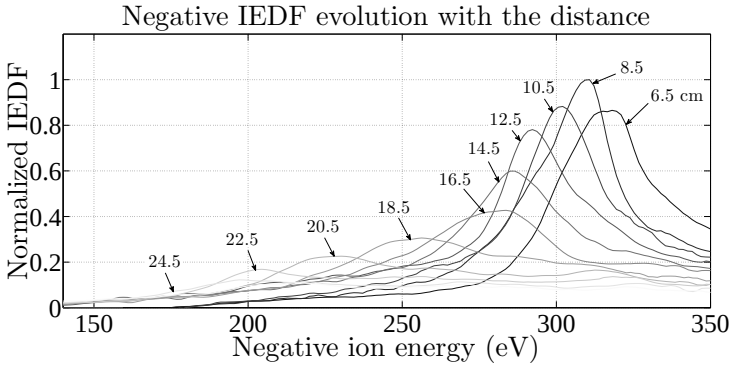

Figure 6.13: Evolution with distance of the negative IEDF for a 300 eV plume with 0.326 mg/s of pure SF_6.

The negative ion energy distribution function shows some interesting features. First of all, since its peak increases between 6.5 and 8.5 cm distance, it shows some evidence of beam focusing. Secondly, its peak tends to shift to a lower voltage (or energies) with the distance. This can be due to an electrostatic deceleration, instabilities (two-stream for example) or the effect of collisional processes. The first reason seems to be unlikely (unless there is some important time averaging effect of some strongly correlated phenomena) because the time-averaged electric potential variations with distance are of the order of 10 V, as shown in Fig. 6.9, while the voltage shifts identified in Fig. 6.13 are much bigger. Therefore, we do not exclude that some inelastic processes (like recombination for example) between fast positive and negative ions or some plume instabilities are responsible for the observed behaviour of the ion energy distribution evolution with distance.

If the IEDF of the negative ions is integrated in voltage, the evolutions of the time-averaged negative ion current densities can be obtained for all experimental

cases, as shown in Fig. 6.14 (a). With the knowledge of the expected ion velocity and the current density, an estimation of the time-averaged negative ion density can be finally obtained and it is shown in Fig. 6.14 (b). A quick check shows that the obtained density is quite lower (by at least one order of magnitude) than the expected ion density, which can be obtained from the known values of mass flow rate (3-6 SCCMs), exhaust ion velocity ($\simeq$ 20 km/s), and extraction area (6$\times$6 cm). This difference could be due to a quite low ionization efficiency and a misalignment of the MRFEA center from the plume centerline (which are important at low distances). Moreover, the time-averaged negative ion density is half the instantaneous density inside the beam packets, given the 50% duty cycle considered here.

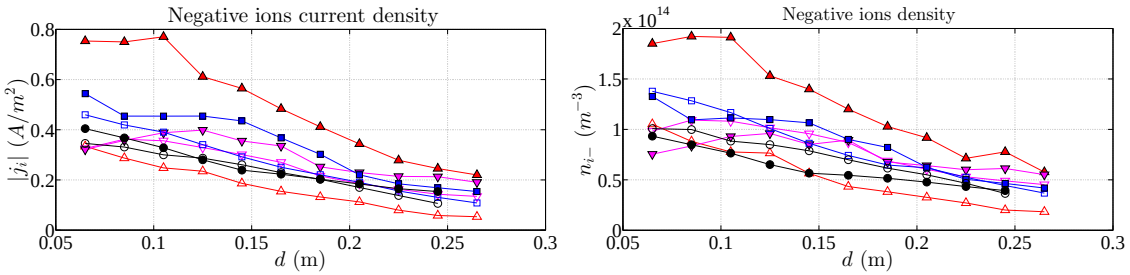

Figure 6.14: Time-averaged negative ion properties Vs distance from the thruster: (a) negative ion current densities, and (b) negative ion densities. Empty markers refer to the 250 V case, while filled markers to the 350 V case. Regarding the experimental cases, case N.1 is shown with red upwards triangles, case N.2 in magenta downwards triangles, case N.3 in blue squares and case N.4 in black circles.

In any case, if we compare these density results with Fig. 6.10 (a) and (b), we see that the time-averaged electronegativity in the plume is between 1 and 5. Inside the instantaneous negative ion beam packets, however, this ratio could be higher. Low values of the electronegativity are compatible with the Langmuir probe measurements, which were dominated by the electron current contribution and did not show the typical ion-ion plasma shape.

6.4.2. Time-resolved campaign

During the time resolved campaign, some thruster instabilities were clearly observed. In fact, by decreasing the applied positive voltage amplitude below 150 $-$ 200 V, a transition to a "dark mode" was observed, in which the plume was almost invisible and, in addition, hardly measurable because of the very low level of the signal from the probes. Such a mode persisted if we then returned to the original symmetric applied voltage conditions. A transition of this type is shown in Fig. 6.15, where the normal mode of operation is referred to as "bright mode". As it can be clearly seen, the time-averaged voltage changes from a positive to a negative value. Further investigation on the reasons of such a mode transition should be carried out in the future. For what concerns this work, the dark mode was no longer analyzed.

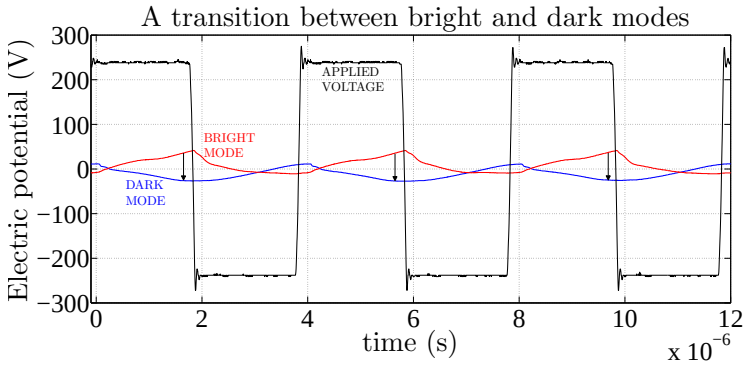

Figure 6.15: Transition in measured plasma potential voltage between bright (red) and dark (blue) mode. The applied voltage is shown in black and the time is measured from the start of the positive voltage half period.

In the normal (bright) mode, it was possible to study the evolution of the measured signal as a function of the distance from the thruster, as shown for the 250 V case in Fig. 6.16 (a). It can be clearly observed that the plasma oscillations become smaller as we get farther away (from an initial value of 60 V down to 20 V at distances higher than 10 cm). In addition, no clear signal shift can be observed with the distance, indicating that there is no clear sign of ion beam packets. The fact that all curves drop together at the start of the negative half period (at 2, 6 and 10 μs), indicates that electrons are still being extracted from the thruster and that, given their extremely high mobility, they smooth out the electric potential everywhere.

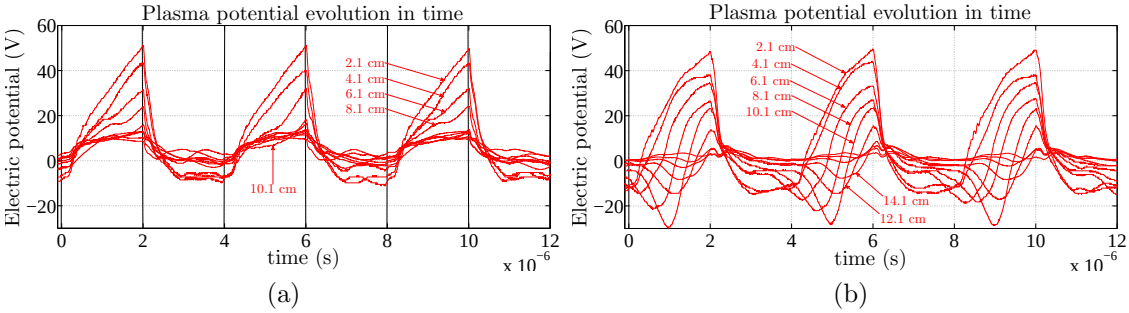

Figure 6.16: Measured voltages at different distances from the thruster with bright mode, for the (a) 250 V case, and (b) 350 V case. Black straight lines refer to the half periods of the applied waveform.

For the 350 V case, the results are shown in Fig. 6.16 (b). In this case, there is a clear shift of the measurements with the distance from the thruster, indicating that the electric potential is affected by some travelling ion beam packet. Nevertheless, during the negative voltage half periods, any evidence of beam packets is immediately cancelled, thus confirming the fact that electrons are still being emitted by the thruster.

An interesting picture of the electric potential as a function of the distance from the thruster can be obtained if we consider the voltage measurements of Fig. 6.16

(b), at specific instants of time. If we take them at 4, 4.5 and 5 µs, we obtain the plot of Fig. 6.17.

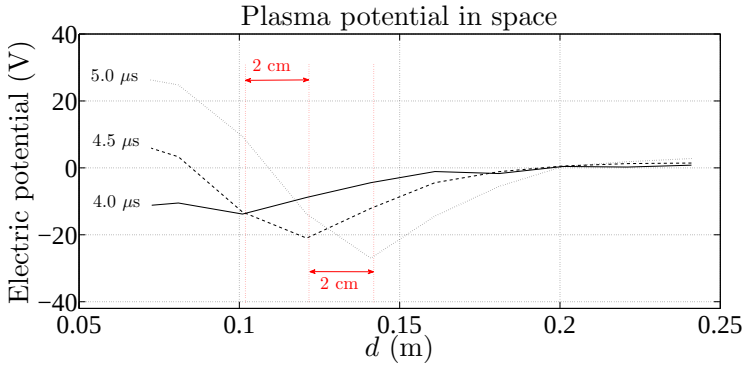

Figure 6.17: Measured voltage as a function of the distance at three instants of time: 4, 4.5 and 5 µs. The spatial resolution is 2 cm.

It is apparent that a travelling beam packet is displacing to the right at a constant velocity. Since the distance between the minima in Fig. 6.17 is 2 cm and the required time is 0.5 µs, we deduce that the travelling beam packet is roughly moving at 40 km/s, an intermediate velocity between the 20 km/s (for SF_6 negative ions) and the 60 km/s (for F ions), corresponding to ions energies of 350 eV.

6.5 Conclusions and future work

The work presented in this section has permitted characterizing experimentally, for the first time, the peculiar alternate ions plume of the PEGASES thruster. This has been carried out through two dedicated campaigns: a spatial characterization and a time-resolved characterization campaign.

With the first one, it has been possible to obtain the time-averaged 1-D evolutions (with the distance from the thruster) of plasma potential, floating potential, electron density and temperature, and negative ion density. It has been found that the electronegativity inside the plume is very low, indicating that either the electrons are generated outside the thruster by secondary processes or that they are directly extracted from the thruster grids. The evolution of the negative ion distribution function has also been obtained with a dedicated magnetic retarding field energy analyzer. This energy distribution has been found to shift to lower energies, while becoming wider, as we get farther downstream. A possible explanation of this behaviour is that of the collisions between the plume ions and the neutral atoms, however, given the expected mean free paths for ions, this phenomenon alone cannot fully explain the measurements. It is not excluded, therefore, that some recombination between positive and negative ions is taking place at distances between 5 and 25 cm from the thruster exit.

With the time-resolved characterization campaign, on the other hand, the evolutions in time and space of the plasma potential inside the plume have been ob-

tained. Measurements have shown that electrons are certainly being extracted from the thruster during the negative voltage half period. So, the strategy of blocking the half of the thruster grids close to the lateral surface, from which electrons are expected to come, has proved not to be very efficient. In any case, measurements have provided some evidence of well localized ion beam packets, during the positive voltage half periods.

Regarding future work, the two operating modes of the PEGASES thruster, identified during the time-resolved characterization campaign, should be further investigated, as a transition from a bright to a dark mode yields an abrupt change in the performance and should be avoided.

Moreover, the MRFEA measurements should be repeated with a new probe design, not affected by the film formation/destruction phenomenon observed during this campaign. In this way, the evolution of the positive ion energy distribution function and density would be obtained and would help understand the overall plume physics. Repeating the experiments with a different propellant like iodine, instead of SF_6, should be seriously considered in future experiments as it might simplify enormously the interpretation of the experimental results.

Finally, regarding the electron extraction from the thruster grids, some alternative measures to prevent it from happening, should be investigated and tested.

Chapter 7

Conclusions

In this chapter, the major contributions of this thesis are first summarized in Sec. 7.1, while the future research directives are outlined in Sec. 7.2.

7.1 Summary of contributions

This work has led to the development and validation of two codes for the simulation of plasma plumes, which are complementary to each other, and have been applied to different studies.

For what concerns the first developed code, named EASYPLUME, the major contributions have been:

- Formulation of two semi-analytic solution methods of a two-fluid plasma plume model, that allow a fast computation of plasma properties downstream, without the need of integrating the equations with complex numerical schemes. In particular, the existing plasma plume solutions have been unified under a common Self-Similar method (SSM) framework, and a new method, the Asymptotic Expansion Method (AEM), has been proposed.

- Physics discussion of the major factors affecting the plasma plume expansion in the far region: the electron cooling rate γ, the ion Mach number M_0, and the initial divergence angle α_0. It has been found that the closer to isothermal the electrons, and the smaller the ion Mach number, the larger the ambipolar electric fields, and hence the divergence growth of the plasma plume. The electric potential at infinity depends solely on the electron cooling rate, and diverges to $-\infty$ when $\gamma \to 1$. An equivalent divergence angle, at a given downstream section, has then been introduced to evaluate quantitatively the plume divergence growth. It has then been concluded that, in order to decrease this growth, at already low initial divergences, it is more advantageous to increase the ion Mach number than to decrease α_0. Moreover, the electron thermal effects on the plume divergence are more efficiently contained by increasing the emitted ion velocity (by applying a larger acceleration voltage)

than by reducing the electron temperature in the plume (which requires more challenging neutralizer designs).

- Study of the applicability of the proposed fluid model with a polytropic closure to a collisionless plume. In this regard, a comparison with a full-PIC model (from a different research group) has permitted identifying optimal polytropic coefficients to obtain a good match of the results of the two models. Thus, it is possible to assert that a fluid model retains an important part of the plume expansion physics, even when the plume is collisionless (and the fluid closures are theoretically unjustified).

The second developed code, EP2PLUS, permits simulating the three-dimensional plasma plume interaction with the satellite and/or other objects. This code can be applied to a large number of plasma plume studies and represents the largest contribution of this work. Moreover, the flexible and modular code architecture shall enable a quick inclusion of new simulation capabilities in the future. Apart from reaching the state-of-the-art in different algorithms (especially in what concerns the PIC sub-model), the following modeling novelties are worth mentioning:

- New electron fluid model that, while being based on a simple kinetic closure, retains the collisional terms, and permits solving for the electric current in the plasma plume.

- An automatic division of the simulation domain into quasineutral and non-neutral regions, depending on the local plasma properties. While in the former the electric potential is obtained directly by solving the electron conservation equations, in the latter these are coupled with Poisson's equation.

- Bohm's condition forcing algorithm for quasineutral material boundaries. While this approach is quite common for simulations of HET discharges (e.g. HP-Hall code), the use in a plasma plume code is quite innovative, and has not been considered in previous codes.

- Sputtering interaction between macro-particles and specific sputtered surfaces. This is not common in plasma plume codes, except for a few existing exceptions (e.g. SPIS). In addition, the sputtering properties can be obtained using the available software SRIM/TRIM.

- Structured conical mesh as a first population control solution, in plasma plume expansion studies.

Instead of focusing on complex simulation geometries, this work has considered simple structured meshes (in most cases Cartesian meshes), with the goal of validating the above algorithms in the most efficient way. In particular, the automatic subdivision of the simulation domain in quasineutral and non-neutral regions, enables the use of simple meshes, without the need of changing the cell size as a function

of the expected local Debye length (as necessary in full-PIC codes, or quasineutral codes).

Regarding the applications of the developed codes, the following results have been achieved:

- Simulation of the interaction between a plasma thruster plume and the emitting spacecraft with the use of EP2PLUS. This benchmark simulation has demonstrated the most important simulation capabilities, and permitted the evaluation of various phenomena such as the spacecraft electric charging, the ion backscattering flux, and the electric currents structure in the plume. For what regards these, the simulation has demonstrated that the plasma plume becomes current-free very quickly, starting from distances of $30-40$ cm downstream of the NSTAR ion thruster exit area (in which the electric current is maximum and provided by the emitted ions alone). Moreover, the effects of the electron thermodynamics and of the finite non-neutral regions have been evaluated as well, finding that they both have a non-negligible role in determining the backscattered CEX ion flux and the S/C floating potential. For what concerns the former, the closer to isothermal are the electrons, the higher the CEX backscattered flux and the ion wall-impact energy, and the lower the spacecraft floating potential. For what concerns the latter, a significant increase (up to 30%) in the backscattered CEX ion flux has been observed, when switching from the quasineutral to the non-neutral solver.

- Optimization of the electric propulsion subsystem of an IBS spacecraft, with the use of EASYPLUME and a simplified target interaction model. This study has permitted identifying the optimal operational points of both the impulse transfer thruster alone, and of the two thrusters (including the impulse compensation one) operating simultaneously. It has been found that the plume physics affects strongly the design choice: the ITT must guarantee a small initial divergence angle, as the conical beam expansion is the major factor that reduces the momentum transfer to the target, and hence the IBS efficiency. Therefore, the optimal operational point for the beam voltage of the impulse transfer thruster is much larger than that of the impulse compensation thruster, which can be maintained to low values (1 kV), to contain the power demand.

- Simulation of the complex interaction between satellite, plasma plume and debris, in an IBS mission scenario. Important physical effects that can affect significantly the success and performance of the mission have been evaluated: the ion backscattering flux, the backsputtering flux, and the stationary potentials of the IBS satellite and of the debris.

Apart from the main topic of simulations and modeling treated above, an experimental campaign has also been carried out during this thesis activities. The PEGASES plasma plume has been characterized experimentally for the first time. While a spatial characterization campaign has evaluated the 1D profiles (along the

plume axis) of plasma properties of interest, a time-resolved campaign has assessed the time evolution of the plasma potential inside the plume, with the use of an innovative plasma potential sensor (specifically built during my stay), finding also some evidence of localized travelling beam packets. Moreover, it has been found that the electronegativity inside the plume is very low, indicating that the current thruster design is still affected by a direct electron emission (during the negative half-period of the applied voltage waveform), so that future design improvements are necessary.

7.2 Future research directives

The field of plasma thruster plumes features a lot of open topics. In my opinion, two fields are particularly appealing: the collisionless electron cooling in the plume, and the effects of an external magnetic field on the plume expansion. The former topic deals with the understanding of the physical mechanism behind the gradual reduction of the electron temperature as the plume expands, and is amenable to simulations with fully-kinetic or full-PIC models [137]. For what concerns the effects of a magnetic field, on the other hand, these can be studied either numerically, e.g. with an improvement of the electron fluid model of EP2PLUS, or experimentally, with dedicated campaigns in large vacuum chambers. Regarding the latter, the recent LEOSWEEP project did not produce a definite conclusion on this matter, so that it remains an interesting and open investigation topic.

Coming to the research directives directly related to this thesis work, different investigation lines can be identified, as described in the following.

The fluid model of Chapter 2 is collisionless, a condition that permits solving it with the simplified semi-analytic methods of the SSM and AEM. While the inclusion of collisional effects between the emitted ions and neutrals or with the background plasma, is clearly possible, it would have the major drawback of making the proposed solution methods inapplicable. Therefore, at least in the context of the far-region plume modeling, the inclusion of collisional effects is not suggested. Two major investigation lines are proposed:

- The inclusion of the effect of an external magnetic field in the fluid model, which might be amenable to some kind of Self-Similar approach, as suggested by the work of Korsun [51, 52, 53].

- The extension of the fluid model comparison with a kinetic code to a more realistic axisymmetric plasma plume geometry.

In what regards the continued improvement and development of EP2PLUS, several research directives can be identified:

- Modeling new heavy particles collisions. Among these, of particular interest are the momentum exchange collisions between ions and neutrals (MEX), which are amenable to cross-section modeling, like the CEX collisions.

- Finer modeling of the sputtering effects, that include a generic distribution function for the emitted neutral particles (not based on a thermal emission, with predefined mean energy) or backscattered particles (not based on specular reflection with a deterministic energy reduction). Both distribution functions (for sputtered atoms and backscattered particles) can be obtained from the SRIM/TRIM software. Moreover, the possibility of generating clusters of sputtered atoms, with a given residual charge, should also be investigated.

- More effective population control to deal with the plume expansion effects. This should feature, on top of the already existing control, a particle renormalization algorithm, or the use of expanding PIC meshes that adapt to the local plasma density (larger cells where the macro-particles density is expected to drop).

- Extension of the electron fluid model to magnetized plasma plumes, in order to study the distorsion effects caused by any external magnetic field (such as the geomagnetic field) on a plasma plume expansion. This would feature the use of a conductivity tensor, instead of a scalar conductivity, while the Bernoulli's function approach appears to be quite promising in this respect.

- Generalization of the electron fluid model to generic kinetic closures, with coefficients determined by dedicated kinetic studies.

- Inclusion of conductive emissive surfaces, characterized by photo-emission, ion bombardment emission, secondary electron emission. These new surface types would not affect the PIC model, but rather the equivalent circuit and sheath models, having a non-negligible effect in the estimation of the electric charging of conductive objects.

- More complex structured meshes for the simulation of non-rectangular objects (sphere, cylinders, cones, etc...). The present work has not focused on this topic, which would require dedicated algorithms that automatically adapt the original mesh nodes to the requested object geometry.

The EP2PLUS code, with minor adjustments, then appears to be particularly suited for the following studies, which have not been object of research in the present work:

- Study of the beamlets formation and coalescence in an ion thruster grid system. This would require the non-neutral solver, with two independent populations of electrons: one for the outside plasma electrons, and another for the discharge chamber electrons (characterized by reference properties, such as the density and temperature, at different locations).

- Study of the plasma plumes produced by clusters of electric thrusters.

- Study of the interaction between the ambient plasma and electromagnetic tethers.

- Study of the expansion of an alternate ions plasma plume, like that of the PEGASES thruster.

For what concerns the applications considered in this work, the directives for future work have already been presented at the end of the corresponding chapters or sections, and are summarized here for the sake of completeness:

- The study of the interaction between the plasma plume and the satellite can be improved by adding the effects of sputtering on the satellite surfaces (low energy sputtering, quite different from the high energy sputtering on the target debris of an IBS mission). Moreover, the inclusion of other electron emission effects, might have a significant effect on the floating potential of the spacecraft, and needs to be further investigated.

- The electric propulsion subsystem optimization study can be improved by considering additional effects in the mass budget (thrusters, PPUs mass, etc...), different types of thrusters for ITT and ICT (a RIT type has been considered for both here), and a mission scenario featuring the de-orbiting of more than 1 debris object.

- The detailed simulation of the satellite-plasma-debris interaction, in the IBS context, can be improved by considering the effect of the geomagnetic field, and non-rectangular debris object geometries (the more realistic ones being truncated cones, or cylindrical shapes).

Finally, regarding the PEGASES characterization campaign, new thruster designs should be pursued to avoid both electron emission (due to the $\boldsymbol{E} \times \boldsymbol{B}$ drift), and the transition from a bright to a dark operational mode. Moreover, MRFEA measurements should be repeated with a new probe design, that allows to obtain the evolution of the positive ion energy distribution function and density (impossible in the described campaign).

Conclusiones

Resumen de las contribuciones

En esta tesis se han desarrollado y validado dos códigos para la simulación de chorros de plasma, ambos complementarios y utilizados en diferentes estudios.

En lo que respecta el primer código, llamado EASYPLUME, las contribuciones más importantes han sido:

- Formulación de dos métodos de solución semi-analítica de un modelo con dos fluidos, que permiten el cálculo rápido de las propiedades de un chorro de plasma aguas abajo sin la necesidad de integrar las ecuaciones exactas con esquemas numéricos complejos. En particular, las soluciones existentes en la literatura se han reunido bajo un marco común de métodos auto-semejantes (SSM), y se ha desarrollado un nuevo método de expansión asintótica (AEM).

- Discusión física de los factores más importantes en la expansión de un chorro de plasma en su región lejana: el coeficiente politrópico de enfriamiento electrónico γ, el número de Mach iónico M_0 y el ángulo de divergencia inicial α_0. Se ha entendido que cuanto más isotermos son los electrones, y cuanto más pequeño es el número de Mach, más grandes son los campos eléctricos ambipolares, y como consecuencia el crecimiento de la divergencia del chorro. El potencial eléctrico en el infinito depende solamente del coeficiente politrópico y diverge a $-\infty$ cuando $\gamma \to 1$. Se ha introducido un ángulo de divergencia equivalente, a una cierta distancia axial, para evaluar cuantitativamente el crecimiento de la divergencia, y se ha concluido que, para reducirlo en el caso de ángulos de divergencia iniciales ya bajos, conviene aumentar el número de Mach, en lugar de intentar reducir α_0. Además, los efectos térmicos de los electrones sobre la divergencia pueden reducirse de manera más eficiente incrementando la velocidad de emisión de los iones (aplicando un voltaje de aceleración más alto) que reduciendo la temperatura electrónica en el chorro (que puede requerir diseños muy complejos para el neutralizador).

- Estudio de la aplicabilidad del modelo fluido con un cierre politrópico a un chorro sin colisiones. Una comparación con un modelo PIC-PIC (para iones y electrones) de otro grupo de investigación (University of Southern California) ha permitido identificar los coeficientes politrópicos más apropiados para

obtener un buen acuerdo entre los resultados de los dos modelos. Por lo tanto, se ha podido averiguar que un modelo fluido permite reproducir una parte importante de la física de expansión, incluso en el caso de chorros no colisionales (para los cuales los cierres fluidos no están justificados teóricamente).

El segundo código, EP2PLUS, permite simular la interacción tridimensional entre el chorro de plasma, el satélite y otros objetos. Este código puede utilizarse para un gran número de estudios de chorros y representa la contribución más importante de este trabajo. Además, su arquitectura flexible y modular permite incluir, de manera relativamente sencilla, nuevas capacidades de simulación. A parte conseguir llegar al estado del arte en diferentes algoritmos (especialmente en lo que respecta el sub-modelo de PIC), las siguientes novedades merecen una mención particular:

- Nuevo modelo de electrones basado sobre un cierre cinético que incluye los efectos de las colisiones y permite obtener las corrientes eléctricas en el chorro de plasma.

- División automática del dominio de simulación en regiones quasi-neutras y no neutras, en función de las propiedades locales del plasma. En las primeras, el potencial eléctrico se calcula resolviendo directamente las ecuaciones de conservación de los electrones, mientras que en las segundas estas ecuaciones se resuelven acopladas con la ecuación de Poisson.

- Imposición de la condición de Bohm en las superficies materiales quasi-neutras. Este algoritmo es bastante común en las simulaciones de descargas de motores HET (por ejemplo en el código HP-HALL), pero su uso en un código de chorros es innovativo, y no se ha considerado en estudios anteriores.

- Modelado de la erosión generada por la interacción entre macro-partículas altamente energéticas y superficies materiales. La inclusión de dichos efectos no es muy común en códigos de chorros, excepto por algunas excepciones (por ejemplo SPIS). Además, las propiedades de las partículas emitidas por erosión pueden calcularse usando el software externo SRIM/TRIM.

- Malla estructurada cónica como primer solución para el control de población, en estudios de chorros de plasmas.

En lugar de centrarse en geometrías de simulación complejas, este trabajo ha considerado mallas estructuradas sencillas (en el mayor de los casos cartesianas) con el objetivo de validar los algoritmos mencionados anteriormente de la manera más eficiente. En particular, la división automática del dominio de simulación en regiones quasi-neutras y no neutras permite el uso de mallas sencillas, sin la necesidad de ir adaptando el tamaño de las celdas a la longitud local de Debye (como es necesario en códigos PIC-PIC o totalmente quasi-neutros).

En lo que respecta las aplicaciones de los códigos, se han conseguido los siguientes resultados:

- Simulación de la interacción entre un chorro de plasma de un motor iónico y el satélite con el uso de EP2PLUS. Esta simulación ha demostrado las capacidades de simulación del código y ha permitido evaluar diferentes fenómenos como la acumulación de carga, el retorno de iones lentos, y la estructura de las corrientes eléctricas en el chorro cercano. En particular, se ha comprobado que dichas corrientes se extinguen casi por completo muy rápidamente, en los primeros 30-40 cm de distancia desde la superficie de emisión del motor iónico NSTAR (donde la corriente eléctrica es máxima y proporcionada solamente por los iones emitidos). Además, los efectos de la termodinámica de los electrones y de las regiones no neutras ha sido investigado, descubriendo que ambas tienen un efecto importante en determinar el flujo de iones lentos hacia el satélite y el potencial flotante de este último. En lo que respecta la termodinámica de los electrones, cuanto más isotermos sean estos, más alto es el flujo de iones lentos y su energía media de impacto en las paredes, y más negativo es el potencial del satélite. Por otro lado, la simulación de las regiones no neutras conlleva una subida del flujo de iones de hasta el $20 - 30\%$.

- Optimización del sistema de propulsión eléctrico de un satélite IBS con el uso de EASYPLUME (código fluido) y de un modelo simplificado de interacción con el objeto. Este estudio ha permitido identificar los puntos de operación óptimos para el motor de transferencia de momento (ITT) y para ambos motores (ITT + ICT) operando simultáneamente. La física de la expansión del chorro afecta mucho al diseño: el ITT debe garantizar un ángulo de divergencia inicial bajo, siendo la expansión cónica el factor principal que reduce la transferencia de momento. Entonces, el voltaje de aceleración óptimo del ITT supera al voltaje del ICT, que puede ser bajo (1 kV) para contener la potencia necesaria.

- Simulación de la interacción compleja entre el satélite, el chorro y el objeto espacial en el contexto de una misión IBS. Se han evaluado numéricamente unos fenómenos importantes para el éxito y el rendimiento de la misión: el flujo de iones lentos y de partículas erosionadas hacia el satélite y los potenciales eléctricos de éste y del desecho espacial.

Adicionalmente, durante este trabajo de tesis, se ha llevado a cabo una campaña experimental de caracterización del chorro de plasma del motor PEGASES. Una caracterización espacial ha permitido evaluar los perfiles axiales de propiedades de interés, mientras que una campaña de caracterización temporal ha evaluado las variaciones del potencial del plasma dentro del chorro, encontrando evidencia de la expansión de paquetes de iones aguas abajo. Además se ha podido comprobar que la electro-negatividad del chorro es baja, lo cual indica que el diseño actual del motor está todavía caracterizado por una emisión directa de electrones durante el periodo de voltaje negativo de la onda de potencial aplicada en las rejillas. Por esta razón, serían necesarias futuras mejoras en el diseño del motor.

Trabajo futuro

El campo de investigación de los chorros de plasma presenta mucho temas de interés abiertos. En mi opinión dos de ellos son particularmente interesantes: el enfriamiento sin colisiones de los electrones en el chorro y los efectos de un campo magnético externo sobre la expansión. El primer tema consiste en entender el mecanismo físico detrás de la reducción gradual de la temperatura electrónica a lo largo de la expansión, y puede estudiarse con modelos PIC-PIC o completamente cinéticos [137]. Por lo que respecta el campo magnético, sus efectos pueden estudiarse numéricamente, por ejemplo mejorando el modelo electrónico de EP2PLUS, o experimentalmente en cámaras de vacío suficientemente grandes. El reciente proyecto LEOSWEEP no ha conseguido llegar a unas conclusiones definitivas sobre los efectos de dicho campo, por lo que este tema de investigación queda muy abierto.

Pasando a la descripción del trabajo futuro relacionado con esta tesis, pueden seguirse diferentes lineas de investigación.

El modelo fluido del capítulo 2 desprecia los efectos de las colisiones, una hipótesis que permite resolverlo con métodos semi-analíticos como el SSM y el AEM. Aunque sea posible incluir los efectos de las colisiones, dichos métodos de solución no podrían utilizarse. Por lo tanto, en el contexto del modelado de la región lejana la inclusión de dichos efectos no se aconseja y se proponen otras dos lineas de investigación:

- Inclusión de los efectos de un campo magnético en el modelo fluido, que podría seguir un enfoque del tipo "auto-semejantes", como sugerido por el trabajo de Korsun et al. [51, 52, 53].

- Extensión de la comparación entre el modelo fluido y PIC-PIC a un caso más realista axial-simétrico.

En lo que respecta el desarrollo de EP2PLUS, diferentes líneas de mejora del código pueden identificarse:

- Modelado de las colisiones entre especies pesadas. Entre ellas, de particular interés son las colisiones elásticas de intercambio de momento entre iones y neutros (MEX), que pueden modelarse con secciones eficaces, como las colisiones de intercambio de carga (CEX), ya consideradas en este trabajo.

- Modelado más fino de los efectos de la erosión, que incluya una genérica función de distribución para los neutros emitidos (no basada en una emisión puramente térmica con una cierta energía media) y para las partículas reflejadas (no basada en una reflexión especular con una reducción determinista de energía). Ambas funciones de distribución (para átomos erosionados y partículas reflejadas) pueden obtenerse con el código SRIM/TRIM. Además también podría estudiarse la posibilidad de generar aglomeraciones de átomos con una cierta carga residual, que estarían sujetos a los campos eléctricos locales.

- Control activo de población más eficaz para reducir el ruido en la expansión del chorro. En paralelo con el control actualmente considerado, esto puede hacerse con un algoritmo de renormalización de los pesos de las macro-partículas, o con el uso de una malla que se adapte a la densidad de plasma local (celdas más grandes donde la densidad de macro-partículas baja).

- Extensión del modelo de electrones a un chorro de plasma magnetizado para estudiar los efectos de distorsión causados por un campo magnético externo (como el campo geo-magnético) sobre la expansión del chorro. Esto requeriría el uso de un tensor de conductividad en lugar de una conductividad escalar, siendo el uso de la función de Bernoulli muy prometedor.

- Generalización del modelo de electrones a cierres cinéticos genéricos con coeficientes determinados por estudios cinéticos dedicados.

- Inclusión de superficies emisoras para electrones, caracterizadas por foto-emisión, bombardeamiento iónico y emisión secundaria. Estos nuevos tipos de superficie no afectarían al modelo PIC, sino al circuito equivalente y al modelo de vaina y tendrían efectos importantes en la estimación de la acumulación de carga eléctrica de los objetos metálicos.

- Mallas estructuradas más complejas para simular objetos no-rectangulares (esferas, cilindros, conos, etc...). Este trabajo no se ha centrado en este tema que requeriría nuevos algoritmos que adapten las coordenadas de los nodos originales a la geometría requerida.

EP2PLUS, con ajustes menores, es particularmente apropiado para estudiar los siguientes temas, no tratados aquí:

- Estudio de la formación del chorro de un motor iónico en un sistema de rejillas. Esto requeriría utilizar el cierre no neutro, con dos poblaciones independientes de electrones: una para el plasma exterior (en el chorro), y otra para la cámara de ionización (ambas caracterizadas por propiedades de referencia, como densidad y temperatura, en puntos quasi-neutros distintos).

- Estudio del chorro de múltiples motores eléctricos, operando simultáneamente.

- Estudio de la interacción entre el plasma ambiente y una amarra electromagnética.

- Estudio de la expansión de un chorro de iones alternos (positivos y negativos), emitido por motores como el PEGASES.

Por lo que respecta las aplicaciones de este trabajo, las siguientes mejoras son las más prometedoras:

- El estudio de la interacción entre el chorro y el satélite puede mejorarse introduciendo los efectos de erosión de las superficies del satélite (de baja energía, distinta respecto a la erosión de alta energía del desecho espacial, en el contexto de una misión IBS). Además, la inclusión de otros efectos de emisión electrónica puede afectar significativamente al potencial flotante del satélite y debería ser considerada también.

- La optimización del sistema de propulsión eléctrico puede mejorarse considerando efectos adicionales en el balance de masa (motores, masa de las PPU, etc...), diferentes tipos de motores para el ITT y el ICT (en este estudio se ha considerado un motor iónico a radio-frecuencia para ambos) y una misión caracterizada por desorbitar más de un objeto espacial.

- La simulación detallada de la interacción satélite-plasma-objeto en el contexto del IBS puede hacerse más realista estudiando los efectos del campo magnético terrestre y considerando formas no-rectangulares del desecho espacial (como conos truncados o cilindros).

Finalmente, respecto a la campaña de caracterización del PEGASES, deberían estudiarse nuevos diseños para evitar la emisión directa de electrones y la transición entre un modo operacional "luminoso" y uno "oscuro". Además, nuevas medidas con un nuevo diseño del MRFEA (del inglés magnetic retarding potential energy analyzer) permitirían estudiar la evolución de la función de distribución de los iones y su densidad (imposible en la campaña aquí descrita).

Appendix A

i-th order correction of the fluid velocity for AEM models

The i-th order correction to velocity in the AEM solution is given by the following equations, which are integrated in the same fashion as the first-order correction:

$$\upsilon\frac{\partial\tilde{u}_{zi}^{(i)}}{\partial\zeta}+\frac{\upsilon'}{1+\delta'\zeta}\left(\tilde{u}_{ri}^{(i)}-\tilde{u}_{zi}^{(i)}\delta\right)=-\sum_{j=1}^{i-1}\left(\tilde{u}_{zi}^{(j)}\frac{\partial\tilde{u}_{zi}^{(i-j)}}{\partial\tilde{z}}+\tilde{u}_{ri}^{(j)}\frac{\partial\tilde{u}_{zi}^{(i-j)}}{\partial\tilde{r}}\right)-\sum_{j=1}^{i}\mathcal{T}_{\varepsilon}\left(\tilde{n}^{\gamma-1},\varepsilon^{j-1}\right)\frac{\partial\ln\tilde{n}^{(i-j)}}{\partial\tilde{z}},\tag{A.1}$$

$$\upsilon\frac{\partial\tilde{u}_{ri}^{(i)}}{\partial\zeta}+\frac{(\upsilon\delta)'}{1+\delta'\zeta}\left(\tilde{u}_{ri}^{(i)}-\tilde{u}_{zi}^{(i)}\delta\right)=-\sum_{j=1}^{i-1}\left(\tilde{u}_{zi}^{(j)}\frac{\partial\tilde{u}_{ri}^{(i-j)}}{\partial\tilde{z}}+\tilde{u}_{ri}^{(j)}\frac{\partial\tilde{u}_{ri}^{(i-j)}}{\partial\tilde{r}}\right)-\sum_{j=1}^{i}\mathcal{T}_{\varepsilon}\left(\tilde{n}^{\gamma-1},\varepsilon^{j-1}\right)\frac{\partial\ln\tilde{n}^{(i-j)}}{\partial\tilde{r}},\tag{A.2}$$

where $\mathcal{T}_{\varepsilon}\left(\tilde{n}^{\gamma-1},\varepsilon^{j-1}\right)$ denotes the coefficient of ε^{j-1} of the Taylor series of $\tilde{n}^{\gamma-1}$ in ε, which results from expanding the following expression:

$$\tilde{n}^{\gamma-1}=\left(\tilde{n}^{(0)}\right)^{\gamma-1}\cdot\left(1+(\gamma-1)\varepsilon\ln\tilde{n}^{(1)}+\frac{(\gamma-1)^2}{2}\varepsilon^2\ln^2\tilde{n}^{(1)}+\ldots\right)\cdot\left(1+(\gamma-1)\varepsilon^2\ln\tilde{n}^{(2)}+\frac{(\gamma-1)^2}{2}\varepsilon^4\ln^2\tilde{n}^{(2)}+\ldots\right)\cdot(\ldots).\tag{A.3}$$

Similarly, the i-th correction to density is then given by

$$\upsilon\frac{\partial\ln\tilde{n}^{(i)}}{\partial\zeta}=-\sum_{j=1}^{i}\left(\tilde{u}_{zi}^{(j)}\frac{\partial\ln\tilde{n}^{(i-j)}}{\partial\tilde{z}}+\tilde{u}_{ri}^{(j)}\frac{\partial\ln\tilde{n}^{(i-j)}}{\partial\tilde{r}}\right)-\frac{\partial\tilde{u}_{zi}^{(i)}}{\partial\tilde{z}}-\frac{1}{\tilde{r}}\frac{\partial\left(\tilde{r}\tilde{u}_{ri}^{(i)}\right)}{\partial\tilde{r}}\tag{A.4}$$

Appendix B

Non-linear Poisson's solver and electric field computation

Since the electron density is an explicit function $n_e = n_e(\phi, H_e)$, of both the known Bernoulli's function and the unknown potential, Eq. 3.78 becomes a non-linear differential equation in ϕ. In numerical form, if ϕ_l is the unknown potential at the l^{th} mesh node, then the l^{th} non-linear system equation can be written as:

$$f_l = \sum_m A_{lm}\phi_m + \frac{e}{\epsilon_0}\left(n^*_{e,l} - n_{e,l}(\phi_l, H_{e,l})\right) = 0, \tag{B.1}$$

where the summation extends to all mesh nodes, $n^*_{e,l}$ is the known quasineutral electron density at node l, and A_{lm} is the (l, m) element of the sparse coefficients matrix. The generic coefficient A_{lm} can be computed with the knowledge of the Jacobian matrices of the transformation between computational and physical coordinates $\mathcal{J}$ and $\mathcal{J}_i$. The particular expressions here, for a structured mesh, can be consulted in Sec. B.1.

Eq. B.1 can be solved iteratively with a Newton-Raphson method, by linearizing it around the current solution for the electric potential $\phi^{(k)}$, with k representing now the iteration step. The initial estimate $\phi^{(0)}$ is given by either the quasineutral electric potential ϕ^* (at the very first simulation step), or by the previous time step solution (at other simulation steps). The linearization proceeds by evaluating the Jacobian matrix of the non-linear system, at the iteration step k, as:

$$J^{(k)}_{lm} = \frac{\partial f_l}{\partial \phi_m}\Bigg]_{\phi=\phi^{(k)}}, \tag{B.2}$$

and then obtaining the electric potential correction $\Delta\phi^{(k)}$, by solving the linearized system:

$$\sum_{m \in \text{mesh}} J^{(k)}_{lm}\Delta\phi^{(k)}_m = -f^{(k)}_l. \tag{B.3}$$

The new electric potential, for the next iteration step $k+1$, is updated as $\phi^{(k+1)}_l = \phi^{(k)}_l + \Delta\phi^{(k)}_l$ and used to update the Jacobian matrix. This iterative scheme is

repeated until a convergence criterion is met, i.e. until the maximum absolute value of the non linear function f is below a user's defined tolerance.

Once the electric potential has been computed, the corresponding electric field (necessary to move ion macro-particles) is obtained as:

$$\boldsymbol{E} = -\nabla\phi, \tag{B.4}$$

following the gradient reconstruction algorithm of Sec. B.2.

B.1 Poisson's equation coefficients in a structured mesh

At the inner plasma nodes (not at the boundaries), the coefficient A_{lm} expresses the dependency of the Laplacian at node l on the unknown electric potential of node m. In order to obtain it, the Laplacian is first decomposed in derivatives with respect to the computational coordinates:

$$\begin{aligned}
\nabla^2\phi = \frac{\partial^2\phi}{\partial x^2} + \frac{\partial^2\phi}{\partial y^2} + \frac{\partial^2\phi}{\partial z^2} = \ldots \\
= \left(\frac{\partial\xi}{\partial x}\right)^2 \frac{\partial^2\phi}{\partial\xi^2} + \left(\frac{\partial\eta}{\partial x}\right)^2 \frac{\partial^2\phi}{\partial\eta^2} + \left(\frac{\partial\zeta}{\partial x}\right)^2 \frac{\partial^2\phi}{\partial\zeta^2} + \frac{\partial^2\xi}{\partial x^2}\frac{\partial\phi}{\partial\xi} + \frac{\partial^2\eta}{\partial x^2}\frac{\partial\phi}{\partial\eta} + \frac{\partial^2\zeta}{\partial x^2}\frac{\partial\phi}{\partial\zeta} + \ldots \\
+ 2\frac{\partial\xi}{\partial x}\frac{\partial\eta}{\partial x}\frac{\partial^2\phi}{\partial\xi\partial\eta} + 2\frac{\partial\xi}{\partial x}\frac{\partial\zeta}{\partial x}\frac{\partial^2\phi}{\partial\xi\partial\zeta} + 2\frac{\partial\eta}{\partial x}\frac{\partial\zeta}{\partial x}\frac{\partial^2\phi}{\partial\eta\partial\zeta} + \ldots \\
+ \left(\frac{\partial\xi}{\partial y}\right)^2 \frac{\partial^2\phi}{\partial\xi^2} + \left(\frac{\partial\eta}{\partial y}\right)^2 \frac{\partial^2\phi}{\partial\eta^2} + \left(\frac{\partial\zeta}{\partial y}\right)^2 \frac{\partial^2\phi}{\partial\zeta^2} + \frac{\partial^2\xi}{\partial y^2}\frac{\partial\phi}{\partial\xi} + \frac{\partial^2\eta}{\partial y^2}\frac{\partial\phi}{\partial\eta} + \frac{\partial^2\zeta}{\partial y^2}\frac{\partial\phi}{\partial\zeta} + \ldots \\
+ 2\frac{\partial\xi}{\partial y}\frac{\partial\eta}{\partial y}\frac{\partial^2\phi}{\partial\xi\partial\eta} + 2\frac{\partial\xi}{\partial y}\frac{\partial\zeta}{\partial y}\frac{\partial^2\phi}{\partial\xi\partial\zeta} + 2\frac{\partial\eta}{\partial y}\frac{\partial\zeta}{\partial y}\frac{\partial^2\phi}{\partial\eta\partial\zeta} + \ldots \\
+ \left(\frac{\partial\xi}{\partial z}\right)^2 \frac{\partial^2\phi}{\partial\xi^2} + \left(\frac{\partial\eta}{\partial z}\right)^2 \frac{\partial^2\phi}{\partial\eta^2} + \left(\frac{\partial\zeta}{\partial z}\right)^2 \frac{\partial^2\phi}{\partial\zeta^2} + \frac{\partial^2\xi}{\partial z^2}\frac{\partial\phi}{\partial\xi} + \frac{\partial^2\eta}{\partial z^2}\frac{\partial\phi}{\partial\eta} + \frac{\partial^2\zeta}{\partial z^2}\frac{\partial\phi}{\partial\zeta} + \ldots \\
+ 2\frac{\partial\xi}{\partial z}\frac{\partial\eta}{\partial z}\frac{\partial^2\phi}{\partial\xi\partial\eta} + 2\frac{\partial\xi}{\partial z}\frac{\partial\zeta}{\partial z}\frac{\partial^2\phi}{\partial\xi\partial\zeta} + 2\frac{\partial\eta}{\partial z}\frac{\partial\zeta}{\partial z}\frac{\partial^2\phi}{\partial\eta\partial\zeta},
\end{aligned} \tag{B.5}$$

where the terms in black are constant throughout the simulation and depend on the mesh (they can be either known analytically, or computed numerically), while the terms in red have to be evaluated, every time step, with an appropriate 2nd order scheme. In a structured mesh like the one considered here, the following 2nd order scheme can be applied for the second derivatives at a generic non-boundary mesh node with indices (i, j, k) (second derivatives are never required at boundary nodes, where only first derivatives are imposed):

$$\left.\frac{\partial^2\phi}{\partial\xi^2}\right|_{(i,j,k)} \approx \phi_{i-1,j,k} - 2\phi_{i,j,k} + \phi_{i+1,j,k} \tag{B.6}$$

while the first derivatives can be evaluated numerically as (again for the ξ derivatives):

$$\begin{cases} \left.\dfrac{\partial\phi}{\partial\xi}\right|_{(i,j,k)} \approx \dfrac{\phi_{i+1,j,k}-\phi_{i-1,j,k}}{2} & \text{for inner plasma nodes,} \\ \left.\dfrac{\partial\phi}{\partial\xi}\right|_{(i,j,k)} \approx \dfrac{-\phi_{i+2,j,k}+4\phi_{i+1,j,k}-3\phi_{i,j,k}}{2} & \text{for left boundary nodes,} \\ \left.\dfrac{\partial\phi}{\partial\xi}\right|_{(i,j,k)} \approx \dfrac{\phi_{i-2,j,k}-4\phi_{i-1,j,k}+3\phi_{i,j,k}}{2} & \text{for right boundary nodes.} \end{cases} \tag{B.7}$$

Finally, the crossed derivatives of Eq. B.5 are computed by applying two first derivative schemes, one after the other.

For what concerns the coefficients of the boundary nodes (those featuring a Neumann condition) they refer to the normal derivative of the electric potential, which can be expressed as:

$$\begin{aligned} \frac{\partial\phi}{\partial\mathbf{1}_\perp} &= \frac{\partial\phi}{\partial x}\frac{\partial x}{\partial\mathbf{1}_\perp}+\frac{\partial\phi}{\partial y}\frac{\partial y}{\partial\mathbf{1}_\perp}+\frac{\partial\phi}{\partial z}\frac{\partial z}{\partial\mathbf{1}_\perp}=\dots \\ &= \left(\frac{\partial\phi}{\partial\xi}\frac{\partial\xi}{\partial x}+\frac{\partial\phi}{\partial\eta}\frac{\partial\eta}{\partial x}+\frac{\partial\phi}{\partial\zeta}\frac{\partial\zeta}{\partial x}\right)\frac{\partial x}{\partial\mathbf{1}_\perp}+\dots \\ &+ \left(\frac{\partial\phi}{\partial\xi}\frac{\partial\xi}{\partial y}+\frac{\partial\phi}{\partial\eta}\frac{\partial\eta}{\partial y}+\frac{\partial\phi}{\partial\zeta}\frac{\partial\zeta}{\partial y}\right)\frac{\partial y}{\partial\mathbf{1}_\perp}+\dots \\ &+ \left(\frac{\partial\phi}{\partial\xi}\frac{\partial\xi}{\partial z}+\frac{\partial\phi}{\partial\eta}\frac{\partial\eta}{\partial z}+\frac{\partial\phi}{\partial\zeta}\frac{\partial\zeta}{\partial z}\right)\frac{\partial z}{\partial\mathbf{1}_\perp}, \end{aligned} \tag{B.8}$$

in which the direction cosines of the normal unit vector $\mathbf{1}_\perp$ depend on the mesh, and only 3 partial derivatives with respect to the computational coordinates ξ,η,ζ need to be evaluated, again using the schemes of Eq. B.7 for the red terms in the equation.

The generic coefficient A_{lm} for the non-linear system is finally given by the total coefficient that multiplies the generic m^{th} node potential in the Laplacian or normal derivative expressions, evaluated at the l^{th} node, by using the 2nd order schemes of Eqs. B.7 and B.6.

B.2 Gradient reconstruction in a structured mesh

A common operation done in field reconstruction algorithms is that of the gradient reconstruction. This is needed, for example, in order to compute the electric field vector, once the electric potential solution has been obtained with either the quasineutral or the non-neutral solver.

The spatial gradient of any quantity, in the considered structured mesh, is obtained numerically by first computing its derivatives with respect to the computational coordinates, and then applying the chain rule for multi-variable functions,

with the use of the physical to computational transformation matrix $\mathcal{J}$ (providing the partial derivatives of the computational coordinates with respect to the physical ones). The three components of the electric potential gradient (the opposite vector to the electric field), at the mesh node with indices (i, j, k), are then obtained as:

$$\begin{cases} \nabla\phi|^{(x)}_{(i,j,k)} = \dfrac{\partial\phi}{\partial\xi}\left.\dfrac{\partial\xi}{\partial x}\right|_{(i,j,k)} + \dfrac{\partial\phi}{\partial\eta}\left.\dfrac{\partial\eta}{\partial x}\right|_{(i,j,k)} + \dfrac{\partial\phi}{\partial\zeta}\left.\dfrac{\partial\zeta}{\partial x}\right|_{(i,j,k)} \\ \nabla\phi|^{(y)}_{(i,j,k)} = \dfrac{\partial\phi}{\partial\xi}\left.\dfrac{\partial\xi}{\partial y}\right|_{(i,j,k)} + \dfrac{\partial\phi}{\partial\eta}\left.\dfrac{\partial\eta}{\partial y}\right|_{(i,j,k)} + \dfrac{\partial\phi}{\partial\zeta}\left.\dfrac{\partial\zeta}{\partial y}\right|_{(i,j,k)} \\ \nabla\phi|^{(z)}_{(i,j,k)} = \dfrac{\partial\phi}{\partial\xi}\left.\dfrac{\partial\xi}{\partial z}\right|_{(i,j,k)} + \dfrac{\partial\phi}{\partial\eta}\left.\dfrac{\partial\eta}{\partial z}\right|_{(i,j,k)} + \dfrac{\partial\phi}{\partial\zeta}\left.\dfrac{\partial\zeta}{\partial z}\right|_{(i,j,k)} \end{cases} \tag{B.9}$$

Appendix C

The EP2PLUS validation tests

The validation tests that have been considered in this work are summarized in Tab. C.1. They can be divided in 2 categories: functional and integration tests. While the former test a specific functionality of the code, the latter verify, for a specific scenario, the correct functioning of integrated functions and modules.

C.1 Particle mover

In the particle mover test, the trajectory of a test ion macro-particle is computed, assuming constant electric and magnetic fields. The position and velocity relative errors $\epsilon_p = |\boldsymbol{r} - \boldsymbol{r}_{ex}| / \Delta r_{f,ex}$ and $\epsilon_v = |\boldsymbol{v} - \boldsymbol{v}_{ex}| / v_{f,ex}$ of the mover solution with respect to the exact analytical one are shown in Fig. C.1(a), for the trajectory of Fig. C.1(b) ($\boldsymbol{E} \times \boldsymbol{B}$ plane cross-section). The expected drift and Larmor motion can be appreciated, while the relative errors remain small after many Larmor orbits.

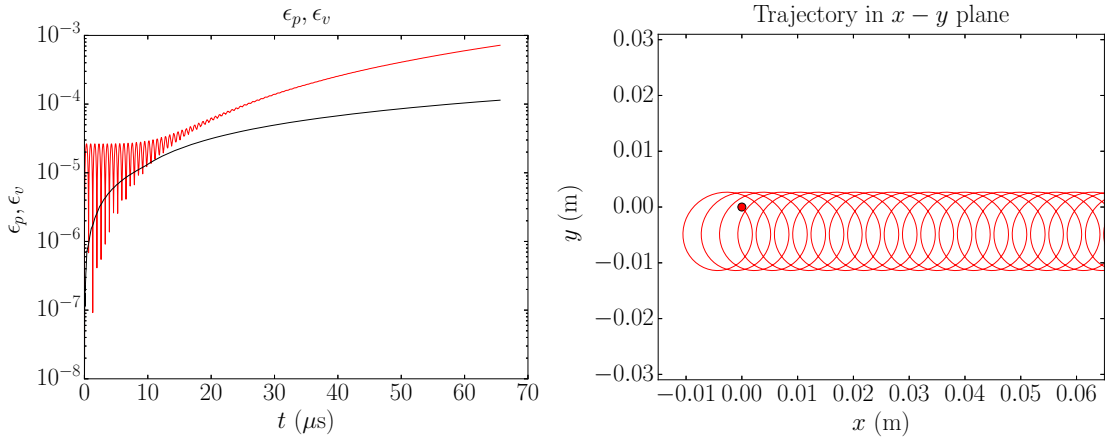

Figure C.1: Particle mover test results: (a) relative errors in the predicted ion position (red) and velocity (black), (b) corresponding 2D trajectory in the $\boldsymbol{E} \times \boldsymbol{B}$ plane, showing the initial position (red dot).

Table C.1: Description of the EP2PLUS validation tests

Test name	**Test type**	**Success criteria description**
Particle mover	functional	Trajectory error with respect to the exact solution below a given tolerance
Volume weighting	functional	Weighted density for given input populations with the expected errors
Surface weighting	functional	Weighted surface density for known particle flux with the expected errors
Surface-crossing check	functional	Absorption of particles crossing test surfaces
Particle injection	functional	Moments of the injected populations within expected errors from input values
Field computation	functional	Reconstructed electric field, for a known potential distribution, within a max. error from the analytic exact solution
CEX collisions	functional	Expected density of the colliding ions
Ionization collisions	functional	Expected density of the ionized neutrals
Surface interaction	functional	Mass conservation in a closed box
Population control	functional	Number of macro-particles per cell within the control interval
Sputtering	functional	Sputtered/backscattered particles from a test target, with the expected distribution
Non-linear Poisson	functional	Error in Poisson's equation below threshold
Collisionless plume expansion	integrated	Density errors with respect to the SSM fluid solution, below a threshold, for different fluid closures and meshes
Bohm's condition forcing	integrated	Achievement of ion sonic conditions, at the simulation material boundaries
IBS-like scenario	integrated	Correct functioning for an IBS-like scenario, with quasineutral and non-neutral closures
Neutralizer-thruster interaction scenario	integrated	Error in both non-linear Poisson's solver and H_e solver, below a threshold

C.2 Volume weighting

In the volume weighting test, two populations of ion macro-particles are considered, as shown in Fig. C.2 (a):

1. a randomly generated population with a uniform spatial distribution,
2. a population consisting of one macro-particle per cell at a fixed off-set position from the cell center

The dispersion in the weighted density of the first population is then compared with an expected value, while the second population density must be exactly constant everywhere in the simulation domain.

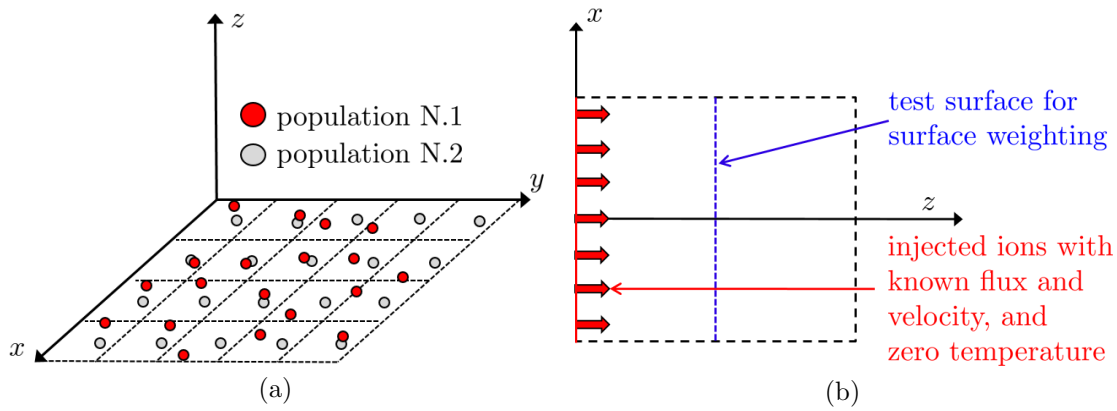

Figure C.2: Configurations for (a) the volume weighting test (an $x-y$ cross section is shown), and (b) the surface weighting test (an $x-z$ cross section is shown).

C.3 Surface weighting

In the surface weighting test, a population of ion macro-particles is injected with a known flux, density and velocity from one side of the simulation domain, and is surface weighted at a test surface, as shown in Fig. C.2 (b). A direct comparison between the expected density and velocity, and the ones obtained with surface-weighting, then permits validating these algorithms.

C.4 Surface-crossing check

In this test case, the configuration of Fig. C.3 is considered. A particle source generates particles with a spherical velocity field (i.e. with their velocity aligned with the radial direction from the sphere center), and these interact with 6 absorbing walls, of a given size and at a known distance. All macro-particles whose trajectories cross these absorbing surfaces have to be eliminated from the domain. The expected

fraction of particles to be absorbed by the surfaces, is then compared with those that have been actually eliminated in the simulation.

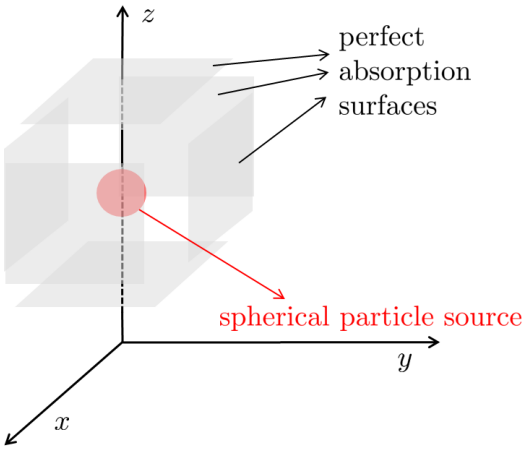

Figure C.3: Configuration for the surface-crossing check test.

C.5 Particle injection

In the particle injection test, two populations are injected:

1. Drifting Maxwellian population, with assigned particle flux, fluid velocity and temperature, from a given injection plane.

2. Thermal ion population (of assigned temperature, density, and with a zero fluid velocity), injected towards the center from the lateral surfaces of a cube.

The weighted density and temperatures at the injection plane (for the first population), and at the center of the injection cube (for the second population) are compared with the expected values. Moreover, for the second population, the particle distribution function at the cube center, must resemble an exact Maxwellian distribution (with zero mean velocity). The results for the weigthed density and temperature of the first population are shown in Fig. C.4 (a) and (b).

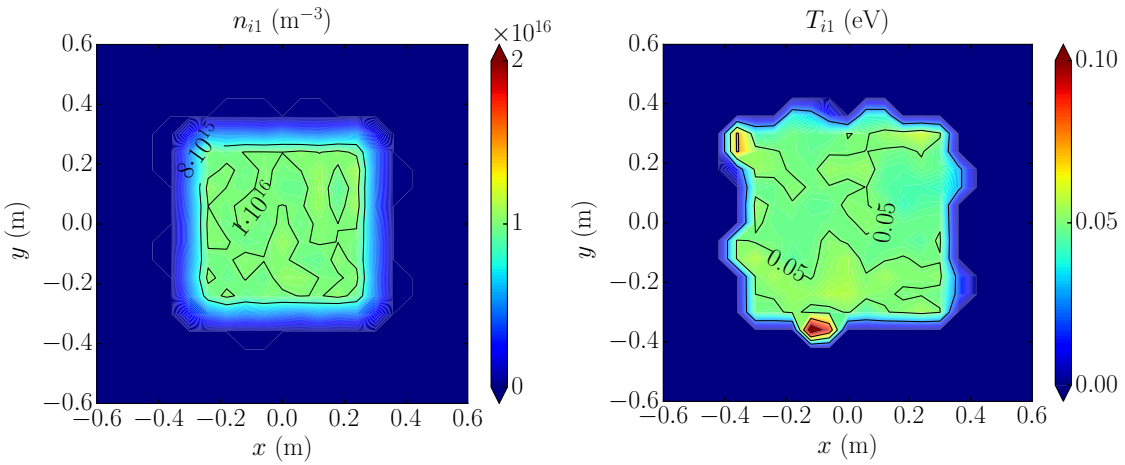

Figure C.4: Injection test results: (a) density, and (b) temperature, of the first population, at the injection plane. The expected density and temperature are respectively 10^{16} m^{-3} and 0.05 eV.

The weighted density and temperatures of the second population, at a plane that crosses the injection cube center, are then shown in Fig. C.5 (a) and (b), while the corresponding normalized probability distribution functions $\tilde{f}(v_x)$ and $\tilde{f}(v_y)$ at the cube center are shown in Fig. C.5 (c) and (d).

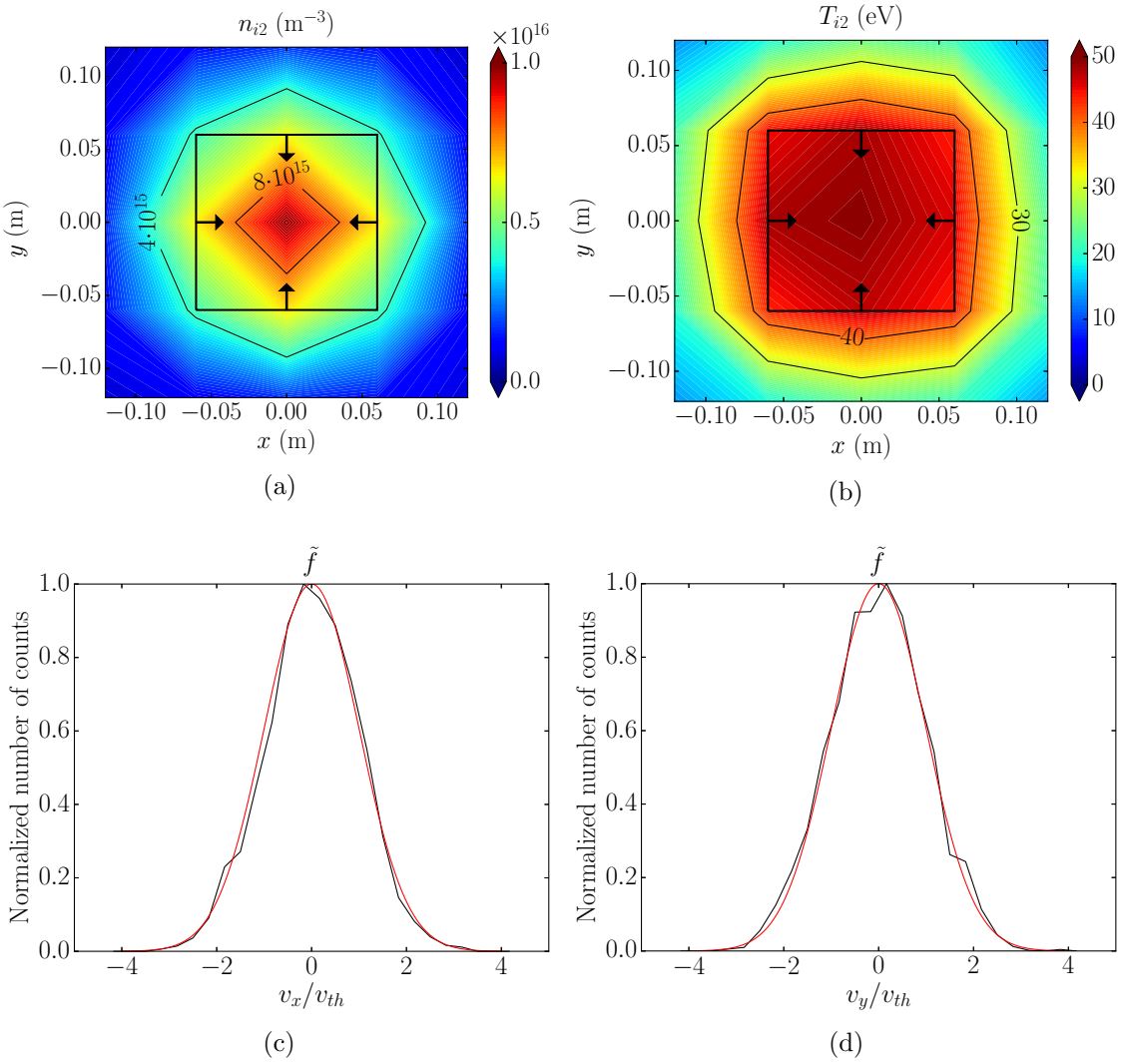

Figure C.5: Injection test results: (a) second population density and (b) temperature, at a plane crossing the injection cube center, and normalized probability distribution functions at the cube center, for (c) the x velocity and (d) the y velocity. Particles are injected inwards from the cube sides, which are shown in the sub-figures (a) and (b), and are transparent to particles. The expected density and temperature, at the cube center, are respectively 10^{16} m^{-3} and 50 eV. Regarding the sub-figures (c) and (d), the normalization velocity is the thermal velocity $v_{th} = \sqrt{eT/m}$, while the expected Maxwellian distribution is indicated by the red line.

C.6 Electric field computation

In this test case, an analytic electric potential (the one corresponding to a self-similar plasma plume expansion) is used to compute numerically the electric field. This is then compared with the exact electric field solution, that can be obtained by differentiating analytically the known electric potential. The committed absolute and relative errors, computed respectively as $\epsilon_{abs} = |\boldsymbol{E}_{comp} - \boldsymbol{E}_{exact}|$ and $\epsilon_{rel} =$

$\epsilon_{abs}/\,|\boldsymbol{E}_{exact}|$, are shown in Fig. C.6 (a) to (d), for two cross sections (one at the $z = 0$ plume injection plane, and another at the $y = 0$ plane).

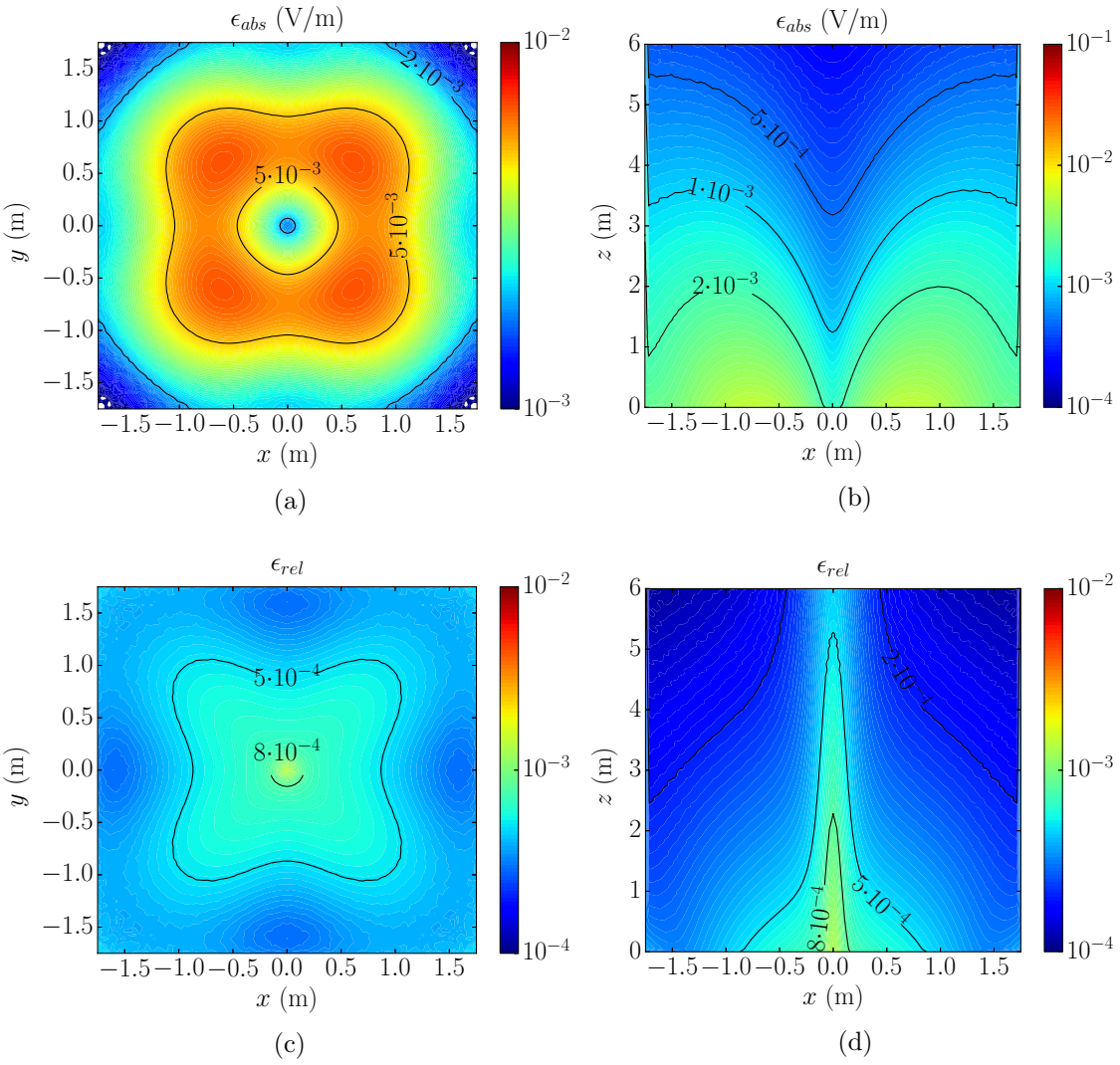

Figure C.6: Field computation test results: (a) absolute and (c) relative electric field error in the $z = 0$ plane, (b) absolute and (d) relative electric field error in the $y = 0$ plane. The plume is injected at $z = 0$ and features a 95% ion current streamline radius of 1 m, with a corresponding divergence angle of 10 deg. The considered mesh has a total of $101 \times 101 \times 121$ nodes.

C.7 CEX collisions

For the CEX collisions tests, the configuration is shown in Fig. C.7 (a). Two populations of ions with different axial velocities are injected from the $z = 0$ plane and collide with 2 still populations of neutral macro-particles (with CEX). The expected density of the injected ions, along z at the centerline, can be predicted as:

$$n_{i,c} = n_{i0} \exp\left(-\frac{z}{\lambda_{c,CEX}}\right), \tag{C.1}$$

where the mean free path $\lambda_{c,CEX}$ depends on the relative velocity between the injected ions and the neutrals, and is different for the 2 populations. Fig. C.7 (b) shows the comparison between the predicted densities and those obtained by simulating the collisions with either DSMC or MCC sampling (for both populations).

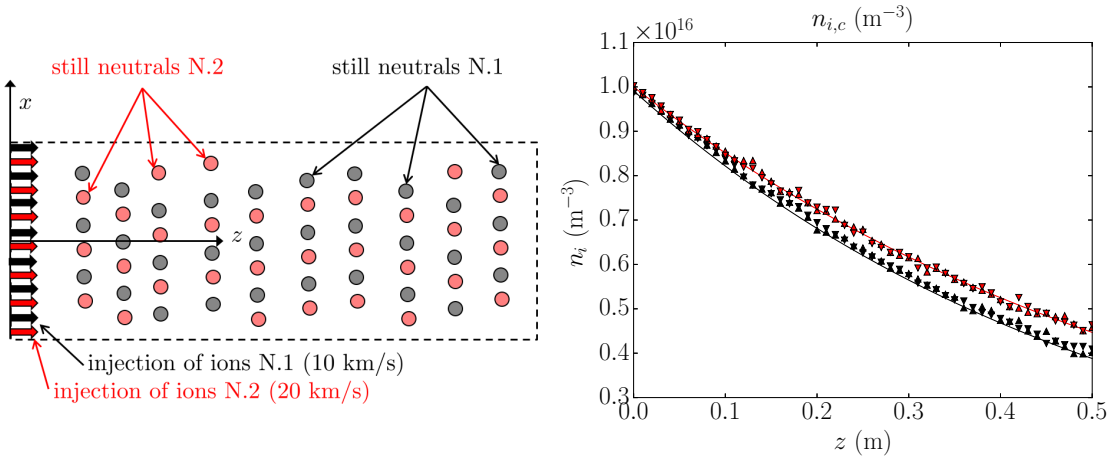

(a) (b)

Figure C.7: (a) Configuration of the CEX collisions test: two populations of injected ions with different velocities collide with two populations of neutrals, of constant density. (b) Centerline fast ion density: the expected evolution is shown with a solid line, the obtained values with DSMC sampling are shown with upwards triangles, and those obtained with MCC sampling with downwards triangles. The black lines refer to injected ions with 10 km/s velocity, while the red lines to injected ions with 20 km/s. The simulation results refer to cross section average values, at fixed z.

C.8 Ionization collisions

The ionization test is very similar to the CEX collisions test, and features an injected neutral population that is progressively ionized by a dense plasma background (generated by ion macro-particles). The configuration is shown in Fig. C.8 (a). Once again, the expected centerline density evolution for the injected neutrals depends on the ionization rate, and is given by:

$$n_{n,c} = n_{n0} \exp\left(-\frac{n_e R_i z_f}{u_n}\right), \tag{C.2}$$

where R_i is the constant ionization rate (a constant electron temperature is assumed), and u_n is the neutral injection velocity. The results for the neutral density obtained with EP2PLUS is finally compared with this predicted evolution in Fig. C.8 (b).

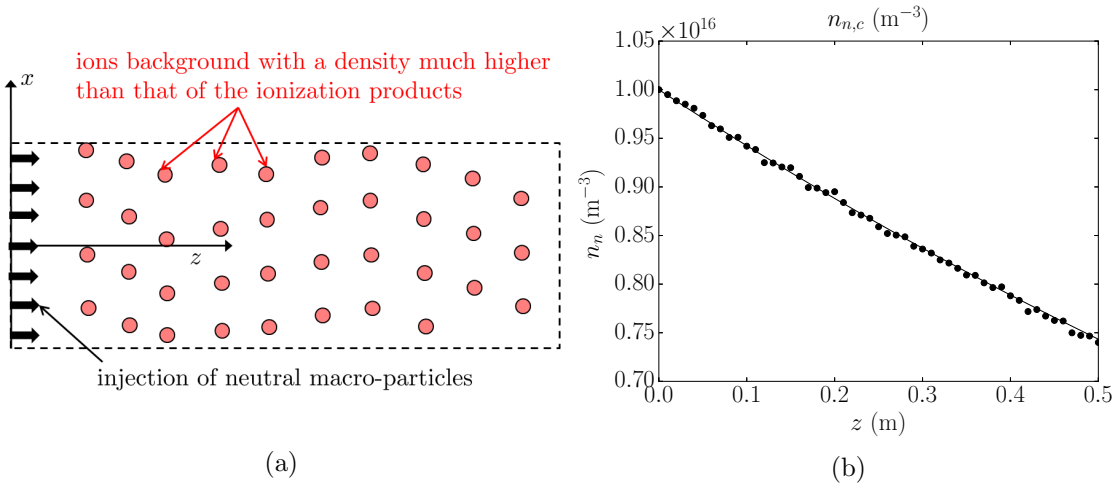

Figure C.8: (a) Configuration of the ionization test: a neutral population is injected from $z = 0$ and is gradually ionized by a dense background plasma, with a constant density and electron temperature across the domain. (b) Centerline neutral density: the expected evolution is shown with a solid line, while the simulated evolution with black circles. The simulation results refer to cross section average values, at fixed z.

C.9 Surface interaction

In this test, whose configuration is depicted in Fig. C.9, a certain number of ion and neutral macro-particles are generated at the center of a box, with material walls. As the ions hit such walls they recombine into neutrals, while neutrals get reflected either specularly or diffusely. This test checks that the correct distribution function of reflected and re-injected neutrals is achieved, and also that mass is conserved within the domain.

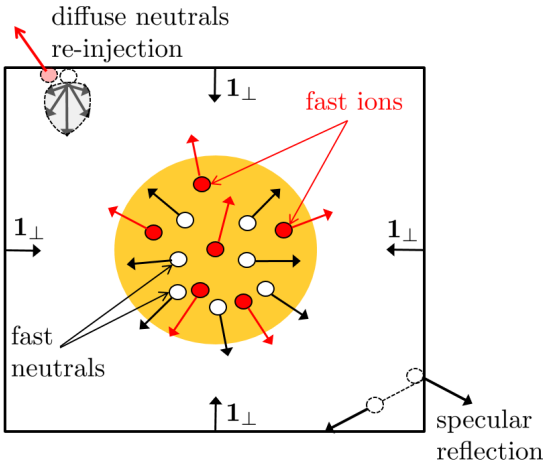

Figure C.9: Configuration of the surface interaction test. The lateral walls of the box are of material type, thus causing ions to recombine, and neutrals to reflect (either specularly or diffusely).

C.10 Population control

In this test, an ion population is injected from the left boundary ($z = 0$) with an SSM profile. As the ions reach the material wall at the right boundary, they recombine into neutrals and the population control algorithms dictate the generation weights of these new neutral macro-particles. The control interval for the number of macro-particles per cell is $[45 - 55]$. The configuration is shown in Fig. C.10 (a), while Fig. C.10 (b) shows the ion density at the $y = 0$ cross section (clearly non-uniform at the material wall).

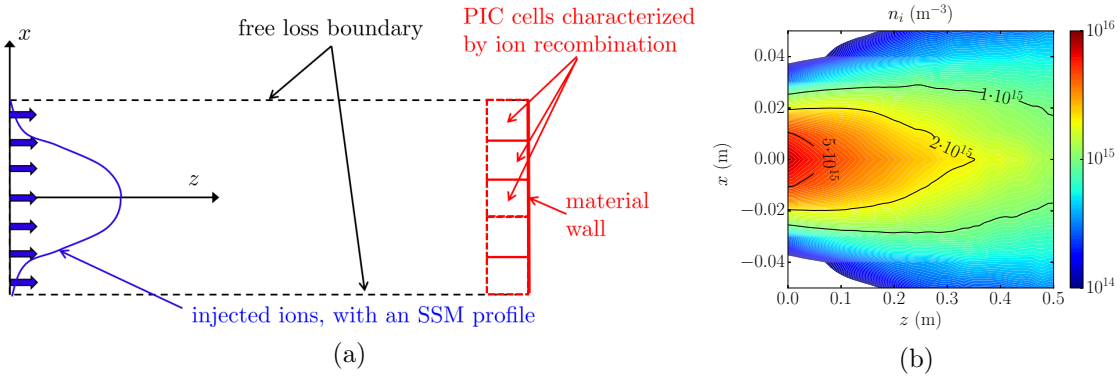

Figure C.10: (a) Configuration of the population control test: an ion population is injected from $z = 0$ with a SSM profile, and hits a right hand side material wall, where it recombines. The control algorithm ensures that the recombined neutral population at the material wall cells presents the requested number of macro-particles per cell. (b) Impacting ion density at the $y = 0$ cross section.

Fig. C.11 (a) and (b) finally show the number of macro-particles per cell for the recombined neutrals at two cross sections: the $y = 0$ cross section, and the material wall plane.

C.11 Sputtering

In the sputtering test, two thermal populations of ions and neutrals are injected at $z = 0$ with a large temperature of 1500 eV and collide with a sputtering target at the right hand side of the domain. The test configuration is shown in Fig. C.12 (a), while the resulting sputtered neutral density is shown in Fig. C.12 (b).

Fig. C.13 (a) and (b) then show respectively the average sputtered atoms energy evolution in the domain, and the parallel versus perpendicular velocities of either sputtered or backscattered particles from the target. Regarding the former plot, the energy is compatible with the sputtering data for the mean sputtered atoms energy and diminishes after a first peak because the fastest sputtered atoms tend to leave the domain earlier. Regarding the second plot, the backscattered particles only exist with large ratios between the parallel and the perpendicular velocity, because the

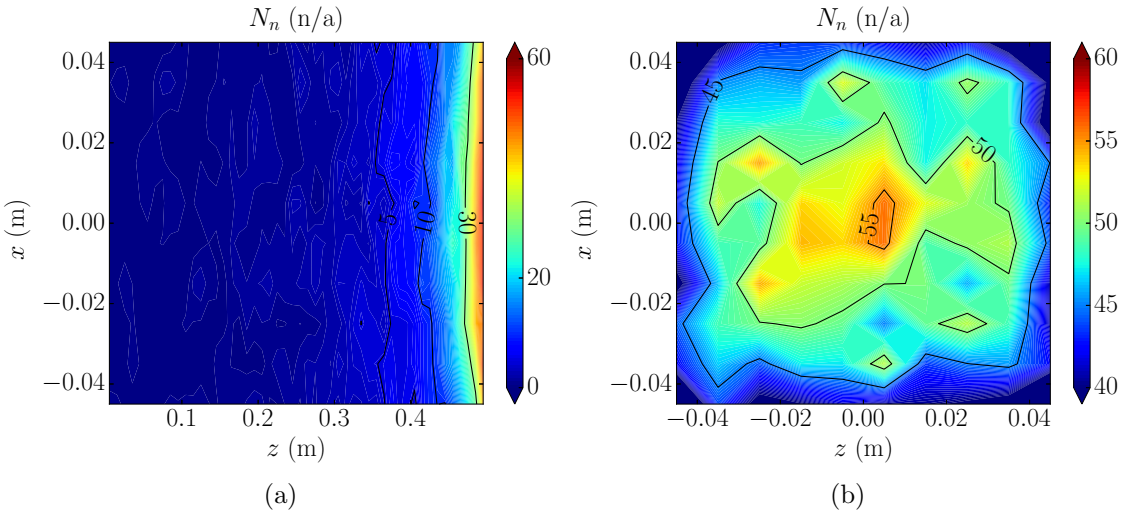

Figure C.11: (a) Number of neutral macro-particles per cell at the $y = 0$ plane. (b) Number of neutral macro-particles per cell at the material wall plane.

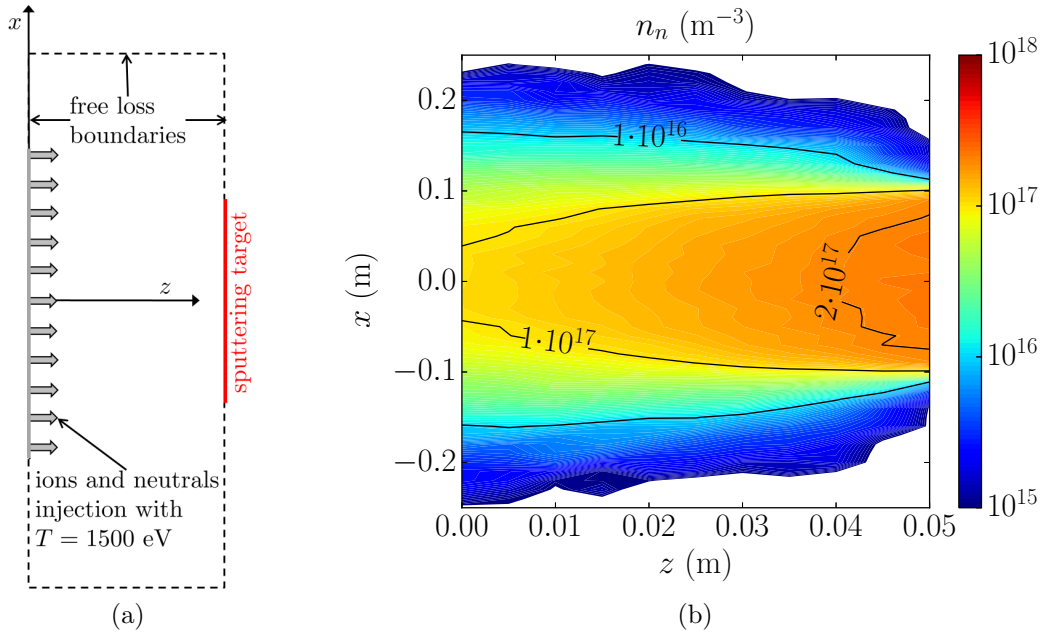

Figure C.12: (a) Configuration of the sputtering test: two thermal populations of ions and neutrals with high temperature (1500 eV) are injected from $z = 0$ with a constant flux, and hit a sputtering target at the right hand side. (b) Sputtered neutral density at the $y = 0$ cross section.

backscattering probability is 0 for impact angles lower than approx. 50 degrees, and reaches the highest values for grazing incidences.

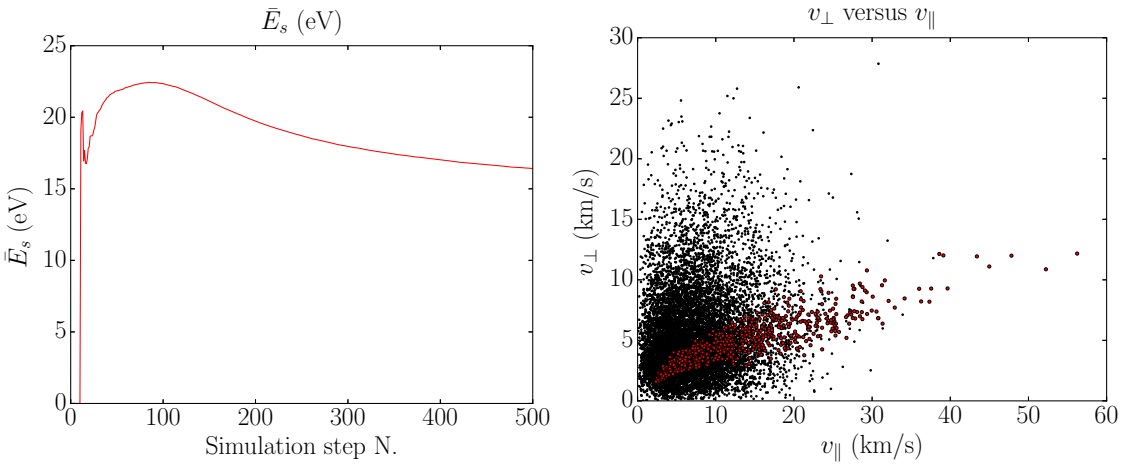

Figure C.13: (a) Evolution with time of the average kinetic energy of the sputtered atoms in the domain. (b) Perpendicular Vs parallel velocity of sputtered (black circles) and backscattered (red circles) particles.

C.12 Non-linear Poisson

In this test, a uniform sphere of ions is at the center of the simulation domain, surrounded by vacuum. The non-linear Poisson solver is then run to obtain the corresponding electric potential solution, with the boundary conditions shown in Fig. C.14 (a). The ion density is shown in Fig. C.14 (b).

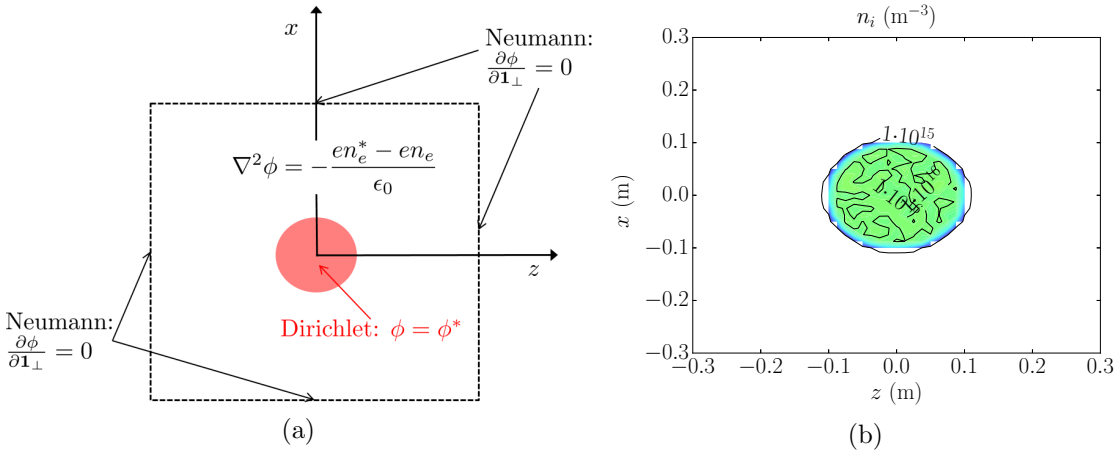

Figure C.14: (a) Configuration of the non-linear Poisson test: a uniform sphere of ions is at the center of the domain, surrounded by vacuum. (b) Ion density at the $y = 0$ cross section.

The quasineutral and Poisson's solution for the electric potential are compared in Fig. C.15 (a) and (b), while the corresponding charge density and the relative error in Poisson's equation solution are shown respectively in Fig. C.16 (a) and (b).

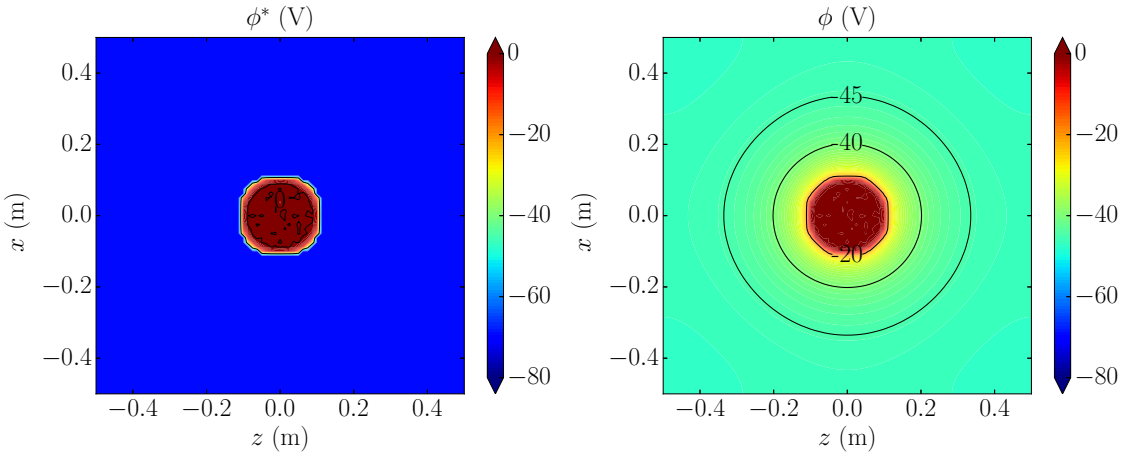

Figure C.15: Non-linear Poisson's solver test results, shown at the $y = 0$ cross section: (a) quasineutral electric potential, (b) Poisson's solver solution for the electric potential.

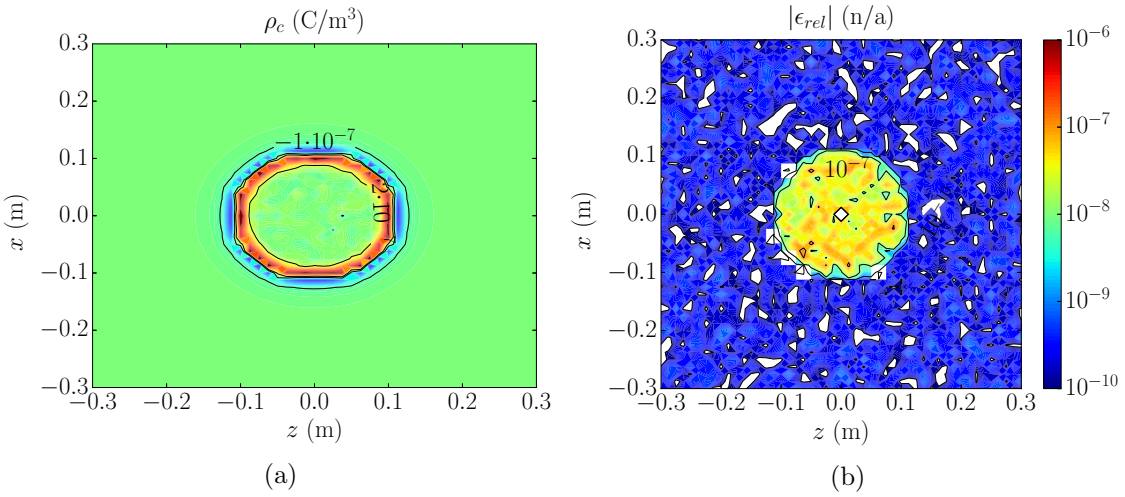

Figure C.16: Non-linear Poisson's solver test results, shown at the $y = 0$ cross section: (a) corresponding charge density, and (b) Poisson's equation error, evaluated as: $\epsilon_{rel} = \left(\nabla^2\phi + \rho_c/\epsilon_0\right)/(en_{e0}/\epsilon_0)$, where n_{e0} is the quasineutral plasma density at the ion sphere center.

C.13 Collisionless plume expansion

In this test, the plasma plume solution obtained with EP2PLUS is compared with the Parks-Katz plume solution, generalized to polytropic electrons, Eq. 2.38 (the corresponding plume injection conditions are considered). Both a Cartesian and a conical mesh (refer to Sec. 3.2.1.1) are considered, with either a self-consistent polytropic electrons closure (with $H_e = 0$), or with an assigned constant electric field (as dictated by the SSM solution). The results, in terms of the centerline and 95% ion current streamline density are shown in Fig. C.17 (a), with the corresponding number of macro-particles per cell shown in Fig. C.17 (b). All cases show a good match with the quasi-exact SSM solution, with the self-consistent field with conical mesh simulation having the largest accuracy, as expected. It is noticed that the Cartesian mesh cases feature 500 macro-particles per cell at injection, versus the 100 for the conical mesh cases.

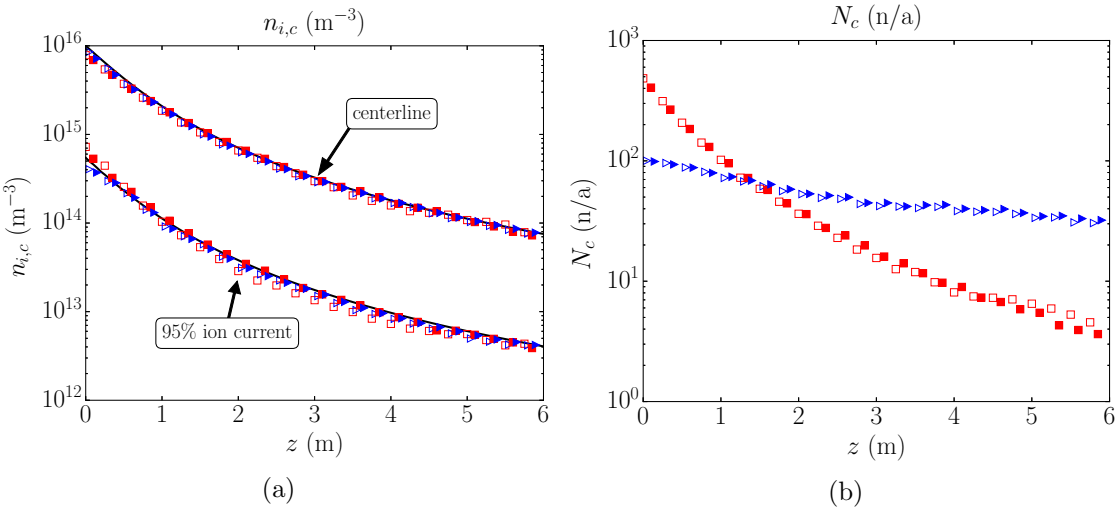

Figure C.17: Collisionless plume expansion tests: (a) centerline and 95% ion current streamline densities, and (b) number of macro-particles per cell along the centerline. The SSM solution is shown with a solid black line, triangles are used for the simulations with conical mesh, while squares for the simulations with Cartesian mesh. Filled markers are used for the self-consistent field simulations, while empty markers for the fixed input electric field (from SSM solution).

C.14 Bohm's condition forcing

This test features a simulation domain with a left hand side ($z = 0$) used for the purely axial injection of a uniform density ion population, an open free-loss right hand side, and the lateral sides consisting of material walls. The test thus verifies the formation of a pre-sheath region that accelerates the ions radially outwards towards the material walls, until reaching sonic conditions. The configuration is shown in

Fig. C.18 (a), while Fig. C.18 (b) shows the evolution with z of the cross-section average of the normal ion Mach number, at the lateral walls.

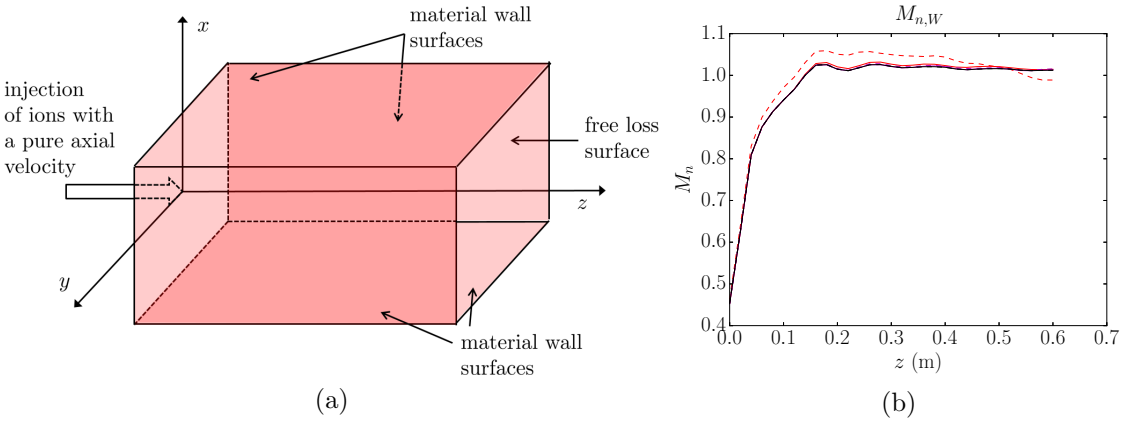

Figure C.18: (a) Configuration of the Bohm's condition forcing test: a uniform ion population is injected axially from the $z = 0$ cross section. The lateral sides of the domain are made of material walls. (b) Axial (along z) and time evolution of the cross section average of the normal ion Mach number, at the lateral walls. The final time step is shown with a black solid line.

Fig. C.19 (a) and (b) finally show respectively the electric potential and the ion Mach number along x, for the $y = 0$ cross section.

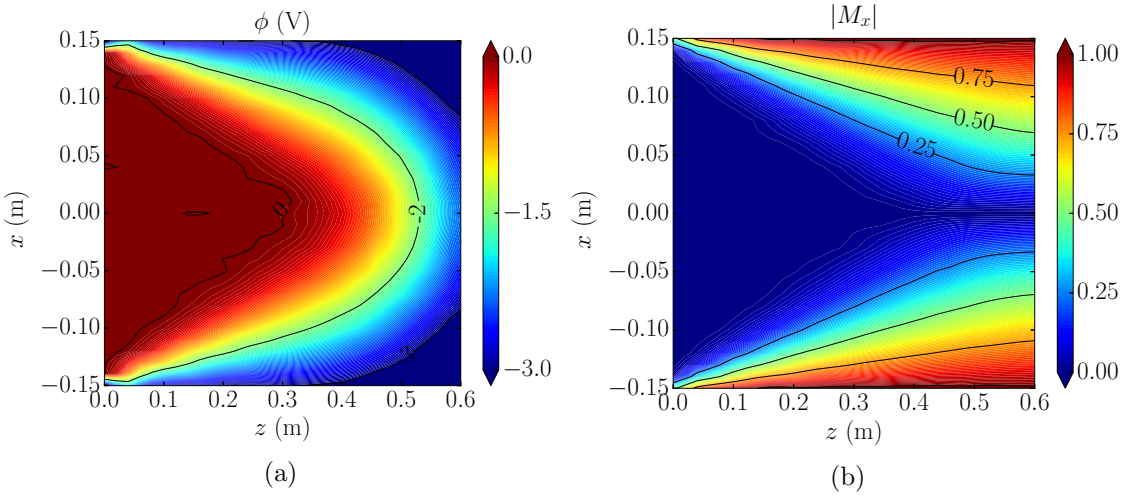

Figure C.19: Bohm's condition forcing test results at the $y = 0$ cross section: (a) electric potential, and (b) ion Mach number along the x direction. The electron temperature is constant and equal to $T_e = 3$ eV.

Sonic conditions are achieved at the material boundaries, except for a small region close to the injection plane (where injection conditions are dominant). Moreover, a pre-sheath forms with potential drops of the order of $T_e/2$, as expected (the electron temperature in this test case is constant and equal to $T_e = 3.0$ eV).

C.15 IBS-like scenario

This test considers a simulation configuration which is similar to that of Sec. 5.3.1, although featuring a smaller number of mesh nodes (to enable a quicker verification), and no solar arrays. Both the quasineutral and the non-neutral solvers are tested.

The electric potential solutions of both solvers are compared in Fig. C.20 (a), while Fig. C.20 (b) shows the normal Mach number at the S/C front surface (the one facing the debris), for the quasineutral solver. As expected the ion Mach number approaches 1 at the S/C surfaces, except for the thruster emission area, in which Bohm's conditions are not applied.

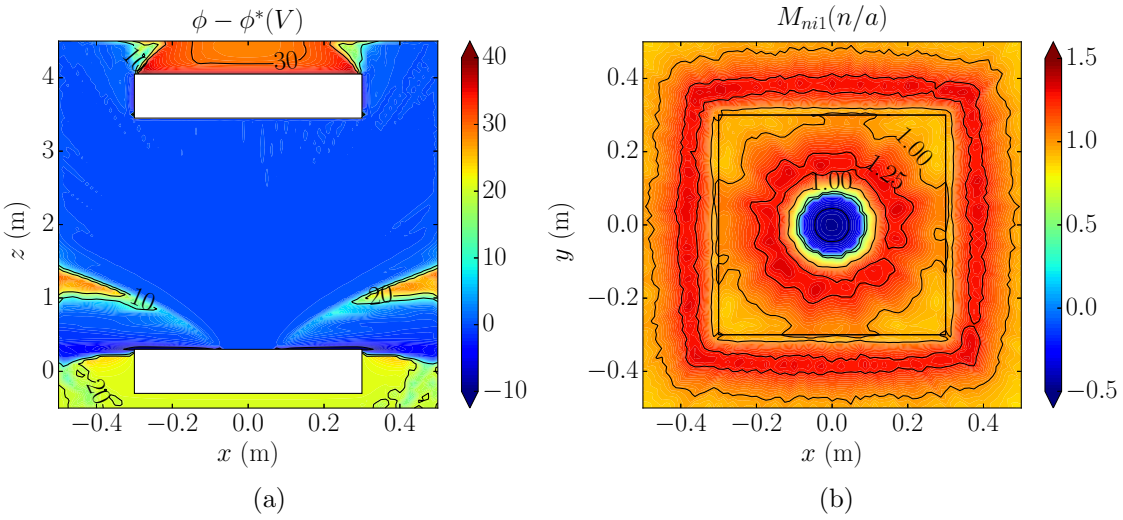

Figure C.20: IBS-like scenario test results, at the $y = 0$ cross section: (a) difference in the electric potential between the non-neutral and quasineutral solutions, and (b) normal Mach number at the cubic S/C surface, for the quasineutral solver (an isothermal electron population is considered with $T_e = 3$ eV).

Regarding the non-neutral solver solution, Fig. C.21 (a) to (d) show the number densities of electrons, ions, neutrals and sputtered atoms.

Finally, Fig. C.22 (a) to (d) show the number of macro-particles per cell for the slow CEX ions, the recombination neutrals, the injected ions, and the aluminium sputtered atoms from the target debris.

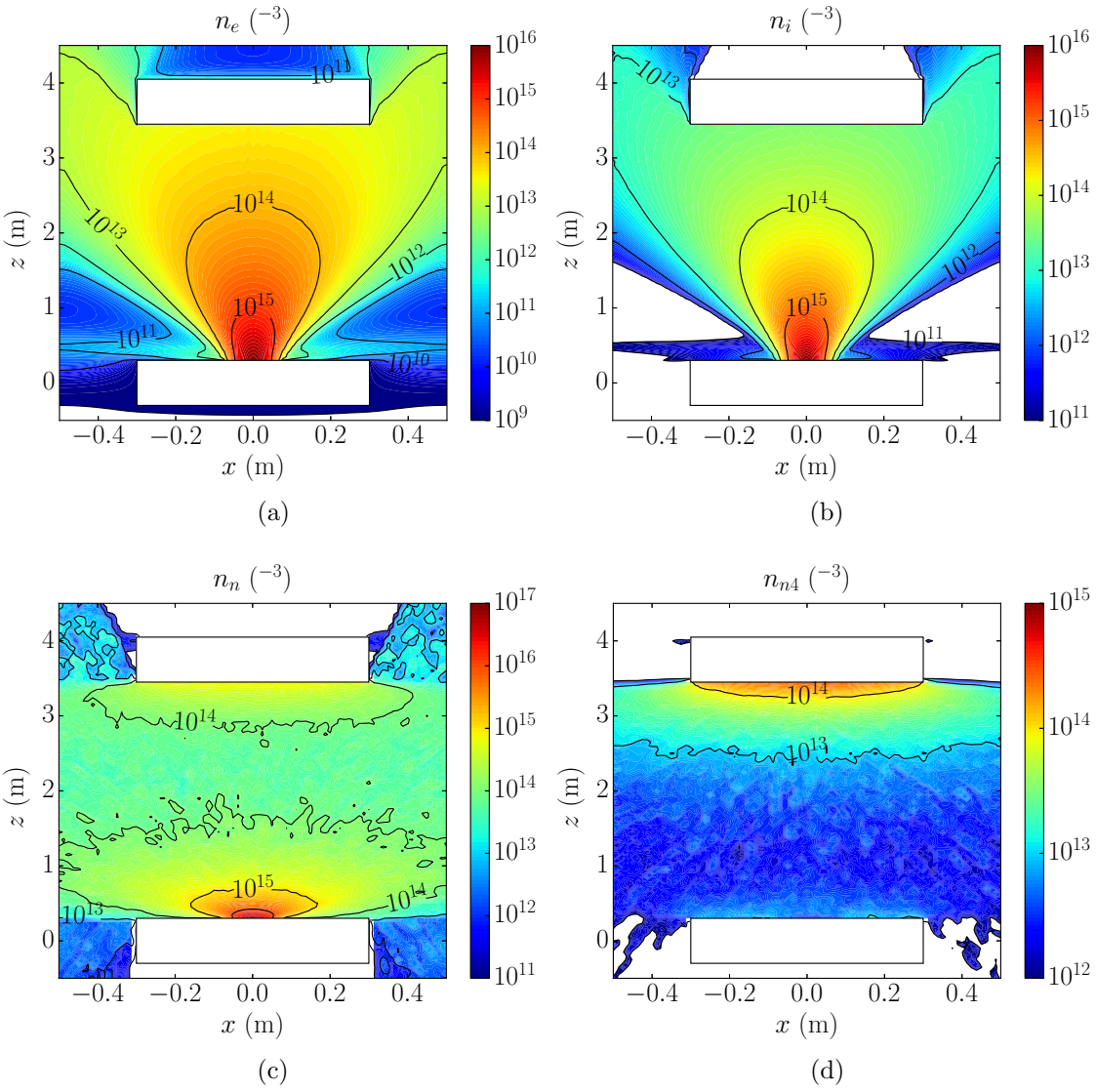

Figure C.21: IBS-like scenario test: densities at the $y = 0$ cross section of (a) electrons, (b) ions (both injected and CEX), (c) neutrals (both injected and recombination), and (d) sputtered neutrals from the target debris.

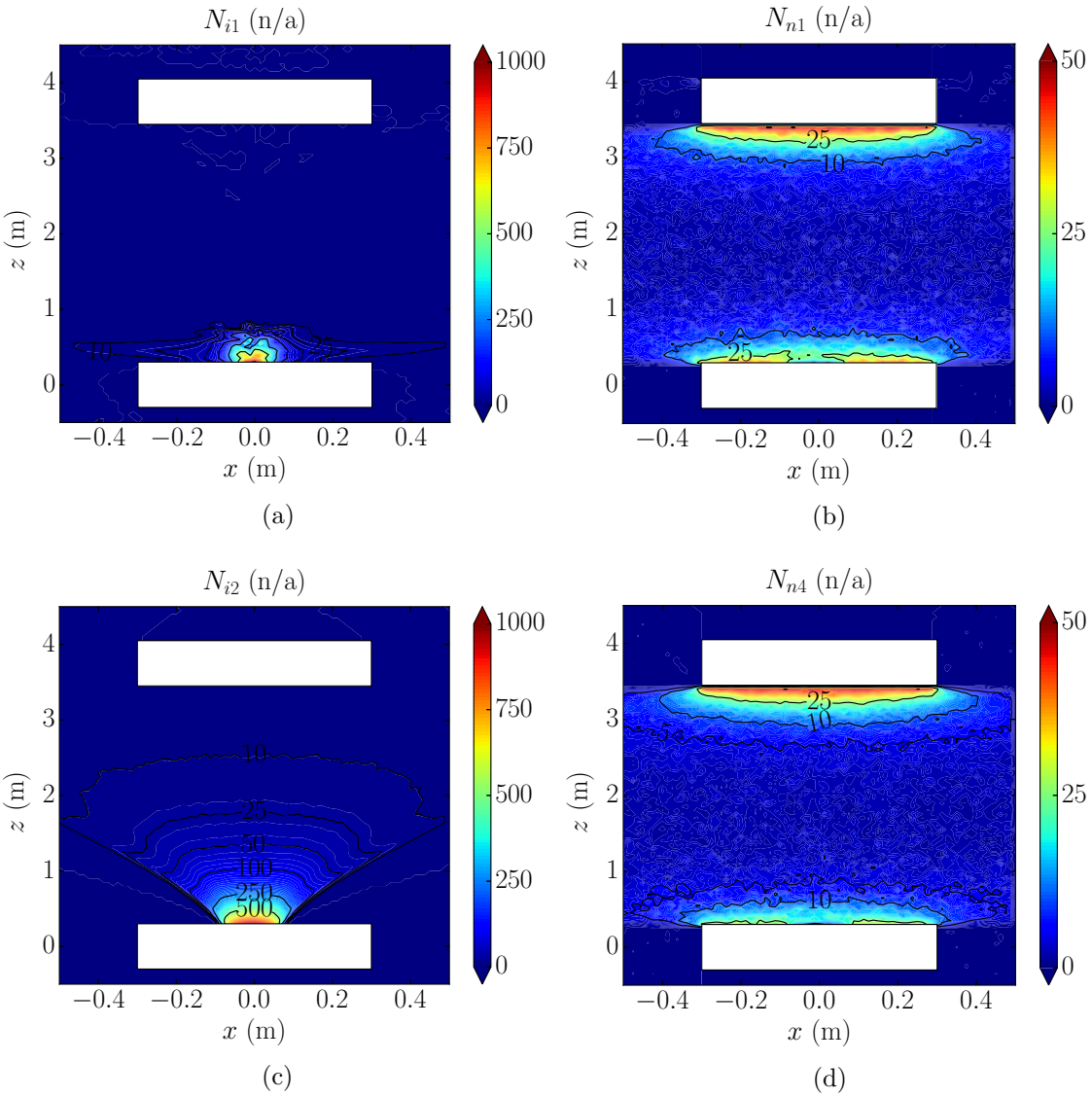

Figure C.22: IBS-like scenario test: number of macro-particles per cell at the $y = 0$ cross section for (a) CEX ions, (b) recombination neutrals, (c) injected ions, and (d) sputtered neutrals. The targeted number per cell for ions is 1000, while for neutrals it is 50.

C.16 Neutralizer-thruster interaction scenario

This test presents a configuration that is similar to that of Sec. 4.1, although featuring a smaller number of mesh nodes (to enable a quicker verification). The main objective of the test is to validate the H_e solver, by comparing the emitted neutralizer electron current with the expected value (from continuity), which is given by the sum of the following terms:

1. electron current to the material walls,
2. electron current to the external boundaries (equal to that of the ions), and
3. electron current generated inside the simulation domain (due to ionization).

The result of the test is quite satisfactory, being the relative error in the emitted electron current of the order of 1%. This error can be further decreased by adopting a finer mesh close to the neutralizer emission surface, or by imposing a more uniform electron conductivity close to the neutralizer (due to the effect of the conductivity gradient in the differential equation). The H_e differential equation error is then shown in Fig. C.23 (a), while the corresponding Bernoulli's function is shown in Fig. C.23 (b).

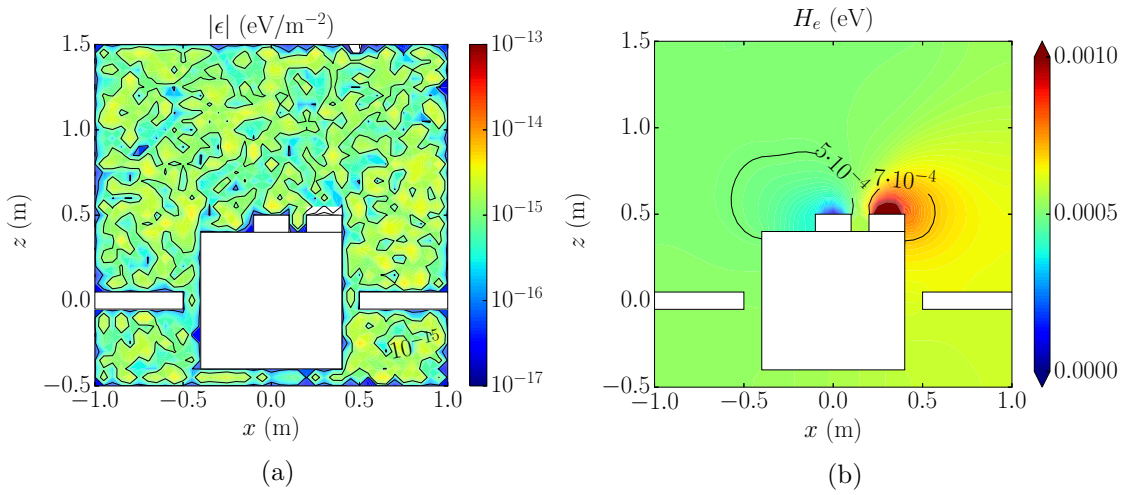

Figure C.23: Neutralizer-thruster interaction test results, at the $y = 0$ cross section: (a) local error (in absolute value) in the differential equation for H_e, and (b) Bernoulli's function H_e.

The solutions for both the electron current density and the electric potential, at the same cross section, are then shown in Fig. C.24 (a) and (b).

Finally, Fig. C.25 (a) and (b) show respectively the evolutions with time of the plasma currents to the different conductive objects, and of their electric potentials. The thruster is short-circuited with the S/C, thus showing no difference of electric potential, while the neutralizer is set to be 13 V positive and the acceleration grid −180 V negative, with respect to the S/C ground. This test then allows to verify that the equivalent circuit is working as expected.

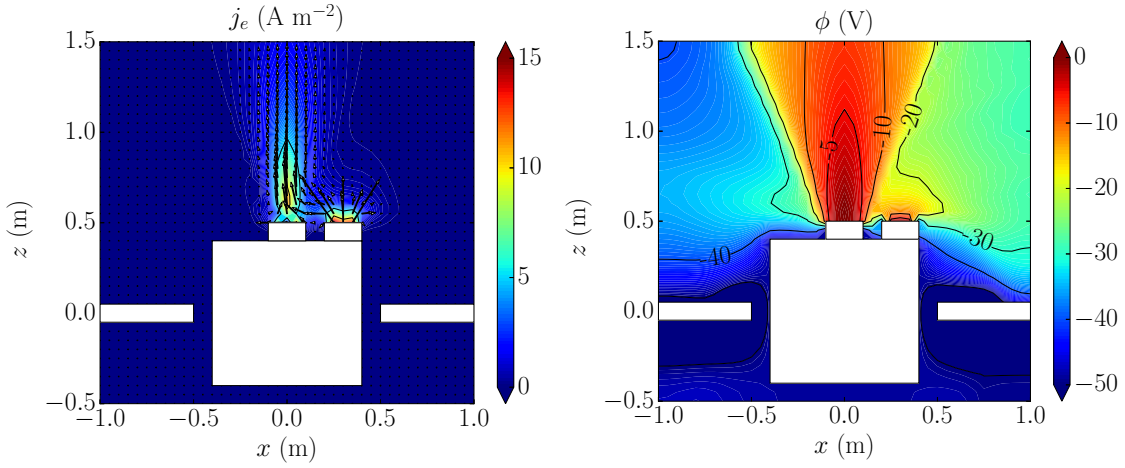

Figure C.24: Neutralizer-thruster interaction test results, at the $y = 0$ cross section: (a) electron current density (the vector direction is along the electron velocity), and (b) electric potential.

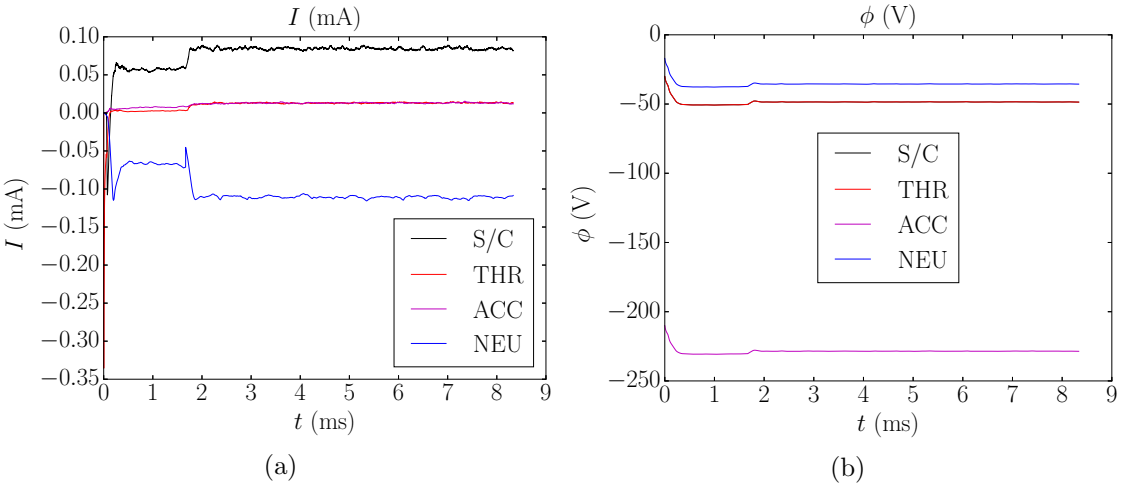

Figure C.25: Neutralizer-thruster interaction test results: evolutions with time of (a) the plasma currents to the different conductive objects, and (b) the conductive objects potentials. In these figures, the S/C cubic body is shown with black lines, the neutralizer with blue lines, the thruster case with red lines, and the acceleration grid with magenta lines. The neutralizer and thruster currents do not include respectively the emitted electron and ion currents, which are set to balance one another.

Bibliography

[1] D.M. Goebel and I. Katz. *Fundamentals of Electric Propulsion: Ion and Hall Thrusters*. Jet Propulsion Laboratory, Pasadena, CA, 2008.

[2] E. Ahedo. Plasmas for space propulsion. *Plasma Physics and Controlled Fusion*, 53(12):124037, 2011.

[3] R.H. Frisbee. Advanced space propulsion for the 21st century. *Journal of Propulsion and Power*, 19(6):1129–1154, 2003.

[4] M. Auweter-Kurtz, T. Gölz, H. Habiger, F. Hammer, H. Kurtz, M. Riehle, and C. Sleziona. High-power hydrogen arcjet thrusters. *Journal of Propulsion and Power*, 14(5):764–773, 1998.

[5] M. Martínez-Sánchez and A. Sakamoto. Simplified analysis of arcjet thrusters. In *29th Joint Propulsion Conference and Exhibit*, Monterey, California, June 28-30, 1993. AIAA, Reston, VA.

[6] S.A. Miller and M. Martínez-Sánchez. Two-fluid nonequilibrium simulation of hydrogen arcjet thrusters. *Journal of Propulsion and Power*, 12(1):112–119, 1996.

[7] H. Bassner, R. Killinger, H. Leiter, and J. Müller. Development steps of the RF-ion thrusters RIT. In *27th International Electric Propulsion Conference*, paper 2001-105, Pasadena, California, October 15-19, 2001. Electric Rocket Propulsion Society, Fairview Park, OH.

[8] J.R. Brophy and P.J. Wilbur. Simple performance model for ring and line cusp ion thrusters. *AIAA journal*, 23(11):1731–1736, 1985.

[9] D.G. Fearn. The application of gridded ion thrusters to high thrust, high specific impulse nuclear-electric missions. *Journal of the British Interplanetary Society*, 58:257–267, 2005.

[10] D.M. Goebel. Analytical discharge model for RF ion thrusters. *IEEE Transactions on Plasma Science*, 36(5):2111–2121, 2008.

[11] J.E. Foster, G.C. Soulas, and M.J. Patterson. Plume and discharge plasma measurements of an NSTAR-type ion thruster. In *36th Joint Propulsion Conference and Exhibit*, paper 2000-3812, Huntsville, Alabama, July 16-19, 2000. AIAA, Reston, VA.

[12] J. Gonzalez, G. Saccoccia, and H.J. Von Rohden. Field emission electric propulsion: experimental investigations on microthrust FEEP thrusters. In *23rd International Electric Propulsion Conference*, paper 1993-157, Seattle, Washington, September 13-16, 1993. Electric Rocket Propulsion Society, Fairview Park, OH.

[13] S. Marcuccio, A. Genovese, and M. Andrenucci. FEEP microthruster technology status and potential applications. In *48th International Astronautical Congress*, Torino, Italy, October 6–10, 1997. IAF, Paris, France.

[14] M. Martínez-Sánchez and J.E. Pollard. Spacecraft electric propulsion - an overview. *Journal of Propulsion and Power*, 14(5):688–699, 1998.

[15] S. Mazouffre, P. Echegut, and M. Dudeck. A calibrated infrared imaging study on the steady state thermal behaviour of Hall effect thrusters. *Plasma Sources Science and Technology*, 16(1):13, 2006.

[16] K. Dannenmayer, S. Mazouffre, E. Ahedo, and M. Merino. Hall effect thruster plasma plume characterization with probe measurements and self-similar fluid models. In *48th Joint Propulsion Conference and Exhibit*, paper 2012-4117, Atlanta, Georgia, July 30 - August 1, 2012. AIAA, Reston, VA.

[17] K. Koch and M. Schirra. The HEMPT concept - a survey on theoretical considerations and experimental evidences. In *32nd International Electric Propulsion Conference*, paper 2011-236, Wiesbaden, Germany, September 11-15, 2011. Electric Rocket Propulsion Society, Fairview Park, OH.

[18] F.F. Chen. Plasma ionization by helicon waves. *Plasma Physics and Controlled Fusion*, 33(4):339, 1991.

[19] F.N. Gesto, B.D. Blackwell, C. Charles, and R.W. Boswell. Ion detachment in the helicon double-layer thruster exhaust beam. *Journal of Propulsion and Power*, 22(1):24–30, 2006.

[20] S. Pottinger, V. Lappas, C. Charles, and R. Boswell. Performance characterization of a helicon double layer thruster using direct thrust measurements. *Journal of Physics D: Applied Physics*, 44(23):235201, 2011.

[21] E. Ahedo and J. Navarro-Cavallé. Helicon thruster plasma modeling: Two-dimensional fluid-dynamics and propulsive performances. *Physics of Plasmas*, 20(4):043512, 2013.

[22] R. Winglee, T. Ziemba, L. Giersch, J. Prager, J. Carscadden, and B.R. Roberson. Simulation and laboratory validation of magnetic nozzle effects for the high power helicon thruster. *Physics of Plasmas*, 14(6):063501, 2007.

[23] H. Kuninaka and S. Satori. Development and demonstration of a cathodeless electron cyclotron resonance ion thruster. *Journal of Propulsion and Power*, 14(6):1022–1026, 1998.

[24] J. Jarrige, P.Q. Elias, F. Cannat, and D. Packan. Performance comparison of an ECR plasma thruster using argon and xenon as propellant gas. In *33rd International Electric Propulsion Conference*, Paper 2013-420, Washington D.C., October 7-10, 2013. Electric Rocket Propulsion Society, Fairview Park, OH.

[25] M. LaPointe and P. Mikellides. High power MPD thruster development at the NASA Glenn Research Center. In *37th Joint Propulsion Conference and Exhibit*, paper 2001-3499, Salt Lake City, Utah, July 8-11, 2001. AIAA, Reston, VA.

[26] E.Y. Choueiri and J.K. Ziemer. Quasi-steady magnetoplasmadynamic thruster performance database. *Journal of Propulsion and Power*, 17(5):967–976, 2001.

[27] R.J. Cassady, W.A. Hoskins, M. Campbell, and C. Rayburn. A micro pulsed plasma thruster (PPT) for the 'Dawgstar' spacecraft. In *Aerospace Conference Proceedings*, volume 4, pages 7–14. IEEE, Piscataway, NJ, 2000.

[28] J. Ziemer, E. Cubbin, E. Choueiri, D. Birx, J. Ziemer, E. Cubbin, E. Choueiri, and D. Birx. Performance characterization of a high efficiency gas-fed pulsed plasma thruster. In *33rd Joint Propulsion Conference and Exhibit*, paper 1997-2925, Seattle, Washington, July 6-9, 1997. AIAA, Reston, VA.

[29] F. Diaz and R. Chang. The VASIMR rocket. *Scientific American*, 283(5):90–97, 2000.

[30] T.W. Glover, D. Chang, R. Franklin, J.P. Squire, V.P. Jacobson, D.G. Chavers, M.D. Carter, M.S. El-Genk, and M.J. Bragg. Principal VASIMR results and present objectives. In *AIP Conference Proceedings*, volume 746, pages 976–982. AIP Publishing, Melville, NY, 2005.

[31] E. Ahedo and M. Merino. On plasma detachment in propulsive magnetic nozzles. *Physics of Plasmas*, 18(5):053504, 2011.

[32] M. Merino and E. Ahedo. Plasma detachment in a propulsive magnetic nozzle via ion demagnetization. *Plasma Sources Science and Technology*, 23(3):032001, 2014.

[33] J. Navarro-Cavallé, M. Martínez-Sánchez, and E. Ahedo. Collisionless electron cooling in a magnetic nozzle. In *50th Joint Propulsion Conference*, paper 2014-4028, Cleveland, Ohio, July 28-30, 2014. AIAA, Reston, VA.

[34] A. Aanesland, A. Meige, and P. Chabert. Electric propulsion using ion-ion plasmas. In *Journal of Physics: Conference Series*, volume 162, page 012009. IOP Publishing, Bristol, UK, 2009.

[35] D. Rafalskyi, L. Popelier, and A. Aanesland. Experimental validation of the dual positive and negative ion beam acceleration in the plasma propulsion with electronegative gases thruster. *Journal of Applied Physics*, 115(5):053301, 2014.

[36] D. Rafalskyi and A. Aanesland. Electron-less negative ion extraction from ion-ion plasmas. *Applied Physics Letters*, 106(10):104101, 2015.

[37] T. Lafleur, D. Rafalskyi, and A. Aanesland. Alternate extraction and acceleration of positive and negative ions from a gridded plasma source. *Plasma Sources Science and Technology*, 24(1):015005, 2015.

[38] T.A. Lafleur, D. Rafalskyi, P. Chabert, and A. Aanesland. Proof-of-concept demonstration of the PEGASES plasma thruster. In *34th International Electric Propulsion Conference*, paper 2015-114, Kobe, Japan, July 6-10, 2015. Electric Rocket Propulsion Society, Fairview Park, OH.

[39] D. Rafalskyi and A. Aanesland. Coincident ion acceleration and electron extraction for space propulsion using the self-bias formed on a set of RF biased grids bounding a plasma source. *Journal of Physics D: Applied Physics*, 47(49):495203, 2014.

[40] H.B. Garrett. The charging of spacecraft surfaces. *Reviews of Geophysics*, 19(4):577–616, 1981.

[41] I.D. Boyd and A. Ketsdever. Interactions between spacecraft and thruster plumes. *Journal of Spacecraft and Rockets*, 38(3):380–380, 2001.

[42] C. Bombardelli and J. Peláez. Ion beam shepherd for contactless space debris removal. *Journal of Guidance, Control, and Dynamics*, 34(3):916–920, 2011.

[43] C. Bombardelli, H. Urrutxua, M. Merino, E. Ahedo, and J. Peláez. Relative dynamics and control of an ion beam shepherd satellite. In *Advances in the Astronautical Sciences, proceedings of Space Flight Mechanics conference 2012*, volume 143, pages 2145–2158. Univelt, Inc., 2012.

[44] C. Bombardelli, H. Urrutxua, M. Merino, E. Ahedo, and J. Peláez. The ion beam shepherd: A new concept for asteroid deflection. *Acta Astronautica*, 90(1):98–102, 2013.

[45] M. Merino, E. Ahedo, C. Bombardelli, H. Urrutxua, and J. Peláez. Ion beam shepherd satellite for space debris removal. In *Progress in Propulsion Physics*, volume 4 of *EUCASS Advances in Aerospace Sciences*, pages 789–802. EDP Sciences, Les Ulis, France, 2013.

[46] M.A. Lieberman and A.J. Lichtenberg. *Principles of plasma discharges and materials processing*. John Wiley and Sons, Hoboken, NJ, 2005.

[47] K. Wilhelm, L. Abbo, F. Auchère, N. Barbey, L. Feng, A.H. Gabriel, S. Giordano, S. Imada, A. Llebaria, W.H. Matthaeus, et al. Morphology, dynamics and plasma parameters of plumes and inter-plume regions in solar coronal holes. *The Astronomy and Astrophysics Review*, 19(1):35, 2011.

[48] D. Mascali, S. Tudisco, A. Bonanno, N. Gambino, S. Ivanovski, A. Anzalone, S. Gammino, R. Miracoli, and F. Musumeci. Colliding laser-produced plasmas: a new tool for nuclear astrophysics studies. *Radiation Effects & Defects in Solids: Incorporating Plasma Science & Plasma Technology*, 165(6-10):730–736, 2010.

[49] F. Cichocki, M. Merino, and E. Ahedo. Modeling and simulation of EP plasma plume expansion into vacuum. In *50th Joint Propulsion Conference*, paper 2014-3828, Cleveland, Ohio, July 28-30, 2014. AIAA, Reston, VA.

[50] M. Merino, F. Cichocki, and E. Ahedo. Collisionless plasma thruster plume expansion model. *Plasma Sources Science and Technology*, 24(3):035006, 2015.

[51] A.G. Korsun, E.M. Tverdokhlebova, and F.F. Gabdullin. Earth's magnetic field effect upon plasma plume expansion. In *25th International Electric Propulsion Conference*, paper 1997-178, Cleveland, Ohio, August 24-28, 1997. Electric Rocket Propulsion Society, Fairview Park, OH.

[52] A.G. Korsun, E.M. Tverdokhlebova, and F.F. Gabdullin. Mathematical model of hypersonic plasma flows expanding in vacuum. *Computer physics communications*, 164(1-3):434–441, 2004.

[53] F.F. Gabdullin, A.G. Korsun, and E.M. Tverdokhlebova. The plasma plume emitted onboard the international space station under the effect of the geomagnetic field. *IEEE Transactions on Plasma Science*, 36(5):2207–2213, 2008.

[54] D. Rapp and W.E. Francis. Charge exchange between gaseous ions and atoms. *Journal of Chemical Physics*, 37(11):2631–2645, 1962.

[55] J.S. Miller, S.H. Pullins, D.J. Levandier, Y. Chiu, and R.A. Dressler. Xenon charge exchange cross sections for electrostatic thruster models. *Journal of Applied Physics*, 91(3):984–991, 2002.

[56] L. Brieda, M.R. Nakles, D.R. Garrett, W.A.Jr. Hargus, and R.L. Spicer. Experimental and numerical examination of the BHT-200 Hall thruster plume. In *30th International Electric Propulsion Conference*, paper 2007-73, Florence, Italy, September 17-20, 2007. Electric Rocket Propulsion Society, Fairview Park, OH.

[57] R.M. Myers and D.H. Manzella. Stationary plasma thruster plume characteristics. In *23rd International Electric Propulsion Conference*, paper 1993-096, Seattle, Washington, September 13-16, 1993. Electric Rocket Propulsion Society, Fairview Park, OH.

[58] B.E. Beal, A. Gallimore, W.A. Hargus, and J.M. Haas. Plasma properties in the plume of a Hall thruster cluster. *Journal of Propulsion and Power*, 20(6):985–991, 2004.

[59] J. Snyder, D.M. Goebel, R.R. Hofer, J.E. Polk, N.C. Wallace, and H. Simpson. Performance evaluation of the T6 ion engine. *Journal of Propulsion and Power*, 28(2):371–379, 2012.

[60] D.E. Parks and I. Katz. A preliminary model of ion beam neutralization. In *14th International Electric Propulsion Conference*, paper 1979-2049, Princeton, New Yersey, October 30 - November 1, 1979. Electric Rocket Propulsion Society, Fairview Park, OH.

[61] J. Ashkenazy and A. Fruchtman. Plasma plume far field analysis. In *27th International Electric Propulsion Conference*, paper 2001-260, Pasadena, California, October 15-19, 2001. Electric Rocket Propulsion Society, Fairview Park, OH.

[62] F. Cichocki, M. Merino, E. Ahedo, Y. Hu, and J. Wang. Fluid vs PIC modeling of a plasma plume expansion. In *34th International Electric Propulsion Conference*, paper 2015-035, Hyogo-Kobe, Japan, July 6-10, 2015. Electric Rocket Propulsion Society, Fairview Park, OH.

[63] B.E. Beal, A. Gallimore, and W.A. Hargus. Plasma properties downstream of a low-power Hall thruster. *Physics of plasmas*, 12(12):123503, 2005.

[64] L.B. King and A.D. Gallimore. Ion-energy diagnostics in the plasma exhaust plume of a Hall thruster. *Journal of Propulsion and Power*, 16(5):916–922, 2000.

[65] S.K. Absalamov, V.B. Andreev, T. Colbert, M. Day, V.V. Egorov, R.U. Gnizdor, H. Kaufman, V. Kim, A.I. Koriakin, and K.N. Kozubskii. Measurement of plasma parameters in the stationary plasma thruster (SPT-100) plume and its effect on spacecraft components. In *28th Joint Propulsion Conference and Exhibit*, paper 1992-3156, Nashville, Tennessee, July 6-8, 1992. AIAA, Reston, VA.

[66] M. Ruiz, I. Urdampilleta, C. Bombardelli, E. Ahedo, M. Merino, and F. Cichocki. The FP7 LEOSWEEP project: Improving low Earth orbit security with enhanced electric propulsion. In *Space Propulsion Conference*, paper 2014-2980908, Cologne, Germany, May 19-22, 2014. 3AF, Paris, France.

[67] A.E. Marini, G.D. Racca, and B.H. Foing. SMART-1 technology preparation for future planetary missions. *Advances in Space Research*, 30(8):1895–1900, 2002.

[68] M. Tajmar, W. Meissl, J. González, B. Foing, H. Laakso, C. Noci, M. Capacci, W.S. Mälkki, and F. Darnon. Charge-exchange plasma contamination on SMART-1: First measurements and model verification. In *40th Joint Propulsion Conference and Exhibit*, paper 2004-3437, Fort Lauderdale, Florida, July 11-14, 2004. AIAA, Reston, VA.

[69] R.W. Hockney and J.W. Eastwood. *Computer simulation using particles*. CRC Press, Boca Ratón, FL, 1988.

[70] C. Cercignani. The Boltzmann equation. In *The Boltzmann Equation and Its Applications*, pages 40–103. Springer, Berlin, Germany, 1988.

[71] J. Büchner, C. Dum, and M. Scholer. *Space plasma simulation*, volume 615. Springer, Berlin, Germany, 2003.

[72] M. Martínez-Sánchez, J. Navarro-Cavallé, and E. Ahedo. Electron cooling and finite potential drop in a magnetized plasma expansion. *Physics of Plasmas*, 22(5):053501, 2015.

[73] G.A. Bird. *Molecular Gas Dynamics and the Direct Simulation of Gas Flows*. The Oxford Engineering Science Series. Oxford University Press, Oxford, UK, 1994.

[74] D. Tskhakaya, K. Matyash, R. Schneider, and F. Taccogna. The particle-in-cell method. *Contributions to Plasma Physics*, 47(8-9):563–594, 2007.

[75] H.Y. Wang, W. Jiang, and Y. Wang. Implicit and electrostatic particle-in-cell/Monte Carlo model in two-dimensional and axisymmetric geometry: I. analysis of numerical techniques. *Plasma Sources Science and Technology*, 19(4):045023, 2010.

[76] J. Wang, O. Chang, and Y. Cao. Electron-ion coupling in mesothermal plasma beam emission: Full particle PIC simulations. *IEEE Transactions on Plasma Science*, 40(2):230–236, 2012.

[77] Y. Hu and J. Wang. Fully kinetic simulations of collisionless, mesothermal plasma expansion. In *13th Spacecraft Charging Technology Conference*, Pasadena, California, June, 23-27, 2014.

[78] J. Wang, D. Han, and Y. Hu. Kinetic simulations of plasma plume potential in a vacuum chamber. *IEEE Transactions on Plasma Science*, 43(9):3047–3053, 2015.

[79] G. Lapenta. Automatic adaptive multi-dimensional particle-in-cell. *Advanced Methods for Space Simulations*, page 61–76, 2007.

[80] D.C. Rapaport. *The art of molecular dynamics simulation*. Cambridge University Press, Cambridge, UK, 2004.

[81] F.J. Alexander and A.L. Garcia. The direct simulation Monte Carlo method. *Computers in Physics*, 11(6):588–593, 1997.

[82] C.P. Robert. *Monte Carlo methods*. John Wiley and Sons, Hoboken, NJ, 2004.

[83] V. Vahedi and M. Surendra. A Monte Carlo collision model for the particle-in-cell method: applications to argon and oxygen discharges. *Computer Physics Communications*, 87(1-2):179–198, 1995.

[84] A.G. Korsun and E.M. Tverdokhlebova. The characteristics of the EP exhaust plume in space. In *33rd Joint Propulsion Conference and Exhibit*, paper 1997-3065, Seattle, Washington, July 6-9, 1997. AIAA, Reston, VA.

[85] A.L. Ortega, I. Katz, I.G. Mikellides, and D.M. Goebel. Self-consistent model of a high-power Hall thruster plume. *IEEE Transactions on Plasma Science*, 43(9):2875–2886, 2015.

[86] D.L. Kahnfeld. Hybrid plume modeling. Master's thesis, Mathematisch-Naturwissenschaftliche Fakultät Ernst-Moritz-Arndt-Universität Greifswald, Greifswald, Germany, 2015.

[87] B. Korkut and D.A. Levin. Three dimensional DSMC-PIC simulations of ion thruster plumes with SUGAR. In *50th Joint Propulsion Conference*, paper 2014-3447, Cleveland, Ohio, July 28–30, 2014. AIAA, Reston, VA.

[88] B. Korkut, Z. Li, and D.A. Levin. 3-D simulation of ion thruster plumes using octree adaptive mesh refinement. *IEEE Transactions on Plasma Science*, 43(5):1706–1721, 2015.

[89] S.J. Araki, R.S. Martin, D. Bilyeu, and J.W. Koo. SM/MURF: Current capabilities and verification as a replacement of AFRL plume simulation tool COLISEUM. In *52nd Joint Propulsion Conference*, paper 2016-4939, Salt Lake City, Utah, July 25-27, 2016. AIAA, Reston, VA.

[90] C. Cai. Numerical studies on plasma plume flows from a cluster of electric propulsion devices. *Aerospace Science and Technology*, 41:134–143, 2015.

[91] F. Taccogna, D. Pagano, F. Scortecci, and A. Garulli. Three-dimensional plume simulation of multi-channel thruster configuration. *Plasma Sources Science and Technology*, 23(6):065034, 2014.

[92] I. Boyd and J. Yim. Hall thruster plume simulation using a detailed hybrid model. In *40th Joint Propulsion Conference and Exhibit*, paper 2004-3952. AIAA, Reston, VA, 2004.

[93] M. Celik, M. Santi, S. Cheng, M. Martínez-Sánchez, and J. Peraire. Hybrid-PIC simulation of a Hall thruster plume on an unstructured grid with DSMC collisions. In *28th International Electric Propulsion Conference*, paper 2003-134, Toulouse, France, March 17-21, 2003. Electric Rocket Propulsion Society, Fairview Park, OH.

[94] F. Cichocki, A. Domínguez, M. Merino, and E. Ahedo. A 3D hybrid code to study electric thruster plumes. In *Space Propulsion Conference*, paper 2016-3124968, Rome, Italy, May 2-6, 2016. 3AF, Paris, France.

[95] M.M. Santi. *Hall thruster plume simulation using a hybrid-PIC algorithm.* PhD thesis, Massachusetts Institute of Technology, Boston, MA, 2003.

[96] J. Forest, L. Eliasson, and A. Hilgers. A new spacecraft plasma simulation software, PicUp3D/SPIS. In *7th Spacecraft Charging Technology Conference*, volume 476, page 515, The Netherlands, April 23-27, 2001.

[97] M. Masselin. Development of a hybrid PIC code for the simulation of plasma spacecraft interactions. Master's thesis, University of Stockholm, Sweden, 2012.

[98] M. Wartelski, C. Theroude, C. Ardura, and E. Gengembre. Self-consistent simulations of interactions between spacecraft and plumes of electric thrusters. In *33rd International Electric Propulsion Conference*, paper 2013-73, Washington D.C., October 7-10, 2013. Electric Rocket Propulsion Society, Fairview Park, OH.

[99] D.Y. Oh, D.E. Hasting, C.M. Marrese, J.M. Haas, and A.D. Gallimore. Modeling of SPT-100 thruster plumes and implications for satellite design. *Journal of Propulsion and Power*, 15(2):345–357, 1999.

[100] L. Garrigues, J. Bareilles, J.P. Boeuf, and I.D. Boyd. Modeling of the plasma jet of a stationary plasma thruster. *Journal of applied physics*, 91(12):9521–9528, 2002.

[101] S. Cheng, M. Santi, M. Celik, M. Martínez-Sánchez, and J. Peraire. Hybrid PIC-DSMC simulation of a Hall thruster plume on unstructured grids. *Computer physics communications*, 164(1):73–79, 2004.

[102] L. Brieda, J. Pierru, R. Kafafy, and J. Wang. Development of the DRACO code for modeling electric propulsion plume interactions. In *40th Joint Propulsion Conference and Exhibit*, paper 2004-3633. AIAA, Reston, VA, 2004.

[103] O. Kalentev, K. Matyash, J. Duras, K.F. Lüskow, R. Schneider, N. Koch, and M. Schirra. Electrostatic ion thrusters-towards predictive modeling. *Contributions to Plasma Physics*, 54(2):235–248, 2014.

[104] R.L. Estergaard. Ion beam shepherd: Analysis of the plasma bridge interaction. Master's thesis, University Carlos III de Madrid (UC3M), Leganés, Madrid, Spain, 2015.

[105] J. Szabo, N. Warner, M. Martínez-Sánchez, and O. Batishchev. Full particle-in-cell simulation methodology for axisymmetric Hall effect thrusters. *Journal of Propulsion and Power*, 30(1):197–208, 2013.

[106] S. Cho, K. Komurasaki, and Y. Arakawa. Kinetic particle simulation of discharge and wall erosion of a Hall thruster. *Physics of Plasmas*, 20(6):063501, 2013.

[107] F. Taccogna, R. Schneider, S. Longo, and M. Capitelli. Kinetic simulations of a plasma thruster. *Plasma Sources Science and Technology*, 17(2):024003, 2008.

[108] A. Cohen-Zur, A. Fruchtman, and A. Gany. The effect of pressure on the plume divergence in the Hall thruster. *IEEE Transactions on Plasma Science*, 36(5):2069–2081, 2008.

[109] E. Ahedo and M. Merino. Two-dimensional supersonic plasma acceleration in a magnetic nozzle. *Physics of Plasmas*, 17:073501, 2010.

[110] C. Charles, R.W. Boswell, and M.A. Lieberman. Xenon ion beam characterization in a helicon double layer thruster. *Applied Physics Letters*, 89:261503, 2006.

[111] E. Ahedo and J. Navarro. Helicon thruster plasma modeling: Two-dimensional fluid-dynamics and propulsive performances. *Physics of Plasmas*, 20:043512, 2013.

[112] M.J. Zucrow and J.D. Hoffman. *Gas dynamics*. John Wiley and Sons, Hoboken, NJ, 1976.

[113] D.G. Courtney and M. Martínez-Sánchez. Diverging cusped-field Hall thruster. In *30th International Electric Propulsion Conference*, paper 2007-039, Florence, Italy, September 17-20, 2007. Electric Rocket Propulsion Society, Fairview Park, OH.

[114] I.G. Mikellides, G.A. Jongeward, B.M. Gardner, I. Katz, M.J. Mandell, and V.A. Davis. A Hall-effect thruster plume and spacecraft interactions modeling package. In *27th International Electric Propulsion Conference*, paper 2001-251, Pasadena, California, October 15-19, 2001. Electric Rocket Propulsion Society, Fairview Park, OH.

[115] N. Brenning, T. Hurtig, and M.A. Raadu. Conditions for plasmoid penetration across abrupt magnetic barriers. *Physics of plasmas*, 12(1):012309, 2005.

[116] Y. Hu and J. Wang. Electron properties in collisionless mesothermal plasma expansion: Fully kinetic simulations. *IEEE Transactions on Plasma Science*, 43(9):2832–2838, 2015.

[117] Y. Hu and J. Wang. On the validity of the Boltzmann assumption for electrons in plasma plume modeling. In *52nd Joint Propulsion Conference*, paper 2016-4938, Salt Lake City, Utah, July 25-27, 2016. AIAA, Reston, VA.

[118] Y. Hu and J. Wang. Fully kinetic simulations of collisionless, mesothermal plasma emission: Macroscopic plume structure and microscopic electron characteristics. *Physics of Plasmas*, 24(3):033510, 2017.

[119] J. Ashkenazy, A. Fruchtman, Y. Raitses, and N.J. Fisch. Modelling the behaviour of a Hall current plasma accelerator. *Plasma physics and controlled fusion*, 41(3A):A357, 1999.

[120] F. Cichocki, A. Domínguez, M. Merino, and E. Ahedo. Hybrid 3D model for the interaction of plasma thruster plumes with nearby objects. *Plasma Sources Science and Technology*, 26(12):125008, 2017.

[121] F. Cichocki, M. Merino, and E. Ahedo. Spacecraft-plasma-debris interaction in an ion beam shepherd mission. *Acta Astronautica*, 2017 (submitted).

[122] C.K. Birdsall and D. Fuss. Clouds-in-clouds, clouds-in-cells physics for many-body plasma simulation. *Journal of Computational Physics*, 135(2):141–148, 1997.

[123] K. Nanbu and Y. Kitatani. An ion-neutral species collision model for particle simulation of glow discharge. *Journal of Physics D: Applied Physics*, 28(2):324, 1995.

[124] Y. Azziz, M. Martínez-Sánchez, and J. Szabo. Determination of in-orbit plume characteristics from laboratory measurements. In *42nd Joint Propulsion Conference and Exhibit*, paper 2006-4484, Sacramento, California, July 9-12, 2006. AIAA, Reston, VA.

[125] Y. Azziz. *Experimental and theoretical characterization of a Hall thruster plume*. PhD thesis, Massachusetts Institute of Technology, Boston, MA, 2007.

[126] F.I. Parra, E. Ahedo, J.M. Fife, and M. Martínez-Sánchez. A two-dimensional hybrid model of the Hall thruster discharge. *Journal of Applied Physics*, 100(2):023304, 2006.

[127] M. Mitchner and C.H. Kruger Jr. *Partially ionized gases*. John Wiley and Sons, Hoboken, NJ, 1973.

[128] E.W. Bell, N. Djurić, and G.H. Dunn. Electron-impact ionization of In^+ and Xe^+. *Physical Review A*, 48(6):4286, 1993.

[129] J.F. Ziegler, M.D. Ziegler, and J.P. Biersack. SRIM - The stopping and range of ions in matter (2010). *Nuclear Instruments and Methods in Physics Research B*, 268(11-12):1818–1823, 2010.

[130] Y. Yamamura. Theory of sputtering and comparison to experimental data. *Nuclear Instruments and Methods in Physics Research*, 194(1-3):515–522, 1982.

[131] P. Sigmund. Recollections of fifty years with sputtering. *Thin Solid Films*, 520(19):6031–6049, 2012.

[132] R. Santos and E. Ahedo. Implementation of the kinetic Bohm condition in a Hall thruster hybrid code. In *45th Joint Propulsion Conference*, paper 2009-4913, Denver, Colorado, August 2-5, 2009. AIAA, Reston, VA.

[133] E. Ahedo, R. Santos, and F. Parra. Fulfillment of the kinetic Bohm criterion in a quasineutral particle-in-cell model. *Physics of Plasmas*, 17(7):073507, 2010.

[134] E.R. Harrison and W.B. Thompson. The low pressure plane symmetric discharge. *Proceedings of the Physical Society*, 74(2):145, 1959.

[135] G. Lapenta. Particle rezoning for multidimensional kinetic particle-in-cell simulations. *Journal of computational physics*, 181(1):317–337, 2002.

[136] R.S. Martin and J.L. Cambier. Octree particle management for DSMC and PIC simulations. *Journal of Computational Physics*, 327:943–966, 2016.

[137] M. Merino, P. Fajardo, and E. Ahedo. Collisionless electron cooling in unmagnetized plasma thruster plumes. In *52nd Joint Propulsion Conference*, paper 2016-5037, Salt Lake City, Utah, July 25-27, 2016. AIAA, Reston, VA.

[138] J. Navarro-Cavallé, S. Correyero, and E. Ahedo. Collisionless electron cooling on magnetized plasma expansions: advances on modelling. In *34th International Electric Propulsion Conference*, paper 2015-117, Kobe, Japan, July 6-10, 2015. Electric Rocket Propulsion Society, Fairview Park, OH.

[139] R.J. Goldston and P.H. Rutherford. *Introduction to Plasma Physics*. CRC Press, Boca Ratón, FL, 1995.

[140] P.M. Bellan. *Fundamentals of Plasma Physics*. Cambridge University Press, Cambridge, UK, 2006.

[141] J.A. Bittencourt. *Fundamentals of plasma physics*. Springer, Berlin, Germany, 2013.

[142] M. Hayashi. Bibliography of electron and photon cross sections with atoms and molecules published in the 20th century. Xenon. Technical report, National Institute for Fusion Science, 2003.

[143] J. Polk, R. Kakuda, J. Anderson, J. Brophy, V. Rawlin, M. Patterson, J. Sovey, and J. Hamley. Validation of the NSTAR ion propulsion system on the Deep Space One mission - overview and initial results. In *35th Joint Propulsion Conference and Exhibit*, paper 1999-2274, Los Angeles, California, June 20-24, 1999. AIAA, Reston, VA.

[144] J.R. Brophy. NASA's Deep Space 1 ion engine (plenary). *Review of Scientific Instruments*, 73(2):1071–1078, 2002.

[145] J.E. Foster, G.J. Williams, and M.J. Patterson. Characterization of an ion thruster neutralizer. *Journal of propulsion and power*, 23(4):828–835, 2007.

[146] J.R. Brophy, C.E. Garner, and S.C. Mikes. Dawn ion propulsion system: Initial checkout after launch. *Journal of Propulsion and Power*, 25(6):1189–1202, 2009.

[147] R.I.S. Roy, D.E. Hastings, and N.A. Gastonis. Ion-thruster plume modeling for backflow contamination. *Journal of Spacecraft and Rockets*, 33(4):525–534, 1996.

[148] R.I.S. Roy, D.E. Hastings, and N.A. Gastonis. Numerical study of spacecraft contamination and interactions by ion-thruster effluents. *Journal of Spacecraft and Rockets*, 33(4):535–542, 1996.

[149] J. Wang, D. Brinza, and M. Young. Three-dimensional particle simulation modeling of ion propulsion plasma environment for Deep Space One. *Journal of Spacecraft and Rockets*, 38(3):433–440, 2001.

[150] F. Taccogna and G. Dilecce. Non-equilibrium in low-temperature plasmas. *The European Physical Journal D*, 70(11):251, 2016.

[151] F. Cichocki, M. Merino, E. Ahedo, M. Smirnova, A. Mingo, and M. Dobkevicius. Electric propulsion subsystem optimization for "Ion Beam Shepherd" missions. *Journal of Propulsion and Power*, 33(2):370–378, 2017.

[152] F. Cichocki, M. Merino, E. Ahedo, D. Feili, and M. Ruiz. Electric propulsion subsystem optimization for "Ion Beam Shepherd" missions. In *34th International Electric Propulsion Conference*, paper 2015-420, Hyogo-Kobe, Japan, July 6-10, 2015. Electric Rocket Propulsion Society, Fairview Park, OH.

[153] J.C. Liou, N.L. Johnson, and N.M. Hill. Controlling the growth of future LEO debris populations with active debris removal. *Acta Astronautica*, 66(5):648–653, 2010.

[154] D.J. Kessler, N.L. Johnson, J.C. Liou, and M. Matney. The Kessler syndrome: implications to future space operations. In *AAS Guidance and Control Conference*, paper 2010-016. American Astronautical Society, Springfield, VA, 2010.

[155] J.C. Liou and N.L. Johnson. A sensitivity study of the effectiveness of active debris removal in LEO. *Acta Astronautica*, 64(2):236–243, 2009.

[156] L. Jasper, P. Andersony, H. Schaubz, and D. McKnight. Economic and risk challenges of operating in the current space debris environment. In *3rd European Workshop on Space Debris Modeling and Remediation*, Paper 8.2, CNES, Paris, France, 2014.

[157] D. Feili, M. Ruiz, M. Merino, F. Cichocki, E. Ahedo, M. Smirnova, and M. Dobkevicius. Impulse transfer thruster for an ion beam shepherd mission. In *34th International Electric Propulsion Conference*, paper 2015-382, Kobe, Japan, July 6-10, 2015. Electric Rocket Propulsion Society, Fairview Park, OH.

[158] A. Alpatov, F. Cichocki, A. Fokov, S. Khoroshylov, M. Merino, and A. Zakrzhevskii. Determination of the force transmitted by an ion thruster plasma plume to an orbital object. *Acta Astronautica*, 119:241–251, 2016.

[159] J.R. Anderson, K.D. Goodfellow, J.E. Polk, V.K. Rawlin, J.S. Sovey, and M.J. Patterson. Performance characteristics of the NSTAR ion thruster during an on-going long duration ground test. In *Aerospace Conference Proceedings*, volume 4, pages 99 – 122. IEEE, Piscataway, NJ, 2000.

[160] G.C. Soulas. Improving the total impulse capability of the NSTAR ion thruster with thick-accelerator-grid ion optics. In *27th International Electric Propulsion Conference*, paper 2001-081, Pasadena, California, October 15-19, 2001. Electric Rocket Propulsion Society, Fairview Park, OH.

[161] F. Cichocki, D. Rafalskyi, A. Aanesland, and M. Merino. The plume neutralization process of the PEGASES thruster. In *Space Propulsion Conference*, paper 2016-3124967, Rome, Italy, May 2-6, 2016. 3AF, Paris, France.

[162] N. Oudini, A. Aanesland, P. Chabert, S. Lounes-Mahloul, and A. Bendib. Near-field plume properties of an ion beam formed by alternating extraction and acceleration of oppositely charged ions. *Plasma Sources Science and Technology*, 25(5):055013, 2016.

[163] A. Aanesland, J. Bredin, P. Chabert, and V. Godyak. Electron energy distribution function and plasma parameters across magnetic filters. *Applied Physics Letters*, 100(4):044102, 2012.

[164] T. Lafleur and A. Aanesland. Ambipolar and non-ambipolar diffusion in an RF plasma source containing a magnetic filter. *Physics of Plasmas*, 21(6):063510, 2014.

[165] M.B. Thomas, D. Rafalskyi, T. Lafleur, and A. Aanesland. Experimental investigation of electron transport across a magnetic field barrier in electropositive and electronegative plasmas. *Plasma Sources Science and Technology*, 25(4):045018, 2016.

[166] D. Rafalskyi, S. Dudin, and A. Aanesland. Magnetized retarding field energy analyzer measuring the particle flux and ion energy distribution of both positive and negative ions. *Review of Scientific Instruments*, 86(5):053302, 2015.